Physics at the International Linear Collider

Physics Chapter of the ILC Detailed Baseline Design Report

Preliminary Version: Draft of September 3, 2012

please address questions or comments to: mpeskin@slac.stanford.edu

Editorial Team:

Howard Baer[1], Tim Barklow[2], Keisuke Fujii[3], Yuanning Gao[4], Andre Hoang[5], Shinya Kanemura[6], Jenny List[7], Heather E. Logan[8], Andrei Nomerotski[9], Jürgen Reuter[10], Maxim Perelstein[11], Michael E. Peskin[12], Roman Poeschl[13], Aurore Savoy-Navarro[14], Geraldine Servant[15], Tim M. P. Tait[16], Jaehoon Yu[17]

[1]University of Oklahoma, Norman, OK 73019, USA
[2]SLAC, Stanford University, 2575 Sand Hill Rd., Menlo Park, CA 94025, USA
[3]KEK, 1-1 Oho, Tsukuba-shi, Ibaraki-ken 305-0801, JAPAN
[4]Department of Engineering Physics, Tsinghua University, Beijing, CHINA
[5]Inst. für Theor. Physik, Universität Wien, Boltzmanngasse 5, A-1090 Vienna, AUSTRIA
[6]Department of Physics, University of Toyama, 3190 Gofuku, Toyama 930-8555, JAPAN
[7]DESY, Notkestrasse 85, D-22607 Hamburg, GERMANY
[8]Ottawa-Carleton Inst. for Physics, Carleton University, Ottawa, Ontario K1S 5B6, CANADA
[9]Department of Physics, University of Oxford, Keble Road, Oxford OX1 3RH, UK
[10]DESY, Notkestrasse 85, D-22607 Hamburg, GERMANY
[11]Department of Physics, Cornell University, Ithaca NY 14853, USA
[12]SLAC, Stanford University, 2575 Sand Hill Rd., Menlo Park, CA 94025, USA
[13]LAL, Université Paris Sud, F-91898 Orsay CEDEX, FRANCE
[14]Astroparticle and Cosmology Laboratory, Université Paris-Diderot, Paris 7/CNRS, FRANCE
[15]TH Division, Case C01600, CERN, CH-1211 Geneva 23, SWITZERLAND
[16]Department of Physics, University of California, Irvine, CA USA
[17]Physics Department, University of Texas, Arlington, TX 76019, USA

Contents

1 Introduction **6**

1.1 Physics at the ILC 6

1.2 Advantages of e^+e^- Colliders 7

1.2.1 Cleanliness 7

1.2.2 Democracy 9

1.2.3 Calculability 10

1.2.4 Detail 10

1.3 Key Physics Explorations at the ILC 11

2 Standard Model Higgs **16**

2.1 The Standard Model Higgs mechanism 17

2.2 Higgs coupling deviations in extended models 20

2.2.1 The Decoupling Limit 20

2.2.2 New states to solve the gauge hierarchy problem 21

2.2.3 Composite Higgs 23

2.2.4 Additional sources of electroweak symmetry breaking 24

2.2.5 Mixing of the Higgs with an electroweak-singlet scalar 26

2.2.6 Conclusions 26

2.3 Status and prospects for Higgs measurements at LHC 27

2.3.1 The LHC Higgs discovery 27

2.3.2 Prospects for measuring the Higgs mass and quantum numbers at LHC 28

2.3.3 Prospects for determining the Higgs couplings from LHC data 29

2.3.4 Prospects for measurement of the triple Higgs coupling at the LHC 32

2.4 Higgs measurements at ILC at 250 GeV 32

2.4.1 Mass and Quantum Numbers 34

2.4.2 Inclusive cross section 38
2.4.3 Branching Ratios 38
2.5 Higgs measurements at ILC at 500 GeV 42
2.5.1 Top Yukawa Coupling 43
2.5.2 Higgs Self-coupling 44
2.5.3 WW Fusion and HWW Coupling 46
2.5.4 Expected Improvements of Branching Ratio Measurements . . 47
2.6 Higgs measurements at ILC at 1000 GeV 47
2.6.1 Measurement of $H \to \mu^+\mu^-$ decay using $e^+e^- \to \nu\bar{\nu}H$ 49
2.6.2 Top Yukawa Coupling 49
2.6.3 Higgs Self-coupling in the $e^+e^- \to \nu\bar{\nu}HH$ Process 50
2.7 Conclusion 50

3 Two-Fermion Processes **60**
3.1 Systematics of $e^+e^- \to f\bar{f}$ 60
3.2 Z' physics 61
3.2.1 Benchmark Z' Models 62
3.2.2 Current Limits on Z' and the ILC Reach 63
3.2.3 Measurement of Z' couplings 63
3.2.4 Example: $SO(10)$ Z' at 3 TeV 65
3.3 Quark and Lepton Compositeness 65
3.4 Extra Dimensions 66
3.4.1 Flat, TeV-Sized Extra Dimensions 67
3.4.2 Large Extra Dimensions 67
3.4.3 Randall-Sundrum Warped Extra Dimensions 69

4 W and Z Boson Physics **72**
4.1 Introduction 72

4.2 Beyond the SM W/Z sector: the EW chiral Lagrangian 72
4.2.1 Electroweak effective Lagrangian 73
4.2.2 Trilinear and quartic vector boson couplings 76
4.2.3 Resonances in the strongly coupled Higgs sector 78
4.2.4 Vector boson scattering and unitarity 81
4.3 $e^+e^- \to W^+W^-$ 87
4.4 $e^+e^- \to ZZ$ 88
4.5 $\gamma\gamma \to W^+W^-$ 88
4.6 Triple vector boson production 89
4.7 WW, ZZ scattering at high energy 91
4.8 Giga-Z 95

5 Top quark **100**
5.1 Top quark properties from hadron colliders 100
5.1.1 Top quark hadronic cross section 101
5.1.2 Top quark mass and width 101
5.1.3 Helicity of the W boson 103
5.1.4 Top coupling to Z^0 and γ 103
5.1.5 Asymmetries at hadron colliders 104
5.2 $e^+e^- \to t\bar{t}$ at Threshold 105
5.2.1 Status of QCD Theory 105
5.2.2 Simulations and Measurements 107
5.3 Probing the top quark vertices at the ILC 108
5.3.1 Models with Top and Higgs Compositeness 109
5.3.2 ILC measurements 111
5.3.3 An example: the Randall Sundrum scenario 113
5.4 Concluding remarks 114

6 Extended Higgs Sectors **119**
6.1 Motivation for extended Higgs sectors 119
6.2 General description of extended Higgs sectors 119
6.2.1 The Two Higgs Doublet Model 120
6.2.2 Models with Higgs Singlets 122
6.2.3 Models with Higgs Triplets 124
6.3 Extended Higgs bosons searches at the ILC 126
6.3.1 Constraints from the LHC experiments 126
6.3.2 Higher mass neutral Higgs Production at ILC 130
6.3.3 Charged Higgs boson Productions 132
6.3.4 Measurement of $\tan\beta$ 135
6.4 More possibilities 137
6.5 Summary 140

7 SUSY **145**
7.1 Introduction 145
7.2 Setting the Scene 146
7.3 Direct and Indirect Experimental Constraints 148
7.3.1 Particle Sectors of a Supersymmetric Model 148
7.3.2 Indirect Constraints on SUSY Models 148
7.3.3 Impact of Higgs Searches 150
7.3.4 Direct Searches for Supersymmetric Particles 151
7.3.5 Impact of the constraints on the SUSY particle sectors 152
7.4 Two benchmark points for the ILC 153
7.4.1 Natural SUSY and light higgsinos 153
7.4.2 An MSSM model with light sleptons 154
7.5 Experimental Capabilities and Parameter Determination 154
7.5.1 Neutralino and Chargino Sector 156

7.5.2 Gravitinos 158
7.5.3 Third generation squarks 160
7.5.4 Scalar charged leptons 161
7.5.5 Sneutrinos 164
7.5.6 Beyond the CP and RP conserving MSSM 165
7.5.7 Parameter Determination and Model Discrimination 167
7.6 Conclusions 168

8 Cosmological Connections **179**
8.1 Baryogenesis at the Electroweak Scale 179
8.1.1 MSSM EW baryogenesis: The light stop scenario under pressure 179
8.1.2 EW baryogenesis in Composite Higgs models 183
8.1.3 Effective field theory approach to the EW phase transition . . 186
8.2 Dark Matter and the ILC 188
8.2.1 Status of dark matter 188
8.2.2 Theories of WIMPs 190
8.2.3 Prospects for ILC determination of dark matter parameters . 192

9 Conclusion **205**

1 Introduction

1.1 Physics at the ILC

For more than twenty years, an advanced electron-positron collider has been put forward as a key component of the future program of elementary particle physics. We have a well-established Standard Model of particle physics, but it is known to be incomplete. Among the many questions that this model leaves open, there are two — the origin of the masses of elementary particles and the particle identity of cosmic dark matter – that should be addressed at energy scales below 1 TeV. It has been appreciated for a long time that a next-generation electron-positron collider would give us the ability to make precision measurements that would shed light on these mysteries.

Now the technology to build this electron-positron collider has come of age. This report is a volume of the Detailed Baseline Design report for the International Linear Collider (ILC). The accompanying volumes of this report lay out the technical design of a high-luminosity e^+e^- collider at 500 GeV in the center of mass and of detectors that could make use of the collisions to perform high-precision measurements. In this volume, we summarize the physics arguments for building this collider and their appropriate relation to the situation of particle physics as of August 2012. The discussion in this volume supplements the presentation of the physics opportunities for a 500 GeV e^+e^- collider given in the review articles [1,2,3], the 2001 regional study reports [4,5,6], and the 2007 ILC Reference Design Report [7].

There are two important reasons to review the physics arguments for the ILC now. First, the Large Hadron Collider (LHC) has now begun to explore the energy region up to 1 TeV in proton-proton collisions. The LHC experiments have discovered a resonance that is a strong candidate for a Higgs boson similar to that of the Standard Model and have measured the mass of this resonance to be about 125 GeV [8]. It has been understood for a long time that there are intrinsic limitations to the ability of hadron colliders to study color-singlet scalar particles, and that precision measurements, to the few percent level, are needed to place a new scalar particle correctly within our model of particle physics. The ILC is an ideal machine to address this question. In this report, we will describe the system of measurements that will be needed to probe the identity of the Higgs boson and present new estimates of the capability of the ILC to make those measurements.

We will also describe many other opportunities that the ILC provides to probe for and study new physics, both through the production of new particle predicted by models of physics beyond the Standard Model and through the study of indirect effects of new physics on the W and Z bosons, the top quark, and other systems that can be studied with precision at the ILC. It is important to re-evaluate the merits of these experiments in view of new constraints from the LHC, and we will do that in this report.

The experience of operating the LHC and its detectors also allows us to make more concrete projections of the long-term capabilities of the LHC experiments and the complementarity of the measurements from the ILC experiments. We have tried to incorporate the best available information into this report.

A second reason to revisit to physics case for the ILC is that the studies for the technical design and benchmarking of the ILC detectors have given us a more precise understanding of their eventual capabilities. In many cases, the performance of the detectors found in full-simulation studies exceeds the capabilities claimed from studies done at earlier stages of the conceptual detector design process. Our estimates here will be based on these new results.

To support a major accelerator project such as the ILC, it should be a criterion that this project will advance our knowledge of particle physics *qualitatively* beyond the information that will be available from currently operating accelerators, including the results expected from the future stages of the LHC. In this report, we will address this question. We will demonstrate the profound advances that the ILC will make in our understanding of fundamental physics.

1.2 Advantages of e^+e^- Colliders

Over the past forty years, experiments at proton and electron colliders have played complementary roles in illuminating the properties of elementary particles. For example, the bottom quark was first discovered in 1977 through the observation of the Υ resonances in proton-proton collisions. However, many of the most revealing properties of the b quark, from its unexpectedly long lifetime to its decays with time-dependent CP violation, were discovered at e^+e^- colliders.

Today, the LHC offers obvious advantages for experimenters in providing very high energy and very high rates in typical reactions. The advantages of the ILC are different and perhaps more subtle to appreciate. In this section, we will review these advantages in general terms. We will revisit these points again and again in our discussions of specific processes that will be studied at the ILC.

1.2.1 Cleanliness

An elementary difference between hadron and electron collisions is apparent in the design of detectors: The environment for electron-positron collisions is much more

Figure 1: Material depth in units of interaction length (a) for the CMS detector at the LHC as a function of pseudorapidity η, (b) for the SiD detector at the ILC as a function of the polar angle.

benign. At LHC energies, the proton-proton total cross section is roughly 100 mb. In the current scheme for running the LHC, proton-proton bunch collisions occur every 50 nsec, each bunch crossing leads to about 30 proton-proton collisions, and each of these produces hundreds of energetic particles. At the ILC, the most important chronic background source comes from photon-photon collisions, for which the cross section is hundreds of nb. Bunch crossings are spaced by about 300 nsec; at each bunch crossing we expect about 1 photon-photon collision, producing a few hadrons in the final state. Each e^+e^- bunch crossing does produce a large number of secondary electron-positron pairs, but these are mainly confined to a small volume within 1 cm of the beam.

The difference between hadron-hadron and e^+e^- collisions has profound implications for the detectors and for experimentation. The LHC detectors must be made of radiation-hard materials to handle a high occupancy rate. They must have thick calorimeters to contain particles with a wide range of energies, requiring also the placement of solenoids inside the calorimeter volume. They must have complex trigger systems that cut down rates to focus on the most interesting events. At the ILC, tracking detectors can be made as thin as technically feasible. All elements, from the vertex detector to the calorimeter, can be brought much closer to the interaction point and contained inside the solenoid. Figure 1 shows a comparison of the CMS detector for the LHC and the SiD detector for ILC, in terms of the material depths in unit of interaction length of each detector component. The ILC detectors are projected to improve the momentum resolution from tracking by a factor of 10 and the jet energy resolution of the detector by a factor of 3 or better. The very close placement of the innermost pixel vertex detector layer leads to excellent b, charm and τ tagging capabilities. In addition, the complications in analyzing LHC events due to hadrons from the underlying-event and pileup from multiple collisions in each beam crossing are essentially removed at the ILC. The e^+e^- environment thus provides a setting in which the basic high-energy collision can be measured with high precision.

1.2.2 Democracy

The elementary coupling e of the photon is the same for all species of quarks and leptons, and the same also for new particles from beyond the Standard Model. Thus, e^+e^- annihilation produces pairs of all species, new and exotic, at similar rates.

At the LHC, the gluon couples equally to all quarks and to new colored particles. However, here, this democracy is hardly evident experimentally. Soft, non-perturbative strong interactions are the dominant mechanism for particle production and involve only the light quarks and gluons. Further, because the proton is a composite object with parton distributions that fall steeply, the production cross sections are much lower for heavy particles than for light ones. At the LHC, the cross section for producing bottom quarks is of the order of 1 mb, already much lower than the total inelastic cross section. The cross section for top quark pair production at the 14 TeV LHC is expected to be about 1 nb. Production cross sections for new particles will be 1 pb or smaller. Thus, interesting events occur at rates of 10^{-7} to 10^{-13} of the total event rate. This implies, first, that a trigger system is needed to exclude all events but 1 in 10^6 before any data analysis is possible. Beyond this, only events with unusual and striking properties can be recognized in the much larger sample of background QCD events. A new particle or process can be studied only if its signals can be clearly discriminated from those of QCD reactions.

At the ILC, the cross sections for light quark and lepton pair production are much smaller, but also more comparable to the cross sections for interesting new physics processes. The main Standard Model processes in e^+e^- annihilation — annihilation to quark and lepton pairs, annihilation to W^+W^-, and single W and Z production – all have cross sections at the pb level at 500 GeV. New particle production processes typically have cross sections of order 10–100 fb and result in events clearly distinguishable from the basic Standard Model reactions.

This has a number of important implications for e^+e^- experimentation. First, no trigger is needed. The ILC detectors can record all bunch crossings and performed any needed event reduction offline. Second, no special selection is needed in classifying events. That is, all final states of a decaying particle, not only the most characteristic ones, can be used for physics analyses. At the LHC, it is not possible to measure absolute branching ratios or total widths; at the ILC, these quantitites are directly accessible. Third and perhaps most importantly, at the ILC, it is much easier to recognize W and Z bosons in their hadronic decay modes than at the LHC. Since most W and Z decays are to hadronic modes, this is a tremendous advantage in the systematic study of heavy particles whose decay products typically include the weak bosons. We will see that this advantage applies not only to exotic particles but also in the study of the top quark and the Higgs boson.

1.2.3 Calculability

At the LHC, all cross section calculations rely on QCD. Any theoretical calculation of signal or background has systematic uncertainties from the proton structure functions, from unknown higher-order perturbative QCD corrections, and from nonperturbative QCD effects. NLO QCD corrections to cross section calculations are typically at the 30-50% level. For the Higgs boson cross section, the first correction is +100%. To achieve theoretical errors smaller than 10% requires computations to NNLO or beyond, a level that is not feasible now except for the simplest reactions.

At the ILC, the initial-state e^- and e^+ are pointlike elementary particles, coupling only to the electroweak interactions. The first radiative corrections to cross sections are at the few-percent level. With effort, one can reach the part-per-mil level of theoretical precision, a level already achieved in the theoretical calculations for the LEP program.

Thus, it is possible to study heavy particles through their effects in perturbing the Standard Model at lower energies. For example, the LHC will be able to detect Z' bosons up to 4-5 TeV by searches for production of high-mass $\mu^+\mu^-$ pairs. The ILC at 500 GeV is sensitive to the presence of bosons with comparably high masses by searching for deviations from the precise Standard Model predictions for $e^+e^- \to f\overline{f}$ cross sections. By studying the dependence of these deviations on flavor and polarization, the ILC experiments can reconstruct the complete phenomenological profile of the heavy boson. Similar precision measurements can give new information about heavy particles that couple to the top quark and the Higgs boson.

Beyond this, the high precision theoretical understanding of Standard Model signal and background processes available at the ILC can make it possible to find elusive new physics interactions, and to characterize these interactions fully.

1.2.4 Detail

Because of the simplicity of event selections at the ILC and the absence of a complicating underlying event, physics analyses at the ILC can be done by reconstructing complete events and determining quark and lepton momenta by kinematic fitting. Such an analysis reveals the spin-dependence of production and decay processes. The ILC will also provide polarized electron and positron beams, and so the processes studied there can be completely characterized for each initial and final polarization state.

We are used to thinking of quarks and leptons at low energy as single massive

Figure 2: Spin asymmetries in $e^+e^- \to t\bar{t}$.

objects. However, at energies above the Z^0 mass, the left- and right-handed components of quarks and leptons behave as distinct particles with different $SU(2) \times U(1)$ quantum numbers. The weak-interaction decays of heavy particles, including the top quark and the W and Z bosons, have order-1 spin asymmetries. These spin effects are typically small and subtle at hadron colliders, but at the ILC they are obvious aspects of the physics. In Fig. 2, we present an array of different spin asymmetries visible in the process $e^+e^- \to t\bar{t}$. In every process studied at the ILC, polarization effects provide a crucial new handle on the physics, allowing us to make interpretations at the basic level of the underlying weak-interaction quantum numbers.

1.3 Key Physics Explorations at the ILC

In the following sections of this volume, we will present the major aspects of the physics program of the ILC. We will see explicitly how the key features of e^+e^- experimentation outlined above translate into measurements with direct and illuminating physical interpretation.

We will begin by discussing the ILC program on the Higgs boson. There is now great excitement over the discovery of a bosonic resonance at the LHC whose properties are consistent with those of the Higgs boson. This particle might indeed be the Higgs boson predicted by the Standard Model, a similar particle arising from a different model of electroweak symmetry breaking, or a particle of totally different origin that happens to be a scalar resonance. To choose among these options, detailed precision measurements of this particle are needed.

In Section 2, we will present the program of precision measurements of the properties of this new boson that would be made by the ILC experiments. Since the new boson is observed to decay to WW and ZZ at rates comparable to the predictions for the Standard Model Higgs boson, we already know that its production cross section at the ILC will be sufficient to carry out this program. We will first set out the requirements for an experimental program that has sufficient sensitivity to distinguish the various hypotheses for the nature of the new scalar. Very high precision—at the level of several percent accuracy in the new coupling constants—is needed. It is unlikely that the LHC experiments will reach this level of performance. We will then describe the variety of measurements that the ILC experiment would be expected to carry out for this particle at the various stage of ILC operation. We will show that these measurements will be extremely powerful probes. They will definitively settle the question of the nature of the new boson and will give insight into any larger theory of which it might be a part.

The LHC has not yet provided evidence for signals of new physics beyond the Standard Model from its early running at 7 and 8 TeV. There are two distinct attitudes to take toward the current situation. The first is that it is premature to draw any conclusions at the present time. The LHC experimental program is still in its early stages. The accelerator has not yet reached its design energy and has so far accumulated only 1% of its eventual data set. The second is that the discovery of the new scalar boson—especially if turns out to have the properties similar to the Standard Model Higgs boson—and the deep exclusions already made for supersymmetry and other new physics models have already changed our ideas about new physics at the TeV energy scale. Our information from the LHC is certainly incomplete. We look forward to new information and new discoveries in the LHC run at 14 TeV that will take place in the latter years of this decade. And, yet, we must take seriously the implications of what we have already learned.

Though the Standard Model of particle physics is internally consistent and, so far, is not significantly challenged experimentally, it is incomplete in many respects. We have reviewed the problems earlier in this section. What are the solutions?

Traditionally, there have been three classes of models of new physics beyond the Standard Model. The first class postulates that electroweak symmetry is broken by new strong interactions at the TeV energy scale. In these models, the key observables are the parameters of weak vector boson scattering at TeV energies. The discovery of a new light scalar, especially if its couplings to W and Z are seen to be those characteristic of a Higgs boson with a nonzero vacuum expectation value, deals a signficant blow to this whole set of models.

The second class of models posulates that electroweak symmetry breaking is due to the expectation value of an effective Higgs field that is composite at a higher mass scale. Little Higgs models, in which the Higgs boson is a Goldstone boson of a higher energy theory, and Randall-Sundrum models and other theories with new dimensions of space, are examples of theories in this class. These theories predict new particles with the quantum numbers of the top quark and the W and Z bosons, with TeV masses. These particles should eventually be discovered at the LHC in its 14 TeV program. The other crucial predictions of these models are modifications of the couplings of the heaviest particles of the Standard Model, the W, Z, and top quark.

The ILC is ideally suited to observe these effects through precision measurement of the properties of W, Z, and t. Extreme energies are not required; the ILC design center of mass energy of 500 GeV is quite sufficient.

The third class of models postulates the Higgs field as an elementary scalar field, requiring supersymmetry to tame its ultraviolet divergences. The LHC has now excluded the constrained supersymmetric models that were considered paradigmatic in the period up to 2009 for masses low enough that supersymmetry dynamics naturally drives electroweak symmetry breaking. However, supersymmetry has a large parameter space, and compelling regions are still consistent with the LHC exclusions. The typical property of these regions is that the lightest supersymmetric particles are the fermionic partners of the Higgs bosons. These particles are very difficult to discover or study at the LHC but are expected to be readily accessible to the ILC at 500 GeV. Models of this type are also likely to contain additional Higgs bosons at relatively low masses that would be targets of study at the ILC.

Thus, we argue, the exclusion of new physics at this early stage of the LHC program, combined with the observation of a new boson resembling the Standard Model Higgs boson, strengthens the case for the ILC as probe of new physics beyond the Standard Model.

In Sections 3–7 of this report, we will explain this viewpoint in full detail. We will begin in Section 3 with a review of the ILC program on $e^+e^- \to f\overline{f}$ processes, where f is a light quark or lepton. The precision study of these processes is sensitive to new heavy gauge bosons. These reactions also probe models with extra space dimensions, and models in which the electron is composite with a very small size. We will explain how experiments at 500 GeV can reveal the nature of any such boson or composite structure, qualitatively improving on the information that we will obtain from the LHC.

In Sections 4–5, we will describe the ILC program relevant to models with a light Higgs boson that is composite at a higher energy scale. In Section 4, we will review the ILC program on the W and Z bosons. We will describe the capabilities of the ILC for the measurement of W boson couplings and W boson scattering. We will show that how these measurements are capable of revealing new terms in the couplings of W and Z induced by Higgs composite structure.

In Section 5, we will review the ILC program on the top quark. We will describe the study of top quark production at threshold and at higher energies near the maximum of the cross section for $e^+e^- \to t\bar{t}$. This study gives new, nontrivial, tests of QCD and also gives access to couplings of the top quark that are extremely difficult to study at the LHC. In models in which the top quark couples to a composite Higgs boson or a strongly interacting Higgs sector, the couplings of the top quark to the Z

boson provide crucial tests not available at the LHC. We will describe the beautiful probes of these couplings availabe at the 500 GeV ILC.

In Sections 6–7, we will discuss the ILC program in searching for and measuring the properties of new particles predicted by supersymmetry and other models in which the Higgs boson is an elementary scalar field. We will discuss particles that, although they are within the energy range of the ILC, they would not be expected to be found at the LHC at the current stage of its program. These particles might be discovered at the LHC with higher energy or luminosity, or their discovery might have to wait for the ILC. In either case, the ILC will make measurements that will be key to understanding their role in models of new physics.

In Section 6, we will review ILC measurements on new bosons associated with the Higgs boson within a larger theory of electroweak symmetry breaking. We will note many aspects of these more complex theories that the ILC will be able to clarify, beyond the results anticipated from the LHC.

In Section 7, we will review the program of ILC measurements on supersymmetric particles that might be present in the ILC mass range. In this discussion, we will review the current constraints on supersymmetry. We will observe that many scenarios are still open in which new particles can found at the 500 GeV ILC. We will present the detailed program of measurements that the ILC can carry out on these particles. This discussion will also illustrate that broad capabilities that the ILC experiments provide to understand the nature of new particles discovered at the LHC, whatever their origin in terms of an underlying model.

As we have already noted, the current exclusions of new particles by the LHC experiments drive us, in models of supersymmetry, to models in which the lightest supersymmetric particles are the charged and neutral Higgsinos, which would naturally lie in the 100–200 GeV mass range. These particles are very difficult to identify at the LHC but would be easily seen and studied at the ILC. More generally, if supersymmetry is indeed realized in nature, the ILC can be expected to directly probe those parameters of supersymmetry most intimately connected to the mechanism of electroweak symmetry breaking. We will explain this point of view in detail in Section 7.

Finally, in Section 8, we will discuss the role of the ILC in understanding cosmology and, in particular, the unique experiments possible at the ILC that will shed light on the nature of the dark matter of the universe. Section 9 will give some general conclusions.

References

[1] H. Murayama and M. E. Peskin, Ann. Rev. Nucl. Part. Sci. **46**, 533 (1996) [hep-ex/9606003].

[2] E. Accomando *et al.* [ECFA/DESY LC Physics Working Group Collaboration], Phys. Rept. **299**, 1 (1998) [hep-ph/9705442].

[3] S. Dawson and M. Oreglia, Ann. Rev. Nucl. Part. Sci. **54**, 269 (2004) [hep-ph/0403015].

[4] T. Abe *et al.* [American Linear Collider Working Group Collaboration], "Linear collider physics resource book for Snowmass 2001." hep-ex/0106055,0106056,0106057,0106058.

[5] F. Richard, J. R. Schneider, D. Trines, and A. Wagner, eds., "TESLA: The superconducting electron positron linear collider with an integrated X-ray laser laboratory. Technical design report." hep-ph/0106314.

[6] K. Abe *et al.* [ACFA Linear Collider Working Group Collaboration], "Particle physics experiments at JLC," hep-ph/0109166.

[7] G. Aarons *et al.* [ILC Collaboration], "International Linear Collider Reference Design Report Volume 2: Physics At The ILC," Volume 2, (2007). `http://www.linearcollider.org/about/Publications/Reference-Design-Report`, arXiv:0709.1893 [hep-ph].

[8] `http://indico.cern.ch/conferenceDisplay.py?confId=197461`.

2 Standard Model Higgs

Precision studies of the weak interactions at LEP, Tevatron, and LHC have shown that they are described by a spontaneously broken $\mathrm{SU}(2)_L \times \mathrm{U}(1)_Y$ gauge theory. The quantum numbers of all fermions are verified experimentally, and the properties of the heavy vector bosons W and Z predicted by the theory are in excellent accord with the theory at the level of one-loop electroweak corrections [1]. However, the basic $SU(2) \times U(1)$ symmetry of the model forbids the generation of mass for all quarks, leptons, and vector bosons. Thus, this symmetry must be spontaneously broken. The theory of weak interactions then requires a vacuum condensate that carries charge under the $\mathrm{SU}(2)_L \times \mathrm{U}(1)_Y$ gauge groups.

In local quantum field theory, it is not possible to simply postulate the existence of a uniform vacuum condensate. This condensate must be associated with a field that has dynamics and quantum excitations. To prove the correctness of our theory of weak interactions, it is essential to study this field directly and to prove through experiments that the field and its quantum excitations have the properties required to generate mass for all particles. We have little direct or indirect information about the nature of this field. The Standard Model postulates the simplest possibility, that the needed spontaneous symmetry breaking is generated by one $SU(2)$ doublet scalar field, the Higgs field, with one new physical particle, the Higgs boson. The true story of electroweak spontaneous symmetry breaking could be much more complex.

The Higgs field, or a more general Higgs sector, couples to every type of particle. It likely plays an important role in all of the unanswered questions of elementary particle physics, including the nature of new forces and underlying symmetries, CP violation and baryogenesis, and the nature and relation of quark and lepton flavors. To make progress on these problems, we must understand the Higgs sector in detail.

In July 2012, the ATLAS and CMS experiments presented very strong evidence for a new particle whose properties are consistent with those of the Standard Model Higgs boson [2]. This gives us a definite point of entry into the exploration of the Higgs sector. It would be ideal to produce this particle in a well-controlled setting and measure its mass, quantum numbers, and couplings with high precision. The particle is at a mass, 125 GeV, that is readily accessible to a next-generation e^+e^- collider. It has been observed to couple to ZZ and WW, insuring that the major production reactions in e^+e^- collisions are present. The ILC is precisely the right accelerator to make these experiments available.

Though there is no reason to believe that the simple picture given by the Standard Model is correct, the minimal theory of electroweak symmetry breaking given by the Standard Model is a convenient place to begin in describing the capabilities of any experimental facility. This is especially true because, as we will describe in Section 2.2, most models with larger and more complex Higgs sectors contain a particle that strongly resembles the Standard Model Higgs boson.

In this section, then, we will describe the capabilities of the ILC to obtain a comprehensive understanding of the Standard Model Higgs boson. In Section 2.1, we will review the Higgs mechanism and write its basic formulae. In Section 2.2, we will discuss the relation of the Standard Model Higgs boson to similar particles in more general theories of elementary particles. We will review the Decoupling Theorem that requires a boson similar to the Standard Model Higgs boson in a wide variety of models, and we will review the expected sizes of deviations from the simplest Standard Model expectation. In Section 2.3, we will review the prospects for measurements on the Higgs boson at the LHC. In Sections 2.4-2.6, we will discuss the capabilities of the ILC to measure properties of the Higgs boson in stages of center of mass energy—250 GeV, 500 GeV, and 1 TeV.

The prospects for the ILC to investigate other possible states of the Higgs sector will be discussed separately in Section 6 of this report.

2.1 The Standard Model Higgs mechanism

We begin by briefly reviewing the Higgs mechanism in the Standard Model (SM). In the SM, electroweak symmetry is broken by an SU(2)-doublet scalar field,

$$\Phi = \begin{pmatrix} G^+ \\ (h+v)/\sqrt{2} + iG^0/\sqrt{2} \end{pmatrix} . \tag{1}$$

Here h is the physical SM Higgs boson and G^+ and G^0 are the Goldstone bosons eaten by the W^+ and Z. Electroweak symmetry breaking is caused by the Higgs potential, the most general gauge-invariant renormalizable form of which is,

$$V = \mu^2 \Phi^\dagger \Phi + \lambda \left(\Phi^\dagger \Phi \right)^2 . \tag{2}$$

A negative value of μ^2 leads to a minimum away from zero field value, causing electroweak symmetry breaking. Minimizing the potential, the Higgs vacuum expectation value (vev) and the physical Higgs mass are

$$v^2 = -\mu^2/\lambda \simeq (246 \text{ GeV})^2, \quad m_h^2 = 2\lambda v^2 = 2|\mu^2|. \tag{3}$$

For $m_h \sim 125\,\text{GeV}$, we have a weakly coupled theory with $\lambda \sim 1/8$ and $|\mu^2| \sim m_W^2$. The potential also gives rise to triple and quartic interactions of h, with Feynman rules given by

$$hhh: \ -6i\lambda v = -3i\frac{m_h^2}{v}, \quad hhhh: \ -6i\lambda = -3i\frac{m_h^2}{v^2}. \tag{4}$$

The couplings of the physical Higgs boson to other SM particles are predicted entirely in terms of v and the known particle masses via the SM Higgs mass generation mechanism. The couplings of the W and Z bosons to the Higgs arise from the gauge-kinetic terms,

$$\mathcal{L} \supset (\mathcal{D}^\mu \Phi)^\dagger (\mathcal{D}_\mu \Phi), \quad \mathcal{D}_\mu = \partial_\mu - igA_\mu^a T^a - ig' B_\mu Y, \tag{5}$$

where g and g' are the $\mathrm{SU}(2)_L$ and $\mathrm{U}(1)_Y$ gauge couplings, respectively, and the hypercharge of the Higgs doublet is $Y = 1/2$. This gives rise to the W and Z masses,

$$M_W = g\frac{v}{2}, \quad M_Z = \sqrt{g^2 + g'^2}\frac{v}{2}, \tag{6}$$

and couplings to the Higgs given by

$$\begin{aligned} W_\mu^+ W_\nu^- h:\ i\frac{g^2 v}{2} g_{\mu\nu} = 2i\frac{M_W^2}{v} g_{\mu\nu}, &\qquad W_\mu^+ W_\nu^- hh:\ i\frac{g^2}{2} g_{\mu\nu} = 2i\frac{M_W^2}{v^2} g_{\mu\nu}, \\ Z_\mu Z_\nu h:\ i\frac{(g^2 + g'^2)v}{2} g_{\mu\nu} = 2i\frac{M_Z^2}{v} g_{\mu\nu}, &\qquad Z_\mu Z_\nu hh:\ i\frac{(g^2 + g'^2)}{2} g_{\mu\nu} = 2i\frac{M_Z^2}{v^2} g_{\mu\nu} \end{aligned} \tag{7}$$

The photon remains massless and has no tree-level coupling to the Higgs.

The couplings of the quarks and charged leptons to the Higgs arise from the Yukawa terms,

$$\mathcal{L} \supset -y_{ij}^u \overline{u}_{Ri} \tilde{\Phi}^\dagger Q_{Lj} - y_{ij}^d \overline{d}_{Ri} \Phi^\dagger Q_{Lj} - y_{ij}^\ell \overline{\ell}_{Ri} \Phi^\dagger L_{Lj} + \text{h.c.}, \tag{8}$$

where $Q_L = (u_L, d_L)^T$, $L_L = (\nu_L, e_L)^T$, $\tilde{\Phi} = i\sigma^2 \Phi^*$ is the conjugate Higgs doublet, and y^u, y^d, and y^ℓ are 3×3 Yukawa coupling matrices for the up-type quarks, down-type quarks, and charged leptons, respectively. The Yukawa matrices can be eliminated in favor of the fermion masses, yielding Higgs couplings to fermions proportional to the fermion mass,

$$h\overline{f}f:\ -i\frac{y^f}{\sqrt{2}} = -i\frac{m_f}{v}, \tag{9}$$

where $y^f v/\sqrt{2} = m_f$ is the relevant fermion mass eigenvalue.

Thus we see that, in the SM, all the couplings of the Higgs are predicted with no free parameters once the Higgs mass is known. This allows the Higgs production cross sections and decay branching ratios to be unambiguously predicted. The key regularity is that each Higgs coupling is proportional to the mass of the corresponding particle. One-loop diagrams provide additional couplings and decay modes to gg, $\gamma\gamma$, and γZ. In the SM, the Higgs coupling to gg arises mainly from the one-loop diagram involving a top quark. The Higgs couplings to $\gamma\gamma$ and γZ arise at the one-loop level mainly from diagrams with W bosons and top quarks in the loop.

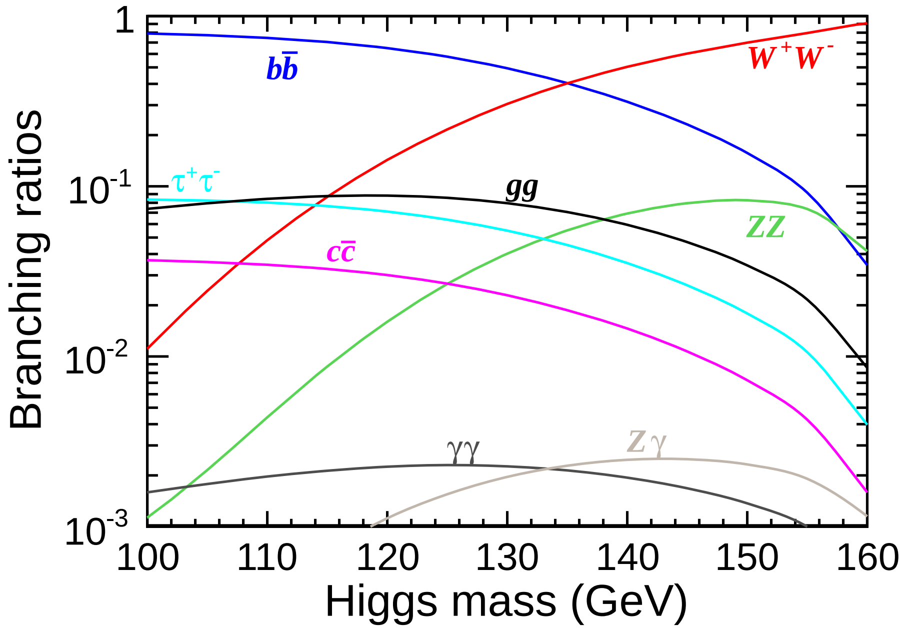

Figure 3: Branching fractions of the Standard Model Higgs as a function of the Higgs mass.

Figure 3 plots the branching fraction of the Standard Model Higgs boson as a function of the Higgs mass. The figure tells us that the Higgs boson mass of $M_h \simeq$ 125 GeV provides a very favorable situation in which a large number of decay modes have similar sizes and are accessible to experiments that provide a large Higgs event sample. The ILC, including its eventual 1 TeV stage, will allow measurement of the Higgs boson couplings to W, Z, b, c, τ, and μ, plus the loop-induced couplings to gg and $\gamma\gamma$ [**and** γZ**?**]. The regularity of the SM that the Higgs couplings are precisely proportional to mass can thus be verified or refuted through measurements of many couplings spanning a large dynamic range.

A deviation of any of the tree-level Higgs boson couplings to WW, ZZ, or SM fermions indicates that additional new physics—either additional Higgs boson(s) or electroweak symmetry-breaking strong dynamics—is needed to generate the full masses of these particles and to unitarize the associated scattering amplitudes in the high-energy limit [3,4].

2.2 Higgs coupling deviations in extended models

2.2.1 The Decoupling Limit

In this section, we will discuss possible modifications of the Higgs boson couplings that might be searched for in precision Higgs experiments. It is a general property of of models of new physics beyond the Standard Model that they contain a light scalar field, elementary or effective, whose vacuum expectation value is the main source of electroweak symmetry breaking. It is possible that this particle can look very different from the Standard Model Higgs boson. At the moment, there is much interest in this question, stimulated by the values of the first measured Higgs production rates. Models predicting such large deviations can be found in [20,6,5,7] and other recent theoretical papers. If it turns out that the new boson has couplings very different from the Standard Model predictions, it will of course be important to measure those couplings as accurately as possible.

However, it is much more common that the lightest Higgs boson of new physics models has coupling that differ at most at the 5-10% level from the Standard Model expectations. This point was made recently through the study of a number of examples by Gupta, Rzehak, and Wells [8]; we will provide some additional examples here. A future program of Higgs physics must acknowledge this point and strive for the level of accuracy that is actually called for in these models.

The logic of this prediction is expressed by the Decoupling Limit of Higgs models described by Haber in [9]. Consider a model with many new particles, in which all of these new particles are heavy while an $SU(2)$ doublet of scalars has a relatively small mass parameter. There are many reasons why the mass parameter of the doublet might be smaller than the typical mass scale of new particles. It might be driven small by renormalization group running, as happens in supersymmetry; it might be suppressed because the scalar is a pseudo-Goldstone boson, as happens in Little Higgs models. In any event, if there is separation between the masses of other new particles and the mass parameter of the scalar doublet, we can integrate out the heavy particles and write an effective Lagrangian for the light doublet. The resulting effective theory is precisely the Standard Model, plus possible higher-dimension operators. If the light doublet acquires a vev, its physical degree of freedom is an effective Higgs particle, with precisely the properties of the Standard Model Higgs up to the effects of the higher-dimension operators. These effects are then required to be of the order of

$$m_h^2/M^2 \quad \text{or} \quad m_t^2/M^2 \ , \tag{10}$$

where M is the mass scale of the new particles. The following sections will give quantitative examples of Higgs coupling deviations that follow this systematic dependence.

2.2.2 New states to solve the gauge hierarchy problem

Many models of new physics are proposed to solve the *gauge hierarchy problem* by removing the quadratic divergences in the loop corrections to the Higgs field mass term μ^2. Supersymmetry and Little Higgs models provide examples. Such models require new scalar or fermionic particles with masses below a few TeV that cancel the divergent loop contributions to μ^2 from the top quark. For this to work, the couplings of the new states to the Higgs must be tightly constrained in terms of the top quark Yukawa coupling. Usually the new states have the same electric and color charge as the top quark, which implies that they will contribute to the loop-induced hgg and $h\gamma\gamma$ couplings. The new loop corrections contribute coherently with the Standard Model loop diagrams.

For scalar new particles (e.g., the two top squarks in the MSSM), the resulting effective hgg and $h\gamma\gamma$ couplings are given by

$$\begin{aligned} g_{hgg} &\propto \left| F_{1/2}(m_t) + \frac{2m_t^2}{m_T^2} F_0(m_T) \right| , \\ g_{h\gamma\gamma} &\propto \left| F_1(m_W) + \frac{4}{3} F_{1/2}(m_t) + \frac{4}{3} \frac{2m_t^2}{m_T^2} F_0(m_T) \right| . \end{aligned} \tag{11}$$

Here F_1, $F_{1/2}$, and F_0 are the loop factors defined in [10] for spin 1, spin 1/2, and spin 0 particles in the loop, and m_T is the mass of the new particle(s) that cancels the top loop divergence. For application to the MSSM, we have set the two top squark masses equal for simplicity. For fermionic new particles (e.g., the top-partner in Little Higgs models), the resulting effective couplings are

$$\begin{aligned} g_{hgg} &\propto \left| F_{1/2}(m_t) + \frac{m_t^2}{m_T^2} F_{1/2}(m_T) \right|, \\ g_{h\gamma\gamma} &\propto \left| F_1(m_W) + \frac{4}{3} F_{1/2}(m_t) + \frac{4}{3} \frac{m_t^2}{m_T^2} F_{1/2}(m_T) \right|. \end{aligned} \quad (12)$$

For simplicity, we have ignored the mixing between the top and its partner. For $m_h = 120$–130 GeV, the loop factors are given numerically by $F_1(m_W) = 8.2$–8.5 and $F_{1/2}(m_t) = -1.4$. For $m_T \gg m_h$, the loop factors tend to constant values, $F_{1/2}(m_T) \to -4/3$ and $F_0(m_T) \to -1/3$.

Very generally, then, such models predict deviations of the loop-induced Higgs couplings from top-partners of the decoupling form. Numerically, for a scalar top-partner,

$$\frac{g_{hgg}}{g_{h_{\rm SM}gg}} \simeq 1 + 1.4\% \left(\frac{1 \text{ TeV}}{m_T} \right)^2, \qquad \frac{g_{h\gamma\gamma}}{g_{h_{\rm SM}\gamma\gamma}} \simeq 1 - 0.4\% \left(\frac{1 \text{ TeV}}{m_T} \right)^2, \quad (13)$$

and for a fermionic top-partner,

$$\frac{g_{hgg}}{g_{h_{\rm SM}gg}} \simeq 1 + 2.9\% \left(\frac{1 \text{ TeV}}{m_T} \right)^2, \qquad \frac{g_{h\gamma\gamma}}{g_{h_{\rm SM}\gamma\gamma}} \simeq 1 - 0.8\% \left(\frac{1 \text{ TeV}}{m_T} \right)^2. \quad (14)$$

A "natural" solution to the hierarchy problem that avoids fine tuning of the Higgs mass parameter thus generically predicts deviations in the hgg and $h\gamma\gamma$ couplings at the few percent level due solely to loop contributions from the top-partners. These effective couplings are typically also modified by shifts in the tree-level couplings of h to $t\bar{t}$ and WW.

We quote two concrete examples. First, the Littlest Higgs model [11,12] cancels the one-loop Higgs mass quadratic divergences from top, gauge, and Higgs loops using a new vector-like fermionic top-partner, new W' and Z' gauge bosons, and a triplet scalar. For a top-partner mass of 1 TeV, the new particles in the loop together with tree-level coupling modifications combine to give [13]

$$\begin{aligned} \frac{g_{hgg}}{g_{h_{\rm SM}gg}} &= 1 - (5\% \sim 9\%) \\ \frac{g_{h\gamma\gamma}}{g_{h_{\rm SM}\gamma\gamma}} &= 1 - (5\% \sim 6\%), \end{aligned} \quad (15)$$

where the ranges correspond to varying the gauge- and Higgs-sector model parameters. Note that the Higgs coupling to $\gamma\gamma$ is also affected by the heavy W' and triplet scalars running in the loop. The tree-level Higgs couplings to $t\bar{t}$ and WW are also modified by the higher-dimension operators arising from the nonlinear sigma model structure of the theory.

Second, the MSSM cancels the Higgs mass quadratic divergences using the SUSY partners of the SM particles. The tree-level Higgs couplings are also modified by the mixing between the two MSSM Higgs doublets. We consider the $m_h^{\max}$ benchmark scenario [17,18] with $m_A = 1$ TeV, $\tan\beta = 5$. This parameter set yields masses for the two top squarks of 857 GeV and 1200 GeV. We compute the Higgs couplings using `HDECAY4.43` [19], which yields

$$\begin{aligned} \frac{g_{hgg}}{g_{h_{\rm SM}gg}} &= 1 - 2.7\% \\ \frac{g_{h\gamma\gamma}}{g_{h_{\rm SM}\gamma\gamma}} &= 1 + 0.2\%, \end{aligned} \tag{16}$$

where the Higgs coupling to $\gamma\gamma$ is also affected by charginos in the loop (the lightest chargino mass is 201 GeV in this benchmark scenario) and both couplings are affected by the modification of the tree-level $ht\bar{t}$ coupling due to the presence of the second Higgs doublet. Much larger, even order 1, changes in these couplings are available elsewhere in the MSSM parameter space [20], but the values above are closer to typical ones.

2.2.3 Composite Higgs

Another approach to solve the hierarchy problem makes the Higgs a composite bound state of fundamental fermions with a compositeness scale around the TeV scale. Such models generically predict deviations in the Higgs couplings compared to the SM due to higher-dimension operators involving the Higgs suppressed by the compositeness scale. This leads to Higgs couplings to gauge bosons and fermions of order

$$\frac{g_{hxx}}{g_{h_{\rm SM}xx}} \simeq 1 \pm \mathcal{O}(v^2/f^2), \tag{17}$$

where f is the compositeness scale.

As an example, the Minimal Composite Higgs model [14] predicts [15]

$$\begin{aligned} a \equiv \frac{g_{hVV}}{g_{h_{\rm SM}VV}} &= \sqrt{1-\xi} \\ c \equiv \frac{g_{hff}}{g_{h_{\rm SM}ff}} &= \begin{cases} \sqrt{1-\xi} & \text{(MCHM4)} \\ (1-2\xi)/\sqrt{1-\xi} & \text{(MCHM5)}, \end{cases} \end{aligned} \tag{18}$$

with $\xi = v^2/f^2$. Here MCHM4 refers to the fermion content of the original model of Ref. [14], while MCHM5 refers to an alternate fermion embedding [16]. Again, naturalness favors $f \sim$ TeV, leading to

$$\begin{aligned}
\frac{g_{hVV}}{g_{h_{\rm SM}VV}} &\simeq 1 - 3\% \left(\frac{1 \text{ TeV}}{f}\right)^2 \\
\frac{g_{hff}}{g_{h_{\rm SM}ff}} &\simeq \begin{cases} 1 - 3\% \left(\frac{1 \text{ TeV}}{f}\right)^2 & \text{(MCHM4)} \\ 1 - 9\% \left(\frac{1 \text{ TeV}}{f}\right)^2 & \text{(MCHM5).} \end{cases}
\end{aligned} \tag{19}$$

2.2.4 *Additional sources of electroweak symmetry breaking*

Models that address the gauge hierarchy problem often contain more than one Higgs doublet, so that electroweak symmetry breaking comes from more than one source. All doublets with vevs contribute to the W and Z masses. Fermions, on the other hand, can acquire masses from one or the other doublet. This happens in the MSSM, in which up-type fermions get masses from one Higgs doublet while down-type fermions get masses from the other, leading to couplings of the light SM-like Higgs h (at tree level) of

$$\begin{aligned}
\frac{g_{hVV}}{g_{h_{\rm SM}VV}} &= \sin(\beta - \alpha) \\
\frac{g_{htt}}{g_{h_{\rm SM}tt}} = \frac{g_{hcc}}{g_{h_{\rm SM}cc}} &= \sin(\beta - \alpha) + \cot\beta \cos(\beta - \alpha) \\
\frac{g_{hbb}}{g_{h_{\rm SM}bb}} = \frac{g_{h\tau\tau}}{g_{h_{\rm SM}\tau\tau}} &= \sin(\beta - \alpha) - \tan\beta \cos(\beta - \alpha).
\end{aligned} \tag{20}$$

The constrained form of the MSSM Higgs potential lets us express the couplings in terms of the mass M_A of the CP-odd Higgs boson A^0 (for large M_A, the other Higgs states H^0 and $H^\pm$ are nearly degenerate with A^0). For $\tan\beta$ larger than a few, this yields [18]

$$\begin{aligned}
\frac{g_{hVV}}{g_{h_{\rm SM}VV}} &\simeq 1 - \frac{2c^2 m_Z^4 \cot^2\beta}{m_A^4} \\
\frac{g_{htt}}{g_{h_{\rm SM}tt}} = \frac{g_{hcc}}{g_{h_{\rm SM}cc}} &\simeq 1 - \frac{2c m_Z^2 \cot^2\beta}{m_A^2} \\
\frac{g_{hbb}}{g_{h_{\rm SM}bb}} = \frac{g_{h\tau\tau}}{g_{h_{\rm SM}\tau\tau}} &\simeq 1 + \frac{2c m_Z^2}{m_A^2},
\end{aligned} \tag{21}$$

where c captures the SUSY radiative corrections to the CP-even Higgs mass matrix.

We will review the LHC capabilities for detecting the heavy Higgs states in Section 6. The reach depends strongly on $\tan\beta$, but for moderate values of $\tan\beta$ it will be very difficult for the LHC to observe these states if their masses are 200 GeV. If we choose this value as a reference point, then, for $\tan\beta = 5$ and taking $c \simeq 1$, the h^0 couplings are approximately given by

$$\begin{aligned}
\frac{g_{hVV}}{g_{h_{\rm SM}VV}} &\simeq 1 - 0.3\% \left(\frac{200 \text{ GeV}}{m_A}\right)^4 \\
\frac{g_{htt}}{g_{h_{\rm SM}tt}} = \frac{g_{hcc}}{g_{h_{\rm SM}cc}} &\simeq 1 - 1.7\% \left(\frac{200 \text{ GeV}}{m_A}\right)^2 \\
\frac{g_{hbb}}{g_{h_{\rm SM}bb}} = \frac{g_{h\tau\tau}}{g_{h_{\rm SM}\tau\tau}} &\simeq 1 + 40\% \left(\frac{200 \text{ GeV}}{m_A}\right)^2 .
\end{aligned} \tag{22}$$

At the lower end of the range, the LHC experiments should see the deviation in the hbb or $h\tau\tau$ coupling. However, the heavy MSSM Higgs bosons can easily be as heavy as a TeV without fine tuning of parameters. In this case, the deviations of the gauge and up-type fermion couplings are well below the percent level, while those of the Higgs couplings to b and τ are at the percent level,

$$\frac{g_{hbb}}{g_{h_{\rm SM}bb}} = \frac{g_{h\tau\tau}}{g_{h_{\rm SM}\tau\tau}} \simeq 1 + 1.7\% \left(\frac{1 \text{ TeV}}{m_A}\right)^2 . \tag{23}$$

In this large-m_A region of parameter space, vertex corrections from SUSY particles are typically also at the percent level.

As a concrete example, we again consider the MSSM $m_h^{\rm max}$ benchmark scenario [17,18] with $m_A = 1$ TeV, $\tan\beta = 5$. We compute the Higgs couplings using `HDECAY4.43` [19],* which yields

$$\begin{aligned}
\frac{g_{hVV}}{g_{h_{\rm SM}VV}} &= 1 - \mathcal{O}(10^{-4}), \qquad & \frac{g_{hcc}}{g_{h_{\rm SM}cc}} = 1 - 0.3\% \\
\frac{g_{hbb}}{g_{h_{\rm SM}bb}} &= 1 + 3.5\%, & \frac{g_{h\tau\tau}}{g_{h_{\rm SM}\tau\tau}} = 1 + 2.5\%.
\end{aligned} \tag{24}$$

The difference in the shifts in the hbb and $h\tau\tau$ couplings is due to SUSY vertex corrections.

More general two-Higgs-doublet models follow a similar pattern, with the largest deviation appearing in the Higgs coupling to fermion(s) that get their mass from the Higgs doublet with the smaller vev. The decoupling with m_A in fact follows the same quantitative pattern so long as the dimensionless couplings in the Higgs potential are not larger than $\mathcal{O}(g^2)$, where g is the weak gauge coupling.

*For the comparison with the SM Higgs couplings, we turn off the electroweak radiative corrections to $h_{\rm SM} \to W^*W^*, Z^*Z^* \to 4f$ which are not included for the MSSM Higgs.

2.2.5 *Mixing of the Higgs with an electroweak-singlet scalar*

If the SM Higgs mixes with an electroweak-singlet scalar, all Higgs couplings become modified by the same factor,

$$\frac{g_{hVV}}{g_{h_{\rm SM}VV}} = \frac{g_{hff}}{g_{h_{\rm SM}ff}} = \cos\theta \simeq 1 - \frac{\delta^2}{2}, \qquad (25)$$

where $h = h_{\rm SM}\cos\theta + S\sin\theta$, S is the singlet, and the last approximation holds when $\delta \equiv \sin\theta \ll 1$. The orthogonal state, $H = -H_{\rm SM}\sin\theta + S\cos\theta$, has couplings to SM particles proportional to $-\sin\theta$.

When H is heavy, the size of $\sin\theta$ is constrained by precision electroweak data (assuming no cancellations due to other BSM physics). At one loop, the contributions to the T parameter from h and H are given by [8]

$$T = T_{\rm SM}(m_h)\cos^2\theta + T_{\rm SM}(m_H)\sin^2\theta, \qquad (26)$$

where $T_{\rm SM}(m)$ refers to the SM T parameter evaluated at a Higgs mass m. The same form holds for the S parameter. Large m_H is therefore only consistent with precision electroweak constraints for small $\sin\theta$; for example, for $M_H = 1$ TeV, Ref. [8] finds $\sin^2\theta \leq 0.12$, corresponding to $g_{hxx}/g_{H_{\rm SM}xx} \simeq 1 - 6\%$.

Similar effects follow from mixing of the SM Higgs with a radion in Randall-Sundrum models or a dilaton in models with conformally-invariant strong dynamics. The couplings of a radion or dilaton to SM particles are suppressed by a factor v/f compared to those of the SM Higgs, where f is the scale of the warped or conformal dynamics. The couplings of the mass eigenstate $h = H_{\rm SM}\cos\theta + \chi\sin\theta$ are modified according to

$$\frac{g_{hVV}}{g_{H_{\rm SM}VV}} = \frac{g_{hff}}{g_{H_{\rm SM}ff}} = \cos\theta + \frac{v}{f}\sin\theta \simeq 1 - \frac{\delta^2}{2} + \frac{v}{f}\delta. \qquad (27)$$

For $f \simeq 1$ TeV and $\sin^2\theta$ as above, this corresponds to $g_{hxx}/g_{H_{\rm SM}xx} \simeq 1 - 6\% \pm 8.5\%$, where we allow for either sign of δ.

2.2.6 *Conclusions*

Though large deviations are possible in some models, the more general expectation in models of new physics is that a light Higgs boson has couplings to vector bosons, fermions, gg, and $\gamma\gamma$ similar to those of the Higgs boson of the Standard Model. Thus, the study of the Higgs boson couplings is likely to require precision measurements.

Nevertheless, there are many models in which some of the Higgs couplings have 5-10% discrepancies from their Standard Model values. Discovery of these discrepancies would be an important clue to the nature of new physics at higher mass scales. To recognize these effects, it is important to be able to measure the Higgs boson couplings comprehensively and with high accuracy. We will now discuss how that can be done.

2.3 Status and prospects for Higgs measurements at LHC

The ATLAS and CMS experiments have now demonstrated that they have the capability to study the Standard Model Higgs boson. They have presented strong evidence for a scalar particle of mass about 125 GeV that is consistent with the profile of the Standard Model Higgs. The isolation of this signal in the LHC environment is extremely challenging. The strongest signal of the Higgs boson so far observed at the LHC comes in the Higgs decay to $\gamma\gamma$, a process that occurs less than once in 10^{12} proton-proton collisions. However, the Tevatron and LHC experiments have proven that they can make measurements of such rare events in the high background conditions of hadron colliders. In this section, we will review how far the LHC experiments are expected to go toward a comprehensive understanding of the Higgs boson in the case in which this particle has the couplings expected in the Standard Model.

2.3.1 The LHC Higgs discovery

As of July 2012, ATLAS and CMS presented Higgs results based on integrated luminosities up to 5.1 fb^{-1} at 7 TeV plus 5.9 fb^{-1} at 8 TeV [21,22]. Each experiment observes an excess in $\gamma\gamma$ with local significance of 4.1–4.5σ and an excess in 4ℓ (consistent with being from ZZ^*) with local significance of 3.2–3.4σ. The signal strengths in these channels are consistent with SM expectations. The LHC experiments made a measurement of the resonance mass in these two final states with the result 125.3$\pm$0.4 (stat)$\pm$0.5 (syst) GeV (CMS) and 126.0$\pm$0.4 (stat)$\pm$0.4 (syst) GeV (ATLAS).

CMS also presented results including 8 TeV data for the final states bb, $\tau\tau$, and WW [22]. ATLAS has presented results including 8 TeV data for the WW final state [23]; results for the other channels are expected soon. These final states have poorer mass resolution than $\gamma\gamma$ and $ZZ^* \to 4\ell$. ATLAS observes an excess in the WW channel at the 3.2σ level. CMS sees a modest excess in WW at the 1.5σ level and no excess in the bb and $\tau\tau$ channels. The rates in these channels are also broadly consistent with SM expectations.

In addition to inclusive Higgs production, which is dominated in the SM by gluon fusion, the ATLAS and CMS analyses include event selections with enhanced sensitivity to vector boson fusion (VBF) and Higgs production in association with W, Z, or $t\bar{t}$. As of July 2012, these subdominant production modes have not been conclusively observed.

Observation of the Higgs candidate in $\gamma\gamma$ excludes the possibility of the resonance being a spin-1 particle via the Landau-Yang theorem [24]. Observation of a signal in the ZZ^* final state strongly disfavors the possibility that it is a pseudoscalar because in this case the ZZ coupling must be loop-induced; most pseudoscalar models predict a ratio of rates in ZZ^* versus $\gamma\gamma$ much smaller than observed. Prospects for direct LHC measurements of the spin and CP quantum numbers will be discussed below.

2.3.2 *Prospects for measuring the Higgs mass and quantum numbers at LHC*

The mass of the Higgs boson is an intrinsically important parameter of the Standard Model. Moreover, the Higgs mass must be known accurately in order to interpret other measurements in precision Higgs physics. In particular, because the Higgs decay widths to WW and ZZ depends sensitively on m_h below the WW threshold, a precise measurement of the Higgs mass is necessary in order to extract the Higgs couplings from branching ratio measurements. For $m_h = 115$–130 GeV, each 100 MeV of uncertainty in m_h introduces 0.6–0.5% uncertainty in the ratio of the $hb\bar{b}$ and hWW couplings, g_b/g_W.

The LHC is expected to make a precision measurement of the mass of the Higgs boson. As of this writing, the LHC experiments have already measured the Higgs mass with an uncertainty of 0.4 GeV (statistical) and 0.4–0.5 GeV (systematic) [21,22]. Most of the sensitivity to the Higgs mass around 125 GeV comes from the $\gamma\gamma$ channel, with a subleading contribution from the $ZZ^* \to 4\ell$ channel. The ATLAS and CMS experiments estimate that, with large data samples ~ 300 fb^{-1}, they can determine the Higgs mass in absolute terms to an accuracy of 0.1 GeV [25,26,27]. Interference of the continuum $gg \to \gamma\gamma$ background with the diphoton signal shifts the peak downward by ~ 150 MeV or more [28] and must be taken into account at this level of precision.

The LHC also has excellent prospects to answer the question of the spin and parity of the Higgs boson. The SM Higgs coupling has the special form $HV_\mu V^\mu$, arising specifically from the gauge-covariant derivative of the vev-carrying, weak-charged Higgs doublet. In contrast, generic loop-induced couplings for a neutral scalar take the form $\phi V_{\mu\nu} V^{\mu\nu}$ for a CP-even scalar, or $\phi V_{\mu\nu} \widetilde{V}^{\mu\nu}$ for a CP-odd scalar, with $\widetilde{V}^{\mu\nu} = \epsilon^{\mu\nu\rho\sigma} V_{\rho\sigma}$. These loop-induced couplings are typically suppressed in size by a factor $\alpha/4\pi$. So, already, the fact that the boson found by ATLAS and CMS is seen in is decay to ZZ^* provides *prima facie* evidence that the this boson is a CP even scalar with a vacuum expectation value. The true test of this hypothesis will come in the study of angular correlations in the boson's decays. The study of $h \to ZZ^* \to 4$ leptons is especially powerful [29,30]. The possible structures of couplings can also distinguished experimentally using angular correlations of the forward tagging jets in weak boson fusion Higgs production or the four final-state fermions in $h \to VV$ decays. For example, the azimuthal angle $\Delta\phi_{jj}$ of the forward tagging jets in weak boson fusion has a fairly flat distribution for the SM $hV_\mu V^\mu$ coupling, while for the CP-even (CP-odd) loop-induced vertex the distribution peaks at $\Delta\phi_{jj} \sim 0$, π ($\pi/2$, $3\pi/2$) [31].

2.3.3 Prospects for determining the Higgs couplings from LHC data

The LHC experiments are in principle sensitive to almost the full range of SM Higgs couplings. The decays to $\gamma\gamma$, ZZ and WW are already seen. The decay to $\tau^+\tau^-$ is expected to be straightforward to observe with luminosity samples of 30 fb^{-1} at 14 TeV. The decay to $b\bar{b}$ and the process $pp \to t\bar{t}h$ should also be observed with similar luminosity samples, although that observation is much less straightfoward. We will discuss the observation of $h \to b\bar{b}$ further below. The LHC observations are sensitive to the hgg coupling because $gg \to h$ is a primary model for production of the Higgs boson at the LHC. The only significant decay mode of the SM Higgs boson omitted from this list is $h \to c\bar{c}$, for which there current is no strategy proposed. However, this is a relatively minor mode, with a branching ratio of about 3% for a Higgs boson of mass 125 GeV. In addition, it is possible to discover or bound invisible modes of Higgs decay by observing the WW fusion production of a Higgs with two forward tagging jets [33].

By measuring the $\sigma \cdot BR$ for the various Higgs production modes and decay into the observable final states, it is possible to measure the couplings of the Higgs boson in a model-independent way from LHC data. There is one problem that must be understood. An observable $\sigma(A\overline{A} \to h) \cdot BR(h \to B\overline{B})$ depends on the Higgs boson couplings through the factor

$$\frac{g^2(hAA)g^2(hBB)}{\Gamma_T} \ . \tag{28}$$

where Γ_T is the total width of the Higgs. For a Higgs boson of mass 125 GeV, the total width is expected to be about 4 MeV. Such a small value cannot be measured directly at any collider, so it must be determined by this fit. However, there might always be decay modes of the Higgs boson that are unobservable in the LHC experimental environment. The presence of such modes would increase Γ_T, and so we need a constraint that puts an upper limit on Γ_T.

This constraint comes from the fact that each scalar with a vev makes a positive contribution to the masses of the W and Z. Since the Higgs couplings to the W and Z also arise from the vev, this implies that the coupling of any single Higgs field is bounded above by the coupling that would give the full mass of the vector bosons. This implies

$$g^2(hWW) \leq g^2(hWW)|_{SM} \quad \text{and } g^2(hZZ) \leq g^2(hZZ)|_{SM} \tag{29}$$

Then the measurement of the $\sigma \cdot BR$ for a process such as WW fusion to h with decay to WW^*, which is proportional to $g^4(hWW)/\Gamma_T$, puts an upper limit on Γ_T. This constraint was first noticed and applied to Higgs coupling fitting by Dührssen *et al.* [34]. In the literature, this constraint is sometimes applied together with the relation

$$g^2(hWW)/g^2(hZZ) = \cos^2\theta_w \ . \tag{30}$$

The relation (30), however, requires models in which the Higgs is a mixture of $SU(2)$ singlet and doublet fields only, while (29) is more general [35].

This observation allows model-independent fits to the Higgs couplings from LHC data, but it still leaves an important source of difficulty. A SM Higgs boson of mass 125 GeV has a 60% branching fraction to the final state $b\bar{b}$. Thus, measurements that involve the $b\bar{b}$ final state play a large role in determining the Higgs total width, and any errors in that determination feed back into all Higgs couplings. Unfortunately, it is very difficult to observe decays $h^0 \to b\bar{b}$ at the LHC. The simple argument for this is that the cross section producing for $h^0 \to b\bar{b}$ is of the order of pb while the cross section for producing a pair of b jets at the Higgs boson mass is of the order of μb. The literature on Higgs boson measurements at the LHC has gone through cycles of optimism and pessimism about the possibility of overcoming this problem. Currently, we are in a state of optimism, due to the observation of Butterworth, Davison, Rubin, and Salam that highly boosted Higgs bosons can be distinguished by recognizing the Higgs as an exotic jet with special internal structure [36]. The Butterworth *et al.* paper discussed the observation of $h \to b\bar{b}$ in the reactions $pp \to W, Z + h$. Plehn, Salam, and Spannowsky have argued that an extension of this technical also allows the study of $pp \to t\bar{t} + h$ with $h \to b\bar{b}$ at the LHC [37]. However, it is one thing to observe these processes and quite another to use them to measure Higgs couplings with high precision. It is not yet understood how to calibrate these methods or what their ultimate systematic errors might be. Further, the selection of particular jet configurations potentially introduces large theoretical errors into the calculation of the relevant cross sections. The uncertainty in the extraction of couplings from these channels propagates back into the whole system of couplings determined from LHC data.

Over the years, there have been many attempts to estimate the ultimate sensitivity of the LHC experiments to the Higgs boson couplings. Most serious work on this

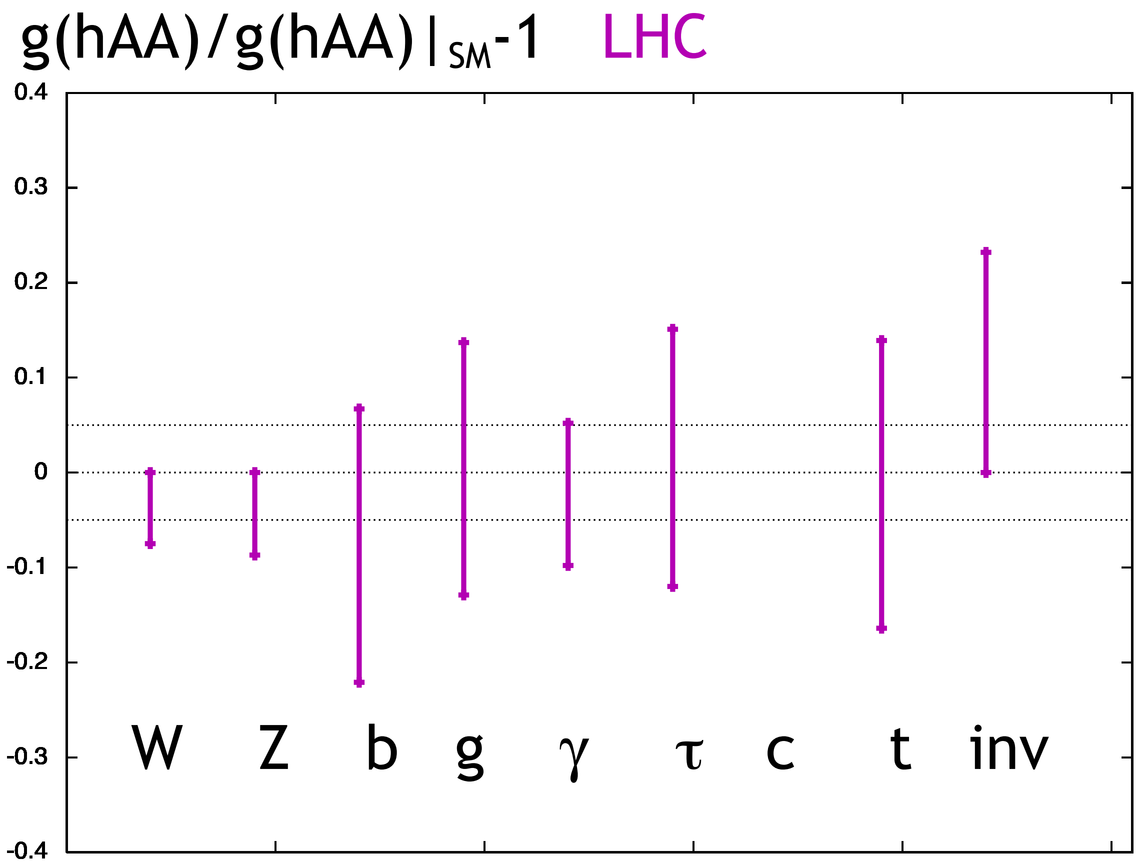

Figure 4: Estimate of the sensitivity of the LHC experiments to Higgs boson couplings in a model-independent analysis. The methodology leading to this figure is explained in [43].

subject to date, is the 2003 Ph. D. thesis of Dührssen [38] and the subsequent analysis of this work with Heinemeyer, Logan, Rainwater, and Weiglein [39]. This work has been updated in [41] and [42]. Other analysis using stronger model assumptions have been given in [32] and [40]. It is clear from the explanation given in the previous paragraph that any such analysis from before 2010 is excessively optimistic.

We have tried to make our own analysis of the model-independent LHC sensitivity to Higgs couplings, also bringing up to date the estimates in [38]. The results are shown in Fig. 4. The details of the analysis are given in [43]. The results differ in some details from [42], but they are qualitatively similar.

This estimate leads to a surprisingly strong conclusion. The LHC experiments will be able to make model-independent determinations of the Higgs boson couplings, and these determinations should be accurate enough to confirm or refute the hypothesis that the particle recently observed has the profile of the Standard Model Higgs boson. However, these experiments will not provide sufficient accuracy in the Higgs couplings to test for the deviations expected in new physics models in the Decoupling Limit, the generic models, that is, described in Section 2.2. To make this study, a stronger tool is needed.

2.3.4 Prospects for measurement of the triple Higgs coupling at the LHC

Measurement of the Higgs quartic coupling parameter λ provides a test of the electroweak symmetry breaking mechanism through the structure of the Higgs potential. This coupling can be probed via a measurement of the triple-Higgs vertex, which contributes along with other diagrams to Higgs pair production. This coupling can be significantly modified in models with extended Higgs sectors, in particular in models that increase the strength of the electroweak phase transition to provide viable baryogenesis [44]. For Higgs pair production via $gg \to hh$, low-mass new physics in the loops can rather significantly affect the cross section even if it does not have a large effect on the $gg \to h$ cross section [45,46].

Measuring the triple Higgs coupling at the LHC is very challenging for a 125 GeV Higgs boson. The largest production cross section is $gg \to hh$, with other potential production modes (VBF $qq \to qqhh$, $q\bar{q} \to Vhh$, and $gg, q\bar{q} \to t\bar{t}hh$) being severely rate-limited. The $4W$ final state has been studied for $M_h > 150$ GeV [47] and was found to be promising for $M_h \simeq 170$–200 GeV at the high-luminosity (10^{35} cm^{-2}s^{-1}) LHC [48]; however, this final state is suppressed by the falling $h \to WW$ branching ratio at lower masses (a factor of $(0.22)^2 = 0.048$ at $M_h = 125$ GeV, compared to 0.92 (0.55) at $M_h = 170$ (200) GeV). This suppression will be compensated somewhat by an enhanced production cross section at lower masses, but no LHC study has been done in the $4W$ final state for a low-mass Higgs.

The $4b$ and $bb\tau\tau$ final states were studied for a 120 GeV Higgs in Ref. [49] and the more promising $bb\gamma\gamma$ final state was studied in Ref. [50]. The expected triple-Higgs coupling sensitivity can be expressed as $\Delta\lambda_{hhh} \equiv \lambda/\lambda_{\rm SM} - 1$, assuming no new particles contribute to the $gg \to h$ and $gg \to hh$ loops. The results, summarized in Table 1, indicate that only order-1 sensitivity will be possible.

2.4 Higgs measurements at ILC at 250 GeV

The physics program of the LHC should be contrasted with the physics program that becomes available at the ILC. The ILC, being an e^+e^- collider, inherits traditional virtues of past e^+e^- colliders such as LEP and SLC: well defined initial states,

	LHC (300 fb^{-1})	SLHC (3000 fb^{-1})
$4b$ [49]	$-6.8 < \Delta\lambda_{hhh} < 10.1$	$-3.1 < \Delta\lambda_{hhh} < 6.0$
$bb\tau\tau$ [49]	–	$-1.6 < \Delta\lambda_{hhh} < 3.1$
	LHC (600 fb^{-1})	SLHC (6000 fb^{-1})
$bb\gamma\gamma$ [50]	$-0.74 < \Delta\lambda_{hhh} < +0.94$	$-0.46 < \Delta\lambda_{hhh} < +0.52$

Table 1: Expected Higgs self-coupling 1σ sensitivity limits for $M_h = 120$ GeV, from Refs. [49,50]. Sensitivity is expressed in terms of $\Delta\lambda_{hhh} \equiv \lambda/\lambda_{\rm SM} - 1$. The $bb\tau\tau$ final state signal cross section is too small to be observed at the 300 fb^{-1} LHC [49].

clean environment, and reasonable signal-to-noise ratios even before any selection cuts. Thanks to the clean environment, it can be equipped with ultra high precision detectors that enable us to reconstruct events in terms of fundamental particles, namely, quarks, leptons, and gauge bosons. At the ILC, therefore, we will be able to analyze events as viewing Feynman diagrams. By controlling beam polarization, we can even select Feynman diagrams that participate in the reaction in question. It should be emphasized that this is largely due to the experimental technique called the Particle Flow Analysis (PFA), which allows us to detect the Higgs boson with high efficiency, using its major modes, i.e., decays into hadronic jets. This is a great advantage over the experiments at the LHC and provides opportunities for various precision measurements of the properties of the Standard-Model-like Higgs boson candidate found at the LHC.

The precision Higgs study program will start at around $\sqrt{s} = 250\,\mathrm{GeV}$ with the Higgs-strahlung process, $e^+e^- \to ZH$ (Fig.5 (left)).The production cross section for this process is plotted in Fig.6 as a function of $\sqrt{s}$ together with that for the weak boson fusion processes (Figs.5-(center and right)). We can see that the Higgs-strahlung process attains its maximum at around $\sqrt{s} = 250\,\mathrm{GeV}$ and dominates the fusion processes there. The cross section for the fusion processes increases with the energy and takes over that of the Higgs-strahlung process above $\sqrt{s} \gtrsim 500\,\mathrm{GeV}$. The production cross section of the Higgs-strahlung process at $\sqrt{s} \simeq 250\,\mathrm{GeV}$ is substantial for the low mass Standard-Model-like Higgs boson. Its discovery would require only a few fb^{-1} of integrated luminosity. With $250\,\mathrm{fb}^{-1}$, about 8.8×10^4 Higgs boson events can be collected. The precise determination of the properties of the Higgs boson is one of the main goals of the ILC regardless of its nature, SM or otherwise. Of particular importance are the Higgs boson mass, m_h, and its branching ratios.

Before we elaborate more on the Higgs branching fraction measurements, let us turn our attention to the measurements of the mass and spin of the Higgs boson, which are necessary to confirm that the Higgs-like object found at the LHC has the

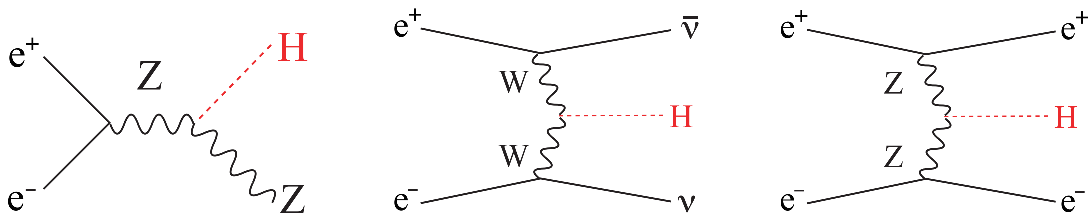

Figure 5: Feynman diagrams for the three major Higgs production processes at the ILC: $e^+e^- \to ZH$ (left), $e^+e^- \to \nu\bar{\nu}H$ (center), and $e^+e^- \to e^+e^-H$ (right).

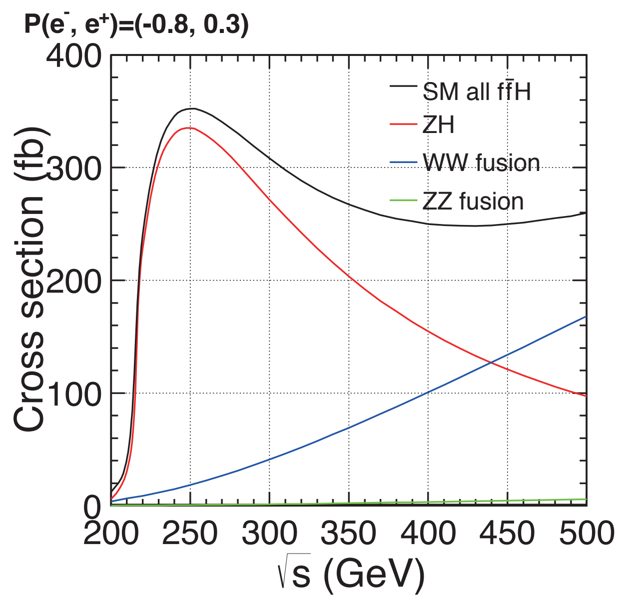

Figure 6: Production cross section for the $e^+e^- \to ZH$ process as a function of the center of mass energy for $M_H = 120\,\text{GeV}$, plotted together with those for the WW and ZZ fusion processes: $e^+e^- \to \nu\bar{\nu}H$ and $e^+e^- \to e^+e^-H$.

properties expected for the Higgs boson.

2.4.1 Mass and Quantum Numbers

We have discussed in the previous section that the LHC already offers excellent capabilities to measure the mass and quantum numbers of the Higgs boson. However, the ILC offers new probes of these quantities that are very attractive experimentally. We will review them here.

We first discuss the precision mass measurement of the Higgs boson at the ILC. This measurement can be made particularly cleanly in the process $e^+e^- \to ZH$, with $Z \to \mu^+\mu^-$ and $Z \to e^+e^-$ decays. Here the distribution of the invariant mass recoiling against the reconstructed Z provides a precise measurement of M_H, independently of the Higgs decay mode. In particular, the $\mu^+\mu^- X$ final state provides a particularly precise measurement as the $e^+e^- X$ channel suffers from larger experimental uncertainties due to bremsstrahlung. It should be noted that it is the capability to precisely reconstruct the recoil mass distribution from $Z \to \mu^+\mu^-$ that defines the momentum resolution requirement for an ILC detector.

The reconstructed recoil mass distributions, calculated assuming the ZH is produced with four-momentum $(\sqrt{s}, 0)$, are shown in Fig.7. In the $e^+e^- X$ channel FSR and bremsstrahlung photons are identified and used in the calculation of the $e^+e^-(n\gamma)$ recoil mass. Fits to signal and background components are used to extract M_H. Based on this model-independent analysis of Higgs production in the ILD detector, it is shown that M_H can be determined with a statistical precision of 40 MeV (80 MeV) from the $\mu^+\mu^- X$ $(e^+e^- X)$ channel. When the two channels are combined an uncertainty of 32 MeV is obtained [51]. The corresponding model independent uncertainty on the Higgs production cross section is 2.5 %. Similar results were obtained from SiD [52]. It should be emphasized that these measurements only used the information from the leptonic decay products of the Z and are independent of the Higgs decay mode. As such this analysis technique could be applied even if the Higgs decayed invisibly and hence allows us to determine the absolute branching ratios including that of invisible Higgs decays. By combining the branching ratio to ZZ with the production cross section, which involves the same g_{HZZ} coupling, one can determine the total width and the absolute scale of partial widths with no need for the theoretical assumptions needed for the LHC case. We will return to this point later.

It is worth noting that for the $\mu^+\mu^- X$ channel the width of the recoil mass peak is dominated by the beam energy spread. In the above study Gaussian beam energy spreads of 0.28 % and 0.18 % are assumed for the incoming electron and positron beams respectively. For ILD the detector response leads to the broadening of the recoil mass peak from 560 MeV to 650 MeV. The contribution from momentum resolution is therefore estimated to be 330 MeV. Although the effect of the detector resolution is not negligible, the dominant contribution to the observed width arises from the incoming beam energy spread rather than the detector response. This is no coincidence; the measurement of m_h from the $\mu^+\mu^- X$ recoil mass distribution was one of the benchmarks used to determine the momentum resolution requirement for a detector at the ILC.

If there are additional Higgs fields with vacuum expectation values that contribute to the masses of the Z, the corresponding Higgs particles will also appear in reactions

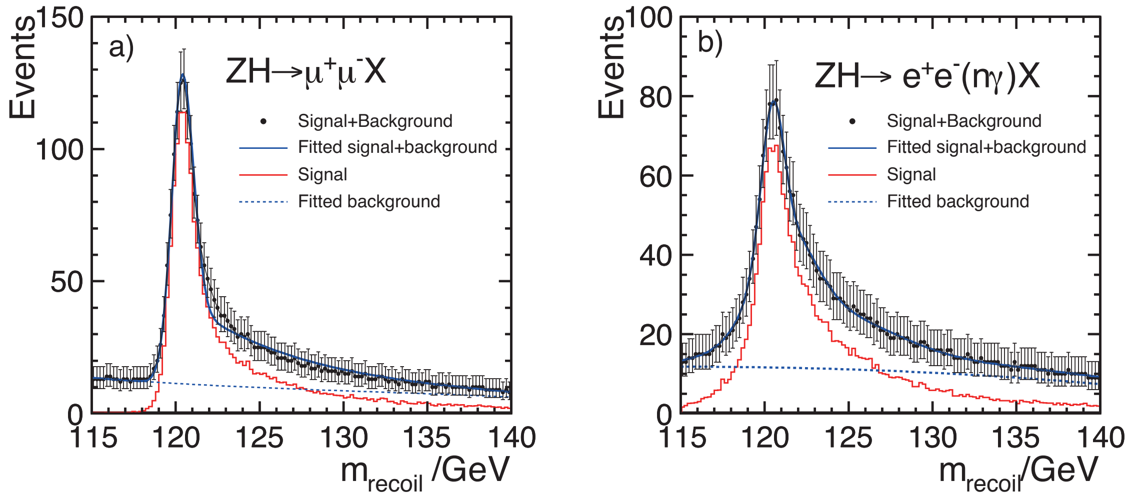

Figure 7: Results of the model independent analysis of the Higgs-strahlung process $e^+e^- \to ZH$ in which a) $Z \to \mu^+\mu^-$ and b) $Z \to e^+e^-(n\gamma)$. The results are shown for $P(e^+, e^-) = (+30\%, -80\%)$ beam polarization.

$e^+e^- \to Zh'$, and their masses can be determined in the same way.

We now turn to the determination of the spin and CP properties of the Higgs boson. The $H \to \gamma\gamma$ decay observed at the LHC rules out the possibility of spin 1 and restricts the charge conjugation C to be positive. We have already noted that the discrete choice between CP even and CP odd can be settled by the study of Higgs decay to ZZ^* to 4 leptons.

The ILC offers an additional, orthogonal, test of these assignments. The threshold behavior of the Zh cross section has a characteristic shape for each spin and each possible CP parity. If the boson's spin is 2 or less, there is a clear discrimination: The cross section rises as β near the threshold for a CP even state and as β^3 for a CP odd state. If the spin is higher than 2, the cross section will grow as a higher power of β. With a three-20 fb^{-1}-point threshold scan of the $e^+e^- \to ZH$ production cross section we can clearly separate these possibilities as shown in Fig. 8 (left). At energies well above the Zh threshold, the Zh process will be dominated by longitudinal Z production as implied by the equivalence theorem. The reaction will then behave like a scalar pair production, showing the characteristic $\sim \sin^2\theta$ dependence if the H particle's spin is zero. The measurement of the angular distribution will hence strongly corroborate that the h is indeed a scalar particle.

It is possible that the h is not a CP eigenstate but rather a mixture of CP even and CP odd components. This occurs if there is CP violation in the Higgs sector. It

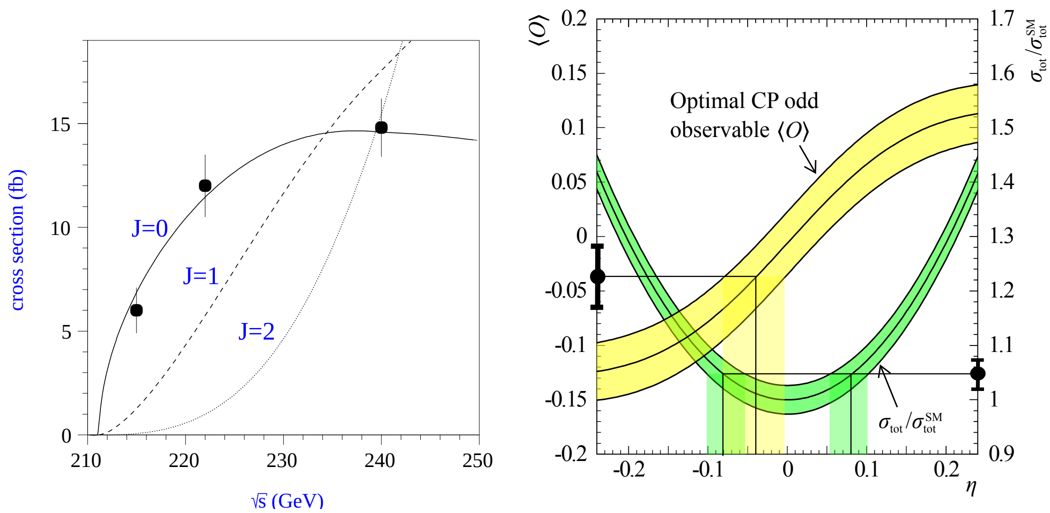

Figure 8: Left: Threshold scan of the $e^+e^- \to ZH$ process for $M_H = 120\,\text{GeV}$, compared with theoretical predictions for $J^P == 0^+$, 1^-, and 2^+ [53]. Right: Determination of CP-mixing with 1-σ bands expected at $\sqrt{s} = 350\,\text{GeV}$ and $500\,\text{fb}^{-1}$ [54].

is known that CP violation from the CKM matrix cannot explain the cosmological excess of baryons over antibaryons; thus, a second source of CP violation in nature is needed. One possibility is that this new CP violation comes from the Higgs sector and gives rise to net baryon number at the electroweak phase transitions, through mechanisms that we will discuss in Section 9 of this report. For these models, the h mass eigenstates can be mainly CP even but contain a small admixture of a CP odd component.

A small CP odd contribution to the hZZ coupling can affect the threshold behavior. The right-hand side of Fig. 8 shows the determination of this angle at a center of mass energy of 350 GeV from the value of the total cross section and from an appropriately defined optimal observable [54].

Tests of mixed CP property using the hZZ coupling may not be the most effective ones, since the CP odd hZZ coupling is of higher dimension and may be generated only through loops. It is more effective to use a coupling for which the CP even and CP odd components are on the same footing. An example is the h coupling to $\tau^+\tau^-$, given by

$$\Delta\mathcal{L} = -\frac{m_\tau}{v} h\ \overline{\tau}(\cos\alpha + i\sin\alpha\gamma^5)\tau \tag{31}$$

for a Higgs boson with a CP odd component. The polarizations of the final state τs can be determined from the kinematic distributions of their decay products; the CP even and odd components interfere in these distributions [55]. In [56], it is estimated that the angle α can be determined at the ILC to an accuracy of 6°.

2.4.2 Inclusive cross section

Whereas all Higgs boson measurements at the LHC are measurements of $\sigma \cdot BR$, the ILC allows us to measure the absolute size of a Higgs inclusive cross section. This can be done by applying the recoil technique discussed above to the measurement of (σ_{ZH}) for the $e^+e^- \to Zh$ process. The measurement gives the cross section to a relative accuracy of 2.5 % at 250 fb^{-1} without looking at the h decay at all. This cross section is indispensable for extracting branching ratio (BR) from the event rate, which is proportional to $\sigma_{Zh} \cdot BR$, and limits its precision.

It is worth noting that the inclusive cross section is a direct measure of the h to ZZ coupling (g_{HZZ}). This single measurement at the ILC is capable of determining this coupling to 1.3 %. If the h particle is a scalar particle, this coupling must originate from a gauge-kinetic term of the form given by Eq.(5) with one Φ leg replaced by the vacuum expectation value associated with the h particle. The observation of this coupling is, therefore, a strong evidence of the existence of a vacuum condensate associated with the h particle. Moreover, the vacuum expectation value here has no solid reason to saturate the standard model value, $v = 246$ GeV. The g_{hZZ} coupling hence measures to what extent the vacuum expectation value associated with the multiplet to which the h particle belongs explain the mass of the Z boson. The power of the recoil mass measurement is this ability to unambiguously determine the g_{hZZ} coupling and probe the vacuum condensate, thereby making it the flagship measurement of the ILC.

2.4.3 Branching Ratios

The measurement of the inclusive cross section of the $e^+e^- \to ZH$ process allows us to extract the H particle's branching fractions in a completely model-independent manner. A precise measurement of the absolute branching ratios of the Higgs bosons is an important test of the mass generation mechanism and provides a window into effects beyond the SM. For the branching ratio measurements we again use the $e^+e^- \to ZH$ process, but this time exploiting all the decay modes of the Z boson including the $Z \to q\bar{q}$ and $Z \to \nu\bar{\nu}$ decays. The use of fully hadronic final states is possible only in a very clean environment of an e^+e^- collider. In the clean environment of the ILC we can also use a high performance micro-vertex detector, which is placed very close to the interaction point, and hence it is possible to measure $H \to c\bar{c}$ and $H \to b\bar{b}$

separately. Figure 9 shows a lego plot of the b-likeness v.s. c-likeness for the template samples of the signal and the SM background events. We can see the clear differences between the different decay modes of the Higgs boson. Together with the measurement of the $H \to \tau^+\tau^-$ decays, we can access the Yukawa couplings of both up-type and down-type fermions and test the coupling-mass proportionality. The loop-induced $H \to gg$ decay is indirectly sensitive to the top Yukawa coupling and possibly other new strongly interacting particles that couples to the Higgs particle but is too heavy to produce directly. By the same token, the $H \to \gamma\gamma$ and the $H \to Z\gamma$ decays are also important as a tool to probe heavy particles in the loop. The ex-

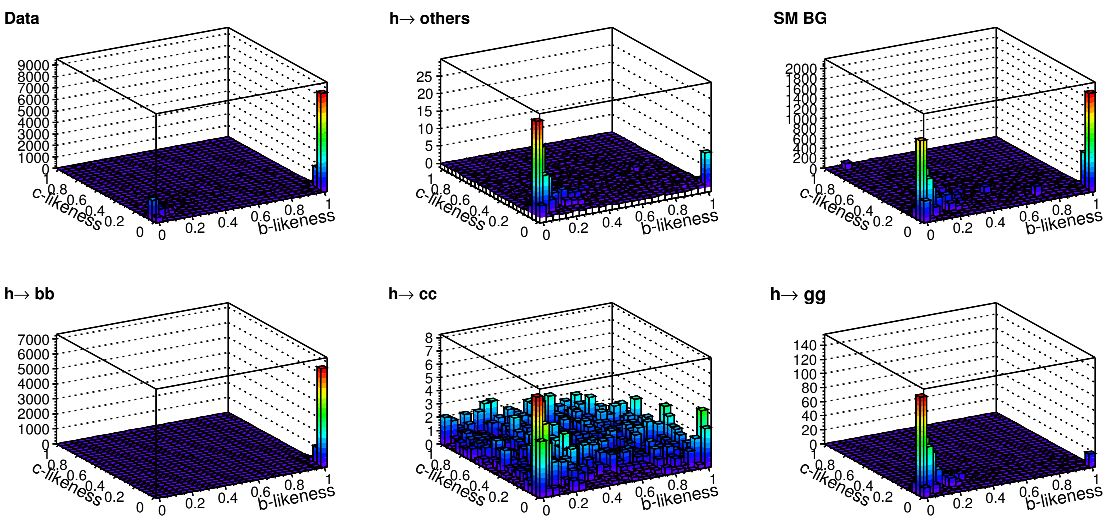

Figure 9: Two-dimensional image of the three-dimensional template samples in b-likeness v.s. c-likeness [57]

pected accuracies on the branching ratios are summarized in Table 2. It is worth noting that these full simulation results are consistent with the past fast simulation results [60,61,62,63,64].

The h decay to invisible final states, if any, can be measured by looking at the recoil mass under the condition that nothing observable is recoiling against the Z boson. The main background is $e^+e^- \to ZZ$ followed by one Z decaying into a lepton pair and the other into a neutrino pair. With an integrated luminosity of $250\,\mathrm{fb}^{-1}$ at $\sqrt{s} = 250\,\mathrm{GeV}$, the ILC can set a 95% CL limit on the invisible branching ratio to 4.8% with the golden $Z \to \mu^+\mu^-$ mode alone[65]. Using other modes including $Z \to q\bar{q}$, we could improve this significantly to 0.8% [66]. [**I have received the corrected number from Hiroaki, which is slightly worse than the fast simulation result by A.Yamamoto I used in the current svn version. 95%CL**

Table 2: Expected accuracies for the H boson branching ratios obtained with full detector simulations at the $\sqrt{s} = 250$ GeV assuming $\mathcal{L} = 250$ fb^{-1} and $(e^-, e^+) = (-0.8, +0.3)$ beam polarization[57,59,58]. The errors on BR include the error on σ of 2.5% from the recoil mass measurement. The $H \to WW^*$ measurement assumes the opposite $(e^-, e^+) = (+0.8, -0.3)$ beam polarization combination. The $H \to \tau^+\tau^-$ and $H \to \gamma\gamma$ results are from fast simulations [**to be replaced by the time of DBD completion**].

mode	BR	$\sigma \cdot BR$ (fb)	$N_{evt}/250\,\text{fb}^{-1}$	$\Delta(\sigma \cdot BR)/(\sigma \cdot BR)$	$\Delta BR/BR$
$H \to b\bar{b}$	65.7%	232.8	58199	1.0%	2.7%
$H \to c\bar{c}$	3.6%	12.7	3187	6.9%	7.3%
$H \to gg$	5.5%	19.5	4864	8.5%	8.9%
$H \to WW^*$	15.0%	53.1	13281	8.2%	8.6%
$H \to \tau^+\tau^-$	8.0%	28.2	7050	4-6%	5-7%
$H \to ZZ^*$	1.7%	6.1	1523	28(?)%	28(?)%
$H \to \gamma\gamma$	0.29%	1.02	255	23-30%	23-30%

upper limit on BR(invisible) = 1.1%, while the relative error on sigma x BR(invisible) = 7.6% for BR(invisible) = 10% (see Hiroaki's slides attached below for detail). These numbers assume Ecm=250GeV, 250fb^{-1}, and P(e+,e-)=(+0.3,-0.8). For right handed combination (-0.3,+0.8), the corresponding numbers are 95%CL upper limit on BR(inv.) = 0.76% relative error on sigma x BR(inv.) = 7.3% for BR(inv.)=10%.]

To determine the absolute normalization of Higgs boson partial widths from the measurements of branching ratios, we need to combine them with an accurate value of one partial width or cross section. As described above, the 250 GeV running of the ILC for 250 fb^{-1} will determine the cross section for $e^+e^- \to Zh$ very accurately, to 2.5%, which can be directly converted to g_{hZZ} or to the absolute partial width $\Gamma(ZZ)$. However, to use this value to normalize the other Higgs partial widths in a completely model-independent analysis, we would need to use the formula

$$\Gamma(A) \quad = \quad \Gamma(ZZ) \cdot \frac{BR(A)}{BR(ZZ)}, \tag{32}$$

and so we would also need to measure the branching ratio for $h \to ZZ^*$. This is not easy to do at the ILC because it is a rare mode giving low statistics for a Higgs boson with $M_H \simeq 120$ GeV. No full simulation study of the $h \to ZZ^*$ branching ratio in $e^+e^- \to ZH$ is currently available. We will therefore use the result of the $H \to WW^*$ study [59] and scale accordingly. The error for the $H \to WW^*$ decay implies a 28% relative error for the $h \to ZZ^*$ branching ratio. The use of the formula (32) then implies that the uncertainties in absolute partial widths or Higgs couplings are those listed convolved with $2.5 \oplus 28\%$. This significantly degrades the precision information obtained at the ILC.

An alternative is to use the theoretical assumption

$$g(HWW)/g(HZZ) \;=\; \cos^2\theta_W \tag{33}$$

to tie together the HZZ and HWW couplings. Now $BR(WW^*)$ can be used in the denominator of Eq.(32), and the error added in converting from branching ratios to partial widths is $2.5 \oplus 8.0\% = 8.4\%$.

As we will see below, the absolute strength of the Higgs coupling to WW is expected to be obtained by a measurement of the cross section for Higgs production through WW fusion, $e^+e^- \to \nu\bar{\nu}H$ at $\sqrt{s} = 500\,\mathrm{GeV}$. The 500 GeV data can also be used to improve the accuracy on the $BR(WW^*)$. These measurements can be combined to obtain Higgs couplings in a completely model-independent way.

So far we have been dealing with the branching ratios and partial widths after phase space integration. The $h \to WW^*$ decay provides an interesting opportunity to study its differential width and probe the Lorentz structure of the hWW coupling through angular analyses of the decay products. The relevant part of the general interaction Lagrangian, which couples the Higgs boson to W bosons in a both Lorentz- and gauge-symmetric fashion, can be parameterized as

$$\mathcal{L}_{\mathrm{HWW}} = 2m_W^2\left(\frac{1}{v}+\frac{a}{\Lambda}\right) h\; W_\mu^+ W^{-\mu} + \frac{b}{\Lambda} h\; W_{\mu\nu}^+ W^{-\mu\nu} + \frac{\tilde{b}}{\Lambda} h\; \epsilon^{\mu\nu\sigma\tau} W_{\mu\nu}^+ W_{\sigma\tau}^- \,, \tag{34}$$

where $W^{\pm}_{\mu\nu}$ is the usual gauge field strength tensor, $\epsilon^{\mu\nu\sigma\tau}$ is the Levi-Civita tensor, v is the VEV of the Higgs field, and Λ is a cutoff scale[†]. The real dimensionless coefficients, a, b, and $\tilde{b}$, are all zero in the Standard Model and measure the anomaly in the HWW coupling, which arise from some new physics at the scale Λ. The coefficient a stands for the correction to the Standard Model coupling. On the other hand, the coefficient b and $\tilde{b}$ parametrize the leading dimension-five non-renormalizable interactions and corresponding to $(\boldsymbol{E}\cdot\boldsymbol{E} - \boldsymbol{B}\cdot\boldsymbol{B})$-type CP-even and $(\boldsymbol{E}\cdot\boldsymbol{B})$-type CP-odd contributions. The a coefficient, if nonzero, would hence modify just the normalization of the Standard Model coupling, while the b and $\tilde{b}$ coefficients would change the angular correlations of the decay planes as seen in Fig.10. Nonzero b and $\tilde{b}$ would also modify the momentum distribution of the W boson in the Higgs rest frame. Simultaneous fits to p_W and ϕ_{plane} result in the contour plots in Figs.11 and 12.

[†] The Lagrangian (34) is not by itself gauge invariant; to restore explicit gauge invariance we must also include the corresponding anomalous couplings of the Higgs boson to Z bosons and photons.

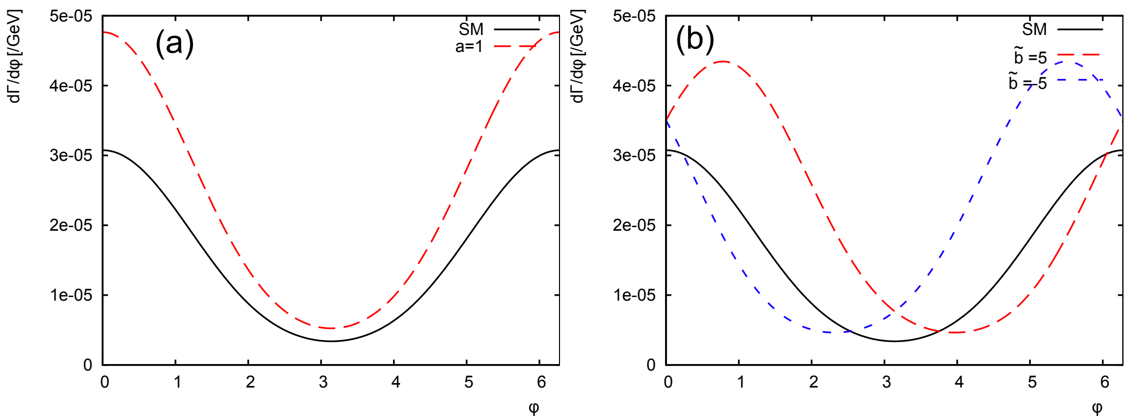

Figure 10: Distribution of the angle ϕ between two decay planes of W and W^* from the decay $H \to WW^* \to 4j$ with the inclusion of anomalous couplings [67]. (a) The SM curve along with that for $a = 1$, $b = \tilde{b} = 0$, $\Lambda = 1$ TeV; the position of the minimum is the same for both distributions. (b) The SM result with the cases $\tilde{b} = \pm 5$, $a = b = 0$, $\Lambda = 1$ TeV; the position of the minimum is now shifted as discussed in the text.

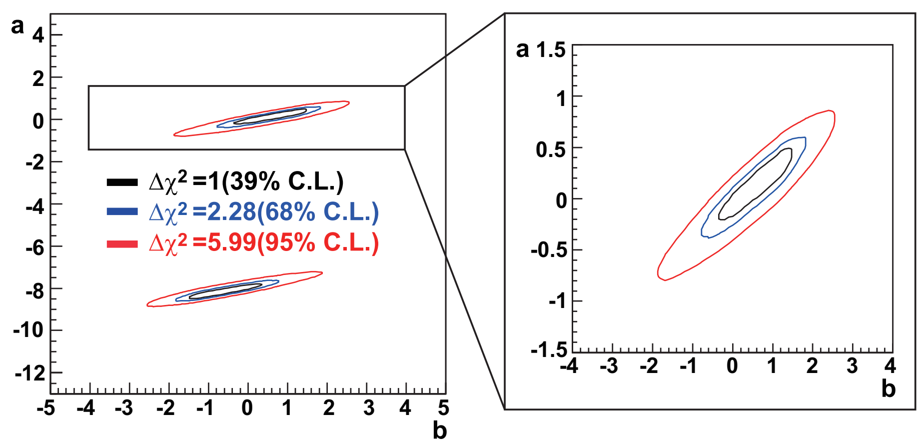

Figure 11: Probability contours for $\Delta\chi^2 = 1$, 2.28, and 5.99 in the a-b plane, which correspond to 39%, 68%, and 95% C.L., respectively.

2.5 Higgs measurements at ILC at 500 GeV

The two very important processes will become accessible at $\sqrt{s} = 500\,\mathrm{GeV}$. The first is the $e^+e^- \to t\bar{t}H$ process [68,69], in which the top Yukawa coupling will appear in the tree level for the first time at the ILC. The top quark, being the heaviest matter fermion in the Standard Model, would be crucial to understand the fermion mass generation mechanism. The second is the $e^+e^- \to ZHH$ process, to which the triple Higgs coupling contributes in the tree level. The self-coupling is the key ingredient

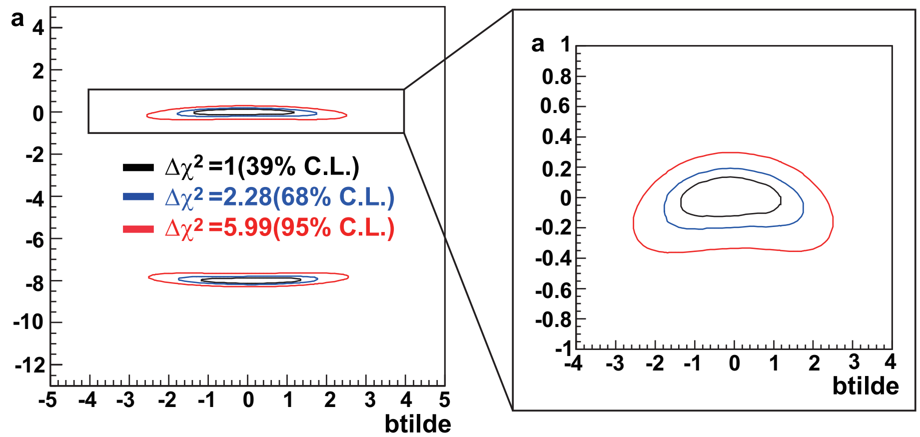

Figure 12: Contours similar to Fig. 11 plotted in the a-$\tilde{b}$ plane.

of the Higgs potential and its measurement is indispensable for understanding the electroweak symmetry breaking.

2.5.1 Top Yukawa Coupling

Past simulation studies for the $e^+e^- \to t\bar{t}H$ process were mostly made at around $\sqrt{s} = 800\,\mathrm{GeV}$, since the cross section attains its maximum there for $M_H \simeq 120\,\mathrm{GeV}$ [70,71]. It was pointed out, however, that the cross section would be significantly enhanced near the threshold due to the bound-state effects between t and $\bar{t}$ [73]-[79] (see Figs.13 left and right) and the measurement of the top Yukawa coupling might be possible already at $\sqrt{s} = 500\,\mathrm{GeV}$ [80]. A serious simulation study at $\sqrt{s} = 500\,\mathrm{GeV}$ was performed for the first time with the QCD bound-state effects consistently taken into account for both signal and background cross sections [81]. The $e^+e^- \to t\bar{t}H$ reaction takes place through the three diagrams shown in Fig.14 As shown in Fig.13 (left), the contribution from the irrelevant H-off-Z diagram is negligible at $\sqrt{s} = 500\,\mathrm{GeV}$, thereby allowing us to extract the top Yukawa coupling g_t by just counting the number of signal events. By combining the 8-jet and 6-jet-plus-lepton modes of $e^+e^- \to t\bar{t}H$ followed by $H \to b\bar{b}$, the analysis showed that a measurement of the top Yukawa coupling to $\Delta g_t/g_t = 10\%$ is possible for $M_H = 120\,\mathrm{GeV}$ with polarized electron and positron beams of $(P_{e^-}, P_{e^+}) = (-0,8,+0.3)$ and an integrated luminosity of 1 ab^{-1}. This result obtained with a fast Monte Carlo simulation has just recently been corroborated by a full simulation [82,83].

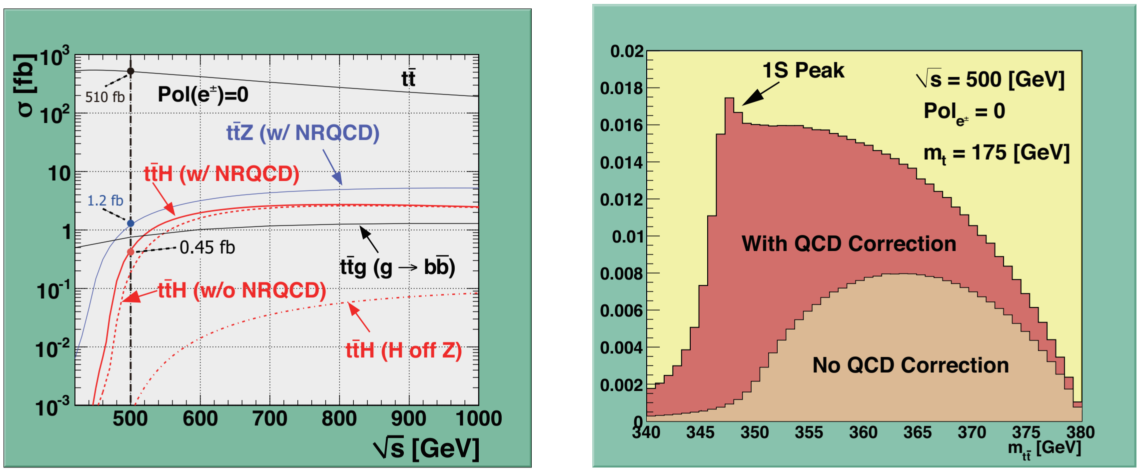

Figure 13: Cross section for the $e^+e^- \to t\bar{t}H$ process as a function of $\sqrt{s}$ together with those of background processes, $e^+e^- \to t\bar{t}Z$, $\to t\bar{t}g^*$, and $\to t\bar{t}$ (left). The invariant mass distribution of the $t\bar{t}$ system from the $e^+e^- \to t\bar{t}H$ process with and without the non-relativistic QCD correction (right).

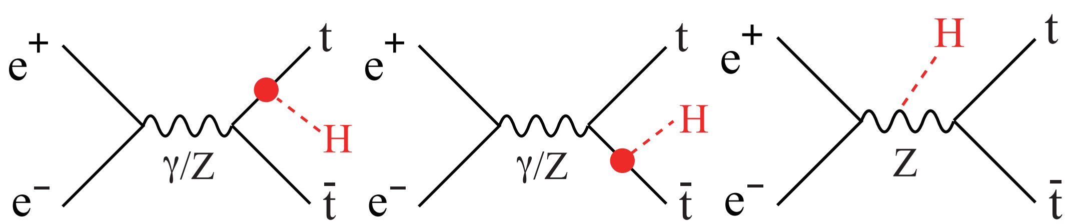

Figure 14: Three diagrams contributing to the $e^+e^- \to t\bar{t}H$ process. The H-off-t or $\bar{t}$ diagrams, (a) and (b), contain the top Yukawa coupling while the H-off-Z diagram (c) does not.

2.5.2 Higgs Self-coupling

The triple Higgs boson coupling can be studied at the ILC through the processes $e^+e^- \to ZHH$ and $e^+e^- \to \nu_e\bar{\nu}_e HH$ (for relevant diagrams see Fig.15). The cross sections for the two processes are plotted as a function of $\sqrt{s}$ for $M_H = 120\,\text{GeV}$ in Fig.16. The cross section reaches its maximum of about 0.18 fb at around $\sqrt{s} = 500\,\text{GeV}$, which is dominated by the former process. A full simulation study [85] of the process $e^+e^- \to ZHH$ followed by $H \to b\bar{b}$ has recently been carried out making use of a new flavor tagging package (LCFIplus) [84] together with the conventional Durham jet clustering algorithm. From the combined result of the three channels corresponding to different Z decay modes, $Z \to l^+l^-$, $\nu\bar{\nu}$, and $q\bar{q}$, it was found that the process can

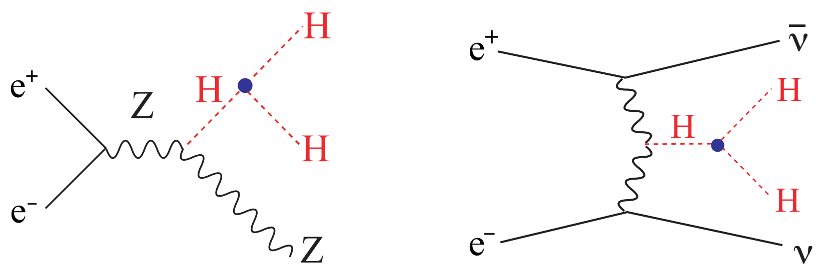

Figure 15: Relevant diagrams containing the triple Higgs coupling for the two processes: $e^+e^- \to ZHH$ (left) and $e^+e^- \to \nu_e\overline{\nu}_e HH$.

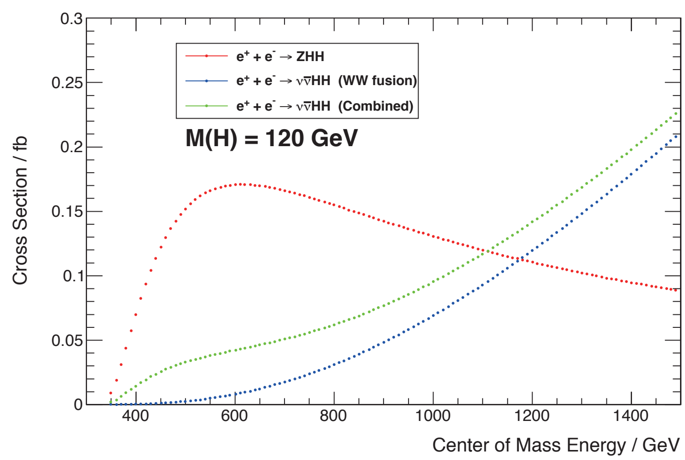

Figure 16: Cross section for the two processes: $e^+e^- \to ZHH$ (left) and $e^+e^- \to \nu_e\overline{\nu}_e HH$ as a function of $\sqrt{s}$ for $M_H = 120\,\mathrm{GeV}$.

be detected with an excess significance of 4.3-σ and the cross section can be measured to $\Delta\sigma/\sigma = 0.29$ for an integrated luminosity of $2\,\mathrm{ab}^{-1}$ with beam polarization $(P_{e^-}, P_{e^+}) = (-0, 8, +0.3)$. Unlike the $e^+e^- \to t\bar{t}H$ case, however, the contribution from the background diagrams without the self-coupling is significant and the relative error on the self-coupling λ is $\Delta\lambda/\lambda = 0.52$, which is not yet very satisfactory compared to the results from earlier fast simulation studies [86,87,88,89,90]. The major problem in the analysis is mis-clustering of color-singlet groups. Figure 17 compares the reconstructed invariant masses for the two Higgs candidates with Durham jet clustering (a) and with perfect jet clustering using Monte Carlo truth (b). We can see that the separation between the signal and the background is significantly improved if there is no mis-jet-clustering. A new jet clustering algorithm is now being developed.

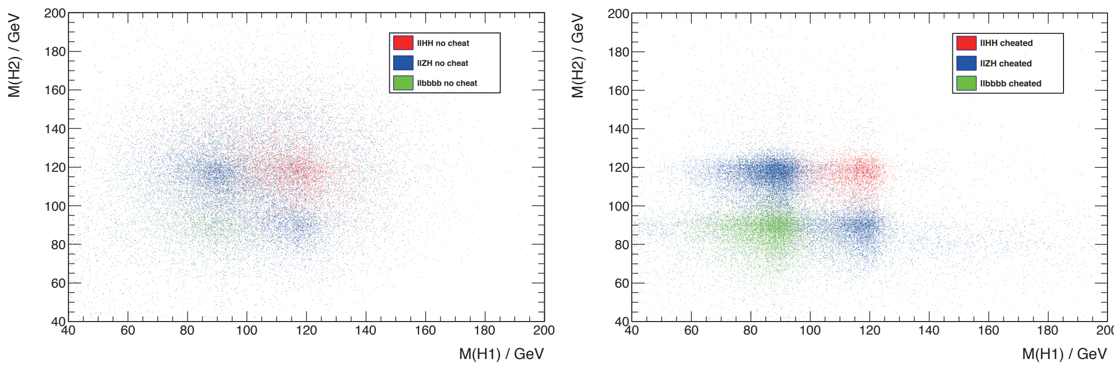

Figure 17: Scatter plot of the invariant masses of the two Higgs candidates (left) with Durham jet clustering and (right) perfect jet clustering using Monte Carlo truth on the color flow.

2.5.3 WW Fusion and HWW Coupling

As shown in Fig.6, the WW fusion process takes over the Higgs-strahlung process at around $\sqrt{s} = 450\,\mathrm{GeV}$. The cross section for the fusion process is about 160 fb at $\sqrt{s} = 500\,\mathrm{GeV}$ for $M_H = 120\,\mathrm{GeV}$. Thanks to this large cross section and the about two times larger luminosity expected at this energy, the fusion process provides a unique opportunity to directly measure the HWW coupling with high precision. With an integrated luminosity of $500\,\mathrm{fb}^{-1}$, we can measure this cross section times the branching fraction to $b\bar{b}$ to a statistical accuracy of $\Delta(\sigma(\nu\bar{\nu}H)\cdot BR(b\bar{b}))/(\sigma(\nu\bar{\nu}H)\cdot BR(b\bar{b})) = 0.60\%$. Combining this with the branching ration measurement at $\sqrt{s} = 250\,\mathrm{GeV}$, we will be able to determine the cross section to $\Delta\sigma(\nu\bar{\nu}H)/\sigma(\nu\bar{\nu}H) = 2.7\%$, which translates to an expected error on the HWW coupling of $\Delta g_{HWW}/g_{HWW} = 1.4\%$. The large data sample of the fusion process is also useful to improve the precision of the $H \to WW^*$ branching ratio, since the background separation is easier at $\sqrt{s} = 500\,\mathrm{GeV}$ than at $\sqrt{s} = 250\,\mathrm{GeV}$, and enables us to determine the cross section times branching ratio to $\Delta(\sigma(\nu\bar{\nu}H) \cdot BR(WW^*)/(\sigma(\nu\bar{\nu}H) \cdot BR(WW^*)) = 3.0\%$. Applying Eq.(32) with ZZ replaced by WW, we can determine the Higgs total width to $\Delta\Gamma_{\mathrm{tot}}/\Gamma_{\mathrm{tot}} \simeq 6\%$. The clean sample of WW^* decays can be also used to investigate the Lorentz structure of the HWW coupling as we discussed in the angular analysis of the $H \to WW^*$ decays in the $e^+e^- \to ZH$ process at $\sqrt{s} = 250\,\mathrm{GeV}$.

2.5.4 Expected Improvements of Branching Ratio Measurements

The Higgs sample from the WW fusion and the Higgs-strahlung processes at $\sqrt{s} = 500\,\text{GeV}$ will enable us to significantly improve the branching ratio measurements described above for the $\sqrt{s} = 250$ GeV run. In particular we can do a template fitting similar to that employed for the $e^+e^- \to ZH$ sample at $\sqrt{s} = 250\,\text{GeV}$. The flavor-tagging performance at $\sqrt{s} = 500\,\text{GeV}$ will be similar, too. The expected relative errors on the cross section times branching ratios are summarized in Table 3. The table shows that the WW fusion process contributes significantly, while the relative error on $\Delta BR(b\bar{b})/BR(b\bar{b})$ is limited by the error on the ZH production cross section at $\sqrt{s} = 250\,\text{GeV}$ from the recoil mass measurement. If we need higher accuracy for $\Delta BR(b\bar{b})/BR(b\bar{b})$, we will need to run longer at $\sqrt{s} = 250\,\text{GeV}$, though slight improvement is also expected from the recoil mass measurement at $\sqrt{s} = 500\,\text{GeV}$. **[The results should be confirmed by full simulations by the time of the DBD completion.]**

Table 3: Expected accuracies for the H boson branching ratios when the 250 GeV measurements assuming $\mathcal{L} = 250\,\text{fb}^{-1}$ in Table 2 are combined with those at $\sqrt{s} = 500$ GeV assuming $\mathcal{L} = 500\,\text{fb}^{-1}$ and $(e^-, e^+) = (-0.8, +0.3)$ beam polarization. The errors on BR include the error on σ of 2.5% from the recoil mass measurement at $\sqrt{s} = 250\,\text{GeV}$.

	$\Delta(\sigma \cdot BR)/(\sigma \cdot BR)$			$\Delta BR/BR$
mode	ZH @ 250 GeV	ZH @ 500 GeV	$\nu\bar{\nu}H$ @ 500 GeV	combined
$H \to b\bar{b}$	1.0%	1.6%	0.60%	2.6%
$H \to c\bar{c}$	6.9%	11%	4.0%	4.2%
$H \to gg$	8.5%	13%	4.9%	4.8%
$H \to WW^*$	8.2%	13(?)%	3.0%	3.8%
$H \to \tau^+\tau^-$	4-6%	6-10(?)%	4-6(?)%	3.6-4.6(?)%
$H \to ZZ^*$	28(?)%	45(?)%	17(?)%	14(?)%
$H \to \gamma\gamma$	23-30%	37-48(?)%	14-18(?)%	12-15(?)%

2.6 Higgs measurements at ILC at 1000 GeV

[There are no full simulation results at this moment.]

Two out of the three processes selected as the DBD benchmark reactions at $\sqrt{s} = 1000\,\text{GeV}$ involve Higgs boson production: $e^+e^- \to t\bar{t}H$ and $e^+e^- \to \nu\bar{\nu}H$. We showed above that we would be able determine the top Yukawa coupling to an accuracy of about 10 % at $\sqrt{s} = 500\,\text{GeV}$ for $M_H = 120\,\text{GeV}$, using the former process. Since the signal cross section grows to its maximum at around $\sqrt{s} = 700$ and only slowly decreases toward $\sqrt{s} = 1000\,\mathrm{GeV}$ and since one of the major background $e^+e^- \to t\bar{t}$ decreases much more rapidly as seen in Figs.13 (left), a more precise measurement of the top Yukawa coupling will be possible there. On the other hand, the other benchmark process (the WW fusion process), $e^+e^- \to \nu\bar{\nu}H$, dominates the s-channel Higgs-sthrahlung process, $e^+e^- \to ZH$, at $\sqrt{s} = 1000\,\mathrm{GeV}$. The cross section for the WW fusion process will be as large as $430\,\mathrm{fb}^{-1}$ for $(P_{e^+}, P_{e^-}) = (+0.2, -0.8)$ and $m_H = 120\,\mathrm{GeV}$ (see Fig.18). Together with the higher luminosity expected

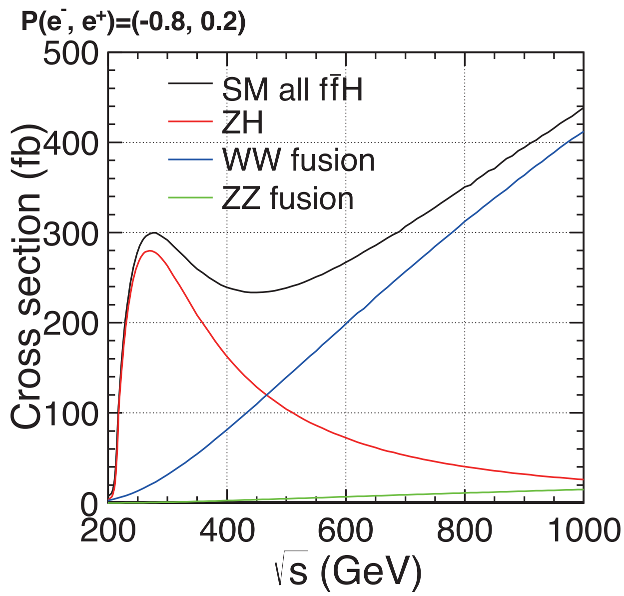

Figure 18: Production cross sections for the Higgs-strahlung, $e^+e^- \to ZH$, the WW fusion, $e^+e^- \to \nu\bar{\nu}H$, and ZZ fusion processes as a function of the center of mass energy for $M_H = 120\,\mathrm{GeV}$ and beam polarization $(P_{e^+}, P_{e^-}) = (+0.2, -0.8)$.

at $\sqrt{s} = 1000\,\mathrm{GeV}$, this process will give us a high statistics Higgs boson sample: 4.3×10^5 events for $1\,\mathrm{ab}^{-1}$. This will allow us to improve the branching ratios to the various modes discussed above as well as to access a rare mode such as $H \to \mu^+\mu^-$. It is also note worthy that one more process, $e^+e^- \to \nu\bar{\nu}HH$ process, will become sizable at $\sqrt{s} = 1000\,\mathrm{GeV}$, which can be used to improve the measurement of the Higgs self-coupling in addition to the $e^+e^- \to ZHH$ process. These possibilities will be discussed below.

2.6.1 Measurement of $H \to \mu^+\mu^-$ decay using $e^+e^- \to \nu\overline{\nu}H$

The branching fraction of the $H \to \mu^+\mu^-$ decay is as small as 0.03 % for the 120 GeV Standard Model Higgs boson. Its measurement thus requires a very good invariant mass resolution for the $\mu^+\mu^-$ pair. The measurement of this rare mode is a challenge to the tracking detectors and hence chosen as one of the benchmark processes. The SiD group performed a full simulation study of the $H \to \mu^+\mu^-$ decay at $\sqrt{s} = 250$ GeV with 250 fb^{-1} for $M_H = 120$ GeV as one of its LoI studies [52]. The expected number of signal events was only 26 before any cuts. After a simple cut-and-count analysis, the expected number of signal events became 8 with 39 background events in the final sample of $e^+e^- \to ZH$ followed by $Z- > q\overline{q}$ and $H \to \mu^+\mu^-$. This corresponds to a statistical significance of 1.1-σ. The WW fusion process at $\sqrt{s} = 1000$ GeV will provide a higher statistics sample of 4.3×10^5 Higgs events for $m_H = 120$ GeV, given the 1 ab^{-1} and $(P_{e^+}, P_{e^-}) = (+0.2, -0.8)$. We hence exact about 130 events to begin with for the $H \to \mu^+\mu^-$ mode. Since the cross sections for the $e^+e^- \to W^+W^- \to \mu^+\nu_\mu\mu^-\overline{\nu}_\mu$ and $^+e^- \to ZZ \to \mu^+\mu^- f\overline{f}$ backgrounds will decrease, while the signal cross section will increase at higher energies, we would expect a meaningful measurement of the muon Yukawa coupling. **[$\nu\overline{\nu}Z$ and $\nu\overline{\nu}W^+W^-$ will increase though.]** An earlier fast simulation result showed that a 5-σ signal peak would be observed with a 1 ab^{-1} sample[91,92]. Together with the tau Yukawa coupling from the $H \to \tau^+\tau^-$ branching ratio, this will provide an insight into the lepton mass generation. With the charm Yukawa coupling from the $H \to c\overline{c}$ branching fraction, this will allow us to probe the mass generation mechanism for the second generation matter fermions. It is also note worthy that the branching ratio measurements for the other decay modes can also be improved. For instance, we can achieve $\Delta BR(H \to \gamma\gamma)/BR((H \to \gamma\gamma) \simeq 5\,\%$ [93]. **Full simulation studies on these measurements are starting now, which should replace the fast simulation results here.**

2.6.2 Top Yukawa Coupling

The 10% accuracy expected at $\sqrt{s} = 500$ GeV can be significantly improved by the data taken at 1000 GeV, thanks to the larger cross section and the less background from $e^+e^- \to t\bar{t}$. Fast simulations at $\sqrt{s} = 800$ GeV showed that we would be able to determine the top Yukawa coupling to 6% for $M_H = 120$ GeV, given an integrated luminosity of 1 ab^{-1} and residual background uncertainty of 5% [70,71]. **Full simulation studies on these measurements are starting now, which should replace the fast simulation result here.**

2.6.3 Higgs Self-coupling in the $e^+e^- \to \nu\overline{\nu}HH$ Process

At $\sqrt{s} = 1000\,\mathrm{GeV}$, the $e^+e^- \to \nu\overline{\nu}HH$ process will become significant and open up the possibility of measuring the triple Higgs coupling in the WW channel[89]. The cross section for this process is only about $0.07\,\mathrm{fb}^{-1}$, but the sensitivity to the self-coupling is potentially higher since the contribution from the background diagrams is smaller, leading to the relation: $\Delta\lambda/\lambda \simeq 0.85 \times (\Delta\sigma_{\nu\overline{\nu}HH}/\sigma_{\nu\overline{\nu}HH})$ as compared to $\Delta\lambda/\lambda \simeq 1.8\times(\Delta\sigma_{ZHH}/\sigma_{ZHH})$ for the $e^+e^- \to ZHH$ process at 500 GeV. An early fast simulation study of $e^+e^- \to \nu\overline{\nu}HH$ showed that one could determine the triple Higgs coupling to an accuracy of $\Delta\lambda/\lambda \simeq 0.12$[90], assuming $1\,\mathrm{ab}^{-1}$ luminosity and 80% left-handed electron polarization. A more recent fast simulation study indicated, however, $\Delta\lambda/\lambda \simeq 0.44$ for $2\,\mathrm{ab}^{-1}$ with unpolarized beams and $\Delta\lambda/\lambda \simeq 0.425$ for $1\,\mathrm{ab}^{-1}$ with $(P_{e^+}, P_{e^-}) = (+0.2, -0.8)$. The difference could be attributed to the more realistic analysis based on jet-clustering after parton showering and hadronization, as well as more background processes considered in the latter study. In addition to the fusion process, we can use the $e^+e- \to ZZH$ process also at $\sqrt{s} = 1000\,\mathrm{GeV}$ though it has even less sensitivity, $\Delta\lambda/\lambda \simeq 2.8 \times (\Delta\sigma_{ZHH}/\sigma_{ZHH})$, than that at $\sqrt{s} = 500\,\mathrm{GeV}$. Assuming the nominal integrated luminosities of $500\,\mathrm{fb}^{-1}$ at $\sqrt{s} = 500\,\mathrm{GeV}$ and $1000\,\mathrm{fb}^{-1}$ at $\sqrt{s} = 1000\,\mathrm{GeV}$ with the left-handed beam combination: $(P_{e^+}, P_{e^-}) = (+0.2, -0.8)$, we would expect that the Higgs self-coupling could be measured to $\Delta\lambda/\lambda \simeq 0.38$. **Full simulation studies on these measurements are starting now, which should replace the fast simulation result here.**

2.7 Conclusion

The landscape of elementary particle physics has been altered by the discovery by the ATLAS and CMS experiments of a new boson that decays to $\gamma\gamma$, ZZ, and WW final states [2]. The question of the identity of this bosons and its connection to the Standard Model of particle physics has become the number one question for our field. In this section, we have presented the capabilities of the ILC to study this particle in detail. The ILC can access the new boson through the reactions $e^+e^- \to Zh$ and through the WW fusion reaction $e^+e^- \to \nu\overline{\nu}h$. Though our current knowledge of this particle is still limited, we already know that these reactions are available at rates close to those predicted for the Higgs boson in the Standard Model. The ILC is ideally situated to give us a full understanding of this particle, whatever its nature.

The leading hypothesis for the identity of the new particle is that it is the Higgs boson of the Standard Model, or a similar particle responsible for electroweak symmetry breaking in a model that includes new physics at the TeV energy scale. We have argued that, if this identification proves correct, the requirements for experiments on the nature of this boson are extremely challenging. Though there are new physics

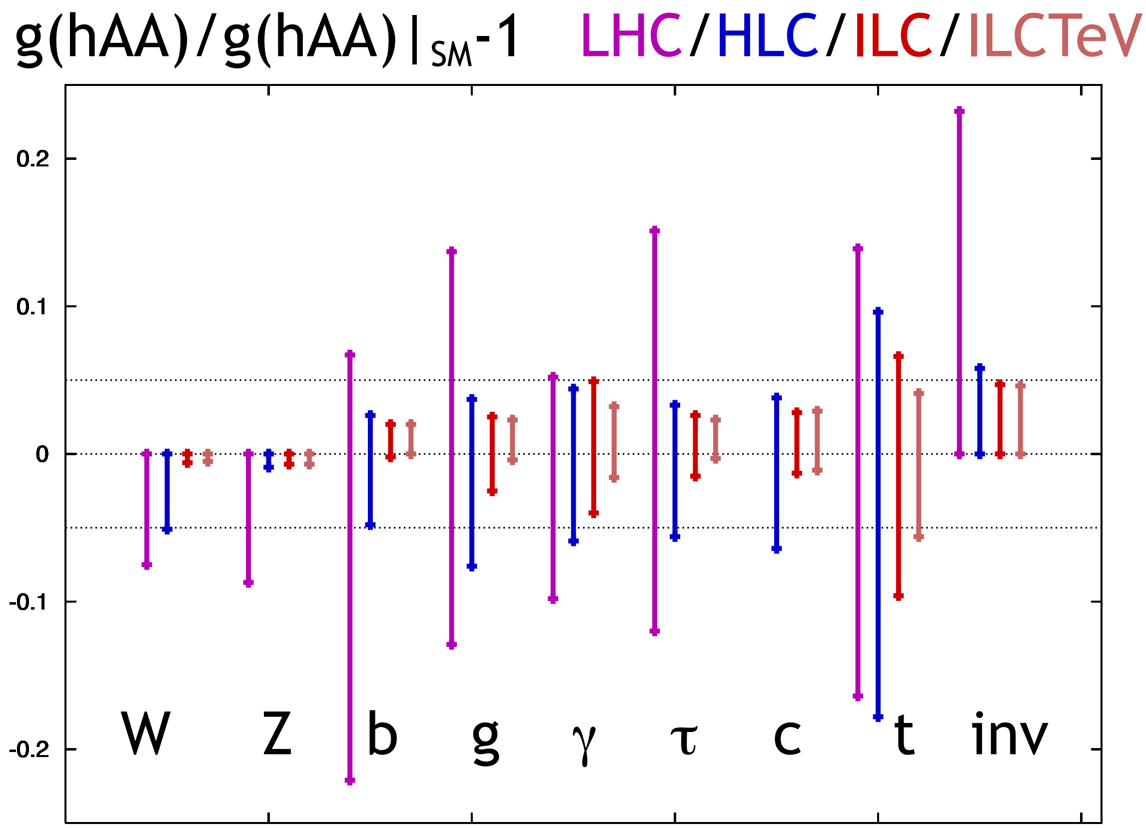

Figure 19: Estimate of the sensitivity of the ILC experiments to Higgs boson couplings in a model-independent analysis. The four sets of errors for each Higgs coupling represent the results for LHC, the threshold ILC Higgs program at 250 GeV, the full ILC program up to 500 GeV, and the extension of the ILC program to 1 TeV. The methodology leading to this figure is explained in [43].

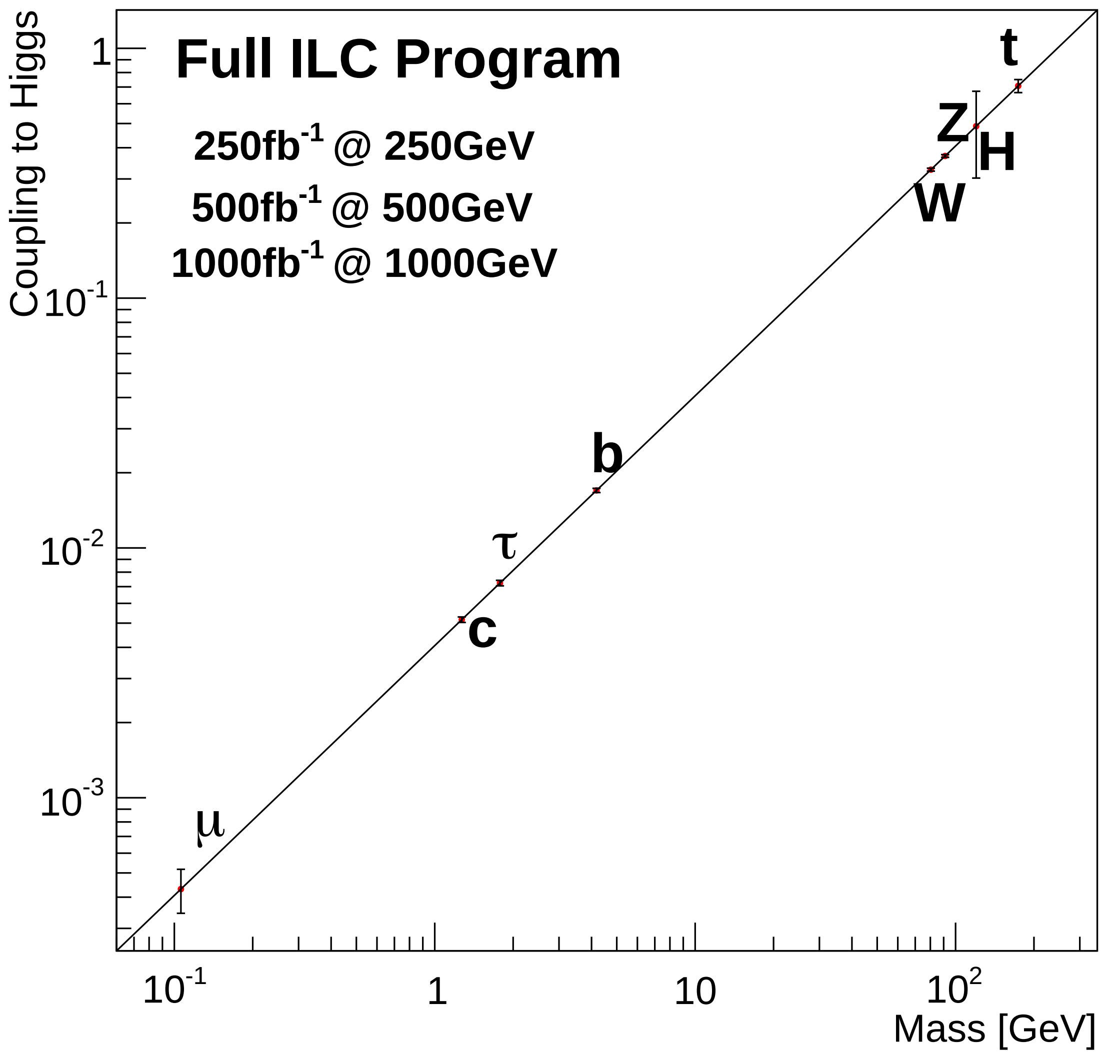

Figure 20: Expected precision from the full ILC program of tests of the Standard Model prediction that the Higgs coupling to each particle is proportional to its mass.

models that predict large deviations of the boson couplings from the Standard Model predictions, the typical expectation in new physics models is that the largest deviations from the Standard Model are at the 5–10% level. Depending on the model, these deviations can occur in any of the boson's couplings. Thus, a comprehensive program of measurements is needed, one capable of being interpreted in a model-independent way. Our estimate of the eventual LHC capabilities, given in Fig. 4, falls short of that goal.

We then presented the capabilities of the ILC for precision measurements of the Higgs boson couplings. The ILC program for Higgs couplings can begin at a center of mass energy of 250 GeV, near the peak of the cross section for $e^+e^- \to Z^0h^0$. This program allows a direct measurement of the cross section, rather than measurement that includes branching ratios, already eliminating an important source of ambiguity from the LHC data. The program also allows the measurement of individual branching channels, observed in recoil against the Z^0 boson. The excellent flavor tagging capabilities of the ILC experiments allow access to the $c\bar{c}$ decay mode of the Higgs boson and sharpen the observation of many other modes. The ILC experiments are highly sensitive to possible invisible or other unexpected decay modes of the Higgs boson, with sensitivity at the percent level.

A later stage of ILC running at the full energy of 500 GeV will enhance these capabilities. At 500 GeV, the W fusion reaction $e^+e^- \to \nu\overline{\nu}h$ turns on fully, giving a very precise constraint on the Higgs boson coupling to WW. The increased statistics sharpens the measurement of rare branching channels such as $\gamma\gamma$. Higher energy also gives improved $g/c/b$ separation in the hadronic decay models. Running at 500 GeV allows the first direct measurements of the Higgs coupling to $t\bar{t}$ and the Higgs self-coupling.

The technology of the ILC will eventually allow extended running at higher energies, up to 1 TeV in the center of mass. A 1 TeV program will add further statistics to the branching ratio measurements in all channels, using the increasing $e^+e^- \to \nu\overline{\nu}h$ cross section. It also very much increases the sensitivity of the determinations of the Higgs coupling to $t\bar{t}$ and the Higgs self-coupling.

The progression of this program is shown graphically in Fig. 19. For each Higgs boson coupling, four sets of error bars are shown, always assuming that the underlying value of the coupling is that of the Standard Model. The first is the estimate of the LHC capability, from Fig. 4. The second is the error that would be obtained by adding the data from a 250 fb^{-1} run of the ILC at 250 GeV. The third is the error that would be obtained by adding to this the data from a 500 fb^{-1} run of the ILC at 500 GeV. The final error bar would be the result of adding a 1 ab^{-1} data set at 1 TeV. Not shown, but also relevant, are the capabilities of the ILC to measure the Higgs self-coupling to about 40% accuracy and the Higgs coupling to $\mu^+\mu^-$ to about

20% accuracy in the 1 TeV program.

The results of this program can also be represented as precision tests of the Standard Model relation that the Higgs coupling to each particle is exactly proportional to the mass of that particle. The expected uncertainties in those tests from the measurements described above are shown in Fig. 20.

This is the program that is needed to fully understand the nature of the newly discovered boson and its implications for the puzzle of electroweak symmetry breaking. The ILC can provide it.

References

[1] [ALEPH and DELPHI and L3 and OPAL and SLD and LEP Electroweak Working Group and SLD Electroweak Group and SLD Heavy Flavour Group Collaborations], Phys. Rept. **427**, 257 (2006) [hep-ex/0509008].

[2] `http://indico.cern.ch/conferenceDisplay.py?confId=197461`.

[3] B. W. Lee, C. Quigg and H. B. Thacker, Phys. Rev. Lett. **38**, 883 (1977); Phys. Rev. D **16**, 1519 (1977).

[4] T. Appelquist and M. S. Chanowitz, Phys. Rev. Lett. **59**, 2405 (1987) [Erratum-ibid. **60**, 1589 (1988)].

[5] F. Goertz, U. Haisch and M. Neubert, Phys. Lett. B **713**, 23 (2012) [arXiv:1112.5099 [hep-ph]].

[6] J. R. Espinosa, C. Grojean and M. Muhlleitner, EPJ Web Conf. **28**, 08004 (2012) [arXiv:1202.1286 [hep-ph]].

[7] J. F. Gunion, Y. Jiang and S. Kraml, arXiv:1207.1545 [hep-ph].

[8] R. S. Gupta, H. Rzehak and J. D. Wells, arXiv:1206.3560 [hep-ph].

[9] H. E. Haber, In *Warsaw 1994, Proceedings, Physics from Planck scale to electroweak scale* 49-63, and In *Budapest 1994, Proceedings, Electroweak symmetry breaking* 1-15, and Calif. U. Santa Cruz - SCIPP-94-039 (94/12,rec.Jan.95) 16 p [hep-ph/9501320].

[10] J. F. Gunion, H. E. Haber, G. L. Kane and S. Dawson, "The Higgs Hunter's Guide" (Addison-Wesley, Reading, MA, 1990).

[11] N. Arkani-Hamed, A. G. Cohen, E. Katz and A. E. Nelson, JHEP **0207**, 034 (2002) [hep-ph/0206021].

[12] T. Han, H. E. Logan, B. McElrath and L. -T. Wang, Phys. Rev. D **67**, 095004 (2003) [hep-ph/0301040].

[13] T. Han, H. E. Logan, B. McElrath and L. -T. Wang, Phys. Lett. B **563**, 191 (2003) [Erratum-ibid. B **603**, 257 (2004)] [hep-ph/0302188].

[14] K. Agashe, R. Contino and A. Pomarol, Nucl. Phys. B **719**, 165 (2005) [hep-ph/0412089].

[15] J. R. Espinosa, C. Grojean and M. Muhlleitner, JHEP **1005**, 065 (2010) [arXiv:1003.3251 [hep-ph]].

[16] R. Contino, L. Da Rold and A. Pomarol, Phys. Rev. D **75**, 055014 (2007) [hep-ph/0612048].

[17] M. S. Carena, S. Heinemeyer, C. E. M. Wagner and G. Weiglein, hep-ph/9912223.

[18] M. S. Carena, H. E. Haber, H. E. Logan and S. Mrenna, Phys. Rev. D **65**, 055005 (2002) [Erratum-ibid. D **65**, 099902 (2002)] [hep-ph/0106116].

[19] A. Djouadi, J. Kalinowski and M. Spira, Comput. Phys. Commun. **108**, 56 (1998) [hep-ph/9704448].

[20] M. Carena, S. Gori, N. R. Shah, C. E. M. Wagner and L. -T. Wang, arXiv:1205.5842 [hep-ph].

[21] ATLAS Collaboration, ATLAS-CONF-2012-093, arXiv:1207.7214.

[22] CMS Collaboration, CMS-PAS-HIG-12-020, arXiv:1207.7235.

[23] ATLAS Collaboration, ATLAS-CONF-2012-098.

[24] L. D. Landau, Dokl. Akad. Nawk. USSR **60**, 207 (1948); C.-N. Yang, Phys. Rev. **77**, 242 (1950).

[25] ATLAS Collaboration, "ATLAS Detector and Physics Performance Technical Design Report," CERN-LHCC-99-15.

[26] CMS Collaboration, "CMS Physics Technical Design Report. Volume II: Physics Performance," CERN-LHCC-2006-001.

[27] F. Gianotti and M. Pepe-Altarelli, Nucl. Phys. Proc. Suppl. **89**, 177 (2000) [hep-ex/0006016].

[28] S. P. Martin, arXiv:1208.1533 [hep-ph].

[29] Y. Gao, A. V. Gritsan, Z. Guo, K. Melnikov, M. Schulze and N. V. Tran, Phys. Rev. D **81**, 075022 (2010) [arXiv:1001.3396 [hep-ph]].

[30] A. De Rujula, J. Lykken, M. Pierini, C. Rogan and M. Spiropulu, Phys. Rev. D **82**, 013003 (2010) [arXiv:1001.5300 [hep-ph]].

[31] V. Hankele, G. Klamke, D. Zeppenfeld and T. Figy, Phys. Rev. **D74**, 095001 (2006).

[32] D. Zeppenfeld, R. Kinnunen, A. Nikitenko and E. Richter-Was, Phys. Rev. D **62**, 013009 (2000); A. Djouadi *et al.*, arXiv:hep-ph/0002258; D. Zeppenfeld, hep-ph/0203123.

[33] O. J. P. Eboli and D. Zeppenfeld, Phys. Lett. B **495**, 147 (2000) [hep-ph/0009158].

[34] M. Dührssen, S. Heinemeyer, H. Logan, D. Rainwater, G. Weiglein and D. Zeppenfeld, Phys. Rev. **D70**, 113009 (2004).

[35] I. Low and J. Lykken, JHEP **1010**, 053 (2010) [arXiv:1005.0872 [hep-ph]].

[36] J. M. Butterworth, A. R. Davison, M. Rubin and G. P. Salam, Phys. Rev. Lett. **100**, 242001 (2008) [arXiv:0802.2470 [hep-ph]].

[37] T. Plehn, G. P. Salam and M. Spannowsky, Phys. Rev. Lett. **104**, 111801 (2010) [arXiv:0910.5472 [hep-ph]].

[38] M. Dührssen, ATLAS report ATL-PHYS-2003-030 (2003).

[39] M. Dührssen, S. Heinemeyer, H. Logan, D. Rainwater, G. Weiglein and D. Zeppenfeld, Phys. Rev. D **70**, 113009 (2004) [hep-ph/0406323], hep-ph/0407190.

[40] A. Belyaev and L. Reina, JHEP **08** (2002) 041.

[41] R. Lafaye, T. Plehn, M. Rauch, D. Zerwas and M. Dührssen, JHEP **08** (2009) 009.

[42] M. Klute, R. Lafaye, T. Plehn, M. Rauch and D. Zerwas, arXiv:1205.2699 [hep-ph].

[43] M. E. Peskin, arXiv:1207.2516 [hep-ph].

[44] S. Kanemura, Y. Okada and E. Senaha, Phys. Lett. B **606**, 361 (2005) [hep-ph/0411354].

[45] E. Asakawa, D. Harada, S. Kanemura, Y. Okada and K. Tsumura, Phys. Rev. D **82**, 115002 (2010) [arXiv:1009.4670 [hep-ph]].

[46] G. D. Kribs and A. Martin, arXiv:1207.4496 [hep-ph].

[47] U. Baur, T. Plehn and D. L. Rainwater, Phys. Rev. Lett. **89**, 151801 (2002) [hep-ph/0206024]; Phys. Rev. D **67**, 033003 (2003) [hep-ph/0211224].

[48] F. Gianotti, M. L. Mangano, T. Virdee, S. Abdullin, G. Azuelos, A. Ball, D. Barberis and A. Belyaev *et al.*, Eur. Phys. J. C **39**, 293 (2005) [hep-ph/0204087].

[49] U. Baur, T. Plehn and D. L. Rainwater, Phys. Rev. D **68**, 033001 (2003) [hep-ph/0304015].

[50] U. Baur, T. Plehn and D. L. Rainwater, Phys. Rev. D **69**, 053004 (2004) [hep-ph/0310056].

[51] ILD Concept Team, Official URL?

[52] SiD Concept Team, Official URL?

[53] M. T. Dova, P. Garcia-Abia, and W. Lohmann, hep-ph/0302113.

[54] M. Schumacher, LC-PHSM-2001-003 (2001).

[55] M. Krämer, J. H. Kühn, M. L. Stong and P. M. Zerwas, Z. Phys. C64, 21 (1994).

[56] K. Desch, A. Imhof, Z. Was and M. Worek, Phys. Lett. B **579**, 157 (2004) [hep-ph/0307331].

[57] H. Ono and A. Miyamoto, arXiv:hep-ex/1207.0300v1

[58] Y. Banda, T. Laštovička, and Andrei Nomerotski, Phys. Rev. **D82**, 033013 (2010)

[59] H. Ono, Talk given at KILC2012.

[60] ACFA Linear Collider Working Group, K. Abe et al., hep-ph/0109166.

[61] M. Battaglia, hep-ph/9910271.

[62] T. Kuhl and K. Desch, LC-PHSM-2007-2.

[63] G. Borisov and F. Richard, hep-ph/9905413.

[64] E. Boos et al., Eur. Phys. J. C19, 455 (2001).

[65] H. Ono. Asian Physics and Software Meeting, Jun. 29, 2012.

[66] A. Yamamoto. Asian Physics and Software Meeting, Jun. 29, 2012.

[67] Y. Takubo, arXiv:hep-ph/1011.5805v3 (2011).

[68] K. Hagiwara, H. Murayama, and I. Watanabe, Nucl. Phys. [22] B367, 257 (1991).

[69] A. Djouadi, J. Kalinowski, and P. M. Zerwas, Mod. Phys. Lett. A 7, 1765 (1992).

[70] A. Juste and G. Merino, arXiv:hep-ph/9910301.

[71] A. Gay, Eur. Phys. J. C49, 489 (2007).

[72] H. Baer, S. Dawson, and L. Reina, Phys. Rev. **D61**, 013002 (1999)

[73] S. Dittmaier, M. Krämer, Y. Liao, M. Spira, and P. M. Zerwas, Phys. Lett. B 441, 383 (1998).

[74] S. Dawson, and L. Reina, Phys. Rev. **D59**, 054012 (1999)

[75] G. Bélanger et al., Phys. Lett. B 571, 163 (2003).

[76] A. Denner, S. Dittmaier, M. Roth, and M. M. Weber, Nucl. Phys. B680, 85 (2004).

[77] Y. You et al., Phys. Lett. B 571, 85 (2003).

[78] C. Farrell and A. H. Hoang, Phys. Rev. **D72**, 014007 (2005).

[79] C. Farrell and A. H. Hoang, Phys. Rev. **D74**, 014008 (2006).

[80] A. Juste et al., Proceedings of the 2005 International Linear Collider Physics and Detector Workshop and 2nd ILC Accelerator Workshop (Snowmass 2005), econf C0508141, PLEN0043 (2005).

[81] R. Yonamine, et al, Phys. Rev. **D84**, 014033 (2011).

[82] T. Tanabe, et al, ILD Workshop, Kyushu, May, 2012.

[83] H. Tabassam and V. Martin arXiv:1202.6013v1.

[84] T. Suehara and T. Tanabe, KILC12.

[85] J. Tian, et al, Private communication.

[86] C. Castanier, P. Gay, P. Lutz, and J. Orloff, hep-ex/0101028.

[87] U. Baur, T. Plehn, and D. Rainwater in LHC/LC Study Group, G. Weiglein et al., Phys. Rept. 426, 47 (2006).

[88] M. Battaglia, E. Boos, and W.-M. Yao, arXiv:hep-ph/0111276.

[89] Y. Yasui et al., arXiv:hep-ph/0211047.

[90] S. Yamashita, talk at LCWS04, Paris. April 2004.

[91] M. Battaglia and A. D. Roeck, arXiv:hep-ph/0111307.

[92] M. Battaglia and A. D. Roeck, arXiv:hep-ph/0211207.

[93] T. L. Barklow, arXiv:hep-ph/0312268

[94] J. Tian, Ph.D. Thesis.

3 Two-Fermion Processes

The reactions $e^+e^- \to f\overline{f}$, where f could be leptons or quarks, provide a powerful tool to search for and characterize physics beyond the Standard Model at the ILC. These processes are distinguished by clean, simple final states, and precise perturbative predictions of the SM contributions are available. As a result, ILC experiments will be sensitive to even small deviations from the SM predictions in these channels, enabling them to study new physics at energy scales far above the center-of-mass energy of the collider.

3.1 Systematics of $e^+e^- \to f\overline{f}$

Despite the simplicity of the two-fermion final state, the process $e^+e^- \to f\overline{f}$ offers a large number of methods with which to probe for deviations from the Standard Model. In this section, we will review the observables that the ILC will make available. In the following sessions, we will review how these observables can be applied to discover and then to analyze any signals of new physics that can appear in these reactions.

For all channels except $e^+e^- \to e^+e^-$, helicity conservation implies that the process $e^+e^- \to f\overline{f}$ is dominated by s-channel spin 1 exchange. This assumption applies whenever fermion mass effects can be neglected, and this is an excellent approximation at 500 GeV for pair-production of all Standard Model fermions except for the top quark. In this case, the angular distribution of $e^+e^- \to f\overline{f}$ is simply written as

$$\frac{d\sigma}{d\cos\theta} = \frac{\pi\alpha^2}{2s}[A_+(1+\cos\theta)^2 + A_-(1-\cos\theta)^2] \ . \tag{35}$$

The coefficients A_+, A_- depend on the electron polarization. Models with gravitational effects at the TeV scale (for example, Randall-Sundrum models) will add terms from s-channel spin 2 exchange that are higher polynomials in $\cos\theta$.

In (35), the term multiplying A_+ is generated by the polarized reactions $e^-_L e^+_R \to f_L\overline{f}_R$ and $e^-_R e^+_L \to f_R\overline{f}_L$, the term multiplying A_- is generated by $e^-_L e^+_R \to f_R\overline{f}_L$ and $e^-_R e^+_L \to f_L\overline{f}_R$, and all other polarized cross sections are zero in the absence of mass corrections. This means that by measuring the cross sections and forward backward asymmetries with highly polarized e^-_L and e^-_R, we obtain 4 independent pieces of information on the s-channel amplitudes. In principle, only the electron beam needs to be polarized, though even a small polarization of the positron beam improves the effective initial-state polarization according to

$$P_{eff} = \frac{P(e^-) + P(e^+)}{1 + P(e^-)P(e^+)} \tag{36}$$

Thus, a measurement with 80% polarization in the electron beam and 30% polarization in the positron beam yields an effective initial-state polarization greater than 90%. At the ILC, polarization is monitored externally, but in addition the actual polarization in collisions can be determined from the high-rate processes of Bhabha scattering and forward W^-W^+ production. [**ACCURACY of the Polarization measurement to be reported in the DBD?**] Theoretical calculations of the 2-fermion cross sections are controlled to below the part-per-mil level.

The four observables described in the previous paragraph are available for any final state that can be distinguished at the ILC. That is, these quantities can be measured separately for light quarks, c quarks, b quarks, e, μ, and τ. The typical c, b and μ identification efficiencies expected at the ILC are 35%, 60%, and over 96%, respectively [1]. [**New DBD numbers?**] In addition, the final state τ lepton polarization can be determined [**ref to LOIs**] as a cross-check on the leptonic coupling measurements.

The dominant contributions to $e^+e^- \to f\overline{f}$ at 500 GeV will probably come from Standard Model s-channel γ and Z^0 exchange. However, additional effects may arise from new gauge bosons, from contact interactions associated with fermion compositeness, or from effects of extra dimensions. These terms can be seen at the ILC as corrections to the $e^+e^- \to f\overline{f}$ cross sections and asymmetries, arising from interference of new physics with the Standard Model amplitudes, and, for example in the case of extra dimensions, can add additional dependence on $\cos\theta$ related to the spin-2 graviton exchange. We will now review the expected sensitivity of the ILC experiments to these effects.

3.2 Z' physics

A canonical, well-motivated example of new physics that can be discovered and studied in $e^+e^- \to f\overline{f}$ is a new, heavy, electrically neutral gauge boson, commonly denoted by Z'. There are many extensions of the SM that predict one or more such particles (for reviews and references, see [2]). For example, Grand Unified Theories (GUTs) based on groups such as $SO(10)$ or E_6 contain extra $U(1)$ factors in addition to the SM gauge group, and hence Z' bosons. Similarly, superstring constructions often involve large gauge symmetries that contain extra $U(1)$ factors. Since the Z' couplings conserve baryon and lepton numbers, its mass may be well below the GUT or string scale, as low as the TeV, without conflict with experiment. In fact, in many supersymmetric GUT and string models, the Z' mass is tied to the soft supersymmetry breaking scale, expected to be at the TeV scale. The motivation for a TeV-scale Z' is particularly strong in supersymmetric models with additional particles that are singlets of the SM $SU(2) \times U(1)$. Such models, *e.g.* the next-to-minimal supersymmetric standard model (NMSSM), recently attracted much interest, since they provide a simple way to reduce the fine-tuning associated with a 125 GeV Higgs [3]. The weak-scale mass of the SM singlet field can be naturally explained if it is charged under a new U(1) symmetry broken at TeV energies; in addition, the domain-wall problem of the NMSSM is avoided in this case. Among non-supersymmetric possibilities, a very interesting example of a model containing a Z' is the Little Higgs, where extra gauge bosons are introduced to cancel quadratic divergences in the Higgs mass renormalization by the SM gauge bosons (for reviews and references, see [4]). Naturalness of electroweak symmetry breaking requires that these new gauge bosons appear at the TeV scale.

Searches for Z' have been conducted, most recently, at LEP and the Tevatron, and are currently in progress at the LHC. The negative results of these searches preclude the possibility of on-shell Z' production at the ILC. Indeed, the LHC now excludes the appearance of large Z' resonances over most of the range of proposed 3 TeV lepton colliders, and this exclusion could be complete by the end of 2013. This makes it likely that our most important tool for the characterization of any Z' discovered at the LHC will be through indirect effects uncovered through the precision measurement of $e^+e^- \to f\overline{f}$ processes. The dominant effects of new physics in this case come from the interference between the diagrams involving the SM γ/Z^0 and those involving the Z'. Thanks to the high precision of the ILC, its capabilities to discover the Z' and measure its couplings actually exceed those of the LHC in most cases.

3.2.1 Benchmark Z' Models

Predictions for the contribution of a Z' to any observable depend on the boson's mass $M_{Z'}$ and its couplings to the SM fermions, which are model-dependent. While a very large variety of models have been proposed, a few canonical benchmark cases have been extensively studied and provide a set of reference points for comparisons between experiments. The Sequential Standard Model (SSM) assumes that all Z' couplings are the same as for the SM Z. The left-right symmetric (LRS) model extends the SM electroweak gauge group to $SU(2)_L \times SU(2)_R \times U(1)_{B-L}$, with the $SU(2)_R \times U(1)_{B-L} \to U(1)_Y$ breaking at the TeV scale. The Z' couples to the linear combination of T_{3R} and $B-L$ currents orthogonal to the SM hypercharge. Another set of popular benchmark models is based on the E_6 GUT, where the TeV-scale Z' is generally a linear combination of the two extra $U(1)$ gauge bosons Z_ψ and Z_χ: $Z' = Z_\chi \cos\beta + Z_\psi \sin\beta$. Some well-motivated possibilities are $\beta = 0$ (the "χ-model"), $\beta = \pi/2$ (the "ψ-model"), and $\beta = \pi - \arctan\sqrt{5/3}$ (the "η-model", which occurs in Calabi-Yau compactification of the heterotic string if E_6 breaks directly to a rank-5 group). It is also possible to embed a left-right symmetric model in E_6, leading to the so-called "alternative" left-right (ALR) model. The Z' couplings to the SM fermions in each of these models can be found, for example, in Table 1 of [5]. Well-studied Little Higgs models which contain Z' candidates include the original "Littlest Higgs" (LH) [6], as well as the Simplest Little Higgs (SLH) [7].

3.2.2 Current Limits on Z' and the ILC Reach

The most restrictive bounds on most Z' models currently come from the LHC experiments. For the SSM, CMS places a 95% c.l. bound of $M(Z'_{\rm SSM}) > 2.59$ TeV, using dielectron and dimuon final states and 4.1 fb^{-1} of data at $\sqrt{s} = 8$ TeV [8]. This is stronger than the indirect LEP-2 bound. For Z'_ψ, the CMS bound from the same analysis is 2.26 TeV. At this time, ATLAS [9] has only published constraints with the 2011 LHC data set at $\sqrt{s} = 7$ TeV, but covering a larger variety of E_6 models. The bounds are in the range $1.76 - 1.96$ TeV, indicating that the model-dependence is rather weak.

The current LHC bounds rule out the possibility of on-shell production of a Z' at the ILC. However, the ILC will be sensitive to Z' even at $\sqrt{s} \ll M_{Z'}$, via contact-interaction corrections to 2-fermion processes. A recent estimate of the ILC reach in various Z' models [10], compared to the LHC reach [5], is shown in Fig. 21. The reach of a 500 GeV ILC exceeds the LHC reach in most models, while a 1 TeV ILC will significantly improve on the LHC performance in all cases, with sensitivity well above 10 TeV in many models.

3.2.3 Measurement of Z' couplings

If a signal consistent with a Z' is discovered, the next task would be to discriminate between the Z' models by measuring its couplings. A study of 2-fermion processes at the ILC provides a powerful tool to do so. For example, expected accuracy of the measurement of the Z' couplings to charged leptons, assuming $M(Z') = 2$ and 4 TeV, is shown in Fig. 22 (from Ref. [11]). The accuracy is sufficient to clearly discriminate between the benchmark models, especially with polarized beams. It should be emphasized that the ILC retains its model-discrimination power for a wide range of Z' masses. An illustration is provided by Fig. 21, which shows that, if one of the 6 models studied in Ref. [10] is true, the other 5 candidates can be ruled out by a 500 GeV ILC for the Z' masses up to $4 - 8$ TeV, depending on the true model. The model identification reach is in fact only slightly below the discovery reach, thanks to order-one differences among the angular distributions in $e^+e^- \to f\overline{f}$ predicted by various models. It is significantly higher than that of the LHC in all cases. It should be noted that beam polarization significantly improves the model identification reach

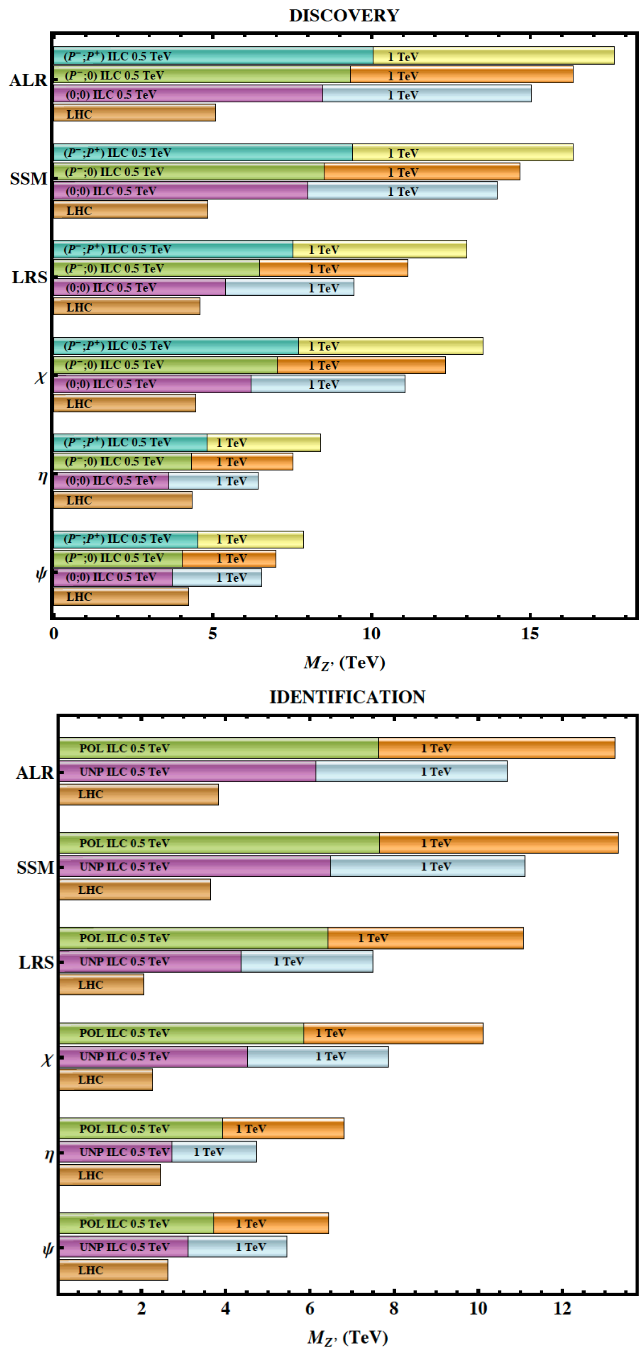

Figure 21: Discovery (top) and identification (bottom) reach of the ILC with $\sqrt{s} = 0.5(1.0)$ TeV and $\mathcal{L}_{\text{int}} = 500(1000)$ fb^{-1}. The sensitivity of the LHC-14 via Drell-Yan process $pp \to \ell^+\ell^- + X$ with 100 fb^{-1} of data are shown for comparison. For details, see [10].

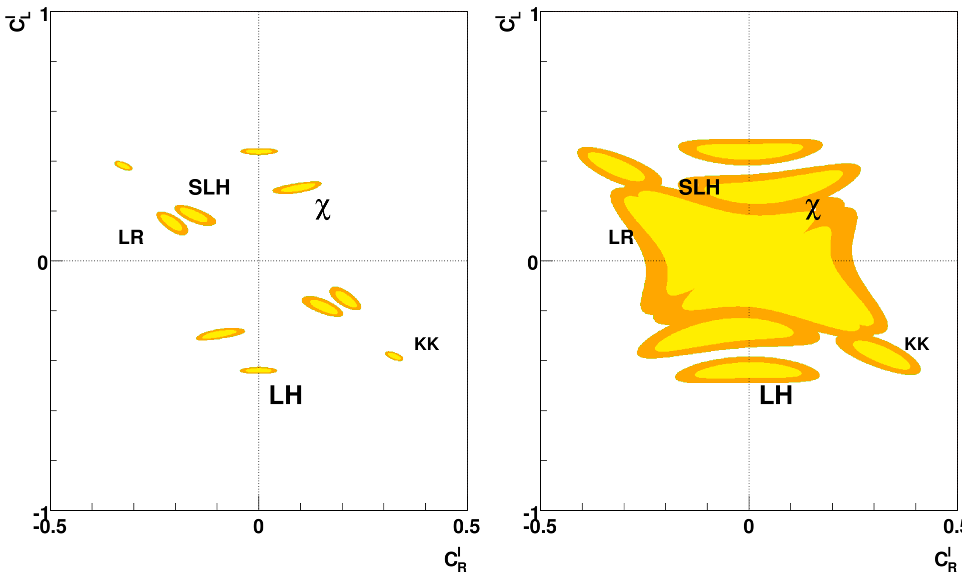

Figure 22: 95% confidence regions in the plane of the couplings of left- and right-handed leptons to a Z' boson, for the ILC with $\sqrt{s} = 500$ GeV and 1000 fb^{-1} and 80%/60% electron and positron polarization, for $M_{Z'} = 2$ TeV (left panel) and 4 TeV (right panel). For further details, see Ref. [11]. **[Michael: let me know if you want to switch back to showing a single plot with a 2 TeV Z', as in the previous version of the draft.]**

of the ILC.

3.2.4 *Example: $SO(10)$ Z' at 3 TeV*

[This section will discuss the study of an $SO(10)$ Z' of mass 3 TeV through precise 2-fermion measurements at the ILC.]

3.3 Quark and Lepton Compositeness

In many extensions of the SM, quarks and leptons themselves are composite particles, resolved into more fundamental constituents at an energy scale Λ. The effect of such compositness in $2 \to 2$ fermion scattering processes at energies well below Λ is to induce contact-interaction type corrections, similar to the corrections due to a heavy resonance discussed above. The effects can be parametrized by adding four-fermion operators to the Lagrangian with coefficients proportional to inverse powers of Λ [12]. Currently, the strongest bounds on four-lepton and $eeqq$ operators are $\Lambda \gtrsim 10$ TeV [30,31]. These bounds come from experiments at LEP. The LHC is unlikely to improve these limits, since at LHC we have only limited polarization observables in

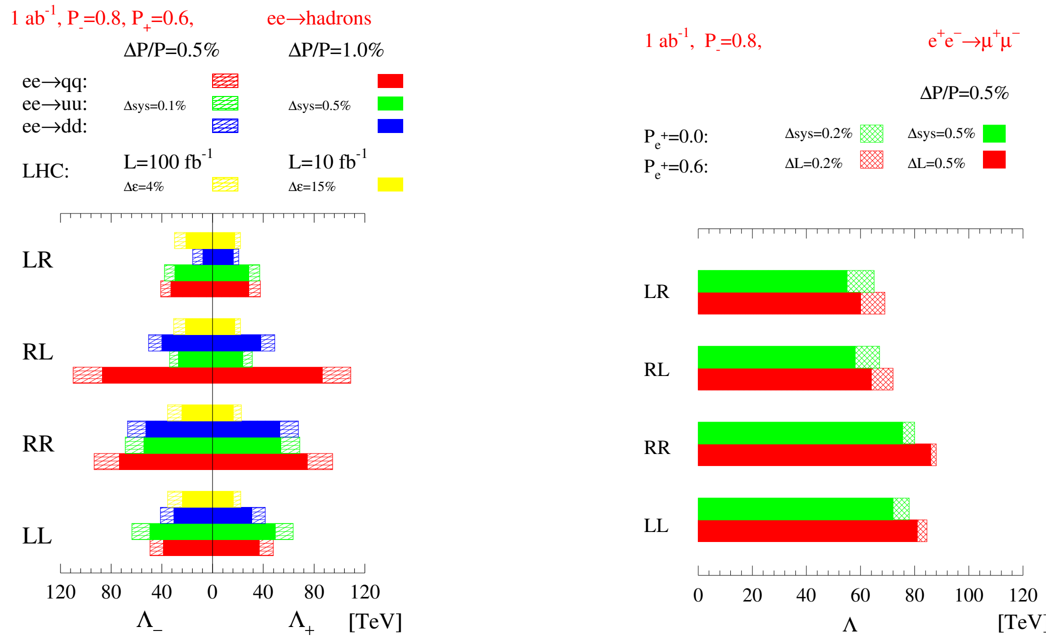

Figure 23: Sensitivities (95% c.l.) of a 500 GeV ILC to contact interaction scales Λ for different helicities in $e^+e^- \to$ hadrons (left) and $e^+e^- \to \mu^+\mu^-$ (right), including beam polarization [13].

4-fermion reactions and we do not know the flavor of initial state quarks. The ILC can dramatically increase the reach, with sensitivity to scales as high as $50 - 100$ TeV depending on the helicity structure of the operators (see Fig. 23.)

3.4 Extra Dimensions

Many interesting extensions of the SM postulate the existence of extra spatial dimensions, beyond the familiar three, which are usually assumed to be compact. Motivation for extra dimensions comes from two sides. From the top-down point of view, consistency of string theory requires that the full space-time be 10-dimensional, and additional dimensions must be compactified. From the bottom-up perspective, models with extra dimensions can address some of the theoretical shortcomings of the SM, such as the gauge hierarchy problem. While the extra dimensions of string theory can have any size, in all phenomenologically interesting models the extra dimensions become experimentally manifest at the TeV scale, within the range of the ILC experiments.

Phenomenologically, the most important feature of models with extra dimensions is the appearance of Kaluza-Klein (KK) resonances. Each SM particle (including the graviton) that is allowed to propagate beyond 4D is accompanied by a tower of KK excitations, particles of the same spin and progressively higher masses. In the simplest case of toroidal compactification of radius R, the n-th KK mode has mass $m_n = n/R$. The effect of the KK modes on $e^+e^- \to f\overline{f}$ are similar to that of a Z': contact interactions, or, if collision energy is sufficient, resonances.

3.4.1 Flat, TeV-Sized Extra Dimensions

The simplest extension is to add k extra dimensions compactified on a torus T^k, and allow all SM fields to propagate in the full space. The most popular model of this type is the "universal extra dimension" (UED) [14], with $k = 1$ and radius $R \sim 1/\text{TeV}$. This model assumes a $\mathcal{Z}_2$ symmetry under which the n-th KK mode has KK-parity $(-1)^n$. As a result, production of a single first-level KK partner in SM collisions is not possible, and the phenomenology of the first-level KK states is similar to that of supersymmetric models with R-parity. The even-level KK states, on the other hand, may be singly produced via KK-number violating interactions, induced by loops [15]. This leads to resonances or contact-interaction corrections in $e^+e^- \to f\overline{f}$ [16,17]. An estimated sensitivity of the ILC to the UED model is shown in Fig. 24; values of $1/R \sim 1$ TeV can be probed. The reach is significantly lower than for conventional Z', due to loop-suppressed couplings. However, it should be noted that the same suppression severely limits the ability of the LHC to search for the single KK-mode production. Any resonance for which the coupling to quarks is suppressed by a factor of 10 would contribute a fluctuation below 1% in the Drell-Yan mass spectrum, and this will be indistinguishable even for rather light KK masses. Small mass splittings among the KK states at the first level make the LHC searches for pair-production very difficult as well. [**Are there quantitative statements about the LHC reach in the literature?**]

3.4.2 Large Extra Dimensions

The extra dimensions may have sizes much larger than TeV^{-1}, if *only* gravity can propagate in them, while the SM fields are confined on a 4D "brane" inside the full space. Arkani-Hamed, Dimopoulos and Dvali (ADD) [18] proposed that such models can provide an alternative solution to the gauge hierarchy problem: gravity is weaker than other forces due to the larger space in which it propagates. The ADD model is characterized by the fundamental Planck scale M_D (required to be $\sim$TeV to solve the hierarchy problem); and the number of extra dimensions k. Constraints on macroscopic modifications of Newtonian gravity imply that only cases $k \geq 2$ are phenomenologically relevant.

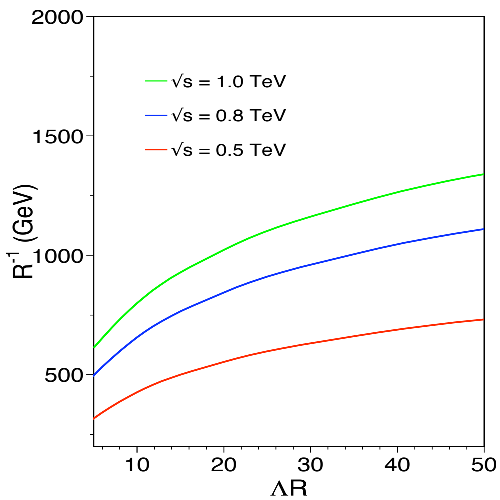

Figure 24: Discovery reach of the ILC, with $\mathcal{L}_{\rm int} = 1000$ fb^{-1} and energy indicated on the plot, for the UED model in the 2-fermion channel. Polarization of 80%/60% for electrons/positrons is assumed. Leptonic and hadronic final states are combined. The scale Λ is the cutoff of the theory, and is somewhat model-dependent. For details, see Ref. [16].

The model predicts a tower of KK gravitons G_{KK}, with very small spacing in mass, of order $1/R$. While each of the G_{KK} couples to the SM with gravitational strength, their large multiplicity may yield observable effects in $e^+e^- \to G_{KK} \to f\overline{f}$, although no individual resonances can be observed. Instead, the effect is a contact-interaction correction, parametrized as a dimension-8 operator [19]

$$\mathcal{L} = \frac{4\lambda}{\Lambda_H^4} T_{\mu\nu} T^{\mu\nu} \,, \tag{37}$$

where $T_{\mu\nu}$ is the SM fermion energy-momentum tensor, $\lambda = \pm 1$, and $\Lambda_H \sim M_D$ is the effective Planck scale.

The strongest bounds on the ADD model currently come from the LHC. A search for anomalous jet+$\not{E}_T$ events at CMS with 5 fb^{-1} at 7 TeV [20] constrains $M_D >$ 2.5 − 4.0 TeV for $k = 2 \ldots 6$ (with lower bounds for higher k). In addition, searches for operators of the form (37) in $\ell^+\ell^-$ [21] and $\gamma\gamma$ [22,23] final states provide a bound $\Lambda_H \gtrsim 2.5$ GeV, independent of k. **[Eventual LHC sensitivity?]** . The estimate of the discovery reach of the 500 GeV ILC is $\Lambda_H \approx 5.0 - 5.5$ TeV [24]. Since the KK graviton is a spin-2 object, the angular distribution of the final-state fermions in the ADD model is quite distinct from the case of a spin-1 Z' or KK gauge boson. A unique identification of the spin-2 origin of the contact-interaction correction at a 500 GeV ILC is possible for Λ_H up to about 3.0 TeV [25]; however, the LHC is likely to have an even higher reach using the dilepton final states [26].

Another crucial test of the gravitational nature of the contact interaction would be an independent determination of the size of the effect in a variety of four-fermion channels. Gravity couples to the total energy-momentum tensor, resulting in a set of four-fermion operators independent of the fermion type. Alternative models for spin-2 contact interactions, such as the exchange of string-Regge excitations of the SM gauge bosons [27], predict effects of different sizes for up-type and down-type quarks and leptons. The ILC will provide an ideal environment to perform this test.

3.4.3 Randall-Sundrum Warped Extra Dimensions

While the ADD model eliminates the usual gauge hierarchy, it faces its own hierarchy problem: the large ratio of the size of the extra dimensions and their natural scale, TeV^{-1}, must be explained. This difficulty is avoided in the Randall-Sundrum (RS) model [28], which extends the space by a single extra dimension, compactified on an orbifold $S_1/\mathcal{Z}_2$, effectively an interval. The characteristic feature of this model is the non-flat "warped" metric, which can be used to generate the observed large hierarchy between the Planck and the weak scale without assuming any hierarchies among the input parameters. Interestingly, AdS/CFT duality has been used to argue that the RS model is simply a weakly-coupled description of a strongly-coupled four-dimensional model with a composite Higgs boson.

In the original RS model, only gravity was assumed to propagate in the full 5D space, while all SM fields were confined on the 4D boundary. As in ADD, potentially observable KK modes of the graviton are predicted; however, their masses are spaced by $\mathcal{O}(\mathrm{TeV})$, and their couplings to the SM are suppressed by a scale of $\mathcal{O}(\mathrm{TeV})$ and not the Planck scale. The LHC experiments search for RS KK graviton resonances in the $\ell^+\ell^-$ and $\gamma\gamma$ final states. The graviton couplings to the SM depend on the curvature of the extra dimension k. The dimensionless ratio $k/\overline{M}_{\mathrm{Pl}}$ is expected to be in a range between 0.01 and 0.1 on naturalness grounds. The current LHC bounds on the KK graviton mass vary from 2.1 TeV for $k/\overline{M}_{\mathrm{Pl}} = 0.1$ to 0.9 TeV for $k/\overline{M}_{\mathrm{Pl}} = 0.01$ [8,9]. The LHC reach with $\sqrt{s} = 14$ TeV, $L_{\mathrm{int}} = 100\ \mathrm{fb}^{-1}$ is expected to be $2.5 - 4.5$ TeV, for the same range of $k/\overline{M}_{\mathrm{Pl}}$ [29]. **[ILC reach?]**

References

[1] J. Brau, (Ed.) *et al.* [ILC Collaboration], *"ILC Reference Design Report: ILC Global Design Effort and World Wide Study,"* arXiv:0712.1950 [physics.acc-ph]; G. Aarons *et al.* [ILC Collaboration], *"International Linear Collider Reference Design Report Volume 2: Physics At The ILC,"* arXiv:0709.1893 [hep-ph].

[2] A. Leike, Phys. Rept. **317**, 143 (1999) [hep-ph/9805494];
P. Langacker, Rev. Mod. Phys. **81**, 1199 (2009) [arXiv:0801.1345 [hep-ph]].

[3] L. J. Hall, D. Pinner and J. T. Ruderman, JHEP **1204**, 131 (2012) [arXiv:1112.2703 [hep-ph]].

[4] M. Schmaltz and D. Tucker-Smith, Ann. Rev. Nucl. Part. Sci. **55**, 229 (2005) [hep-ph/0502182];
M. Perelstein, Prog. Part. Nucl. Phys. **58**, 247 (2007) [hep-ph/0512128].

[5] P. Osland, A. A. Pankov, A. V. Tsytrinov and N. Paver, Phys. Rev. D **79**, 115021 (2009) [arXiv:0904.4857 [hep-ph]].

[6] N. Arkani-Hamed, A. G. Cohen, E. Katz and A. E. Nelson, JHEP **0207**, 034 (2002) [hep-ph/0206021].

[7] M. Schmaltz, JHEP **0408**, 056 (2004) [hep-ph/0407143].

[8] S. Chatrchyan *et al.* [CMS Collaboration], *"Search for resonances in dilepton mass spectra in pp collisions at sqrt(s) = 8 TeV,"* CMS PAS EXO-12-015.

[9] G. Aad *et al.* [ATLAS Collaboration], *Search for high mass dilepton resonances with 5 fb?1 of pp collisions at sqrt(s) = 7 TeV with the ATLAS experiment*, ATLAS-CONF-2012-007;
G. Aad *et al.* [ATLAS Collaboration], Phys. Rev. Lett. **107**, 272002 (2011) [arXiv:1108.1582 [hep-ex]].

[10] P. Osland, A. A. Pankov and A. V. Tsytrinov, Eur. Phys. J. C **67**, 191 (2010) [arXiv:0912.2806 [hep-ph]].

[11] S. Godfrey, P. Kalyniak and A. Tomkins, hep-ph/0511335.

[12] E. Eichten, K. D. Lane and M. E. Peskin, Phys. Rev. Lett. **50**, 811 (1983).

[13] S. Riemann, LC-TH-2001-007.

[14] T. Appelquist, H. -C. Cheng and B. A. Dobrescu, Phys. Rev. D **64**, 035002 (2001) [hep-ph/0012100].

[15] H. -C. Cheng, K. T. Matchev and M. Schmaltz, Phys. Rev. D **66**, 056006 (2002) [hep-ph/0205314].

[16] S. Riemann, eConf C **050318**, 0303 (2005) [hep-ph/0508136].

[17] B. Bhattacherjee and A. Kundu, Phys. Lett. B **627**, 137 (2005) [hep-ph/0508170];
B. Bhattacherjee, Pramana **69**, 855 (2007) [hep-ph/0608227].

[18] N. Arkani-Hamed, S. Dimopoulos and G. R. Dvali, Phys. Lett. B **429**, 263 (1998) [hep-ph/9803315].

[19] J. L. Hewett, Phys. Rev. Lett. **82**, 4765 (1999) [hep-ph/9811356].

[20] CMS EXO-11-059, *Search for Dark Matter and Large Extra Dimensions in Monojet Events in pp Collisions at $\sqrt{s} = 7$ TeV*

[21] S. Chatrchyan *et al.* [CMS Collaboration], Phys. Lett. B **711**, 15 (2012) [arXiv:1202.3827 [hep-ex]].

[22] G. Aad *et al.* [ATLAS Collaboration], Phys. Lett. B **710**, 538 (2012) [arXiv:1112.2194 [hep-ex]].

[23] S. Chatrchyan *et al.* [CMS Collaboration], arXiv:1112.0688 [hep-ex].

[24] T. G. Rizzo, AIP Conf. Proc. **1256**, 27 (2010) [arXiv:1003.1698 [hep-ph]].

[25] T. G. Rizzo, JHEP **0210**, 013 (2002) [hep-ph/0208027].

[26] E. W. Dvergsnes, P. Osland, A. A. Pankov and N. Paver, Phys. Rev. D **69**, 115001 (2004) [hep-ph/0401199].

[27] S. Cullen, M. Perelstein and M. E. Peskin, Phys. Rev. D **62**, 055012 (2000) [hep-ph/0001166].

[28] L. Randall and R. Sundrum, Phys. Rev. Lett. **83**, 3370 (1999) [hep-ph/9905221].

[29] H. Davoudiasl, J. L. Hewett and T. G. Rizzo, Phys. Rev. D **63**, 075004 (2001) [hep-ph/0006041].

[30] K. Nakamura *et al.* [Particle Data Group Collaboration], J. Phys. G G **37**, 075021 (2010).

[31] CMS PAS EXO-11-009, *Search for Contact Interactions in $\mu^+\mu^-$ Events in pp Collisions at $\sqrt{s} = 7$ TeV.*

4 W and Z Boson Physics

4.1 Introduction

In this section, we will describe the ILC program of measurements on the electroweak gauge bosons. The ILC will yield a new level of measurements of the W and Z boson masses, widths, and couplings. Several different ILC processes contribute to these measurements. These include the continuum production of two vector bosons, $e^+e^- \to W^+W^-$, $e^+e^- \to ZZ$, production of weak bosons in $\gamma\gamma$ collisions using the spectrum of Weizsäcker-Williams photons, and triboson production $e^+e^- \to VVV$, where there can be any combination of WWZ, ZZZ, or even $WW\gamma$ in the final state. In addition, the ILC can study vector boson scattering at high energy. Furthermore, the ILC offers the possibility of dedicated low-energy runs at the Z and at the WW threshold. In all cases, these measurements will supersede the precision of existing measurements from the previous colliders, including SLC, LEP and trhe Tevatron, and are expected also to surpass the accuracies that will be available from the LHC.

As we will explain in detail in this section, these measurements will allow us to go beyond the usual description of the W and Z bosons in the Standard Model to probe the next possible level of couplings in the vector boson effective Lagrangian. These new couplings can give evidence of composite structure in the Higgs boson sector that is inherited by the weak vector bosons.

Many models of new physics beyond the Standard Model predict new couplings of the W and Z bosons. These include models with additional heavy vector bosons such as technicolor and topcolor, Little Higgs models, extra-dimensional models with Kaluza-Klein recurrences of the W and Z boson, and Twin Higgs models. In many of these cases, the additional gauge bosons could be quite fermiophobic and would thus evade direct searches at the LHC. The new bosons must then be found through their mixing with the W and Z bosons at the tree or one-loop level. Such mixing effects could be detected by the precision measurements described in this section.

4.2 Beyond the SM W/Z sector: the EW chiral Lagrangian

Measurements at the ILC will seek to discover new bosons at higher energy indirectly through the precision measurement of W and Z properties at 500 GeV and 1 TeV. To analyze these measurements, it is convenient to describe new physics effects by writing an effective field theory (EFT) that includes the most general modifications of the W and Z couplings induced by possible operators according to their mass dimension. Such EFT descriptions of W and Z boson dynamics can be found in the literature [14,15]. A complementary point of view using a simplified model approach including resonances that can couple to the electroweak boson sector has been presented in [1]. It is rather easy to switch between the two descriptions and to translate limits on anomalous couplings parameterized via EFT operator coefficients into the picture of physical resonances with their masses and widths as main parameters.

4.2.1 Electroweak effective Lagrangian

In this section, we will describe the electroweak (EW) effective Lagrangian, presenting its general structure and its parameters that can be constrained from experiment. In the remainder of this section, we will quote constraints on this effective Lagrangian that can be obtained from the ILC experiments.

We will build the EW effective Lagrangian as an explicitly $SU(2)\times U(1)$-invariant model with a nonlinear realization of electroweak symmetry breaking. The degrees of freedom of the EW Lagrangian are the SM fermions, the gauge bosons, and the scalar Goldstone bosons, w^+, w^-, z. The latter provide, after symmetry breaking, the longitudinal polarization states of the massive gauge bosons. The gauge bosons can be written in the gauge basis, W^1, W^2, W^3, B or in the mass basis, W^+, W^-, Z, A. In leading order, the mass and gauge bases are related by

$$W^1 = \tfrac{1}{\sqrt{2}}(W^+ + W^-), \qquad W^3 = c_w Z + s_w A, \tag{38a}$$

$$W^2 = \tfrac{\mathrm{i}}{\sqrt{2}}(W^+ - W^-), \qquad B = -s_w Z + c_w A, \tag{38b}$$

where s_w and c_w are the sine and cosine of the weak mixing angle, respectively. The Goldstone bosons $\mathbf{w}$ are defined in an analogous basis. They enter the Lagrangian only via the Goldstone (or non-linear Higgs) field matrix,

$$\Sigma = \exp\left(-\frac{\mathrm{i}}{v}\mathbf{w}\right). \tag{39}$$

where $\mathbf{w} \equiv w^k \sigma^k$, with σ^k the Pauli matrices. Setting $\mathbf{W} \equiv W^k\sigma^k/2$, we define the matrix-valued field strength tensors for the gauge bosons as

$$\mathbf{W}_{\mu\nu} = \partial_\mu \mathbf{W}_\nu - \partial_\nu \mathbf{W}_\mu + ig[\mathbf{W}_\mu, \mathbf{W}_\nu], \tag{40}$$

$$\mathbf{B}_{\mu\nu} = \Sigma\left(\partial_\mu B_\nu - \partial_\nu B_\mu\right)\frac{\tau^3}{2}\Sigma^\dagger. \tag{41}$$

The covariant derivative of the Higgs field is given by

$$\mathbf{D}\Sigma = \partial\Sigma + \mathrm{i}g\mathbf{W}\Sigma - \mathrm{i}g'\Sigma\left(B\frac{\sigma^3}{2}\right), \tag{42}$$

with $g = e/s_w$ and $g' = e/s_w$, in the absence of anomalous couplings.

To write down the operators in a fashion manifestly invariant under the weak $SU(2)_L$ gauge symmetry, we introduce the fields

$$\begin{aligned}\mathbf{V}_\mu &= \Sigma(\mathbf{D}_\mu\Sigma)^\dagger = -(\mathbf{D}_\mu\Sigma)\Sigma^\dagger \\ \mathbf{T} &= \Sigma\sigma^3\Sigma^\dagger \ .\end{aligned} \tag{43}$$

In the unitarity gauge, the Goldstone boson matrix vanishes and these fields are simply given by the EW gauge bosons,

$$\mathbf{V}_\mu \Rightarrow -\frac{\mathrm{i}g}{2}\left[\sqrt{2}(W^+\sigma^+ + W^-\sigma^-) + \frac{1}{c_w}Z\sigma^3\right] \tag{44}$$

and the isospin projector on the neutral components of fields,

$$\mathbf{T} \Rightarrow \sigma^3 \ . \tag{45}$$

Then, in unitarity gauge, $\mathrm{tr}\mathbf{T}\mathbf{V} = -igZ/c_w$. However, since the high-energy behavior of vector boson scattering is dominated by Goldstone boson scattering [16], it is rather convenient to apply the opposite, gaugeless limit, and keep only the Goldstone bosons modes. In this approximation,

$$\begin{aligned}\mathbf{V}_\mu &= \frac{\mathrm{i}}{v}\left(\partial_\mu w^k + \frac{1}{v}\epsilon^{ijk}w^i\partial_\mu w^j\right)\tau^k + O(v^{-3}) \ , \\ \mathbf{T} &= \tau^3 + 2\sqrt{2}\frac{\mathrm{i}}{v}\left(w^+\tau^+ - w^-\tau^-\right) + O(v^{-2}) \ .\end{aligned} \tag{46}$$

The lowest-order EW chiral Lagrangian contains the kinetic terms for the weak and hypercharge bosons and the kinetic term for the Σ field, which also yields the gauge boson mass terms. There is one additional possible dimension 2 operator. In the next order in mass dimension, there are ten possible dimension 4 operators, assuming C and CP conservation. At this level, the effective Lagrangian reads

$$\mathcal{L}_0 = -\frac{1}{2}\mathrm{tr}\mathbf{W}_{\mu\nu}\mathbf{W}^{\mu\nu} - \frac{1}{2}\mathrm{tr}\mathbf{B}_{\mu\nu}\mathbf{B}^{\mu\nu} - \frac{v^2}{4}\mathrm{tr}\mathbf{V}_\mu\mathbf{V}^\mu + \beta_1\mathcal{L}_0' + \sum_i \alpha_i\mathcal{L}_i \tag{47}$$

where the operators are in detail:

$$\mathcal{L}'_0 = \tfrac{v^2}{4}\mathrm{tr}\mathbf{T}\mathbf{V}_\mu \mathrm{tr}\mathbf{T}\mathbf{V}^\mu \tag{48a}$$
$$\mathcal{L}_1 = gg'\mathrm{tr}\mathbf{B}_{\mu\nu}\mathbf{W}^{\mu\nu} \tag{48b}$$
$$\mathcal{L}_2 = \mathrm{i}g'\mathrm{tr}\mathbf{B}_{\mu\nu}[\mathbf{V}^\mu, \mathbf{V}^\nu] \tag{48c}$$
$$\mathcal{L}_3 = \mathrm{i}g\mathrm{tr}\mathbf{W}_{\mu\nu}[\mathbf{V}^\mu, \mathbf{V}^\nu] \tag{48d}$$
$$\mathcal{L}_4 = (\mathrm{tr}\mathbf{V}_\mu\mathbf{V}_\nu)^2 \tag{48e}$$
$$\mathcal{L}_5 = (\mathrm{tr}\mathbf{V}_\mu\mathbf{V}^\mu)^2 \tag{48f}$$
$$\mathcal{L}_6 = \mathrm{tr}\mathbf{V}_\mu\mathbf{V}_\nu\mathrm{tr}\mathbf{T}\mathbf{V}^\mu\mathrm{tr}\mathbf{T}\mathbf{V}^\nu \tag{48g}$$
$$\mathcal{L}_7 = \mathrm{tr}\mathbf{V}_\mu\mathbf{V}^\mu\left(\mathrm{tr}\mathbf{T}\mathbf{V}_\nu\right)^2 \tag{48h}$$
$$\mathcal{L}_8 = \tfrac{1}{4}g^2\left(\mathrm{tr}\mathbf{T}\mathbf{W}_{\mu\nu}\right)^2 \tag{48i}$$
$$\mathcal{L}_9 = \tfrac{1}{2}\mathrm{i}g\mathrm{tr}\mathbf{T}\mathbf{W}_{\mu\nu}\mathrm{tr}\mathbf{T}[\mathbf{V}^\mu, \mathbf{V}^\nu] \tag{48j}$$
$$\mathcal{L}_{10} = \tfrac{1}{2}\left(\mathrm{tr}\mathbf{T}\mathbf{V}_\mu\right)^2\left(\mathrm{tr}\mathbf{T}\mathbf{V}_\nu\right)^2 \tag{48k}$$

All of these operators modify the 2-, 3- and 4-point functions of the EW gauge bosons: $\mathcal{L}'_0, \mathcal{L}_1, \mathcal{L}_8$ give the oblique corrections which modify the gauge-boson propagators, while $\mathcal{L}_2, \mathcal{L}_3, \mathcal{L}_9$ induce anomalous triple gauge couplings (TGCs). The remaining five operators ($\mathcal{L}_4$–$\mathcal{L}_7$ and $\mathcal{L}_{10}$) only affect the quartic gauge couplings (QGCs). The coefficient of the extra dimension-2 operator, the parameter β_1, is directly related to the $\Delta\rho$ parameter, and thus is rather special. Experimentally it is well-known that this parameter is quite small, such that the leading-order Lagrangian possesses a custodial isospin symmetry which is broken only at next-to-leading order by the non-vanishing EW mixing angle and the mass splittings inside the fermionic isospin doublets. This symmetry – if it were exact in the gauge boson sector – would forbid operators containing $\mathbf{T}$. Sometimes such custodial isospin conservation is assumed. This would then eliminate the operators $\mathcal{L}_6$–$\mathcal{L}_{10}$ from the expression (47).

At the next order in mass dimension, we find the dimension-6 operators

$$\mathcal{L}^\lambda_1 = \mathrm{i}\frac{g^3}{3M_W^2}\mathrm{tr}\mathbf{W}^{\mu\nu}\mathbf{W}_\nu{}^\rho\mathbf{W}_{\rho\mu} \tag{49a}$$
$$\mathcal{L}^\lambda_2 = \mathrm{i}\frac{g^2g'}{M_W^2}\mathrm{tr}\mathbf{B}^{\mu\nu}\mathbf{W}_\nu{}^\rho\mathbf{W}_{\rho\mu} \tag{49b}$$
$$\mathcal{L}^\lambda_3 = \frac{g^2}{M_W^2}\mathrm{tr}[\mathbf{V}^\mu, \mathbf{V}^\nu]\mathbf{W}_\nu{}^\rho\mathbf{W}_{\rho\mu} \tag{49c}$$
$$\mathcal{L}^\lambda_4 = \frac{g^2}{M_W^2}\mathrm{tr}[\mathbf{V}^\mu, \mathbf{V}^\nu]\mathbf{B}_\nu{}^\rho\mathbf{W}_{\rho\mu} \tag{49d}$$
$$\mathcal{L}^\lambda_5 = \frac{gg'}{2M_W^2}\mathrm{tr}\mathbf{T}[\mathbf{V}^\mu, \mathbf{V}^\nu]\mathrm{tr}\mathbf{T}\mathbf{W}_\nu{}^\rho\mathbf{W}_{\rho\mu} \tag{49e}$$

These operators appear in the same order in the power counting of the perturbative expansion as the operators listed above. Of these operators, which can be interpreted as contributions to anomalous magnetic moments of the EW gauge bosons, the first two also induce anomalous TGCs, while the last three one only contribute to the QGCs.

As we have discussed already, the operators (48) and (49) can be generated when integrating out a heavy particle beyond the SM. It is not unlikely that heavy particles that could contribute to the EW effetive Lagrangian in this way could be discovered at the LHC in its run at 14 TeV.

We will see in subsequent sections that the ILC experiments can make precise statements about the values of the α_i parameters. This is model-independent information that can be used to constrain models of the the dynamics of the electroweak sector. For example, the values of the α_i constrain the presence and quantum numbers of possible resonances associated with composite Higgs strong interactions. We will describe this connection in Section 4.2.3.

4.2.2 Trilinear and quartic vector boson couplings

First, however, it will be useful to explain how the formalism presented in the previous section is connected to the trilinear and quartic vector boson couplings. Within the SM, the trilinear and quartic couplings are specified by the constraints of gauge invariance. Beyond the SM, additional couplings may appear. Often, these are represented by effective Lagrangians with many parameters. The systematic effective Lagrangian approach of the previous section organizes these parameters in a useful way.

The EW chiral Lagrangian written in (47) provides an off-shell formulation for a general electroweak section complete through operators of dimension 4. Complete matrix elements for $2 \to 6$ processes can be computed using the Feynman rules derived from this Lagrangian. These Feynman rules include EW boson interactions with anomalous couplings. In this section, we will give the relation between a general parametrization of the anomalous couplings and the effective Lagrangian parameters α_i.

In unitarity gauge, the trilinear gauge interactions are conventionally written

$$\begin{aligned} L_{\mathrm{WWV}} \;=\; & g_{\mathrm{WWV}}[\\ & \mathrm{i}g_1^{\mathrm{V}} V_\mu \left(W_\nu^- W_{\mu\nu}^+ - W_{\mu\nu}^- W_\nu^+ \right) + \mathrm{i}\kappa_{\mathrm{V}} W_\mu^- W_\nu^+ V_{\mu\nu} + \mathrm{i}\frac{\lambda^{\mathrm{V}}}{m_{\mathrm{W}}^2} W_{\lambda\mu}^- W_{\mu\nu}^+ V_{\nu\lambda} \\ & + g_4^{\mathrm{V}} W_\mu^- W_\nu^+ \left(\partial_\mu V_\nu + \partial_\nu V_\mu \right) + g_5^{\mathrm{V}} \epsilon_{\mu\nu\lambda\rho} \left(W_\mu^- \partial_\lambda W_\nu^+ - \partial_\lambda W_\mu^- W_\nu^+ \right) V_\rho \\ & + \mathrm{i}\tilde{\kappa}^{\mathrm{V}} W_\mu^- W_\nu^+ \tilde{V}_{\mu\nu} + \mathrm{i}\frac{\tilde{\lambda}^{\mathrm{V}}}{m_{\mathrm{W}}^2} W_{\lambda\mu}^- W_{\mu\nu}^+ \tilde{V}_{\nu\lambda}] \,, \end{aligned} \tag{50}$$

Similarly, the quartic gauge interactions are expressed as

$$\begin{aligned} \mathcal{L}_{QGC} = & e^2 \left[g_1^{\gamma\gamma} A^\mu A^\nu W_\mu^- W_\nu^+ - g_2^{\gamma\gamma} A^\mu A_\mu W^{-\nu} W_\nu^+ \right] \\ & + e^2 \frac{c_w}{s_w} \left[g_1^{\gamma Z} A^\mu Z^\nu \left(W_\mu^- W_\nu^+ + W_\mu^+ W_\nu^- \right) - 2 g_2^{\gamma Z} A^\mu Z_\mu W^{-\nu} W_\nu^+ \right] \\ & + e^2 \frac{c_w^2}{s_w^2} \left[g_1^{ZZ} Z^\mu Z^\nu W_\mu^- W_\nu^+ - g_2^{ZZ} Z^\mu Z_\mu W^{-\nu} W_\nu^+ \right] \\ & + \frac{e^2}{2 s_w^2} \left[g_1^{WW} W^{-\mu} W^{+\nu} W_\mu^- W_\nu^+ - g_2^{WW} \left(W^{-\mu} W_\mu^+ \right)^2 \right] + \frac{e^2}{4 s_w^2 c_w^4} h^{ZZ} (Z^\mu Z_\mu)^2 \quad . \end{aligned} \tag{51}$$

The overall prefactors are $g_{WW\gamma} = e$ and $g_{WWZ} = e \cos\theta_W / \sin\theta_W$. The symbols $V_{\mu\nu}$ and $\tilde{V}_{\mu\nu}$ are defined as:

$$V_{\mu\nu} = \partial_\mu V_\nu - \partial_\nu V_\mu \qquad \tilde{V}_{\mu\nu} = \epsilon_{\mu\nu\rho\sigma} V_{\rho\sigma}/2 \,. \tag{52}$$

The SM values of the trilinear couplings in (50) are given by

$$g_1^{\gamma,Z} = \kappa^{\gamma,Z} = 1, \quad g_4^{\gamma,Z} = g_5^{\gamma,Z} = \tilde{\kappa}^{\gamma,Z} = 0 \quad \text{and} \quad \lambda^{\gamma,Z} = \tilde{\lambda}^{\gamma,Z} = 0 \qquad , \tag{53}$$

The deviations of the couplings from the SM values are expressed in terms of the α_i parameters as

$$\Delta g_1^\gamma = 0 \qquad \Delta\kappa^\gamma = g^2(\alpha_2 - \alpha_1) + g^2\alpha_3 + g^2(\alpha_9 - \alpha_8) \tag{54}$$

$$\Delta g_1^Z = \delta_Z + \frac{g^2}{c_w^2}\alpha_3 \qquad \Delta\kappa^Z = \delta_Z - g'^2(\alpha_2 - \alpha_1) + g^2\alpha_3 + g^2(\alpha_9 - \alpha_8) \tag{55}$$

and

$$\lambda^\gamma = -\frac{g^2}{2}\left(\alpha_1^\lambda + \alpha_2^\lambda\right) \qquad \lambda^Z = -\frac{g^2}{2}\left(\alpha_1^\lambda - \frac{s_w^2}{c_w^2}\alpha_2^\lambda\right) \tag{56}$$

where δ_Z is determined by the precision electroweak corrections. Note that in this setup only the C- and P-conserving parameters g_1, κ and λ can be generated. The parameters g_5, which violates C and P separately but leaves CP intact, and g_4, $\tilde{\kappa}$ and $\tilde{\lambda}$, which violate CP, are not shifted.

The SM values of the quartic couplings in (51) are given by

$$g_1^{VV'} = g_2^{VV'} = 1 \quad (VV' = \gamma\gamma, \gamma Z, ZZ, WW), \qquad h^{ZZ} = 0. \tag{57}$$

Deviations from these SM values are introduced through the corrections induced by the α_i to the couplings that preserve custodial $SU(2)$ symmetry,

$$\Delta g_1^{\gamma\gamma} = \Delta g_2^{\gamma\gamma} = 0 \qquad \Delta g_1^{\gamma Z} = \Delta g_2^{\gamma Z} = \frac{g'^2}{c_w^2 - s_w^2}\alpha_1 + \frac{g^2}{c_w^2}\alpha_3 \tag{58a}$$

$$\Delta g_1^{ZZ} = 2\Delta g_1^{\gamma Z} + \frac{g^2}{c_w^4}\alpha_4 \qquad \Delta g_2^{ZZ} = 2\Delta g_1^{\gamma Z} - \frac{g^2}{c_w^4}\alpha_5 \tag{58b}$$

$$\Delta g_1^{WW} = 2c_w^2 \Delta g_1^{\gamma Z} + g^2\alpha_4 \qquad \Delta g_2^{WW} = 2c_w^2 \Delta g_1^{\gamma Z} - g^2\left(\alpha_4 + 2\alpha_5\right) \tag{58c}$$

$$h^{ZZ} = g^2\left(\alpha_4 + \alpha_5\right). \tag{58d}$$

Since we have consistently generated the trilinear and quartic couplings from a theory with exact but spontaneously broken $SU(2) \times U(1)$ symmetry, the vertices described in this section fit together into a unified formalism that can be used to compute the scattering amplitudes for complete electroweak processes. In particular, this formalism gives a consistent definition to off-shell propagators and vertices that appear in processes containing the quartic gauge boson vertices. The results of all experiments are expressed in terms of the parameters α_i.

4.2.3 Resonances in the strongly coupled Higgs sector

We now return to the question of the interpretation of the α_i parameters in terms of possible resonances in the electroweak sector. A formalism complementary to that on Section 4.2.1 based on adding resonances to the SM Lagrangian has been described in [1]. We review it briefly here.

There are three different combinations of spin and isospin for which resonances can couple to the EW gauge boson system. The spin of these resonances can be 0, 1, or 2 (scalar, vector, or tensor), and, similarly, the value of the isospin, under the custodial isospin symmetry, can be 0, 1, or 2 (in this context, labeled singlet, triplet, and quintet). To couple invariantly to a pair of weak bosons, the parity in spin and isospin must be equal; hence we consider resonances with the quantum numbers:

- scalar singlet σ, scalar quintet ϕ,

Resonance	σ	ϕ	ρ	f	a
Γ	6	1	$4v^2/3M^2$	1/5	1/30

Table 4: Coefficients G appearing the formula (59) for the partial widths for resonances with various quantum numbers to decay into longitudinally polarized vector bosons.

- vector triplet ρ,
- tensor singlet f, tensor quintet a,

In the model, these resonances are allowed to have arbitrary masses and widths, including $M \to \infty$. We might also list π (scalar triplet) and ω (vector singlet), but their couplings to weak bosons violate custodial isospin. Then either their couplings are small, so that we can ignore them, or require unnatural cancellations to preserve the SM value of the ρ parameter.

An example of such a resonance is the SM Higgs boson itself (σ). The techni-rho resonance of technicolor models is an example of the vector triplet ρ. This set of quantum numbers also appears in an extra-dimensional context as a Kaluza-Klein W' or Z' [17]. An example of the tensor f is the graviton resonance in Randall-Sundrum models [18].

For the purposes of this section, we will assume that resonances in the EW sector have fermionic couplings very suppressed compared to the couplings to the EW sector. The opposite case has been discussed already in Section 3. For resonances that do not couple strongly to fermions, the dominant decays are to longitudinal EW gauge bosons. The widths are given by formulae

$$\Gamma_i = \frac{g_i^2}{64\pi} \frac{M^3}{v^2} \cdot G \ , \tag{59}$$

where the coefficients G are displayed in Table 4. The couplings g_i are the elementary couplings appearing in the resonance Lagrangian. With increasing number of spin and isospin components, the resonance width decreases. Note that, with our normalization convention for the dimensionless couplings g_i, the width of a vector resonance has a scaling behavior different from that of the other cases. If we want to work in a purely phenomenological approach, it is useful to eliminate the couplings g_i in terms of the resonance widths using (59).

At the ILC, we are mainly concerned with precision measurements of electroweak processes at energies below the first resonance in the strongly interacting Higgs sector. Any deviations observed from the Standard Model predictions can be interpreted in terms of the α_i parameters in (47). To understand the relation of these parameters to

Resonance	σ	ϕ	ρ	f	a
$\Delta\alpha_4$	0	$\frac{1}{4}$	$\frac{3}{4}$	$\frac{5}{2}$	$-\frac{5}{8}$
$\Delta\alpha_5$	$\frac{1}{12}$	$-\frac{1}{12}$	$-\frac{3}{4}$	$-\frac{5}{8}$	$\frac{35}{8}$

Table 5: Coefficients H in the relation (60) between the parameters of a Higgs sector resonance and the chiral Lagrangian coefficients α_4 and α_5 that result from integrating out that heavy resonance.

the system of resonances, we can integrate out the resonances and expand the resulting effective Lagrangian in powers of E/M. The terms resulting from this integrating out shift the parameters of the Standard Model Lagrangian, shift the parameters β_1 and α_2, and shift the other α_i parameters. The shifts of the Standard Model couplings are absorbed into the renormalized electroweak parameters. The shifts of α_2 and β_1 appear in the S and T parameters of electroweak interactions. The remaining shifts of the α_i provide new information. The most important effects appear as shifts of α_4 and α_5. The translation from the resonances masses to α_4 and α_5 is given by the relation

$$\Delta\alpha_i = \frac{16\pi\Gamma}{M}\frac{v^4}{M^4}\cdot H \tag{60}$$

where the coefficients H are displayed for each type of resonances in Table 5.

Figure 25 shows the shifts in α_4 and α_5 induced by each particular type of Higgs sector resonance. There is an ambiguity in the values of the α_i associated with a change in the renormalization scale of the effective low-energy Lagrangian

$$\begin{aligned}\alpha_4(\mu) &= \alpha_4(\mu_0) - \frac{1}{12}\frac{1}{16\pi^2}\ln\frac{\mu^2}{\mu_0^2}\\ \alpha_5(\mu) &= \alpha_5(\mu_0) - \frac{1}{24}\frac{1}{16\pi^2}\ln\frac{\mu^2}{\mu_0^2}\end{aligned} \tag{61}$$

where μ_0 is a reference scale. This shift is plotted as a dashed arrow in Fig. 25. Fortunately, this small shift is almost orthogonal, in the (α_4, α_5) plane, to the direction of the shift induced by a resonance.

In the case that there is only one dominant resonance present, a combined fit to both α parameters (as e.g. done in [2]) allows us to disentangle isosinglet from isotriplet or isoquintet resonances. The angular distributions of final vector bosons provide further information on the nature of a resonance. For example, a ρ resonance multiplet would have the characteristic feature that the ZZ decay channel is absent, by virtue of the Landau-Yang theorem

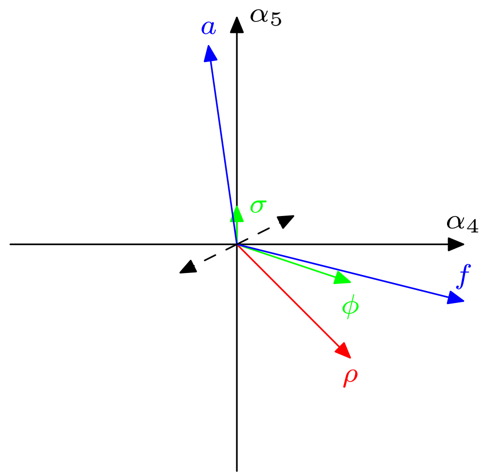

Figure 25: Anomalous couplings $\alpha_{4/5}$ in the low-energy effective theory coming from the different resonances under the assumption of equal masses and widths, $M \sim \Gamma$ (Table 5). The dashed arrow indicates the shift due to renormalization scale variation.

4.2.4 Vector boson scattering and unitarity

There is one more important issue to discuss in setting up the theory of strong interaction corrections to the electroweak sector. This is the question of high-energy behavior and unitarity. At the ILC, experiments on trilinear and quartic couplings in $e^+e^- \to VV$ and related processes can be analyzed by using the low energy effective Lagrangian directly. Even in the study of vector boson scattering, $VV \to VV$, corrections to the effective Lagrangian description come in only at the highest subprocess energies near 1 TeV. However, measurements of these effects at hadron colliders probe a region of higher energies in which expresssions derived from the effective Lagrangian must be greatly modified. The reason for this is that vertices due to higher-dimension operators grow dramatically at high energy and, if left unmodified, violate unitarity. Even at the Tevatron, the analysis of measurements of the trilineaer couplings must include form factors or other modifications so that the theory used to fit the data is internally consistent and avoids violation of unitarity. This is the flip side of the observation that, because it accesses higher energies, the LHC offers the opportunity to discover new states of a strongly interacting Higgs sector as resonances. If resonances are not observed, or are not prominent, or if there are additional resonances beyond the reach of the LHC, there is no definite theoretical prediction, and so results from the LHC will have ambiguity or model-dependence.

In this section, we will describe the problem of unitarity violation in effective models of the Higgs sector in the simplest context, vector boson scattering at high energy. For brevity, we restrict ourselves to the scalar isoscalar case. We will explain how to set up a consistent formalism that can be applied to analyze results from the LHC and the ILC in a common framework. We emphasize that the process of making the effective theory consistent with unitarity entails model-dependent assumptions. We illustrate that here with an especially simple model that fixes the problem.

Consider first the case of the $W^+W^- \to ZZ$ scattering amplitude. The leading term is of order g^0 in the EW coupling and corresponds, at high energy, to the scattering of longitudinally polarized particles. This term rises with s, while the scattering amplitudes of transversally polarized vector bosons come with factors of g and asymptotically do not rise with energy. By the equivalence theorem [16], the leading term is equal to the amplitude $A(s,t,u)$ for $w^+w^- \to zz$ Goldstone scattering,

$$A^{\text{tree}}(s,t,u) = \frac{s}{v^2} + 4\alpha_4 \frac{t^2+u^2}{v^4} + 8\alpha_5 \frac{s^2}{v^4} \ . \tag{62}$$

One-loop corrections to this amplitude in the SM have been calculated in [20,21,19]. Note that the growth of the one-loop corrections does not imply a physical violation of unitarity but simply a breakdown of a perturbative expansion. All five possible individual scattering amplitudes can be determined by means of isospin symmetry through the master amplitude $A(s,t,u)$ above:

$$\begin{aligned}
A(w^+w^- \to zz) &= A(s,t,u) \\
A(w^+z \to w^+z) &= A(t,s,u) \\
A(w^+w^- \to w^+w^-) &= A(s,t,u) + A(t,s,u) \\
A(w^+w^+ \to w^+w^+) &= A(t,s,u) + A(u,s,t) \\
A(zz \to zz) &= A(s,t,u) + A(t,s,u) + A(u,s,t)
\end{aligned} \tag{63}$$

xpanding the amplitudes in powers of the energy, the order-E^2 term is known as the low-energy theorem (LET) [22]:

$$\begin{aligned}
A^{(0)}(w^+w^- \to zz) &= s/v^2 \\
A^{(0)}(w^+z \to w^+z) &= t/v^2 \\
A^{(0)}(w^+w^- \to w^+w^-) &= -u/v^2 \\
A^{(0)}(w^+w^+ \to w^+w^+) &= -s/v^2 \\
A^{(0)}(zz \to zz) &= 0 \ .
\end{aligned} \tag{64}$$

These amplitudes are completely model-independent and only depend on the EW scale v. To include one of the resonances introduced above, one adds a pole in the Goldstone boson amplitude, for example, for σ,

$$A^{\sigma}(s,t,u) = -\frac{g_\sigma^2}{v^2} \frac{s^2}{s-M^2} \tag{65}$$

(The other resonance cases are discussed in [1]). Except for the special case where $g_\sigma = 1$—the case of the SM Higgs boson—in which the rise with energy cancels out, the lowest-order scattering amplitudes show a rise with s/M^2 beyond the resonance pole. This would violate unitarity unless the rise is eventually cancelled by additional contributions from more massive states.

To properly analyze the issue of unitarity, it is useful to project onto channels of definite isospin $I = 0, 1, 2$. The projections are

$$\begin{aligned} A_0(s,t,u) &= 3A(s,t,u) + A(t,s,u) + A(u,s,t) \\ A_1(s,t,u) &= A(t,s,u) - A(u,s,t) \\ A_2(s,t,u) &= A(t,s,u) + A(u,s,t) \end{aligned} \tag{66}$$

These can be further decomposed in the spin-isospin partial wave eigenamplitudes $A_{IJ}(s)$ by means of the Legendre polynomial expansion

$$A_I(s,t,u) = \sum_{J=0}^{\infty} A_{IJ}(s)\,(2J+1)\,P_J(s,t,u)\ , \tag{67}$$

These amplitudes are nonzero only if I and J are both even or both odd. The inverse transformation is given by angular integration:

$$A_{IJ}(s) = \int_{-s}^{0} \frac{dt}{s} A_I(s,t,u)\,P_J(s,t,u). \tag{68}$$

The eigenamplitudes for the lowest-order SM Lagrangian are $A_{00}^{(0)} = 2s/v^2$, $A_{11}^{(0)} = s/3v^2$, and $A_{20}^{(0)} = -s/v^2$. In the presence of a σ resonance, these formulae are modified to

$$A_{00}^{\sigma}(s) = -3\frac{g_\sigma^2}{v^2}\frac{s^2}{s-M^2} - 2\frac{g_\sigma^2}{v^2}\mathcal{S}_0(s) \qquad A_{13}^{\sigma}(s) = -2\frac{g_\sigma^2}{v^2}\mathcal{S}_3(s) \tag{69a}$$

$$A_{02}^{\sigma}(s) = -2\frac{g_\sigma^2}{v^2}\mathcal{S}_2(s) \qquad A_{20}^{\sigma}(s) = -2\frac{g_\sigma^2}{v^2}\mathcal{S}_0(s) \tag{69b}$$

$$A_{11}^{\sigma}(s) = -2\frac{g_\sigma^2}{v^2}\mathcal{S}_1(s) \qquad A_{22}^{\sigma}(s) = -2\frac{g_\sigma^2}{v^2}\mathcal{S}_2(s) \tag{69c}$$

where

$$\mathcal{S}_J(s) = \int_{-s}^{0} \frac{dt}{s}\frac{t^2}{t-M^2} P_0(t,s,u) P_J(s,t,u) \tag{70}$$

is an S-wave coefficient function. The coefficient functions A_{IJ} contain poles in $s-M^2$ as well as finite parts. The poles are confined to those (I, J) combinations which correspond to the (I, J) assignments of the resonances. Other types of resonances contain different coefficient functions; these are given in [1].

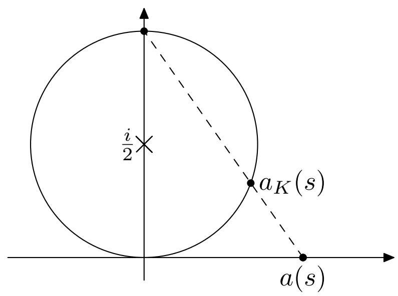

Figure 26: K matrix construction for projecting a real scattering amplitude onto the Argand circle

The optical theorem requires that unitary elastic scattering amplitudes, properly normalized according to $a_{IJ}(s) = A_{IJ}(s)/32\pi$, lie on the Argand circle, $|a_{IJ}(s) - i/2| = 1/2$. Amplitudes $a(s)$ derived in finite-order perturbation theory or in some low-energy effective theory model will usually fail this requirement. A simple way to restore unitarity is the K-matrix unitarization scheme [23], illustrated in Fig. 26. One replaces

$$a(s) \to \hat{a}(s) = 1/\left[Re(1/a(s)) - i\right] \ . \tag{71}$$

If $a(s)$ is real, this simplifies to

$$a(s) \to \frac{a(s)}{1 - ia(s)} \ . \tag{72}$$

For the original amplitude this can be recast as an additive correction term:

$$\hat{A}_{IJ}(s) = A_{IJ}(s) + \Delta A_{IJ}(s), \quad \text{where} \quad \Delta A_{IJ}(s) = \frac{i}{32\pi} \frac{A_{IJ}(s)^2}{1 - \frac{i}{32\pi} A_{IJ}(s)}. \tag{73}$$

The K-matrix prescription transforms the LET amplitude $A(s) = s/v^2$ into an amplitude that approaches a saturation for very high energies,

$$\hat{A}(s) = \frac{(s/v^2)}{\left[1 - is/32\pi v^2\right]} \stackrel{s\to\infty}{\longrightarrow} 32\pi i \tag{74}$$

The method leads to a Breit-Wigner lineshape and can hence be understood a variant of Dyson resummation for s-channel resonance exchange. For more details and comparison to other methods, see [1].

Beyond the first resonances in a given channel, other resonances can be present, as we observe in low-energy QCD. It is best, then, to keep both the explicit resonance in the corresponding channel and the $\alpha_{4/5}$ parameters to account for additional structure at higher energies. Each eigenamplitude then has a zeroth order contribution, a NLO contribution and a part coming from the sum over the possible resonances. It may be parameterized as $A_{IJ}(s) = A^{(0)}_{IJ}(s) + F_{IJ}(s) + G_{IJ}(s)/(s - M^2)$, where $F_{IJ}(s)$ is finite, and $G_{IJ}(s)$ is proportional to s (vector), or s^2 (scalar, tensor). By means of the K-matrix prescription the amplitude gets an additive correction term, $\hat{A}_{IJ}(s) = A_{IJ}(s)/(1 - \frac{i}{32\pi}A_{IJ}(s)) = A^{(0)}_{IJ}(s) + \Delta A_{IJ}(s)$, where the correction term takes the form:

$$\Delta A_{IJ}(s) = 32\pi i \Bigg(1 + \frac{i}{32\pi}A^{(0)}(s) \\ + \frac{s - M^2}{\frac{i}{32\pi}G_{IJ}(s) - (s - M^2)\left[1 - \frac{i}{32\pi}(A^{(0)}(s) + F_{IJ}(s))\right]}\Bigg) \quad (75)$$

Fig. 27 shows in the upper line two of the eigenamplitudes as examples, which show peaks for the resonances with the corresponding spin and isospin quantum numbers. The resonances masses are chosen to be 1 TeV, and the amplitudes reach their saturation value of $32\pi \approx 100$.

For a definite physics simulation one needs to translate these amplitudes back to physical ones, i.e. WW or ZZ. So one has to go back from spin-isospin eigenamplitudes to isospin eigenamplitudes, which is given by relations like

$$\Delta A_0(s,t,u) = \Delta A_{00}(s)\, P_0(s,t,u) + \Delta A_{02}(s)\, 5P_2(s,t,u) \quad (76)$$

The right hand side of the lower line of Fig. 27 shows the angular dependence of the amplitude which reveals the spin of the corresponding resonance. From the isospin eigenamplitudes one can reconstruct the physical amplitudes, for example,

$$\Delta A(w^+w^- \to zz) = (\Delta A_0(s,t,u) - \frac{1}{3}\Delta A_2(s,t,u))/3\ . \quad (77)$$

Clearly, the unitarization of the channels breaks crossing symmetry, as it is inserted only in s-channel like configurations. The other physical amplitudes and the full explicit expressions can be found in [1]. These expressions allow for a full description of on-shell Goldstone boson scattering at the ILC and allows to easily switch to a corresponding one for LHC physics in order to translate limits and parameters between both colliders. They depend on α_4 and α_5, on the renormalization scale μ (when including the NLO terms), and on the mass and width parameters of the presumptive five resonances.

This method of unitarization can be combined with the generic off-shell parameterization of EW boson scattering given in (50) and (51) to give a complete description of Goldstone boson scattering amplitudes. For that purpose, the constant parameters $\alpha_{4/5}$ are replaced by nergy-(s-)dependent form factors. The technical details of

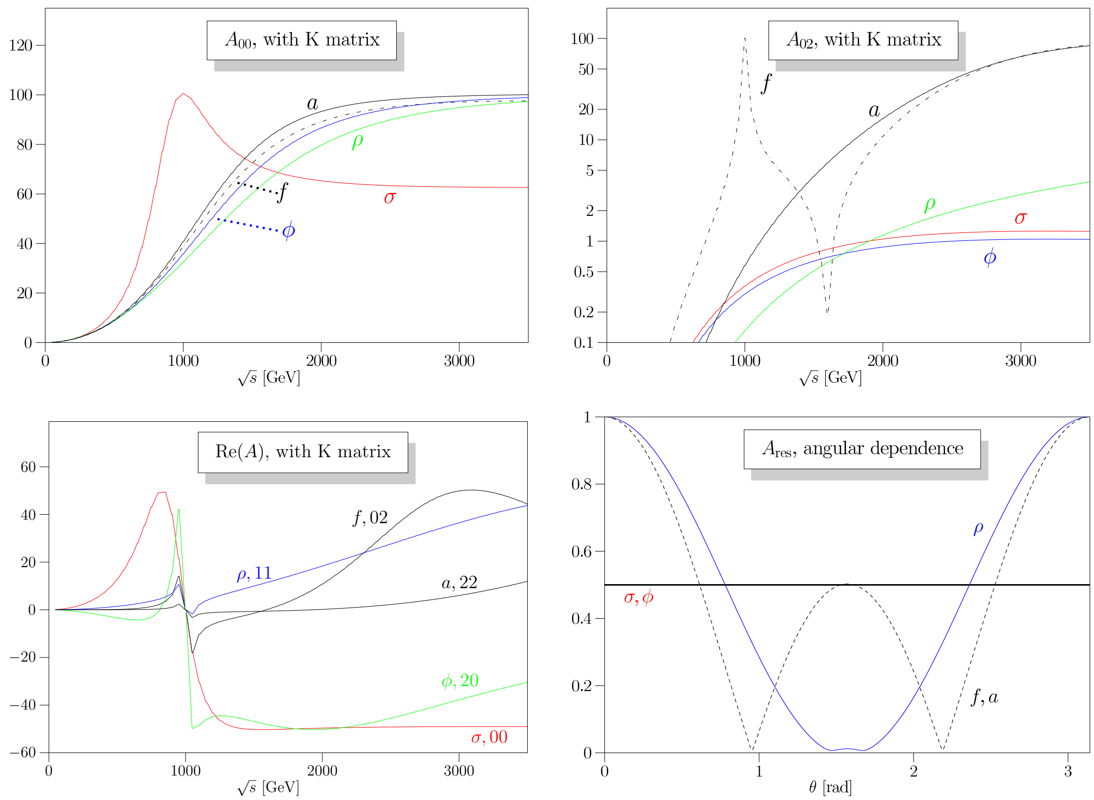

Figure 27: The upper line shows examples for unitarized spin-isospin-eigenamplitudes for Goldstone-boson scattering for each of the five possible resonances σ, ϕ, ρ, f, a, with resonance masses set to 1 TeV, and their couplings to Goldstone bosons being unity: on the left, the $I = J = 0$ amplitudes, on the right, the $I = 0, J = 2$ amplitudes. The lower line shows, on the left, the real part of the eigenamplitudes $|A_{IJ}(s)|$ for $M_R = 1$ TeV (left), and, on the right, the angular dependence of the amplitudes $|A_I(s,t,u)|$ for $I = 0, 1, 2$, each with the corresponding resonance(s) switched on and evaluated at $\sqrt{s}$ equal to the resonance mass.

that implementation can be found in [1]. This implementation does break crossing symmetry, but in fact that is broken already by the K-matrix prescription for unitarization. In principle, anomalous couplings for resonances might also be included. Such couplings are not considered here. We assume that they are subleading in the high-energy regime of a 1 TeV ILC or at LHC.

With the formalism described above one can easily switch between the high-energy measurements in the LHC environment and the much preciser measurements in the cleaner setup of the ILC for VV scattering, but also for di- or triboson production, once a deviation from the SM in these channels might be discovered. In the following subsections we describe in detail diboson production in the channels WW and ZZ, the

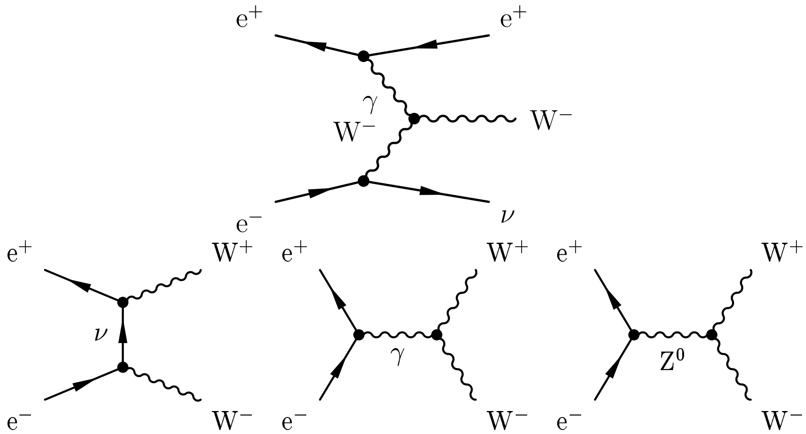

Figure 28: Dominant Feynman diagrams for single W production at the ILC (top), and for W^+W^- production at the ILC.

corresponding photon-induced processes, triboson production, EW boson scattering as well as low-energy precision measurements on the Z and WW threshold.

4.3 $e^+e^- \to W^+W^-$

The major weak processes to be studied at an ILC are pair production of electroweak gauge bosons, $e^+e^- \to W^+W^-$ and $e^+e^- \to ZZ$. Actually, the ILC will be the first collider to allow for W pair production in lepton collisions with polarized beams. Due to the $V - A$ structure of the W boson interactions, polarization of the beam(s) radiating the electroweak boson can substantially enhance or suppress their production. Note, that there is also as a competitive process single W production, originating mostly from photon-W fusion (cf. Fig. 28). Since pair production is dominated by the s-channel pole, its cross section falls off linearly with energy. ILC will be the first lepton collider to enter that regime. On the other hand, single production is kinematically enhanced through the t-channel propagators and rises logarithmically with energy. 1 TeV is roughly the energy where single production starts to exceed over pair production.

WW production at a lepton collider is a theoretically well-studied process for which full next-to-leading (NLO) electroweak corrections are available including the W decays in the double-pole approximation [27]. These results have been casted into dedicated NLO Monte-Carlo programs, namely YFSWW3 and RacoonWW. The effects of finite fermion masses and different cuts on the cross section and distributions have also been studied in [28]. Some leading NNLO corrections have been recently calculated [30]. Furthermore, by means of effective field theory methods, the precise line-shape of W pairs close to the thresholds have been investigated [31]. Also the

Figure 29: Total cross section for single W [4] and W pair production [27] as a function of the center of mass energy. Differential cross section for W pair production for different beam polarizations.

single W production at a lepton collider is available at NLO [29].

The process of WW production at ILC allows for a sensible measurement of triple gauge boson couplings, given in the introduction to this section in Eq. 50. If one replaces the constant parameters by momentum-dependent form factors, this is in fact the most general parameterization, however, restricting again to the two lowest orders in the expansion of the EW chiral Lagrangian takes one back to constant coupling parameters. Note that there are some constraints to be fulfilled by the unbroken electromagnetic gauge invariance, namely $g_1^\gamma(q^2 = 0) = 1$ and $g_5^\gamma(q^2 = 0) = 0$ at zero momentum transfer.

1. measurement of the W boson mass
2. measurement of triple gauge boson couplings
3. Standard Model reference - e.g. in situ polarization measurement ?

4.4 $e^+e^- \to ZZ$

4.5 $\gamma\gamma \to W^+W^-$

Though there is the specific option to produce a high-energy photon-photon collider by means of Compton backscattering and thereby converting a high-energy electron beam into a high-energy photon beam, the physics at such a machine shall not be discussed here. However, γ-induced processes also occur through collinear electron splitting predominantly at lower energies, and they provide a severe

To do: fix citation

background for many new-physics searches (cf. e.g. [**?**]. But, on the other side, they can also provide potential to perform measurement in the EW sector of the SM, by using the γ-induced pair production of W pairs, which has a large cross section of rather 80 pb at 500 GeV. (The physics of this process is similar to the single-W production in $W\gamma$ fusion, whose cross section is roughly 30 pb at 500 GeV). This process has been studied with the focus on the determination of possible anomalous gauge boson couplings, and its NLO corrections have been calculated in the double-pole approximation [32].

1. measurement of quadruple gauge boson couplings

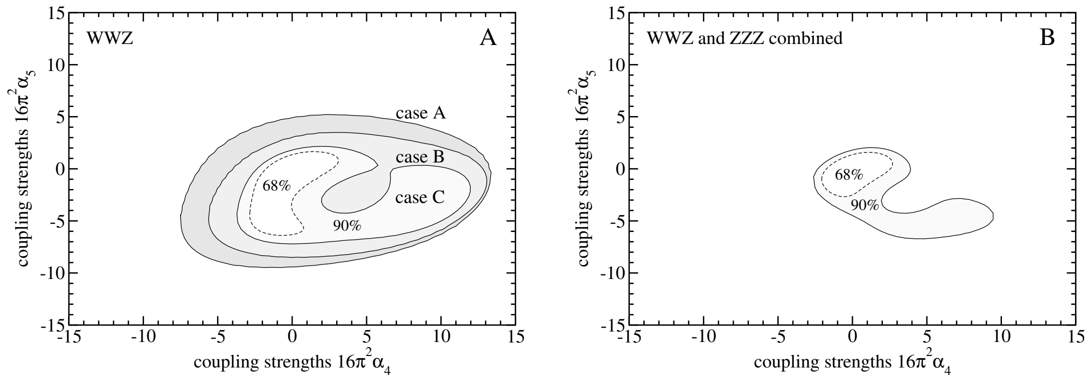

Figure 30: Expected sensitivity of a 1 TeV ILC on anomalous quartic gauge coupling parameters α_4/α_5, assuming an integrated luminosity of 1 ab^{-1}. Left: WWZ alone, right: WWZ and ZZZ combined. The inner (dashed) line shows the 68 % CL, the outer (full) line the 90 % CL. Cases A, B, and C refer to the unpolarized case, the case with 80 % electron polarization and 80% electron plus 60% positron polarization, respectively. From [2].

4.6 Triple vector boson production

The production of three electroweak gauge bosons, i.e. mainly $e^+e^- \to W^+W^-Z$ and $e^+e^- \to ZZZ$ is an important precision test for the structure of the electroweak interactions. It has not been kinematically accessible at LEP, though it is and will be measured at the LHC. The measurement of these processes at the ILC allows for a very clean and precise measurement of the triple and quartic gauge couplings and is complimentary to the corresponding observables in vector boson scattering processes (cf. next subsection 4.7). Though triboson production has already been measured at Tevatron and has and will be measured at LHC, too, the process is much cleaner and offers a much higher precision at ILC, specifically by using the fully hadronic final state (which constitutes 32% of all WWZ and ZZZ events). Though in principle, new-physics parameters that enter oblique corrections and triple gauge couplings can be determined in triple boson production, too, one usually assumes that they have already been measured in WW, ZZ production (or VV scattering). Hence, they will be ignored in this section. In contrast to vector boson scattering, the different α parameters from the electroweak chiral Lagrangian cannot be completely disentangled in this measurement: the process $e^+e^- \to W^+W^-Z$ depends on the two linear combinations $\alpha_4 + \alpha_6$ and $\alpha_5 + \alpha_7$, while $e^+e^- \to ZZZ$ depends on the linear combination $\alpha_4 + \alpha_5 + 2(\alpha_6 + \alpha_7 + \alpha_{10})$.

The main SM background is rather large for the channel W^+W^-Z, coming from $t\bar{t}$ production with hadronically decaying Ws, but can be substantially reduced using electron polarization which populates the longitudinal modes of the EW gauge bosons. For a 1 TeV ILC without polarization, the cross sections are 59 fb for WWZ and

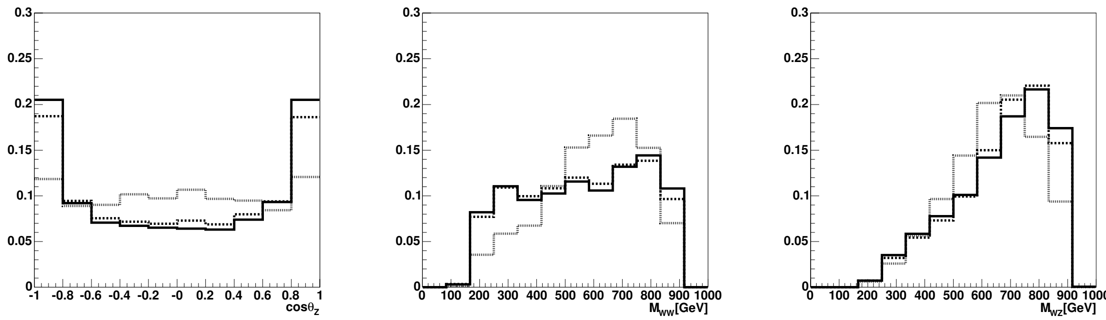

Figure 31: Reconstructed $\cos\theta$, M_{WW}, and M_{WZ} signal distributions for $e^+e^- \to WWZ$ and both beams polarized. To see the shape dependence the distributions are normalized to the respective total number of events for the Standard Model (solid), $\alpha_4 = 1.6\pi^2 \approx 15.8$ (dashed) and $\alpha_5 \approx 15.8$ (dotted).

		WWZ			ZZZ	best
		no pol.	e^- pol.	both pol.	no pol.	
$16\pi^2\Delta\alpha_4$	σ^+	9.79	4.21	1.90	3.94	1.78
	σ^-	-4.40	-3.34	-1.71	-3.53	-1.48
$16\pi^2\Delta\alpha_5$	σ^+	3.05	2.69	1.17	3.94	1.14
	σ^-	-7.10	-6.40	-2.19	-3.53	-1.64

Table 6: Sensitivity of α_4 and α_5 expressed as 1σ errors. WWZ: two-parameter fit; ZZZ: one-parameter fit; best: best combination of both.

0.8 fb for ZZZ production, respectively. Switching on electron polarization reduces the WWZ cross section to 12 fb (for 80% right-handed electrons). For the neutral process, ZZZ, the SM background is negligible. Both processes are available at next-to-leading order [5,6,7], and also most of the corrections are available in a dedicated Monte-Carlo program, LUSIFER [8].

We follow here the phenomenological study in [2]. For the WWZ process, there are three independent kinematical variables that are used, the M^2_{WZ} and M^2_{WW} invariant masses as well as the angle θ between the electron beam axis and the flight direction of the Z boson. From the angular corrections as well as the diboson invariant masses, deviations from the SM can be determined (see Fig. 31, which then enable one to set limits on the anomalous couplings: Fig. 30 shows the expected sensitivity for the parameters α_4 and α_5 at 90 and 68 per cent confidence level. The detailed values are give in Tab. 6.

Furthermore, especially for the search for possibly parity-violating operators, the process $e^+e^- \to W^+W^-\gamma$ can be used, that is rather complimentary to the WWZ

channel mentioned above. Because here one does not have to pay the price for an additional weak boson, a considerable sensitivity could already be achieved at 500 GeV (or even 200 GeV) center-of-mass energy [10].

4.7 WW, ZZ scattering at high energy

The process of WW/ZZ scattering is at the heart of the electroweak symmetry breaking mechanism because it describes the self-interaction of (both transversally and longitudinally) polarized electroweak gauge bosons. While the first one is the equivalent of gluon-gluon scattering in QCD, the second one is in fact the scattering of the Goldstone boson modes inside the electroweak gauge bosons, whose tree-level unitarity has been one of the most profound motivations for the existence of a (relatively light) Higgs boson [11]. Mostly, the scattering of weak gauge bosons has been seen specifically as a means to study the EW sector in the absence of a light Higgs boson, or, alternatively, the presence of strong EW interactions (for an overview, cf. [9]). But even after the discovery of a light Higgs-like boson around 125 GeV [12], the scattering of EW gauge bosons remains one of the most important physical observables in the EW sector. Together with the precise measurements of the properties of the Higgs boson at the LHC and ILC, VV scattering allows to overconstrain the EW sector and search for deviations from the EW setup of the Standard Model. Besides that, it offers by itself the possibility to search for new physics in the EW sector beyond or besides the Standard Model in a rather model-independent way. Clearly, any kind of new physics that has considerable couplings to the SM fermions is very likely to show up earlier in e.g. Drell-Yan like processes at LHC or directly in electroproduction at the ILC. On the contrary, for physics that couples only to the electroweak gauge sector (or has vastly suppressed fermionic couplings like fermiophobic models), VV scattering is the prime process to be studied. Furthermore, there are models like a strongly interacting light Higgs (SILH) [13] which give rise to a more or less SM-like Higgs boson, but feature nevertheless different UV physics. It is therefore inevitable to perform that important measurement and compare it with predictions from the SM.

LHC will measure VV scattering in the upcoming years, there are possibly even events in the final 2012 data set. On the other hand, ILC offers the opportunity to use all final states including the hadronic ones which is not possible at the LHC because of the triggers and the mini-jet veto. Furthermore, at an ILC beam polarization allows to enrich longitudinal polarizations of the SM gauge bosons and to improve the ratio of longitudinal boson signal over transversally polarized boson background.

In order not to deal with a plethora of models, let us discuss the physics of VV scattering in a as model-independent approach as possible: most of this is based on the approach of the EW chiral Lagrangian [14,15]. In the original approach, this is at least formally understandable as taking the limit of an infinitely heavy Higgs boson and removing it from the SM. The left-over is a nonlinear sigma model containing higher-dimensional operators coupling the transversal and longitudinal EW gauge bosons to each other. Such an approach was invented as a low-energy effective theory (LET) for the case of a (very) heavy SM Higgs boson, of technicolor models featuring several strongly interacting resonances in the EW sector, or for Higgsless models (which are in some sense dual to the former class of models). In the light of the discovery of a light scalar boson at LHC, such a view is no longer really viable. However, such an electroweak chiral Lagrangian can be enlarged by the presence of possible resonances in the EW sector that could possibly couple to the EW sector. Such resonances can be classified to their spin and isospin quantum numbers. Such a classification has been performed in [1]: there could be resonances of spin 0, -1 and -2 that couple to a system of two weak gauge bosons, and they could be isoscalar, isovector or isotensor, respectively. A light SM Higgs bosons is just the isoscalar scalar case with special couplings and is hence easily incorporated in that approach. For more details see the introduction to that chapter above.

The performance of a 1 TeV ILC for determining deviations from the triple and quartic gauge couplings of the SM has been given in [2] extending an earlier study [24]. These studies have been performed with full six-fermion matrix elements, hence no simplifications like effective W approximation (EWA), Goldstone-boson equivalence theorem or the narrow-width approximation have been made. For the analysis, an integrated luminosity of 1 ab^{-1} and beam polarization (80 % for electrons, 40 % for electrons) are assumed. Note that a clear distinction of signal and backgrounds is rather intricate, as many EW processes (e..g. triboson production etc.) get intermingled with the pure VV scattering process.

For the simulation we assume a c.m. energy of 1 TeV and a total luminosity of 1000 fb^{-1} in the e^+e^- mode. Beam polarization of 80% for electrons and 40% for positrons is also assumed. Since the six-fermion processes under consideration contain contributions from the triple weak-boson production processes considered in the previous section (ZZ or W^+W^- with neutrinos of second and third generation as well as a part of $\nu_e\overline{\nu}_eWW(ZZ)$, $e\nu_eWZ$ and $e^+e^-W^+W^-$ final states), there is no distinct separation of signal and background. Signal processes in a separate analysis are thus affected by all other signal processes as well as by pure background. The studies have been performed with event samples generated with `WHIZARD` [4], the shower and hadronization with `Pythia` [25] and the ILC detector response with `SimDet` [26]. Initial-state radiation (ISR) from the lepton beams is explicitly included. Studied processes and their cross sections are given in Tab. 7.

Possible observables sensitive to modifications in the (triple and quartic) couplings of longitudinal EW bosons are the total cross section as well as cross sections

Process	Subprocess	σ [fb]
$e^+e^- \to \nu_e\overline{\nu}_e q\overline{q}q\overline{q}$	$W^+W^- \to W^+W^-$	23.19
$e^+e^- \to \nu_e\overline{\nu}_e q\overline{q}q\overline{q}$	$W^+W^- \to ZZ$	7.624
$e^+e^- \to \nu\overline{\nu}q\overline{q}q\overline{q}$	$V \to VVV$	9.344
$e^+e^- \to \nu e q\overline{q}q\overline{q}$	$WZ \to WZ$	132.3
$e^+e^- \to e^+e^- q\overline{q}q\overline{q}$	$ZZ \to ZZ$	2.09
$e^+e^- \to e^+e^- q\overline{q}q\overline{q}$	$ZZ \to W^+W^-$	414.
$e^+e^- \to b\overline{b}X$	$e^+e^- \to t\overline{t}$	331.768
$e^+e^- \to q\overline{q}q\overline{q}$	$e^+e^- \to W^+W^-$	3560.108
$e^+e^- \to q\overline{q}q\overline{q}$	$e^+e^- \to ZZ$	173.221
$e^+e^- \to e\nu q\overline{q}$	$e^+e^- \to e\nu W$	279.588
$e^+e^- \to e^+e^- q\overline{q}$	$e^+e^- \to e^+e^- Z$	134.935
$e^+e^- \to X$	$e^+e^- \to q\overline{q}$	1637.405

Table 7: Generated processes and cross sections for signal and background for $\sqrt{s} = 1$ TeV, polarization 80% left for electron and 40% right for positron beam. For each process, those final-state flavor combinations are included that correspond to the indicated signal or background subprocess.

$e^+e^- \to$	α_4	α_5	α_6	α_7	α_{10}
$W^+W^- \to W^+W^-$	+	+	-	-	-
$W^+W^- \to ZZ$	+	+	+	+	-
$W^\pm Z \to W^\pm Z$	+	+	+	+	-
$ZZ \to ZZ$	+	+	+	+	+

Table 8: Sensitivity to quartic anomalous couplings for all quasi-elastic weak-boson scattering processes accessible at the ILC.

differential in the EW boson production and decay angles. In measuring properties of longitudinal gauge bosons, it is highly non-trivial if not impossible to measure observables like transverse momentum, as there a cut has to used to suppress the background from transversal gauge bosons that is dropping less fast than the distributions from longitudinal bosons. The general steps of this cut-based analysis is to use electron/positron tagging to identify background, with cuts on transverse momentum, missing mass and missing energy, as well as cuts around the EW boson masses to veto against non tightly reconstructed events. For the extraction of parameters like the triple and quartic gauge coupling, a binned likelihood fit has been used where events are described by a total of four kinematical variables.

We summarize the combined results for the measurements of anomalous EW cou-

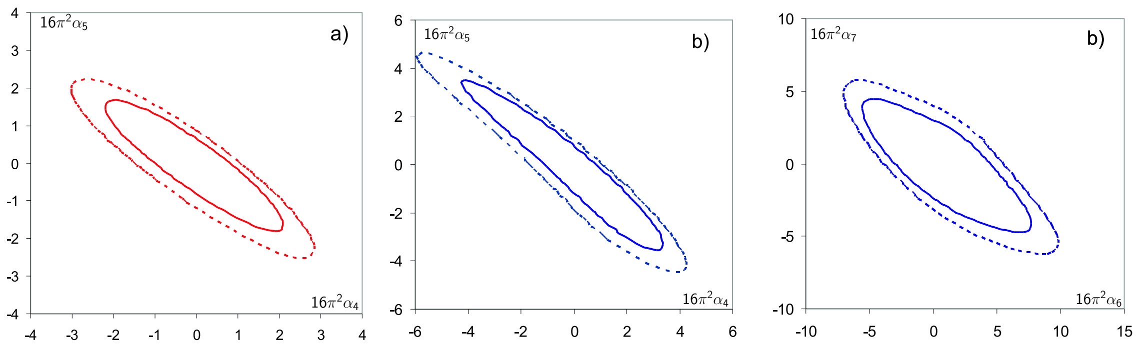

Figure 32: Expected sensitivity (combined fit for all sensitive processes) to quartic anomalous couplings for a 1 TeV ILC with 1 ab^{-1}. The full line (inner one) represents 68%, the dotted (outer) one 90% confidence level. a) case with $SU(2)_c$ conservation b) case with broken $SU(2)_c$.

coupling	$\sigma-$	$\sigma+$
α_4	-1.41	1.38
α_5	-1.16	1.09

Table 9: The expected sensitivity from an integrated luminosity of 1 ab^{-1} in e^+e^- at 1 TeV, under the assumption of custodial $SU(2)$ conservation. Positive and negative 1 sigma errors given separately.

coupling	$\sigma-$	$\sigma+$
α_4	-2.72	2.37
α_5	-2.46	2.35
α_6	-3.93	5.53
α_7	-3.22	3.31
α_{10}	-5.55	4.55

Table 10: The expected sensitivity from a 1 ab$^{-1}e^+e^-$ sample at 1 TeV for the case of broken $SU(2)_c$ case, positive and negative 1 sigma errors given separately.

plings in Tab. 9 and Table 10 where we assume an integrated luminosity of 1 ab^{-1} for e^+e^- processes, taking both the $SU(2)_c$ conserving as well as the violating process into account, respectively. The results are shown in Fig. 32 in graphical form, where projections of the multi-dimensional exclusion region in all αs around the reference point $\alpha_i \equiv 0$ onto the two-dimensional subspaces (α_4, α_5) and (α_6, α_7) have been made. In order to transform these bounds on α_i parameters into more physical terms and also in order to compare the capabilities of ILC with direct resonance searches LHC one can use the formalism described in the introductory section of this chapter to trade the anomalous couplings for parameters of physical resonances. These results for quartic gauge couplings in vector boson scattering can be combined with the ILC measurement results for triple gauge couplings and oblique corrections. Taking one of the resonances into account at each time, one could from the measured value of the α parameters reconstruct the properties and parameters of the resonance producing that particular value. From this, the sensitivity on new physics showing up as resonances in the high-energy region of EW boson scattering can be determined.

The dependence of the different resonances on the α parameters as well as the correlation of the parameters and the technical points of the fit can be found in [2]. Here, we just give the scalar singlet as an example: in that case, α_4 and α_6 are zero, for the isospin-conserving case in addition α_7 and α_{10} are zero. If one uses the relation from integrating out the resonance, $\alpha_5 = g_\sigma^2 \frac{v^2}{8M_\sigma^2}$ and introducing the ratio between the width and the mass of the resonance, $f_\sigma = \Gamma_\sigma/M_\sigma$ one can solve for the mass of the resonance: $M_\sigma = v\,[4\pi f_\sigma/(3\alpha_5)]^{\frac{1}{4}}$. From the fit one can deduce the mass reach for scalar resonances at the LHC depending on scenarios with different widths. The results for the different masses for all cases are shown in 4.7. They can be summarized in the following numbers which hold for the $SU(2)_c$-conserving case: for spin-0 particles, the accessible reach is 1.39, 1.55, and 1.95 TeV for the isospin channels $I = 0$, $I = 1$, and $I = 2$, respectively, assuming a single resonance with optimal width to mass ratio that exclusively couples to the EW boson sector. For a vector resonance, the reach is 1.74 TeV for isosinglet and 2.67 TeV for isotriplets, respectively. Tensors provide the best reach because of the higher number of degrees of freedom participating, namely 3.00, 3.01, and 5.84 TeV for the isospin channels $I = 0$, $I = 1$, and $I = 2$, respectively. In the case of $SU(2)_c$ violation the effects on EW boson scattering are larger or more significant, such that the $SU(2)_c$-conserving limit is a conservative estimate, that is however supported by the EW measurements from SLC, LEP, Tevatron, and LHC.

4.8 Giga-Z

1. measurement of the Z polarization asymmetry and $\sin^2\theta_w$
2. reconciliation of precision electroweak with new particle spectra

$f_{\text{Res.}} = \Gamma_{\text{Res.}}/M_{\text{Res.}}$	1.0	0.8	0.6	0.3
scalar singlet, M_σ [TeV], $SU(2)_c$ cons.	1.55	1.46	1.36	1.15
scalar singlet, M_σ [TeV], $SU(2)_c$ broken	1.39	1.32	1.23	—
scalar triplet, M_{π^0} [TeV]	1.39	1.32	1.23	—
scalar triplet, $M_{\pi^\pm}$ [TeV]	1.55	1.47	1.37	1.15
scalar quintet, M_ϕ [TeV], $SU(2)_c$ cons.	1.95	1.85	1.72	1.45
scalar quintet, $M_{\phi\pm\pm}$ [TeV], $SU(2)_c$ broken	1.95	1.85	1.72	1.45
scalar quintet, $M_{\phi\pm}$ [TeV], $SU(2)_c$ broken	1.64	1.55	1.44	1.21
scalar quintet, $M_{\phi 0}$ [TeV], $SU(2)_c$ broken	1.55	1.46	1.35	1.14
vector singlet, M_ω [TeV], gen. case	2.22	2.10	1.95	1.63
vector triplet, M_ρ [TeV], $SU(2)_c$ cons.	2.49	2.36	2.19	1.84
vector triplet, $M_{\rho^\pm}$ [TeV], no $SU(2)_c$, no mag. mom.	2.67	2.53	2.35	1.98
vector triplet, M_{ρ^0} [TeV], no $SU(2)_c$, no mag. mom.	1.74	1.65	1.53	1.29
vector triplet, $M_{\rho^\pm}$ [TeV], special $SU(2)_c$ viol.	3.09	2.92	2.72	2.29
vector triplet, M_{ρ^0} [TeV], special $SU(2)_c$ viol.	1.78	1.69	1.57	1.32
vector triplet, $M_{\rho^\pm}$ [TeV], gen. case	2.54	2.41	2.34	1.88
vector triplet, M_{ρ^0} [TeV], gen. case	1.71	1.62	1.51	1.27
tensor singlet, M_f [TeV], $SU(2)_c$ cons.	3.29	3.11	2.89	2.43
tensor singlet, M_f [TeV], $SU(2)_c$ viol.	3.00	2.84	2.64	2.22
tensor triplet, M_{a^0} [TeV]	3.01	2.85	2.65	2.23
tensor triplet, $M_{a^\pm}$ [TeV]	2.81	2.66	2.47	2.08
tensor quintet, M_t [TeV], $SU(2)_c$ cons.	4.30	4.06	3.78	3.18
tensor quintet, M_{t^c} [TeV], special $SU(2)_c$ viol.	6.76	6.39	5.95	5.00
tensor quintet, M_{t^0} [TeV], special $SU(2)_c$ viol.	4.53	4.28	3.98	3.35
tensor quintet, $M_{t^{\pm\pm}}$ [TeV], gen. case	5.17	4.89	4.55	3.83
tensor quintet, $M_{t^\pm}$ [TeV], gen. case	3.64	3.44	3.20	2.69
tensor quintet, M_{t^0} [TeV], gen. case	5.84	5.52	5.14	4.32

Table 11: Mass reach at a 1 TeV ILC in VV scattering, assuming a data set of 1 ab^{-1}, for four different values of the ratio of width over mass for the resonances.

3. other high-luminosity Z studies

References

[1] A. Alboteanu, W. Kilian and J. Reuter, JHEP **0811**, 010 (2008) [arXiv:0806.4145 [hep-ph]].

[2] M. Beyer, W. Kilian, P. Krstonosic, K. Monig, J. Reuter, E. Schmidt and H. Schroder, Eur. Phys. J. C **48**, 353 (2006) [hep-ph/0604048].

[3] W. Kilian and J. Reuter, Phys. Rev. D **70**, 015004 (2004) [hep-ph/0311095].

[4] W. Kilian, T. Ohl and J. Reuter, Eur. Phys. J. C **71**, 1742 (2011) [arXiv:0708.4233 [hep-ph]]; M. Moretti, T. Ohl and J. Reuter, In *2nd ECFA/DESY Study 1998-2001* 1981-2009 [hep-ph/0102195].

[5] F. Boudjema, L. D. Ninh, S. Hao and M. M. Weber, Phys. Rev. D **81**, 073007 (2010) [arXiv:0912.4234 [hep-ph]].

[6] S. Ji-Juan, M. Wen-Gan, Z. Ren-You, W. Shao-Ming and G. Lei, Phys. Rev. D **78**, 016007 (2008) [arXiv:0807.0669 [hep-ph]].

[7] S. Wei, M. Wen-Gan, Z. Ren-You, G. Lei and S. Mao, Phys. Lett. B **680**, 321 (2009) [Erratum-ibid. **684**, 281 (2010)] [arXiv:0909.1064 [hep-ph]].

[8] S. Dittmaier and M. Roth, Nucl. Phys. B **642**, 307 (2002) [hep-ph/0206070].

[9] C. T. Hill and E. H. Simmons, Phys. Rept. **381**, 235 (2003) [Erratum-ibid. **390**, 553 (2004)] [hep-ph/0203079].

[10] A. Denner, S. Dittmaier, M. Roth and D. Wackeroth, Eur. Phys. J. C **20**, 201 (2001) [hep-ph/0104057].

[11] B. W. Lee, C. Quigg and H. B. Thacker, Phys. Rev. Lett. **38**, 883 (1977); Phys. Rev. D **16**, 1519 (1977).

[12] J. Incandela, F. Gianotti, seminars, CERN, 4.7.2012, https://indico.cern.ch/contributionDisplay.py?contribId=1&confId=196564

[13] G. F. Giudice, C. Grojean, A. Pomarol and R. Rattazzi, JHEP **0706**, 045 (2007) [hep-ph/0703164].

[14] S. Weinberg, Phys. Rev. **166**, 1568 (1968); C. G. Callan, Jr., S. R. Coleman, J. Wess and B. Zumino, Phys. Rev. **177**, 2239 (1969); Phys. Rev. **177**, 2247 (1969); J. Gasser and H. Leutwyler, Annals Phys. **158**, 142 (1984); Nucl. Phys. B **250**, 465 (1985); T. Appelquist and C. W. Bernard, Phys. Rev. D **22**, 200 (1980); A. C. Longhitano, Phys. Rev. D **22**, 1166 (1980); Nucl. Phys. B **188**, 118 (1981); T. Appelquist and G. -H. Wu, Phys. Rev. D **48**, 3235 (1993) [hep-ph/9304240].

[15] For reviews, see [9]; W. Kilian and P. M. Zerwas, hep-ph/0601217; A. Dobado, A. Gomez-Nicola, A. L. Maroto and J. R. Pelaez, N.Y., Springer-Verlag, 1997. (Texts and Monographs in Physics); W. Kilian, Springer Tracts Mod. Phys. **198**, 1 (2003).

[16] C. E. Vayonakis, Lett. Nuovo Cim. **17**, 383 (1976); M. S. Chanowitz and M. K. Gaillard, Nucl. Phys. B **261**, 379 (1985); G. J. Gounaris, R. Kogerler and H. Neufeld, Phys. Rev. D **34**, 3257 (1986); Y. -P. Yao and C. P. Yuan, Phys. Rev. D **38**, 2237 (1988); J. Bagger and C. Schmidt, Phys. Rev. D **41**, 264 (1990).

[17] C. Csaki, C. Grojean, H. Murayama, L. Pilo and J. Terning, Phys. Rev. D **69** (2004) 055006 [arXiv:hep-ph/0305237]; C. Csaki, C. Grojean, L. Pilo and J. Terning, Phys. Rev. Lett. **92** (2004) 101802 [arXiv:hep-ph/0308038]; Y. Nomura, JHEP **0311** (2003) 050 [arXiv:hep-ph/0309189]; G. Burdman and Y. Nomura, Phys. Rev. D **69** (2004) 115013 [arXiv:hep-ph/0312247].

[18] L. Randall and R. Sundrum, Phys. Rev. Lett. **83** (1999) 3370 [arXiv:hep-ph/9905221].

[19] M. Fabbrichesi and L. Vecchi, Phys. Rev. D **76** (2007) 056002 [arXiv:hep-ph/0703236].

[20] O. Cheyette and M. K. Gaillard, Phys. Lett. B **197**, 205 (1987).

[21] S. Dawson and S. Willenbrock, Phys. Rev. D **40**, 2880 (1989).

[22] S. Weinberg, Phys. Rev. Lett. **17**, 616 (1966); M. S. Chanowitz, M. Golden and H. Georgi, Phys. Rev. Lett. **57**, 2344 (1986).; Phys. Rev. D **36**, 1490 (1987).

[23] S.N. Gupta, *Quantum Electrodynamics*, Gordon and Breach, 1981; M. S. Chanowitz, Phys. Rept. **320**, 139 (1999)

[24] R. Chierici, S. Rosati and M. Kobel, LC-PHSM-2001-038, in *Batavia 2000, Physics and experiments with future linear* e^+e^- *colliders*, 544-549.

[25] T. Sjöstrand, L. Lönnblad and S. Mrenna, hep-ph/0108264; T. Sjöstrand, P. Eden, C. Friberg, L. Lönnblad, G. Miu, S. Mrenna and E. Norrbin, PYTHIA V6.221, Comp. Phys. Commun. 135 (2001) 238.

[26] M. Pohl and H. J. Schreiber, hep-ex/0206009.

[27] A. Denner, S. Dittmaier, M. Roth and D. Wackeroth, Nucl. Phys. B **587**, 67 (2000) [hep-ph/0006307]; Phys. Lett. B **475**, 127 (2000) [hep-ph/9912261]; Eur. Phys. J. direct C **2**, 4 (2000) [hep-ph/9912447]; Comput. Phys. Commun. **153**, 462 (2003) [hep-ph/0209330]; S. Jadach, W. Placzek, M. Skrzypek, B. F. L. Ward and Z. Was, Phys. Rev. D **65**, 093010 (2002) [hep-ph/0007012]; A. Denner, S. Dittmaier, M. Roth and L. H. Wieders, Phys. Lett. B **612**, 223 (2005) [Erratum-ibid. B **704**, 667 (2011)] [hep-ph/0502063]; Nucl. Phys. B **724**, 247 (2005) [Erratum-ibid. B **854**, 504 (2012)] [hep-ph/0505042].

[28] F. Jegerlehner and K. Kolodziej, Eur. Phys. J. C **20**, 227 (2001) [hep-ph/0012250].

[29] G. Passarino, Nucl. Phys. B **578**, 3 (2000) [hep-ph/0001212].

[30] S. Actis, M. Beneke, P. Falgari and C. Schwinn, Nucl. Phys. B **807**, 1 (2009) [arXiv:0807.0102 [hep-ph]].

[31] M. Beneke, P. Falgari, C. Schwinn, A. Signer and G. Zanderighi, Nucl. Phys. B **792**, 89 (2008) [arXiv:0707.0773 [hep-ph]].

[32] A. Bredenstein, S. Dittmaier and M. Roth, Eur. Phys. J. C **36**, 341 (2004) [hep-ph/0405169]; Eur. Phys. J. C **44**, 27 (2005) [hep-ph/0506005].

5 Top quark

The top quark, or t quark, is by far the heaviest particle of the Standard Model. Its large mass implies that this is the Standard Model particle most strongly coupled to the mechanism of electroweak symmetry breaking. For this and other reasons, the top quark is expected to be a window to any new physics at the TeV energy scale. In this section, we will review the ways that new physics might appear in the precision study of the top quark and the capabilities of the ILC to discover these effects.

The top quark was discovered at the Tevatron proton-antiproton collider by the D0 and CDF experiments [1,2]. Up to now, the top quark has only been studied at hadron colliders, at the Tevatron and, only in past two years, at the LHC. The Tevatron experiments accumulated a data sample of about $12\,\mathrm{fb}^{-1}$ in *Run I* and *Run II*, at center of mass energies of 1.8 TeV and 1.96 TeV, respectively. About half of this data is fully analyzed. At the LHC, a data sample of about $5\,\mathrm{fb}^{-1}$ has been recorded at a center-of-mass energy of 7 TeV up to the end of 2011. In 2012, the machine has operated at a center of mass energy of 8 TeV. In the following section, we will review the properties of the top quark determined so far at hadron colliders, based on the currently analyzed data sets. We will also discuss the eventual accuracies that will be reached in this program over the long term.

The ILC would be the first machine at which the top quark is studied using a precisely defined leptonic initial state. This brings the top quark into an evironment in which individual events can be analyzed in more detail, as we have explained in the Introduction. It also changes the production mechanism for top quark pairs from the strong to the electroweak interactions, which are a step closer to the phenomena of electroweak symmetry breaking that we aim to explore. Finally, this change brings into play new experimental observables—weak interaction polarization and parity asymmetries—that are very sensitive to the coupling of the top quark to possible new interactions. It is very possible that, while the top quark might respect Standard Model expectations at the LHC, it will break those expectations when studied at the ILC.

5.1 Top quark properties from hadron colliders

In this section, we will review the present and future capabilities of hadron colliders to study the top quark. This section is based largely on the review published in [3]. Where applicable, the information has been updated.

5.1.1 Top quark hadronic cross section

A central measurement for the top quark at hadron colliders is the $t\bar{t}$ production cross-section. At hadron colliders the following channels are typically measured: (1) lepton+jets channels, (2) dilepton channels, (3) full hadronic channels, (4) channels with jets and missing transverse momentum (MET).For these channels the Tevatron experiments have published values between 7.2 pb and 7.99 pb [3]. The error on these values is typically $6-7\%$. The LHC experiments report values at 7 TeV [4,5]

$$\begin{aligned} \sigma_{t\bar{t}} &= 177 \pm 3\,(\text{stat.})^{+8}_{-7}\,(\text{syst.}) \pm 7\,(\text{lumi.})\,\text{pb} \qquad \text{ATLAS} \\ \sigma_{t\bar{t}} &= 166 \pm 2\,(\text{stat.}) \pm 11\,(\text{syst.}) \pm 8\,(\text{lumi.})\,\text{pb} \qquad \text{CMS} \end{aligned} \tag{78}$$

This is to be compared with theoretical estimates from 'approximate NNLO' QCD predictions, for example, [6,7]

$$\sigma_{t\bar{t}} = 163^{+7}_{-5}\,(\text{scale}) \pm 9\,(\text{PDF})\,\text{pb}. \tag{79}$$

A full NNLO QCD calculation should decrease the first error significantly. The agreement between theory and experiment is excellent at the present stage, both for the LHC and for the Tevatron results. Already at this early stage of data taking the LHC experiments are limited by the systematic uncertainty. For ATLAS, the dominant sources of the systematic error are those from predictions of different event generators together with the uncertainties of the parton distribution function of the proton. On the experimental side, the jet energy resolution constitutes an important source of systematic error. However, there are other sources of comparable influence, from the electron and muon identification. The quoted sources contribute roughly equally to the systematic error.

5.1.2 Top quark mass and width

The mass of the top quark is a fundamental parameter of the electroweak theory. In discussions of physics beyond the Standard Model, the top quark appears ubiquitously. To interpret particle physics measurements in terms of new physics effects, the top quark mass must be known very accurately. Two well known examples are the precision electroweak corrections, where the top quark contributions must be fixed to allow Higgs and other new particle corrections to be determined, and in the theory of the Higgs boson mass in supersymmetry, in which the loop corrections are proportional to $(m_t/m_W)^4$.

Care must be taken in relating the measured top quark mass to the value of the top quark mass that is used as input in these calculations. Loop effects typically take as input a short-distance definition of the top quark mass such as the $\overline{MS}$ mass parameter. We will explain below that the determination of the top quark mass from the threshold cross section in e^+e^- annhilation uses a precise short-distance definition of the top quark mass, though a different one from the $\overline{MS}$ mass.

Another possible definition of the top quark mass is given by the position of the pole in the top quark propagator. This top quark mass is greater than the $\overline{MS}$ mass by about 10 GeV, and this difference contains a nonperturbative correction of the order of a few hundred MeV, due to an infrared sensitivity of the pole mass.

Current determinations of the top quark mass from kinematic distributions do not use either of these, in principle, well defined top quark mass definitions. Insteady, they define the top quark mass as the input mass parameter of a Monte Carlo event generator, which is then constrained by measurements of the kinematics of the $t\bar{t}$ final state. At this time, there is no concrete analysis that relates this mass to either the short distance or the pole value of the top quark mass. For the case of e^+e^- production of top quark pairs, it was shown in [8] how to relate event-shape variables that depend strongly on the top quark mass to an underlying short-distance mass parameter. The analysis requires center of mass energies much larger than $2m_t$. For hadron colliders, the corresponding analysis is much more difficult and has not yet been done.

With the framework that is available now, the Tevatron and LHC experiments have achieved quite a precise determination of the top quark mass from kinematic observables. The value of the top quark mass m_t as published by the Tevatron Electroweak Working Group is given to be $m_t = 173.2 \pm 0.9\,\text{GeV}$ [9]. This value has been obtained from the combined measurements of the Tevatron experiments. The LHC experiments report values of $m_t = 174.5 \pm 0.6 \pm 2.3\,\text{GeV}$ for the ATLAS collaboration [10] and $m_t = 172.6 \pm 0.4 \pm 1.2\,\text{GeV}$ for the CMS collaboration [11], where, in each case, the first error is statistical and the second is systematic. The dominant systematic errors come from jet energy resolution. In both cases, the mass definition used is that of the Monte Carlo event generator. Reduction of the error well below 1 GeV will require a more careful theoretical analysis giving the relation of the mass parameter used in these measurements to a more precise top quark mass definition.

Within the Standard Model the total decay width Γ_t of the top quark is dominated by the partial decay width $\Gamma(t \to Wb)$. The t quark width is predicted to $\Gamma_t \approx 1.5\,\text{GeV}$, which is substantially larger than the hadronization scale Λ_{QCD}. On the other hand, this value is small enough that it is not expected to be directly measured at the LHC.

At hadron colliders the decay width can be determined via

$$\Gamma_t = \Gamma(t \to Wb)/BR(t \to Wb) \ . \tag{80}$$

The partial width $\Gamma(t \to Wb)$ is determined from the cross section for single top events while the branching ratio $BR(t \to Wb)$ is derived from top pair events. D0 gives a value of $\Gamma_t = 1.99^{+0.69}_{-0.55}$ [12]. CDF uses only the top quark mass spectrum and reports the 68% confidence interval to be $0.3 < \Gamma_t < 4.4\,\mathrm{GeV}$ [13]. It is interesting to note here that D0 has published for the ratio of branching ratios $BR(t \to Wb)/BR(t \to Wq)$ a value of 0.9±0.04 [14], which is about 2.5σ away from the Standard Model expectation.

5.1.3 Helicity of the W boson

The t quark has a very short lifetime of about $10^{-25}\,\mathrm{s}$. Since this is about 10 times shorter than typical scales for long range QCD processes, the top quark decays long before hadronization can affect it. Therefore, the structure of the t quark decay is very close to that of a bare quark. Within the Standard Model, the top quark decays almost exclusively via $t \to W^+b$. The V-A nature of the weak decay dictates that the resulting b quark is almost completely left handed polarized. It also dictates the polarization of the W boson, which in turn can be measured by observing the W decay. The prediction is that the W is produced only in the left-handed and longitudinal polarization states, with the fraction of longitudinal W bosons predicted to be

$$f_0 = \frac{m_t^2}{2m_W^2 + m_t^2} \ . \tag{81}$$

The Standard Model predicts a value of $f_0 = 0.703$. The CDF experiment measures this value to be $f_0 - 0.78^{+0.19}_{-0.20}(\mathrm{stat.}) \pm 0.06(\mathrm{syst.})$ [15], in agreement with the Standard Model. The most precise measurements of this value have been achieved with events in which both the W boson from the t and the one from the $\bar{t}$ decay into leptons.

5.1.4 Top coupling to Z^0 and γ

It is particularly interesting to study the coupling of the top quark to γ and the Z^0 boson to search for effects of new physics. Both of these couplings are subdominant effects at hadron colliders. The electroweak production of $t\bar{t}$ is suppressed with respect to QCD production, and this is especially true at the LHC where most of the $t\bar{t}$ production comes from gluon-gluon fusion. Radiation of photons from $t\bar{t}$ has been observed at the Tevatron. So far no precision measurements on the coupling of top quarks to the Z^0 boson have been reported.

Constraints on the top quark couplings to γ and Z^0 have been reported using the expression for the couplings [16]

$$\Gamma_{\mu}^{ttX}(k^2,\, q,\, \overline{q}) = ie\left\{\gamma_{\mu}\,\left(\widetilde{F}_{1V}^{X}(k^2)+\gamma_5\widetilde{F}_{1A}^{X}(k^2)\right)+\frac{(q-\overline{q})_{\mu}}{2m_t}\left(\widetilde{F}_{2V}^{X}(k^2)+\gamma_5\widetilde{F}_{2A}^{X}(k^2)\right)\right\}. \tag{82}$$

where $X=\gamma, Z$ and the $\widetilde{F}$ are related to the usual form factors F_1, F_2 by

$$\widetilde{F}_{1V}^{V} = -\left(F_{1V}^{V}+F_{2V}^{V}\right)\,, \qquad \widetilde{F}_{2V}^{V}=F_{2V}^{V}\,, \qquad \widetilde{F}_{1A}^{V}=-F_{1A}^{V}\,, \qquad \widetilde{F}_{2A}^{V}=-iF_{2A}^{V}\,. \tag{83}$$

In the Standard Model the only form factors which are different from zero are $F_{1V}^{\gamma}(k^2)$, $F_{1VZ}(k^2)$ and $F_{1AZ}(k^2)$. $F_{1V}^{\gamma,Z}(k^2)$ are the electric and weak magnetic dipole moment (MDM) form factors.

$F_{2A}^{\gamma}(k^2)$ is the CP-violating electric dipole moment (EDM) form factor of the t quark, and $F_{2AZ}(k^2)$ is the weak electric dipole moment (WDM). These two form factors violate CP. In the Standard Model they receive contributions only from the three loop level and beyond.

In the case of the $t\bar{t}Z^0$ final state, relatively clean measurements are expected when the Z^0 decays leptonically. HOwever, the cross section is quite small, so that meansingful results with precision of about 10% for $F_{1A}^{Z^0}$ and 40% for $F_{2V,A}^{Z^0}$ can only be expected after a few $100\,\mathrm{fb}^{-1}$. At the SLHC, with an integrated luminosity of about $3000\,\mathrm{fb}^{-1}$, the precision of this measurement is expected to improve by factors between of 1.6 $F_{2V,A}^{Z^0}$ and 3 for $F_{1A}^{Z^0}$ 5.3 The situation is considerably better for measurements of the $t\bar{t}\gamma$ vertex. Already for $30\,\mathrm{fb}^{-1}$ at the LHC, measurements with a precision of about 20% to 35% can be expected. These measurements may improve at the SLHC to values between 2% and 10%

For the related question of the coupling of the top quark to the Higgs boson, both the LHC expectations and the projections for the ILC are discussed in Section 2 of this report.

5.1.5 Asymmetries at hadron colliders

The last few years were marked by a number of publications from the Tevatron experiments which reported on tensions with Standard Model predictions in the measurement of forward backward asymmetries A_{FB}. This observable counts the difference in the number of events in the two hemispheres of the detector. In hadronic collisions, the polar angle is typically reported in terms of the rapidity y, which is invariant under longitudinal boosts and more descriptive at very forward and backward angles. For the study of For the analysis here and at the LHC, see below, at least one member of the $t\bar{t}$ pair is required to decay leptonically to assure the particle identification.

The average asymmetry reported by CDF is $0.201 \pm 0.065\,(\text{stat.}) \pm 0.018\,(\text{syst.})$ [19] which agrees with $0.196 \pm 0.060\,(\text{stat.})^{+0.018}_{-0.026}\,(\text{syst.})$ as reported by D0 [20]. These values can be compared with an asymmetry of about 0.07 predicted by the to Standard Model from NLO QCD and electroweak effects. This result is difficult to verify at the LHC. The LHC is a proton-proton collider, so the two hemispheres are intrinsically symmetric. Further, at the LHC at 7 TeV, only 15% of the interactions arise from $q\overline{q}$ collisions; the 85%, from gg collisions, can have no intrinsic asymmetry. Still, in $q\overline{q}$ collisions at the LHC, it is likely that the q is a valence quark while the $\overline{q}$ is pulled from the sea. This implies that $t\bar{t}$ pairs produced from $q\overline{q}$ are typically boosted in the direction of the q. This offers methods to observe a forward backward asymmetry in $q\overline{q} \to t\bar{t}$. For example, a forward-backward asymmetry in the $q\overline{q}$ reaction translates into a smaller asymmetry A_C in the variable $\Delta|y| = |y_t| - |y_{\bar{t}}|$. For this observable, CMS measures $A_C = 0.004 \pm 0.010\,(\text{stat.}) \pm 0.012\,(\text{syst.})$ [21], which agrees within the Standard Model predictions within the relatively large uncertainties. So far, the LHC experiments have not provided any independent evidence for asymmetries outside the Standard Model predictions [3,22]. The theoretical interpretation of these asymmetries is also very uncertain. Many plausible models of the $t\bar{t}$ asymmetry predict effects in top quark physics at high energy that are excluded at the LHC. For a review of the current situation, see [24,25].

5.2 $e^+e^- \to t\bar{t}$ at Threshold

5.2.1 *Status of QCD Theory*

One of the unique capabilities of an e^+e^- linear collider is the ability to carry out cross section measurements at particle production thresholds. The accurately known and readily variable beam energy of the ILC makes it possible to measure the shape of the cross section at any pair-production threshold within its range. Because of the leptonic initial state, it is also possible to tune the initial spin state, giving additional options for precision threshold measurements. The $t\bar{t}$ pair production threshold, located at a center of mass energy energy $\sqrt{s} \approx 2m_t$, allows for precise measurements of the top quark mass m_t as well as the top quark total width Γ_t and the QCD coupling α_s. Because the top is a spin-$\frac{1}{2}$ fermion, the $t\bar{t}$ pair is produced in an angular S-wave state. This leads to a clearly visible rise of the cross section even when folded with the ILC luminosity spectrum. Moreover, because the top pair is produced in a color singlet state, the experimental measurements can be compared with very accurate and unambiguous analytic theoretical predictions of the cross section with negligible hadronization effects. The dependence of the top quark cross section shape on the top quark mass and interactions is computable to high precision with full control over the renormalization scheme dependence of the top mass parameter. In

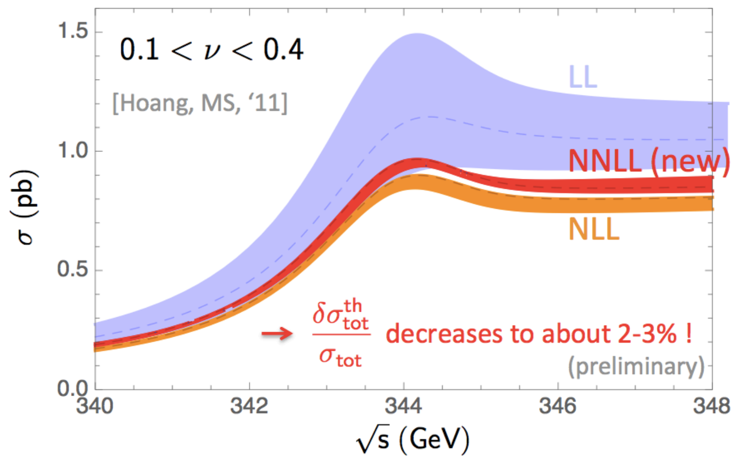

Figure 33: Accuracy on the prediction of the top pair production cross section at the $t\bar{t}$ threshold at the ILC as achieved by recent calculations of QCD corrections (NNLL). For further explanations see text. The figure has been taken from [32]

this section, we will review the expectations for the theory and ILC measurements of the top quark threshold cross section shape. The case of the top quark threshold is not only important in its own right but also serves as a prototype case for other particle thresholds that might be accessible at the ILC.

The calculation of the total top pair production cross section makes use of the method of non-relativistic effective theories. The top quark mass parameter used in this calculation is defined at the scale of about 10 GeV corresponding to the typical physical separation of the t and $\bar{t}$. This mass parameter can be converted to the $\overline{MS}$ mass in a controlled way. The summation of QCD Coulomb singularities treated by a non-relativistic fixed-order expansion is well known up to NNLO [26] and has recently been extended accounting also for NNNLO corrections [27]. Large velocity QCD logarithms have been determined using renormalization-group-improved non-relativistic perturbation theory up to NLL order, with a partial treatment of NNLL effects [28,29]. Recently the dominant ultrasoft NNLL corrections have been completed [30]. The accuracy in this calculation is illustrated in Fig. 33.

Since the top quark kinetic energy is of the order of the top quark width, electroweak effects, which also include finite-lifetime and interference contributions, are crucial as well. This makes the cross section dependent on the experimental prescription concerning the reconstructed final state. Recently a number of partial results have been obtained. [31,34], which put approximate NNLL order predictions within reach. Theoretical predictions for differential cross sections such as the top momentum distribution and forward-backward asymmetries are only known at the NNLO

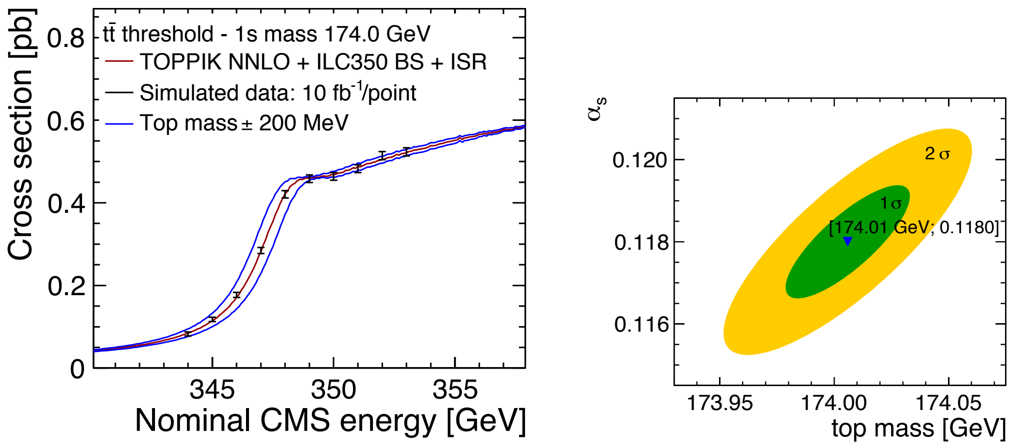

Figure 34: Illustration of a top quark threshold meausurement at the ILC. In the simulation, the top quark mass has been chosen to be 174. GeV. The blue lines show the effect of varying this mass by 200 MeV. The study is based on full detector simulation and takes initial state radiation (ISR) and beamstrahlung (BS) and other relevant machine effects into account: (left) the simulated threshold scan. (right) error ellipse for the determination of m_t and α_s. The figure is taken from [37].

level and are thus much less developed.

5.2.2 Simulations and Measurements

The most thorough experimental study of the top quark threshold has been carried out by Martinez and Miquel in [35]. These authors assumed a total integrated luminosity of 300 fb^{-1}, distributed over 10 equidistant energy points in a 10 GeV range around the threshold, using the TELSA beam parameters. To treat the strong correlation of the input theory parameters, simultaneous fits were carried out for the top quark mass, the QCD coupling and the top quark width from measurments of the total cross section, the top momentum distributions and the forward-backward asymmetry. These were simulated based on the code TOPPIK with NNLO corrections [36]. The study obtained the uncertainties $\Delta m_t = 19$ MeV, $\Delta\alpha_s(m_Z) = 0.0012$ and $\Delta\Gamma_t = 32$ MeV, when all observables were accounted for Using just the total cross section measurements, the results were $\Delta m_t = 34$ MeV, $\Delta\alpha_s(m_Z) = 0.0023$ and $\Delta\Gamma_t = 42$ MeV. The difference shows the discriminating power of additional observables of the threshold region. The analysis included a theory uncertainty in the cross section codes of 3%, which at this time is only approached for total cross section computations. Although the analysis was only based on fixed order NNLO predictions, the quoted uncertainties should be realistic.

The analysis in [35] did not yet include a complete study of experimental systematic uncertainties, including, in particular, uncertainties in the knowledge of the luminosity spectrum. This last point is addressed in a more recent study by Seidel, Simon, and Tesar, for which the results are shown in Fig. 34 [37]. That study was carried with a full detector simulation using the ILD detector. It takes the initial state radiation and beamstrahlung of the colliding beams into account. The figure underlines the high sensitivity of the threshold region to the actual value of the t quark mass. The statistical precision obtained on the t quark mass in this study is of the order of 30 MeV. Due to the QCD corrections relevant for a precise calculation of the t quark mass, the threshold scan is sensitive to the value of α_s. The error ellipse as obtained in a combined determination of α_s. and m_t is shown in the right-hand panel of Fig. 34.

The threshold top quark mass determined in this study must still be converted to the standard top quark $\overline{MS}$ mass. The conversion formula, to three-loop order, is given in [36]. The conversion adds an error of about 100 MeV from truncation of the QCD perturbation series and an error of 70 MeV for each uncertainty of 0.001 in the value of α_s. Both sources of uncertainty should be reduced by the time of the ILC running. In particular, the study of event shapes in $e^+e^- \to q\overline{q}$ at the high energies available at ILC should resolve current questions concerning the precision determination of α_s. We recall that these estimates are the results of a precision theory of the relation between the threshold mass and the top quark $\overline{MS}$ mass. A comparable theory simply does not exist for the conversion of the top quark mass measured in hadronic collisions to the $\overline{MS}$ value.

In principle, the contribution of the Higgs exchance potential to the $t\bar{t}$ threshold makes it possible to measure that Higgs coupling to $t\bar{t}$. However, the precision of this measurement is strongly limited by the fact that the Higgs corrections are suppressed by the inverse square of the Higgs mass. For a Higgs mass of $m_H = 120$ GeV the study in [35] found that uncertainties of at least several 10% should be expected in a measurement of the top quark Higgs Yukawa coupling. This coupling can be measured more accurately from the cross section for $e^+e^- \to t\bar{t}h$, as is explained in Section 2.6 and 2.7 of this report.

5.3 Probing the top quark vertices at the ILC

At higher energy, the study of $t\bar{t}$ pair production at the ILC is the idea setting in which to make precise measurements of the the coupling of the t quark to the Z^0 boson and the photon. In contrast to the situation at hadron colliders, the leading-order pair production process $e^+e^- \to t\bar{t}$ goes directly through the $t\bar{t}Z^0$ and $t\bar{t}\gamma$ vertices. There is no concurrent QCD production of top pairs, which increases greatly the potential for a clean measurement. In the following section, we will review the importance of measuring these couplings precisely. Then we will describe studies of the experimental capabilities of the ILC to perform these measurements.

5.3.1 Models with Top and Higgs Compositeness

There are several classes of models that seek to answer the question of where the Higgs boson comes from and why it acquires a symmetry-breaking vaccum expectation value. Among these is supersymmetry, which will have its own discussion in Section 7 of this report. An alternative point of view is that the Higgs boson is a composite state within a larger, strongly interacting theory at the TeV scale. Though the first models of this type contained no light Higgs bosons, there are now many models in which theories of this type naturally contain a light Higgs boson very similar to the Higgs boson of the Standard Model coupling to new heavy particles at the TeV mass scale. In Sections 2 and 3, we have described tests of models of this type at the ILC in the Higgs boson and W boson sectors.

The top quark is the heaviest known particle that derives its mass entirely from electroweak symmetry breaking. Thus, any composite structure of the Higgs boson must be reflected in composite structure or non-Standard interactions of the top quark. While such interactions may exist, they may not be easy to find. The coupling of the top quark to the gluon and the photon are constrained at $Q^0 = 0$ by requirements from exact QCD and QED gauge invariance. However, the low-energy $t\bar{b}Z$ vertex is much less constrained. It is then likely that this is the crucial place to look for deviations from the Standard Model induced by a strongly interacting Higgs sector.

Models of composite Higgs bosons can be constructed in three ways that seem at first sight to be distinctly different. The Higgs bosons may be Goldstone bosons associated with strong-interaction symmetry breaking at the 10 TeV energy scale, as in Little Higgs models. They may arise as partners of gauge bosons in theories with an extra space dimension, as in Gauge-Higgs Unification. Or, they may arise in extra-dimensional theories as states confined to a lower-dimensional subspace or 'brane'. Randall and Sundrum constructed a model of the last type [38] but also argued that all three classes of models are related by strong coupling-weak coupling duality [39]. That is, it is possible to view the extra-dimensional models as tools that allow weak coupling calculations of effects that are intrinsically manifestations of strong coupling and composite state dynamics.

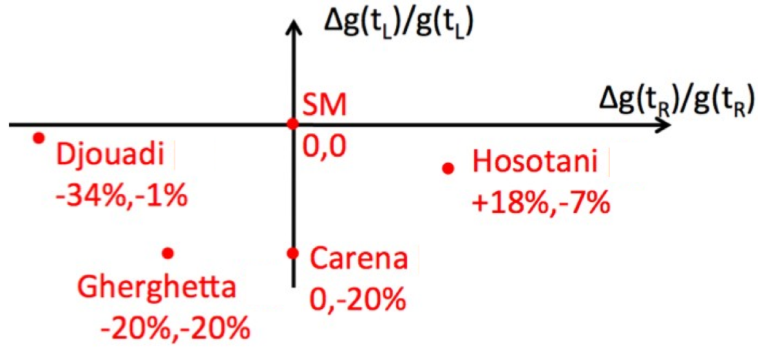

Figure 35: *Predictions of various groups [40,42,43,44] on deviations from Standard Model couplings of the t quark within Randall-Sundrum Models. The cartoon is taken from [47].*

The Randall-Sundrum approach also includes a model explanation of the hierarchy of Higgs-fermion Yukawa couplings. This is one of the most mysterious aspects of the Standard Model, reflected in the fact that the top quark and the up quark have exactly the same quantum numbers but differ in mass by a factor of 10^5. The extra dimension offers the possibility that the different flavors of fermion have wavefunction of different shape in the full space, and therefore different overlap with the wavefunction of the Higgs boson. In general, also, the right and left chiral components of each quark and lepton may have wavefunctions with different dependence on the extra dimensions. It is a typical prediction of Randall-Sundrum theories that the chiral components of the top quark have wavefunctions in the fifth dimension significantly different from those of the other quark, and significant different from one another, with the wavefunction of the right-handed top quark shifted significantly toward the low-energy boundary of the space, called the 'TeV brane', where the Higgs field is located. These difference of the wavefunction are reflected directly in couplings of the top quark to the Z^0 that are shifted from the values predicted in the Standard Model, with larger shifts specifically for the right-handed top quark. Figure 35 collects a number of predictions of the fractional shift in the t_L and t_R coupling to the Z^0 in a variety of models proposed in the literature.

Models with extra-dimensions may also be suited to explain the tensions observed at the Tevatron discussed in Section 5.1.5. The top forward-backward asymmetry may, for example, be explained by a new color octet vector boson G_μ, which couples weakly to light quarks but strongly to the t quark. This difference is required in order to suppress ordinary dijet production from the new colour-octet state. The difference in the coupling can be realised by the arrangement of the t quark wavefunction along the extra-dimension [25].

5.3.2 ILC measurements

In the previous section, we have described theories in which the top quark and Higgs boson are composite, with this compositeness being an essential element of the physics of electroweak symmetry breaking. A key test of this idea would come from the measurement of the $t\bar{t}Z$ couplings, where significant deviations from the predictions of the Standard Model would be expected. The ILC provides an ideal environment to measure these couplings. At the ILC $t\bar{t}$ pairs would be copiously produced, about 570 kEvents for an integrated luminosity of $500\,\mathrm{fb}^{-1}$. The production is by s-channel γ and Z exchange, so the Z couplings enter the cross section in order 1. It is possible to almost entirely eliminate the background from other Standard Model processes. The ILC will allow for polarized electron and positron beams. This allows us to measure not only the total cross section for $t\bar{t}$ production but also the left-right asymmetry A_{LR}, the change in cross-section for different beam polarization. For the b quark, the precision electroweak measurements of A_{LR} and forward-backward asymmetries contain a 3 σ discrepancy that has yet to be resolved [41]. If this effect is real, it is likely to be larger for the heavy t quark.

With the use of polarized beams, t and $\bar{t}$ quarks oriented toward different angular regions in the detector are enriched in left-handed or right-handed polarization [45]. This means that the experiments can independently access the couplings of left- and right-handed polarized quarks to the Z boson. In principle, measurement of the cross section and forward-backward asymmetry for two different polarization settings measures both the photon and Z couplings of the top quark for each handedness. New probes of the top quark decay vertices are also available, although we expect that these will already be highly constrained by the LHC measurements of the W polarization in top decay.

Recent studies based on full simulation of ILC detectors for a centre-of-mass energy of $\sqrt{s} = 500\,\mathrm{GeV}$ demonstrate that a precision on the determination of the couplings the left and the right chiral parts of the t quark wave function to the Z^0 of up to 1% can be achieved [46,47,48]. An example for such a study with full detector simulation is shown in Figure 36. The figure demonstrates the clean reconstruction of the t quark direction, which allows for the precise determination of the forward-backward asymmetry. It has to be noted however, that the final state gives rise to ambiguities in the correct association of the b quarks to the W bosons, see [48] for an explanation. These ambiguities can be nearly eliminated by requiring a high quality of the event reconstruction. The elimination comes however at the expense of a relatively small efficiency. The optimization of the selection criteria in order to improve the efficiency is work in progress. Another solution is the use of the vertex charge to separate the t and $\bar{t}$ decays. It is shown in [46] that the high efficiency of

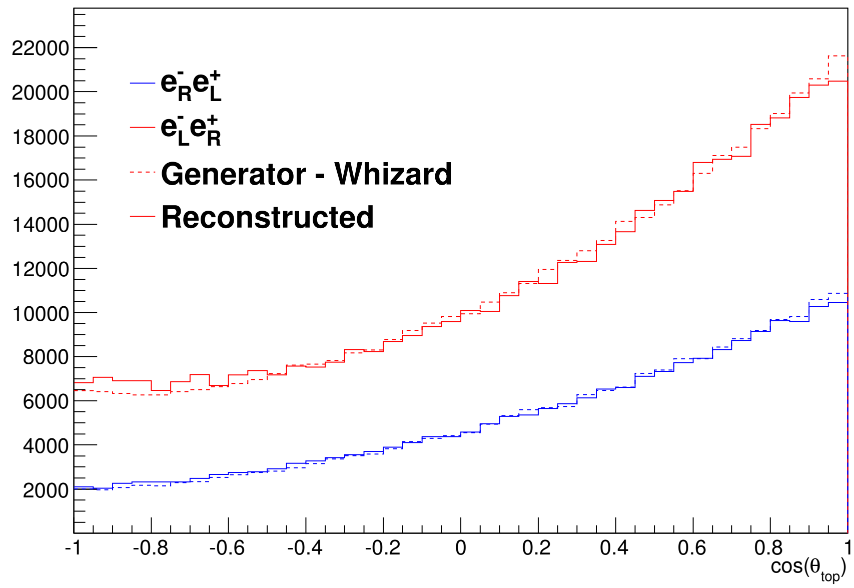

Figure 36: Reconstruction of the direction of the t quark for two different beam polarizations. The population in the two different hemispheres w.r.t. the polar angle θ_{top} allows for the measurement of the forward-backward asymmetry A_{FB}. The plot shown is an update of one presented in [48]. Note that the figure does not include background, however, it is known from the studies in [47] that the background is negligible.

vertex tagging in the ILC detectors will make this strategy available.

A precision of the order of 5% or better would allow for a clear distinction of e.g. the models indicated in Figure 35 which supports the high discriminative power which would be provided by the ILC. The results also support the superiority of ILC measurements with respect to the form factors introduced above.

Even more incisive measurements than presented so far using optimised observables are investigated in [49]. Four independant quantities are measured to disentangle the coupling of the top quark to the photon and to the Z. These quantities are the top pair production cross-section for left and right-handed polarised beams and the fraction of right-handed (t_R) and left handed top quarks (t_L). Following a suggestion by [50] for the TEVATRON, the fraction of t_L and t_R in a given sample can be determined with the helicity asymmetry. In the top quark rest frame the distribution of the polar angle θ_{hel} of a decay lepton is

$$\frac{1}{\Gamma}\frac{d\Gamma}{d\cos\theta_{hel}} = \frac{1+\lambda_t\cos\theta_{hel}}{2} \tag{84}$$

where λ_t varies between $+1$ and -1 depending on the fraction of right-handed (t_R) and left handed top quarks (t_L). The observable $\cos\theta_{hel}$ can easily be measured at

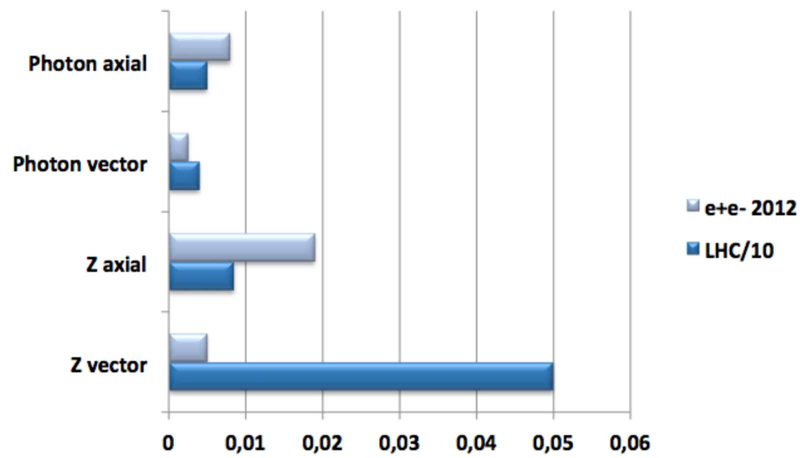

Figure 37: *Comparison of precisions expected at the LHC after an integrated luminosity of $\mathcal{L} = 300$ fb^{-1} and at the ILC. for vector and axial-vector couplings $\widetilde{F}_{1V,A}^{\gamma,Z}$ of the top to photon and Z. The results for the ILC are obtained in a study based on the measurement of polarized cross sections and the fraction of left and right handed top quarks [49]. This study was carried out for an integrated luminosity of $\mathcal{L} = 500$ fb^{-1} at $\sqrt{s} = 500\,GeV$ and a beam polarization of $P_{e^-,+} = \pm 0.8, \mp 0.3$.*

the ILC. Note, that this observable is much less sensitive to ambiguities in the event reconstruction than e.f. the forward backward asymmetry. The slope of the resulting linear distribution provides hence a very robust measure of the net polarisation of a top quark sample. This net polarization is sensitive to new physics. In Figure 37 the precision on the form factors expected from the LHC and that from the ILC using are compared with each other. The numerical values are given in Table 12, which repeats also the result of an earlier linear collider study [23] based on the forward backward asymmetry and in which only one form factor at a time was varied.

5.3.3 An example: the Randall Sundrum scenario

To illustrate the potential of the present analysis, one can invoke the Randall Sundrum scenario [38] which attributes to the top quark, and perhaps also to the b quark, increased couplings to Kaluza Klein particles predicted in this extra dimension scheme. Following a possible interpretation of the two anomalies observed on forward-backward asymmetry for b quarks $A_{FB,b}$ at LEP1 [40] and for top quarks $A_{FB,t}$ at the Tevatron [51] one can predict some relevant parameters of the Randall Sundrum scenario. The Figure 38 shows the expected modifications of the helicity angle distributions within this scenario. One sees that both the slopes and total cross sections are deeply modified in this scenario for the two polarizations. As explained

coupling	LHC	e^+e^- [23]	e^+e^- [49]
	$\mathcal{L} = 300$ fb^{-1}	$P_{e^-} = \pm 0.8$	$\mathcal{L} = 500$ fb^{-1}, $P_{e^-,+} = \pm 0.8, \mp 0.3$
$\Delta\widetilde{F}^{\gamma}_{1V}$	${}^{+0.043}_{-0.041}$	${}^{+0.047}_{-0.047}$, $\mathcal{L} = 200$ fb^{-1}	${}^{+0.003}_{-0.003}$
$\Delta\widetilde{F}^{\gamma}_{1A}$	${}^{+0.051}_{-0.048}$	${}^{+0.011}_{-0.011}$, $\mathcal{L} = 100$ fb^{-1}	${}^{+0.009}_{-0.009}$
$\Delta\widetilde{F}^{Z}_{1V}$	${}^{+0.24}_{-0.62}$	${}^{+0.012}_{-0.012}$, $\mathcal{L} = 200$ fb^{-1}	${}^{+0.005}_{-0.005}$
$\Delta\widetilde{F}^{Z}_{1A}$	${}^{+0.052}_{-0.060}$	${}^{+0.013}_{-0.013}$, $\mathcal{L} = 100$ fb^{-1}	${}^{+0.019}_{-0.019}$
$\Delta\widetilde{F}^{\gamma}_{2V}$	${}^{+0.038}_{-0.035}$	${}^{+0.038}_{-0.038}$, $\mathcal{L} = 200$ fb^{-1}	n.a.
$\Delta\widetilde{F}^{\gamma}_{2A}$	${}^{+0.16}_{-0.17}$	${}^{+0.014}_{-0.014}$, $\mathcal{L} = 100$ fb^{-1}	n.a.
$\Delta\widetilde{F}^{Z}_{2V}$	${}^{+0.27}_{-0.19}$	${}^{+0.009}_{-0.009}$, $\mathcal{L} = 200$ fb^{-1}	n.a.
$\Delta\widetilde{F}^{Z}_{2A}$	${}^{+0.28}_{-0.27}$	${}^{+0.052}_{-0.052}$, $\mathcal{L} = 100$ fb^{-1}	n.a.

Table 12: *Sensitivities achievable at 68.3% CL for the anomalous ttV ($V = \gamma$, Z) couplings $\widetilde{F}^V_{1V,A}$ and $\widetilde{F}^V_{2V,A}$ of Eq. (82) at the LHC for integrated luminosities $\mathcal{L}$ of 300 fb^{-1}, and the ILC with $\sqrt{s} = 500$ GeV and different luminosities and beam polarisations. In the study taken from Ref. [23]) only one coupling at a time is allowed to deviate from its SM value. In the recent study [49] in the last column the four couplings $\widetilde{F}_1$ have been determined simultaneously.*

previously, these LC measurement will allow to fully disentangle the influence of effects due to the Randall Sundrum model on the Z and photon couplings to top quarks allowing for an unambiguous understanding of the origin of these modifications. It can also be shown that by running at two energies, for instance 500 GeV and 1 TeV, one can fully extract the parameters of the model as, for instance the Kaluza Klein mass which can be measured with a $\sim$1% precision.

When the Kaluza Klein particles become very heavy, ILC at 500 GeV can observe >3 standard deviations on top couplings for masses which depend on the details of the model but typically range between 4 to 48 TeV

5.4 Concluding remarks

The top quark could be a window to new physics associated with light composite Higgs bosons and strong coupling in the Higgs sector. The key parameters here are the electroweak couplings of the top quark. We have demonstrated that the ILC offers unique capabilities to access these couplings and measure them to the required high level of precision.

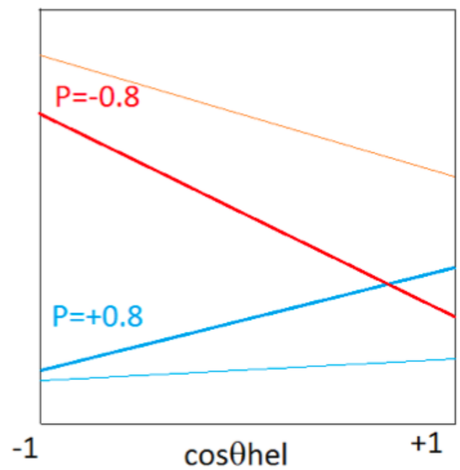

Figure 38: *Schematic view on the distributions of the helicity angle* $\cos\theta_{hel}$ *as expected from the Standard Model (thick lines) and their modifications by the Randall Sundrum framework (thin lines) as described in the text. The study assumes an integrated luminosity of* $\mathcal{L} = 500$ fb^{-1} *at* $\sqrt{s} = 500\,GeV$ *and a beam polarization of* $P_{e^-,+} = \pm 0.8, \mp 0.3$.

References

[1] CDF Collaboration, *F. Abe et al.*, Phys. Rev. Lett. **74** 2626 (1995), arXiv:hep-ex/9503002v2.

[2] D0 Collaboration, *S. Abachi et al.*, Phys. Rev. Lett. **74** 2632, (1995), arXiv:hep-ex/9503003.

[3] K. Lannon, F. Margaroli and C. Neu, arXiv:1201.5873v1 [hep-ex]

[4] ATLAS Collaboration, ATLAS-CONF-2012-024.

[5] The CMS collaboration, CMS-PAS-TOP-11-024.

[6] N. Kidonakis, Phys. Rev. D **82**, 114030 (2010) [arXiv:1009.4935 [hep-ph]].

[7] The current predictions, which have a range of about 8 pb, are reviewed in N. Kidonakis and B. D. Pecjak, arXiv:1108.6063 [hep-ph].

[8] S. Fleming, A. H. Hoang, S. Mantry and I. W. Stewart, Phys. Rev. D **77**, 114003 (2008) [arXiv:0711.2079 [hep-ph]].

[9] Tevatron Electroweak Working Group, CDF, D0 Collaborations, FERMILAB-TM-2504-E, CDF-NOTE-10549, D0-NOTE-6222, arXiv:1107.5255v3 [hep-ex].

[10] ATLAS collaboration, "$t\bar{t} \to lepton + jets$ channel using ATLAS data", submitted to European Physical Journal C, CERN-PH-EP-2012-003, arXiv:1203.5755v1 [hep-ex]

[11] P. Ferreira da Silva, Presentation at Rencontres de Moriond EW 2012, https://indico.in2p3.fr/getFile.py/access?contribId=109&sessionId=9&resId=0&materialId=slides&confId=6001, Remark: Presenter refers to CMS PAS-TOP-11-018, which is not identifiable to me at the moment.

[12] V. M. Abazov, et al. (D0), Phys. Rev. Lett. **106**, 022001 (2011), arXiv:1009.5686v1 [hep-ex].

[13] T. Aaltonen, et al. (CDF Collaboration), Phys.Rev.Lett. **105**, 232003 (2010), arXiv:1008.3891 [hep-ex].

[14] V. M. Abazov, et al. (D0), Phys. Rev. Lett. **107**, 121802 (2011), arXiv:1106.6436v1 [hep-ex].

[15] The CDF Collaboration, CDF Note 10333, http://www-cdf.fnal.gov/physics/new/top/2010/tprop/WhelDilPubWWW_2010/cdf10333_WhelDilPublic48fb_v4_2.pdf, *Remark RP: More adequate citation to be inserted*

[16] A. Juste et al., "Report of the 2005 Snowmass Top/QCD Working Group", ECONFC0508141:PLEN0043 (2005), arXiv:hep-ph/0601112v2.

[17] D. Zeppenfeld, R. Kinnunen, A. Nikitenko, E. Richter-Was, Phys. Rev. **D62** 013009 (2000), arXiv:hep-ph/0002036v1

[18] Alexander Belyaev, Laura Reina, JHEP **0208** 041 (2002), arXiv:hep-ph/0205270v3.

[19] T. Schwarz et al. CDF-Note 10584, http://www-cdf.fnal.gov/physics/new/top/2011/AfbComb/Afb_combo_5invfb.pdf

[20] V. M. Abazov et al. (D0 Collaboration), Phys. Rev. D **84**, 112005 (2011), arXiv:1107.4995v2 [hep-ex].

[21] CMS Collaboration, CMS-PAS-TOP-11-30, http://cdsweb.cern.ch/record/1428152?ln=en.

[22] ATLAS Collaboration, "Measurement of the charge asymmetry in top quark pair production in $p\bar{p}$ collisions at $\sqrt{s} = 7\,\mathrm{TeV}$ using the ATLAS detector", ATLAS-CONF-2011-106+updates, https://cdsweb.cern.ch/record/1372916 .

[23] T. Abe et al. [American Linear Collider Working Group], “Linear collider physics resource book for Snowmass 2001. 3: Studies of exotic and standard model physics,” in *Proc. of the APS/DPF/DPB Summer Study on the Future of Particle Physics (Snowmass 2001)* ed. N. Graf, arXiv:hep-ex/0106057.

[24] M. I. Gresham, I. -W. Kim and K. M. Zurek, Phys. Rev. D **85**, 014022 (2012) [arXiv:1107.4364 [hep-ph]].

[25] J. A. Aguilar-Saavedra, arXiv:1202.2382v1 [hep-ph].

[26] A. H. Hoang, M. Beneke, K. Melnikov, T. Nagano, A. Ota, A. A. Penin, A. A. Pivovarov and A. Signer *et al.*, Eur. Phys. J. direct C **2**, 1 (2000) [hep-ph/0001286].

[27] M. Beneke and Y. Kiyo, Phys. Lett. B **668**, 143 (2008) [arXiv:0804.4004 [hep-ph]].

[28] A. H. Hoang, A. V. Manohar, I. W. Stewart and T. Teubner, Phys. Rev. D **65**, 014014 (2002) [hep-ph/0107144].

[29] A. Pineda and A. Signer, Nucl. Phys. B **762**, 67 (2007) [hep-ph/0607239].

[30] A. H. Hoang and M. Stahlhofen, JHEP **1106**, 088 (2011) [arXiv:1102.0269 [hep-ph]].

[31] A. H. Hoang, C. J. Reisser and P. Ruiz-Femenia, Phys. Rev. D **82**, 014005 (2010) [arXiv:1002.3223 [hep-ph]].

[32] M. Stahlhofen, ”Theory progress in Top-Antitop Threshold Physics at the ILC”, Talk given at Top physics workshop, Paris May 2012, http://indico2.lal.in2p3.fr/indico/getFile.py/access?contribId=8&sessionId=0\&resId=0&materialId=slides&confId=1806

[33] M. Beneke, B. Jantzen and P. Ruiz-Femenia, Nucl. Phys. B **840**, 186 (2010) [arXiv:1004.2188 [hep-ph]].

[34] A. A. Penin and J. H. Piclum, JHEP **1201**, 034 (2012) [arXiv:1110.1970 [hep-ph]].

[35] M. Martinez and R. Miquel, Eur. Phys. J. C **27**, 49 (2003) [hep-ph/0207315].

[36] A. H. Hoang and T. Teubner, Phys. Rev. D **60**, 114027 (1999) [hep-ph/9904468].

[37] K. Seidel, F. Simon, and M. Tesar, CERN-LCD note in preparation; F. Simon, ”Top mass precision measurements at Linear Colliders”, Talk given at Top physics workshop, Paris May 2012, http://indico2.lal.in2p3.fr/indico/getFile.py/access?contribId=5&sessionId=0\&resId=0&materialId=slides&confId=1806

[38] L. Randall and R. Sundrum, Phys. Rev. Lett. **83** (1999) 3370; M. Gogberashvili, Int. J. Mod. Phys. D **11** (2002) 1635.

[39] N. Arkani-Hamed, M. Porrati and L. Randall, JHEP **0108**, 017 (2001) [hep-th/0012148].

[40] A. Djouadi, G. Moreau, and F. Richard., Nucl. Phys. B, **773** (1-2):43 (2007), arXiv:hep-ph/0610173v1.

[41] The LEP, Tevatron and SLC electroweak working groups, Phys. Rep. **427** (2006) 257, arXiv: hep-ex/0509008 and update hep-ex/0911.2604v1;

[42] Y. Hosotani and M. Mabe, Phys. Lett. B **615** 257 (2005), arXiv:hep-ph/0503020v3.

[43] Y. Cui, T. Gherghetta and J. Stokes, JHEP **1012** 075 (2010), arXiv:1006.3322v2 [hep-ph].

[44] M. Carena, E. Ponton, J. Santiago, C. E. M. Wagner,

[45] S. Parke and Y. Shadmi, Phys. Lett. B **387** (1996) 199, arXiv:hep-ph/9606419v2.

[46] E. Devetak, M. Peskin and A. Nomerotski, Phys. Rev. D **84** (2011) 034029, arXiv:1005.1756v5 [hep-ex].

[47] P. Doublet, PhD-Thesis Université de Paris XI and LAL, LAL 11-222.

[48] P. Doublet et al., ”Determination of Top-quark Asymmetries at the ILC”, arXiv:1202.6659v1 [hep-ex].

[49] Note on IFIC/LAL analysis in progress and will be provided soon, please contact *poeschl@lal.in2p3.fr* or *richard@lal.in2p3.fr* in case of further questions

[50] E.L. Barger et al., arXiv:1201.1790v1 [hep-ph].

[51] A. Djouadi et al. Phys. Lett .B **701** (2011) 458, arXiv:1105.3158v2 [hep-ph]
A. Djouadi et al., Phys. Rev. D **82** (2010) 071702, arXiv:0906.0604v2 [hep-ph]

[52] A. Gay, Eur. Phys. J. C **49** 489 (2007), arXiv:hep-ph/0604034v2.

[53] R. Yonamine *et al.*, Phys. Rev. D **84** 014033 (2011), arXiv:1104.5132v1 [hep-ph].

6 Extended Higgs Sectors

6.1 Motivation for extended Higgs sectors

The Higgs sector in the Standard Model (SM) is of the simplest and most minimal form, containing one isospin doublet of scalar fields and one physical particle, the Higgs boson [1]. In Section 2, we have described the phenomenology of this minimal Higgs boson in some detail. However, it must always be kept in mind that the minimal model might not be the correct one. There is no principle that requires the Higgs sector to be of the minimal form. There are many possibilities for extension of the Higgs sector, corresponding to adding further multiplets of scalar fields, which might be singlets, doublets, or higher representations of $SU(2) \times U(1)$.

In fact, many new physics models, proposed to solve problems with the Standard Model or provide missing elements such as dark matter, naturally contain extended Higgs sectors. Among the models proposed to solve the gauge hierarchy problem and provide mechanism for electroweak symmetry breaking are supersymmetry, Little Higgs models, and models such as Gauge-Higgs unification that require new dimensions of space. Each of these models predicts a light Higgs boson similar to the Higgs boson of the Standard Model. In each case, however, this boson is a part of a larger Higgs sector with multiple scalar fields and, in the three cases, the details of the extension are different. Extended Higgs sectors are also introduced to build models for specific phenomena that cannot be explained in the SM, such as baryogenesis, dark matter, and neutrino masses.

In Section 6.2 below, we will give an orientation for models with extended Higgs sectors, defining the sometimes complex notation and clarifying the spectrum of physical Higgs states in various scenarios. In Section 6.3, we will summarize the current constraints on these extended Higgs sectors, and the direct searches for extended Higgs bosons that can be carried out at the ILC. In Section 6.4, we discuss ILC phenomenology of various exotic scenarios for neutrino mass, baryogenesis and dark matter which are strongly relevant to extended Higgs sectors. Conclusions are given in Section. 6.5.

6.2 General description of extended Higgs sectors

The simplest examples of an extended Higgs sector are built by the addition of one $SU(2) \times U(1)$ singlet or one additional $SU(2) \times U(1)$ doublet scalar field. The case of an additional doublet is especially important. Supersymmetry requires distinct Higgs doublets to give mass to the u- and d-type quarks, and so the Minimal Supersymmetric Standard Model (MSSM) contains an extended Higgs sector [2]. In this section, we will describe the structure of these and more complicated Higgs sectors and define the parameters needed for a discussion of the phenomenology of these models.

6.2.1 The Two Higgs Doublet Model

The Two Higgs Doublet Model (THDM) includes two $SU(2) \times U(1)$ scalar doublets with $Y = 1$ [3]. The Higgs doublets can be parameterized as

$$\Phi_i = \left[\begin{array}{c} w_i^+ \\ \frac{1}{\sqrt{2}}(v_i + h_i + iz_i) \end{array} \right], \quad (i = 1, 2). \tag{85}$$

The most general Higgs potential is parametrized by three mass parameters and 7 independent quartic coupling constants.

$$\begin{aligned} V = {} & m_1^2|\Phi_1|^2 + m_2^2|\Phi_2|^2 - (m_3^2\Phi_1^\dagger\Phi_2 + h.c.) + \tfrac{1}{2}\lambda_1|\Phi_1|^4 + \tfrac{1}{2}\lambda_2|\Phi_2|^4 + \lambda_3|\Phi_1|^2|\Phi_2|^2 \\ & +\lambda_4|\Phi_1^\dagger\Phi_2|^2 + \tfrac{1}{2}[\lambda_5(\Phi_1^\dagger\Phi_2)^2 + \lambda_6|\Phi_1|^2\Phi_1^\dagger\Phi_2 + \lambda_7|\Phi_2|^2\Phi_1^\dagger\Phi_2 + h.c.]. \end{aligned} \tag{86}$$

The Higgs potential in the MSSM is a special case of this potential in which the quartic couplings are related to the $SU(2)$ and $U(1)$ gauge couplings by supersymmetry. The model contains 3 degrees of freedom that are eaten by the $W^\pm$ and Z^0 when their masses are generated through the Higgs mechanism. This leaves over 5 physical Higgs bosons, two CP-even scalars h and H, one CP-odd scalar A, and one pair of charged scalars $H^\pm$. The mass eigenstates are related to the fields in (85) by mixng angles α and β according to

$$\begin{aligned} h &= -h_1 \sin\alpha + h_2 \cos\alpha, & H &= h_1 \cos\alpha + h_2 \sin\alpha \\ H^\pm &= w_1^\pm \cos\beta + w_2^\pm \cos\alpha, & A &= z_1 \cos\beta + z_2 \sin\beta, \end{aligned} \tag{87}$$

We define h to be the lighter CP-even boson. The angle β yields the parameter $\tan\beta = v_2/v_1$.

The two vacuum expectation values v_1, v_2 satisfy

$$v_1^2 + v_2^2 = v^2 = (246 \text{ GeV})^2 . \tag{88}$$

The gauge coupling constants for the lighter Higgs boson, hZZ and hWW, are given by that of the SM Higgs boson times $\sin(\beta - \alpha)$, while those for HZZ and HWW are proportional to $\cos(\beta - \alpha)$. The scalars h and H thus share the Higgs field vacuum expectation value and share the strength of the coupling of WW and ZZ to scalar fields. The trilinear couplings $H^\pm W^\mp Z$, $H^\pm W^\mp \gamma$, AW^+W^-, AZZ are zero at tree.

	Φ_1	Φ_2	u_R	d_R	ℓ_R	Q_L, L_L
Type I	$+$	$-$	$-$	$-$	$-$	$+$
Type II (MSSM like)	$+$	$-$	$-$	$+$	$+$	$+$
Type X (lepton specific)	$+$	$-$	$-$	$-$	$+$	$+$
Type Y (flipped)	$+$	$-$	$-$	$+$	$-$	$+$

Table 13: Four possible Z_2 charge assignments that forbid dangerous flavor-changing neutral current effects in the THDM. [5].

Of the two mass parameters in (86), m_1 and m_2 directly related to v_1 and v_2. The third parameter m_3 does not drive electroweak symmetry breaking and can potentially be much larger. When

$$M^2 \equiv m_3^2/\sin\beta\cos\beta \gg v^2 \ , \tag{89}$$

then we approach to the *decoupling limit* where the masses of the added scalar states H, A, and $H^{\pm}$ become much larger than the mass of h:

$$m_h^2 \simeq \lambda_i v^2, (\text{SMlike}), \qquad m_\phi \sim \lambda_i v^2 + M^2, \text{where } \ \phi = H, A, \text{and } \ H^{\pm}, \tag{90}$$

with $\sin(\beta-\alpha) \simeq 1$ [4] . In this case, the phenomenology of h is similar to that of the SM Higgs boson except for small deviations in the Higgs boson couplings. However, it is not necessary that the additional bosons be heavy, and, in this case, there is room for substantial mixing between h and H.

In the THDM, both the doublets can in principle couple to fermions, and this can lead to dangerous flavor-changing neutral current couplings. A well-known way to suppress these couplings is to impose a softly broken Z_2 symmetry so that only one of the two Higgs doublets gives mass to the u-type quarks, the d-type quarks, and to the leptons. The various possible assignments lead to four distinct models, displayed in Table 13 [5,6,7]. In the MSSM, supersymmetry requires the Type II assignment, with one doublet giving mass to the u quarks and the other to the d quarks and the charged leptons. In more general models, though, all four possibilities are open. The Yukawa interactions for these models are expressed as

$$\begin{aligned}\mathcal{L}^Y_{THDM} = \quad & -\textstyle\sum_{f=u,d,e}\left(\frac{m_f}{v}\xi_h^f\overline{f}fh + \frac{m_f}{v}\xi_H^f\overline{f}fH + i\frac{m_f}{v}\xi_A^f\overline{f}\gamma_5 fA\right) \\ & -\left[\sqrt{2}V_{ud}\overline{u}\left(\frac{m_u}{v}\xi_A^u P_L + \frac{m_d}{v}\xi_A^d P_R\right)d\,H^+ + \frac{\sqrt{2}m_\ell\xi_A^\ell}{v}\overline{\nu_L}e_R H^+ + h.c.\right],\end{aligned} \tag{91}$$

where $P_{L/R}$ are projection operators for left-/right-handed fermions, and the factors ξ_φ^f are listed in Table 14.

The decays of the Higgs bosons in the THDM depend on the model chosen for the Yukawa interactions. When $\sin(\beta-\alpha) = 1$ [4], the decay pattern of h is almost

	ξ_h^u	ξ_h^d	ξ_h^d	ξ_H^u	ξ_H^d	ξ_H^ℓ	ξ_A^u	ξ_A^d	ξ_A^ℓ
Type I	$\frac{\cos\alpha}{\sin\beta}$	$\frac{\cos\alpha}{\sin\beta}$	$\frac{\cos\alpha}{\sin\beta}$	$\frac{\sin\alpha}{\sin\beta}$	$\frac{\sin\alpha}{\sin\beta}$	$\frac{\sin\alpha}{\sin\beta}$	$-\cot\beta$	$\cot\beta$	$\cot\beta$
Type II	$\frac{\cos\alpha}{\sin\beta}$	$-\frac{\sin\alpha}{\cos\beta}$	$-\frac{\sin\alpha}{\cos\beta}$	$\frac{\sin\alpha}{\sin\beta}$	$\frac{\cos\alpha}{\cos\beta}$	$\frac{\cos\alpha}{\cos\beta}$	$-\cot\beta$	$-\tan\beta$	$-\tan\beta$
Type X	$\frac{\cos\alpha}{\sin\beta}$	$\frac{\cos\alpha}{\sin\beta}$	$-\frac{\sin\alpha}{\cos\beta}$	$\frac{\sin\alpha}{\sin\beta}$	$\frac{\sin\alpha}{\sin\beta}$	$\frac{\cos\alpha}{\cos\beta}$	$-\cot\beta$	$\cot\beta$	$-\tan\beta$
Type Y	$\frac{\cos\alpha}{\sin\beta}$	$-\frac{\sin\alpha}{\cos\beta}$	$\frac{\cos\alpha}{\sin\beta}$	$\frac{\sin\alpha}{\sin\beta}$	$\frac{\cos\alpha}{\cos\beta}$	$\frac{\sin\alpha}{\sin\beta}$	$-\cot\beta$	$-\tan\beta$	$\cot\beta$

Table 14: The mixing factors in Yukawa interactions in Eq. (91) [6].

the same as that in the Standard Model. However, the decay patterns of H, A, and $H^\pm$ can vary over a large range. Figure 39 shows the decay branching ratios of H, A and $H^\pm$ as a function of $\tan\beta$ for the four models, for boson masses of 150 GeV and $\sin(\beta-\alpha)=1$. The decay pattern of H is typically similar to that of A, but with some important exceptions. In the type I THDM, all fermionic decays, and the gg decay mode, are suppressed at large $\tan\beta$. However, H, but not A couples to H^+H^-, and this allows for H a significant decay through a scalar loop to $\gamma\gamma$.

In general, the complexity of the H, A, $H^\pm$ decay schemes and in the four possible models make it difficult to determine the underlying model unless these bosons are created through a simple and well-characterized pair-production reaction. Thus, even if these bosons are discovered at the LHC, it will be important to study them in e^+e^- pair-production at the ILC.

6.2.2 Models with Higgs Singlets

Another simple extension of the SM Higgs sector is the addition of a singlet scalar field S with $Y=0$. Such a singlet field is introduced in new physics models with an extra $U(1)$ gauge symmetry [8] like $B-L$ conservation [9]. The neutral singlet scalar field is also introduced in the Next-to-Minimal SUSY Standard Model (NMSSM) but with two Higgs doublet fields [10]. Such singlet fields do not couple to quarks, leptons and gauge bosons of the SM directly.

In the model with only one additional neutral singlet scalar field to the SM, we parameterize the SM doublet Φ and S as

$$\Phi = \begin{bmatrix} \varphi^+ \\ \frac{1}{\sqrt{2}}(v+\varphi+i\chi) \end{bmatrix}, \qquad S = \frac{1}{\sqrt{2}}(v_S+\varphi_S+i\chi_S), \tag{92}$$

where v ($\simeq 246$) GeV, and v_S being the vacuum expectation value of the extra $U(1)$.

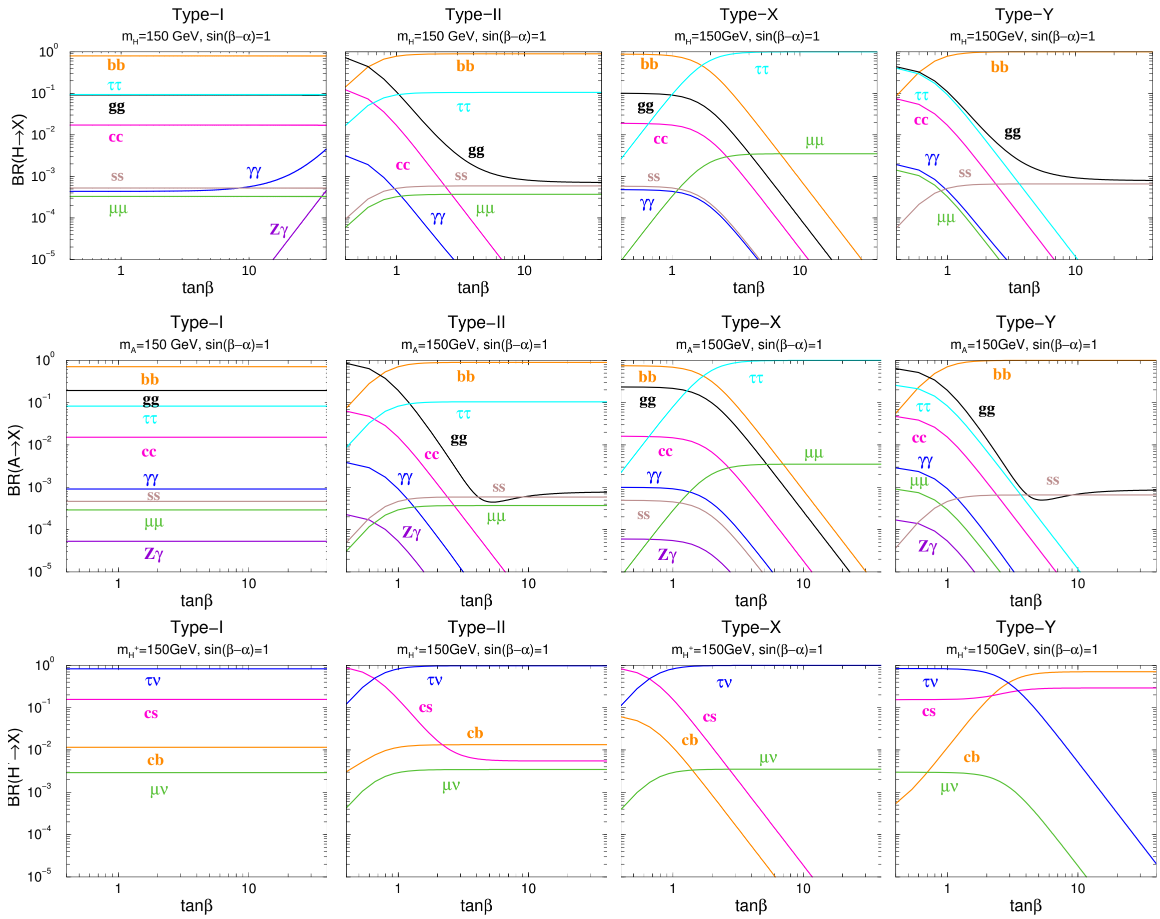

Figure 39: Decay branching ratios of H, A and $H^{\pm}$ in the four different types of THDM as a function of $\tan\beta$ for $m_H = m_A = m_{H^{\pm}} = 150$ GeV. The SM-like limit $\sin(\beta - \alpha) = 1$ is taken.

The two CP-even mass eigenstates h and H are expressed with the mixing angle as

$$h = \varphi \cos\theta - \varphi_S \sin\theta, \qquad H = \varphi \sin\theta + \varphi_S \cos\theta. \tag{93}$$

The CP-odd component χ_S is absorbed by the extra $U(1)$ gauge boson. Therefore, the difference from the SM is just one additional CP-even scalar boson H, and the absence of charged Higgs bosons is the unique feature of neutral singlet extensions. All the SM fields obtain mass from the VEV of the doublet v. Their coupling constants with h and H are obtained by the replacement of $\phi_{\rm SM} \to h\cos\theta + H\sin\theta$.

In the decoupling regime, where h is the SM-like with $\theta \sim 0$, coupling constants of h with the SM fields are commonly but slightly reduced by $\cos\theta (\sim 1 - \theta^2/2)$. On the other hand, when $\tan\theta \sim \mathcal{O}(1)$, both the h and H behave as SM-like Higgs bosons with relatively small mass difference, but each of the width is smaller. Each production cross section is reduced, but if both h and H are almost degenerated in mass and their mass difference is smaller than the mass resolution achievable by LHC experiments, the two Higgs bosons look like only a single SM Higgs boson with similar width. At the ILC with the better resolusion of reconstructed mass (expected error to be $\Delta m = 23$ MeV for $e^+e^- \to Zh \to \mu^+\mu^- X$) [11], the two Higgs bosons could be better separated.

The reduced couplings of h (H) result in the smaller production cross sections as compared to the SM predictions. Therefore, the mass bounds from the collider experiment can be milder. At LEP, the lower mass bound of h in the singlet model is about 110 GeV for $\sin\theta = 1/\sqrt{2}$ while that in the SM is about 114 GeV [12]. The bounds from ATLAS [13] and CMS [14] are also milder (about 110 GeV $< m_h <$ 130 GeV) than those in the SM (about 122 GeV $< m_h <$ 127 GeV). Basso, Moretti and Pruna studied the ILC phenomenology of the Higgs sector in the minimal $B-L$ model [15].

6.2.3 Models with Higgs Triplets

We can go on to consider models that add scalar fields in higher representations of $SU(2)$, models with fields with $I = 1, \frac{3}{2}, \ldots$. There are many such models. However, these models are constrained by the requirement that they do not give tree level corrections to the Standard Model relation

$$\rho = \frac{m_W^2}{m_Z^2 \cos^2\theta} = 1 \ . \tag{94}$$

When electroweak radiative corrections are included, (94) is in excellent agreement with the data, so it is dangerous to add to the model with fields that can modify it. In a general $SU(2) \times U(1)$ model with n scalar multiplets ϕ_i with isospin T_i and hypercharge Y_i, the ρ parameter is given at the tree level by

$$\rho = \frac{\sum_{i=1}^{n} [T_i(T_i+1) - \frac{1}{4}Y_i^2] v_i}{\sum_{i=1}^{n} \frac{1}{2} Y_i^2 v_i}, \tag{95}$$

where v_i are vacuum expectation values of ϕ_i. So, singlets and doublets with $Y_i = \pm\frac{1}{2}$ preserve $\rho = 1$, while adding higher representation generally modifies this relation, unless those fields have very small vacuum expectation values [16].

As example of a model that adds an isospin triplet, we review the case of a Higgs representation with $I = 1$ and $Y = 2$ A vacuum expectation value of this field can produce a Majorana neutrino mass [17].

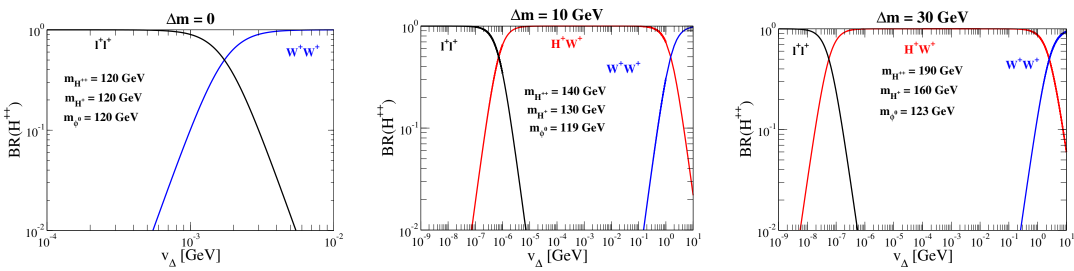

Figure 40: Decay branching ratio of H^{++} as a function of v_Δ. In the left figure, $m_{H^{++}}$ is set to be 120 GeV with $\Delta m = 0$. In the middle figure, $m_{H^{++}}$ is 140 GeV with $\Delta m = 10$ GeV. In the right figure, $m_{H^{++}}$ is 190 GeV with $\Delta m = 30$ GeV.

A model with this triplet field will contain a Higgs doublet Φ in addition to the triplet Δ. The component fields are

$$\Phi = \begin{bmatrix} \varphi^+ \\ \frac{1}{\sqrt{2}}(v_\varphi + \varphi + i\chi) \end{bmatrix}, \qquad \Delta = \begin{bmatrix} \Delta^+/\sqrt{2} & \Delta^{++} \\ \frac{1}{\sqrt{2}}(v_\Delta + \delta + i\eta) & -\Delta^+/\sqrt{2} \end{bmatrix}, \tag{96}$$

where v_φ and v_Δ are the vacuum expectation values. The physical scalar states are two CP-even bosons (h and H), a CP-odd boson (A), singly charged pair ($H^\pm$), and a doubly charged pair ($H^{\pm\pm}$). These are related to the original component fields by mixing angles α, β_0 and $\beta_\pm$,

$$\begin{aligned} h &= \varphi\cos\alpha + \delta\sin\alpha, \quad H = -\varphi\sin\alpha + \delta\cos\alpha, \\ A = -\chi\sin\beta_0 + \eta\cos\beta_0, &\quad H^\pm = -\varphi^\pm\sin\beta_\pm + \Delta^\pm\cos\beta_\pm, \quad H^{\pm\pm} = \Delta^{\pm\pm}. \end{aligned} \tag{97}$$

We must arrange $v_\Delta \ll v_\varphi$ to preserve $\rho \simeq 1$. This constraint implies the mass relations

$$m_h^2 \simeq 2\lambda_1 v^2, \quad m_{H^{++}}^2 - m_{H^+}^2 \simeq m_{H^+}^2 - m_A^2 \ , \quad \text{and} \quad m_H^2 \simeq m_A^2, \tag{98}$$

with $\alpha \ll 1$, $\beta_0 \ll 1$ and $\beta_\pm \ll 1$. Therefore, the model has a Standard Model-like Higgs boson h and additional triplet-like scalar states whose masses become approximately equal in the decoupling limit.

The doubly charged Higgs bosons H^{++} are the most characteristic feature of the model. The requirement that the vacuum expectation value of Δ gives a Majorana neutrino mass requires that this field must be assigned lepton number $L = 2$. Then, if the new Higgs bosons are degenerate, the dominant decays would be to lepton and neutrino pairs. In particular, H^{++} would be expected to decay to $\ell^+\ell^+$. At the LHC, the search for $H^{\pm\pm}$ is underway using this decay mode. The exclusion of the signal implies a lower bound on the mass of H^{++}, $m_{H^{++}} \gtrsim 400$ GeV [18].

However, this analysis is correct only for a limited parameter region in which the vacuum expectation value of Δ is extremely small, $v_\Delta < 10^{-3}$ GeV. For larger, but still small, values of v_Δ, a small mass splittings between H^+ and H^{++} opens up that allows the decay to take advantage of the much larger coupling to H^+W^+ [19]. In Fig. 40, the decay branching ratios for $H^{\pm\pm}$ are shown as a function of v_Δ [20]. For $v_\Delta \sim 1$ GeV, corresponding to mass difference $\Delta m \sim 10$ GeV, the decay into H^+W^+ is dominant for a wide range of v_Δ when $m_{H^{++}} > m_{H^+} > m_{A,H}$. In this case, H^{++} could be identified through its cascade decay. It is also possible to realize the opposite sign of the mass difference. In this case, the H^{++} decays into W^+W^+.

This model gives another illustration that a well-understood production mechanism and broad sensitivity to a wide range of final states are needed in order to understand the possibly complex details of an extended Higgs sector.

6.3 Extended Higgs bosons searches at the ILC

The discovery of additional Higgs bosons such as H, A, $H^\pm$ and $H^{\pm\pm}$ would give direct evidence for extended Higgs sector. As already discussed, there are many possibilities for the decay branching ratios of these particles, illustrated by the various schemes presented in Section 6.2. The searches at LHC are ongoing and mostly rely on specific production and decay mechanisms that occupy only a part of the complete model parameter space. At the ILC, the extended Higgs bosons are produced in electroweak pair production through cross sections that depend only on the $SU(2)\times U(1)$ quantum numbers and the mixing angles. Thus, the reach of the ILC is typically limited to masses less than $\sqrt{s}/2$, but it is otherwise almost uniform over the parameter space.

6.3.1 Constraints from the LHC experiments

The LHC is imposing several types of constraints in the exploration of the Higgs sector, but certainly the main constraint comes from the discovery of the resonance at 125-126 GeV by ATLAS [21] and CMS [22], particularly significative in the decay channels into two γ's and two Z^0 bosons. The exact nature of this new resonance has still to be confirmed. However there are some indications that it could well be the light Higgs neutral boson we have been so long looking for. Let's thus label it here as H126.

As noticed by M. Peskin [23], the fact that WW and ZZ are seen at nearly the SM strength would indicate that H126 is a CP even spin 0 state from a field with vacuum expectation value that breaks $SU(2)xU(1)$.

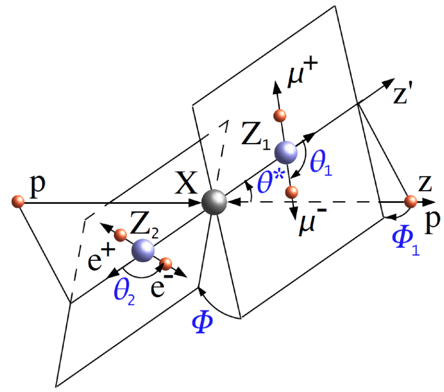

Figure 41: Schema of the angular analysis for studying the Higgs decay into a pair of Z bosons that decay then into 4 leptons, as used by the CMS experiment.

CMS has already performed an angular analysis of the channel $pp \rightarrow ZZ \rightarrow$ 4 charged leptons (see Fig. 41). It allows verifying the quantum numbers of this new object and favors the scalar hypothesis at 1 σ. The separation between scalar and pseudoscalar hypotheses at 3 σ's should be achievable with $30fb^{-1}$ of integrated luminosity. Each LHC experiment will be recording of order $20 - 25fb^{-1}$in 2012, before the first long LHC shutdown in 2013-2014. The total integrated luminosity from 2010 to 2012, might thus allow reaching this crucial result.

Thus the main constraints still have to come from the confirmation of the nature of this new H126 particle with as major inputs: refining its mass measurement, confirming or not if it is a spin 0 particle and verifying and measuring the branching decays into 2 γ's, 2 W or 2 Z bosons, 2 b-quarks and 2 τ leptons. The decay mode into τ lepton, in particular, is quite important especially for many BSM cases [24,25]. Still major results are thus expected by 2013 when all the data at 8 TeV will be recorded. Any deviation from the SM expected rates for each of these decay modes have been already computed with the presently analyzed data and are shown in Fig. 42 for both ATLAS and CMS. The present signal strength, defined as the ratio of the measured cross section for this process and the corresponding expected SM cross section value (σ/σ_{SM}) is 0.8 $\pm$ 0.2 for CMS and 1.2 $\pm$ 0.3 for ATLAS. Thus no real deviation from SM expectations within the experimental errors; but a better accuracy will be already obtained with the overall data recorded by the end of 2012. Moreover, CMS groups the Higgs couplings into two sets: the "vectorial" and the "fermionic" sets. A modifier to the SM prediction is attached to each of those: C_V and C_F. By using a LO theoretical prediction for loop induced $H \rightarrow \gamma\gamma$ and $H \rightarrow gg$ couplings an agreement with SM within the 95% confidence range is currently observed. There

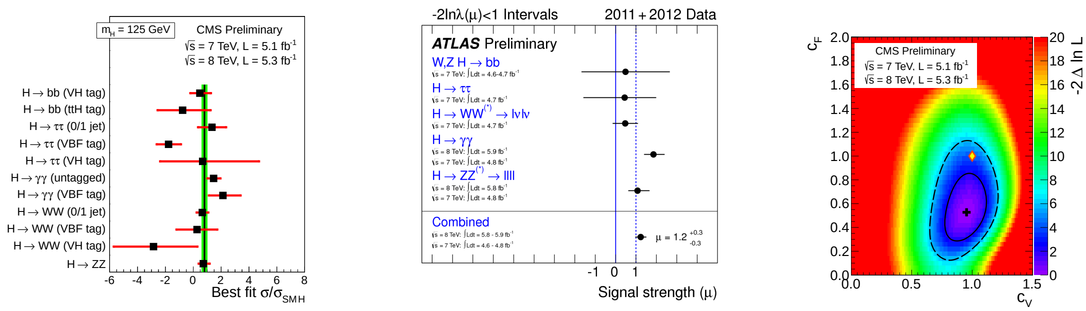

Figure 42: The signal strength for each measured decay mode of the new H126 resonance is shown for CMS (left) and ATLAS (center); Fit to the vectorial (C_V) and fermionic (C_F) sets of Higgs coupling (solid line is the 68% C.L. and dashed line is the 95% CL) by CMS.

also more data are obviously needed [26].

Apart from the crucial constraint provided by the discovery of a light neutral Higgs, the LHC experiments are exploring the whole Higgs and BSM sector. This is in continuation of the work already performed by the Tevatron experiments but with a much larger exploration potential in terms of the parameter space. ATLAS and CMS performed a number of extended Higgs searches. The published results are only based on the 2011 data. Much more will become soon available by adding the first $5fb^{-1}$ data that are already recorded in 2012. The experiments have scanned a mass range up to 350-400 GeV/c^2 in a variety of interesting processes and BSM scenarios. There is presently no evidence for such new BSM heavy Higgs signals. The current results from the charged Higgs searches at hadron colliders are reported in subsection 6.3.3.

In the context of MSSM, the neutral Higgs, h, H and A are searched for in their decay into 2 b-quarks, 2 muons or 2 τ leptons. Doubly charged Higgs boson and Higgs boson in SM reinterpreted with 4th generation of fermions are also investigated. The resonance at 126 GeV decaying into 2 photons is further reinterpreted in terms of a fermiophobic Higgs scenario. Some of the main present results at LHC on these searches are shown in Fig. 43.

No significant excess is observed and limits are set as low as for tan β equal to 10. This is already a drastic improvement compared to the Tevatron results.

ATLAS and CMS are searching for Higgs bosons in the Next-to-MSSM (NMSSM) with a particular interest for a very light CP odd scalar boson that would decay into 2 muons (e.g. CMS in [27]). They both looked for a very low mass Higgs decaying into two muons in a NMSSM scenario and did not find, so far, any significant excess of events. Fig. 44 shows the results obtained by CMS based with only $1.3fb^{-1}$ of data

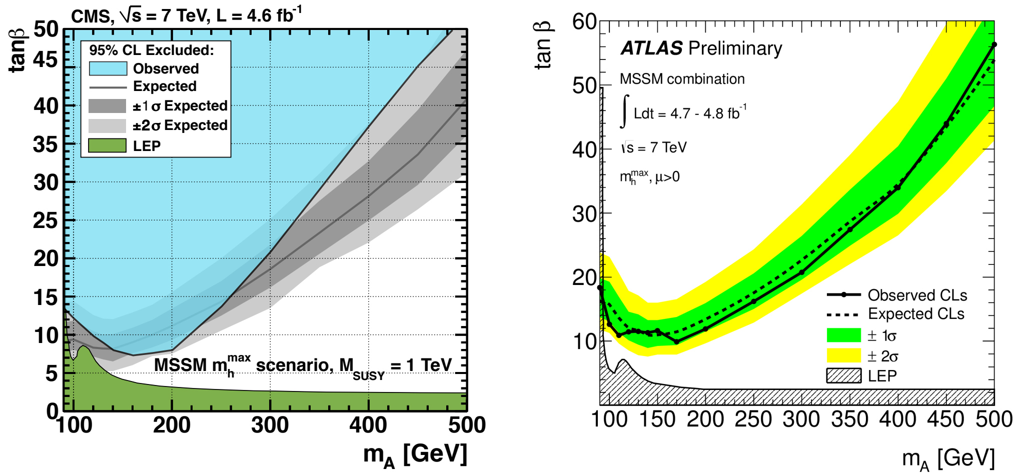

Figure 43: The limits on the signature with two τ leptons are obtained by scanning $\tan\beta$ for each M_A mass hypothesis and taking into account the dependence of M_h and M_H on $\tan\beta$; the results from CMS (left) and the ones of ATLAS (right).

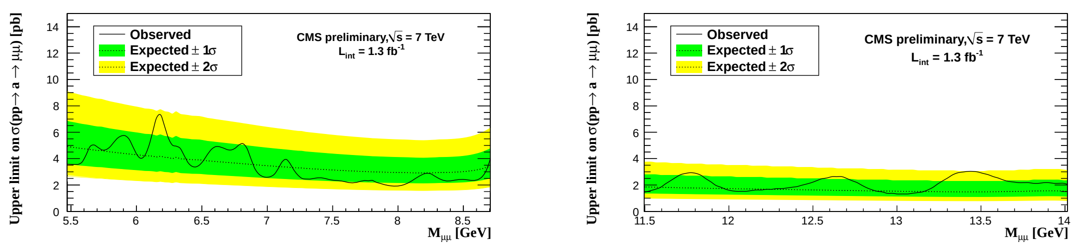

Figure 44: CMS search for a low mass Higgs decaying into two muons in a NMSSM scenario with the first $1.3 fb^{-1}$ data in 2011

taken in 2011. It demonstrates the potential of such a detector to look for relatively low mass objects at LHC.

Other important constraints from LHC experiments when exploring an extended Higgs sector are coming from the outcomes of the searches on BSM processes, including the heavy flavor sector. Any deviation from SM or new particles that might be found, would give an important hint on the extended Higgs sector. For instance by the end of 2012, the CMS and LHCb experiments will reach the SM limit for evidencing the Bs-meson rare decay into dimuons. This was one of the possible flagship for looking for new physics.

These few examples show even in this very early stage of the BSM searches per-

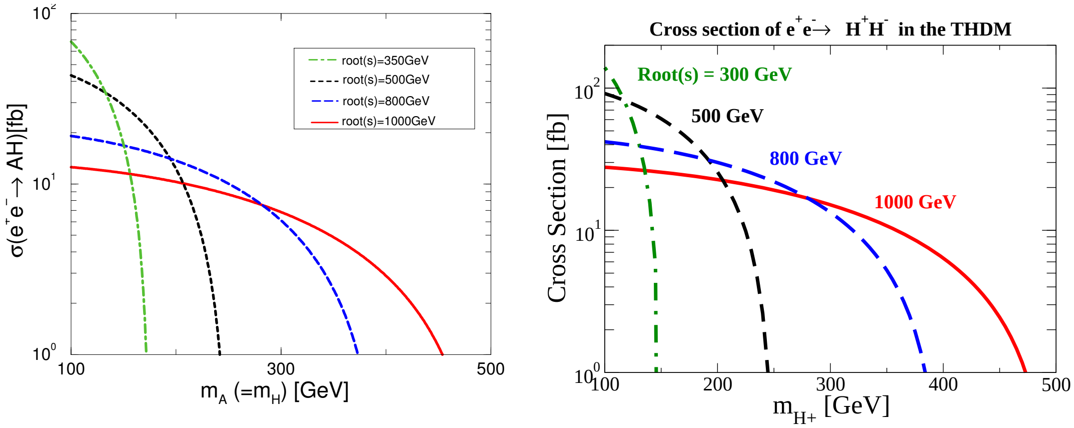

Figure 45: The production cross section of $e^+e^- \to AH$ (left) and $e^+e^- \to H^+H^-$ (right) are shown as a function of the Higgs boson mass. The dot-dashed, dashed, long-dashed, and solid curves correspond to $\sqrt{s} = 350, 500, 800$, and 1000 GeV, respectively.

formed at LHC, the already large capability of these detectors to explore a very large scope of BSM scenarios with a good precision and even trickier event signatures. This higher precision and detection capabilities will be continuously improved thanks to the increase in energy and luminosity of the machine and to the challenging and very complete upgrades that are being undertaken by both experiments on all their components.It makes even more challenging the competition and complementarity issues with a very high precision e^+e^- collider.

6.3.2 Higher mass neutral Higgs Production at ILC

At the ILC, the pair production of extended Higgs bosons $e^+e^- \to AH$ in the THDM case, depends only on the boson masses in the decoupling limit. The production cross sections are shown in Fig. 45 for $\sqrt{s} = 350, 500, 800$, and 1000 GeV as a function of m_A [28]. The decays of the extended Higgs state are mainly to fermion pairs. Thus, the observation of pair-produced Higgs bosons in various decay channels allows us determining the type of Yukawa interaction, in the sense of Section 6.2.1, through the measurement of the corresponding branching ratios. For example, in MSSM, which requires a Type II Higgs structure, the dominant final states for HA production should be $bbbb$ and $bb\tau\tau$, while in the Type X (lepton specific) structure the dominant final state should be $\tau\tau\tau\tau$ for $\tan\beta > 2$. In Type I, the $bbjj$ final states signature is also important in addition to the $bbbb$ and $bb\tau\tau$ signatures, over a wide range of $\tan\beta$ values, while in Type Y (flipped) the $bbbb$ states dominate and the $bb\tau\tau$ and $bbjj$

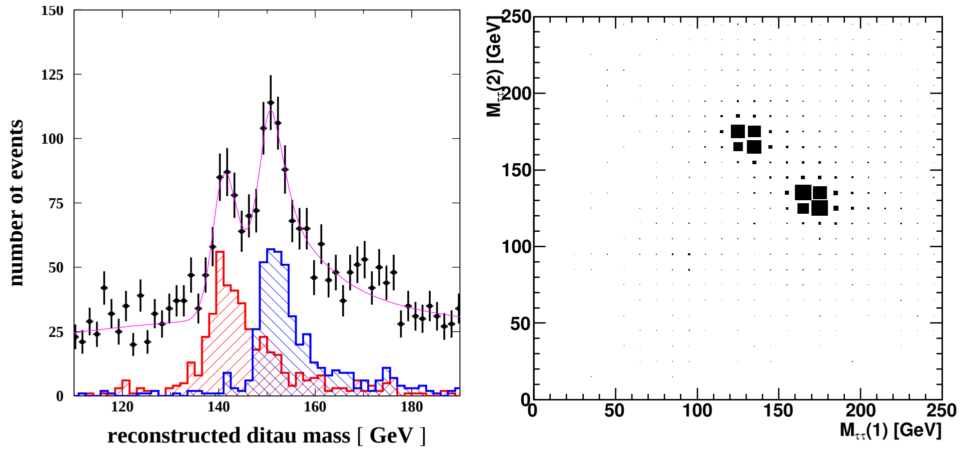

Figure 46: Invariant mass reconstruction from the kinematical fit in the process $e^+e^- \to HA \to b\bar{b}\tau^+\tau^-$ in the Type-II (MSSM like) THDM for $m_A = 140$ GeV and $m_H = 150$ GeV at $\sqrt{s} = 500$ GeV and 500 fb^{-1} [30] (left), and two dimensional invariant mass distributions of tau lepton pairs in $e^+e^- \to HA \to \tau^+\tau^-\tau^+\tau^-$ in Type X (lepton specific) THDM for $m_A = 170$ GeV and $m_H = 130$ GeV for $\sqrt{s} = 500$ GeV and 500 fb^{-1} (right).

states are suppressed for $\tan\beta > 2$.

The study of the signals from HA production was achieved for $bbbb$ and $bb\tau\tau$ event signatures, in the context of the MSSM (Type-II THDM) [29,30]. A rather detailed detector simulation with all the SM backgrounds was performed for $\sqrt{s} = 500$, 800 and 1000 GeV in Ref. [30]. Using a kinematical fit which imposes energy momentum conservation and under the assumed experimental conditions, a statistical accuracy from 0.1 to 1 GeV is found to be achievable on the Higgs boson mass. The topological cross section of $e - +e^- \to HA \to bbbb$ ($e^+e^- \to HA \to \tau\tau bb$) could be determined with a relative precision of 1.5 to 7 % (4 to 30 %). The width of H and A could also be determined with an accuracy of 20 to 40 %, depending on the mass of the Higgs bosons. Figure 46 shows on the left, the result for the $bb\tau\tau$ channel, namely the $\tau^+\tau^-$ invariant mass obtained by the kinematical fit in $e^+e^- \to HA \to b\bar{b}\tau^+\tau^-$ for $m_A = 140$ GeV and $m_H = 150$ GeV at $\sqrt{s} = 500$ GeV and 500 fb^{-1} [30].

The $\tau^+\tau^-\tau^+\tau^-$ and $\mu^+\mu^-\tau^+\tau^-$ final states would be dominant for the type X (lepton specific) THDM. When $\sqrt{s} = 500$ GeV, assuming an integrated luminosity of 500 fb^{-1}, the event number is estimated to be 1.6×10^4 (1.8×10^2) in the type X (type II) THDM for $\tau^+\tau^-\tau^+\tau^-$, and 1.1×10^2 (0.6) for $\mu^+\mu^-\tau^+\tau^-$ assuming $m_H = m_A = m_{H^\pm} = 130$ GeV, $\sin(\beta-\alpha) = 1$ and $\tan\beta = 10$. These numbers do not change much for $\tan\beta \gtrsim 3$. It is important to recognize that the four-momenta of the τ leptons can be solved by a kinematic fit based on the known center of mass energy and momentum, by applying the collinear approximation to each set of τ lepton decay products [31,32]. Figure 46 shows on the right part, the two dimensional invariant mass distribution of the τ lepton pairs from the neutral Higgs boson decays as obtained with a simulation at 500 GeV in which the masses of the neutral Higgs bosons are taken to be 130 GeV and 170 GeV [33].

Although the associated Higgs production process $e^+e^- \to HA$ is a promising one for testing the properties of the extended Higgs sectors, the kinematic reach is restricted by $m_H + m_A < \sqrt{s}$ and not available beyond this limit. Above the threshold of the HA production, associate production of $t\bar{t}\Phi$, $b\overline{\Phi}$ and $\tau^+\tau^-\Phi$ ($\Phi = h, H, A$) could be then used [34]. In particular, for $b\overline{\Phi}$ and $\tau^+\tau^-\Phi$, the mass reach is extended up to almost the collision energy. Their cross sections are proportional to the Yukawa interaction, so that they directly depend on the type of Yukawa coupling in the THDM structure. In MSSM or the Type II THDM (Type I THDM), they are enhanced (suppressed) for large $\tan\beta$ values. In Type X THDM, only the $\tau^+\tau^-H/A$ channels could be significant while only $b\bar{b}H/A$ channels would be important in Type I and Type Y THDMs. They can be used to discriminate the type of the Yukawa interaction.

6.3.3 Charged Higgs boson Productions

The charged Higgs bosons $H^\pm$ are a clear signature for the extended Higgs sectors. They appear in most of the models except for those with additional neutral singlets. One could thus distinguish between Higgs models by measuring the properties of the charged Higgs bosons when/if discovered. In particular, in the MSSM, the mass $m_{H^\pm}$ is related to m_A by $m_{H^\pm} = \sqrt{m_A^2 + m_W^2}$ at the leading order. The precise measurement of the mass is very important in order to distinguish the MSSM from the other models, especially if the SUSY particles are rather heavy.

The direct lower bounds on $m_{H^\pm}$ come from the LEP. The absolute lower bound is obtained as 79.3 GeV by ALEPH, and assuming the type II THDM, the bounds are 87.8 GeV for $\tan\beta \gg 1$ using the decay $\tau\nu$ mode, and 80.4 for relatively low $\tan\beta$ values. Using the characteristic relation in the MSSM, $m_{H^\pm} = \sqrt{m_A^2 + m_W^2}$ with the absolute bounds $m_A > 92$ GeV, $m_{H^\pm} > 122$ GeV is obtained.

It is well known that $m_{H^\pm}$ in the Type II (and Type Y) THDM is stringently constrained by the precision measurements of the radiative decay of $B \to X_s\gamma$ by Belle, BABAR and CLEO. In these types of THDMs the loop contributions of $W^\pm$ and $H^\pm$ are always constructive while this it not the case in the Type I and Type X. Consequently, a stringent lower bound on $m_{H^\pm}$ is obtained in the Type II (and Type Y); i.e., 295 GeV $< m_{H^\pm}$ [35], while $m_{H^\pm} \sim 100$ GeV is not excluded unless

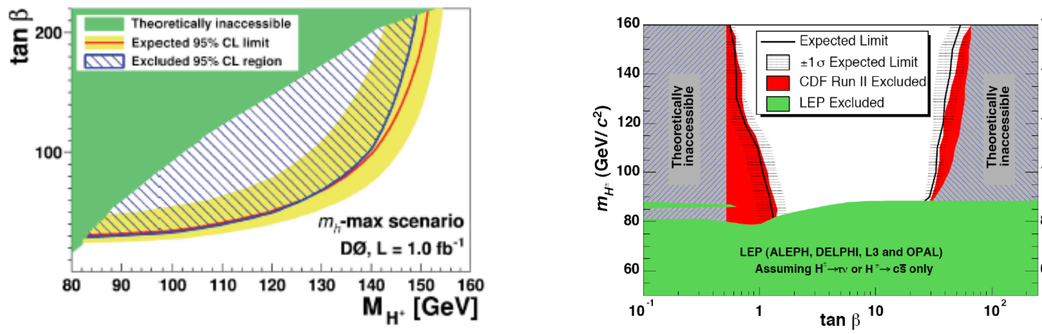

Figure 47: Tevatron results on charged Higgs from D0 experiment with $1fb^{-1}$ data (left) and CDF experiment with $2.2fb^{-1}$ data (right).

$\tan\beta < 2$ in Type Y (Type X). The decay $B \to \tau\nu$ also can be used to constrain the charged Higgs parameters, being sensitive to $\tan\beta^2/m^2_{H^\pm}$ in the Type II THDM. The data already exclude $m_{H^\pm} < 300$ (1100) GeV for $\tan\beta > 40$ (100) at the 95% CL [?]. Similar but milder constraint on $m_{H^\pm}$ comes from tau leptonic decays in the Type II and Type X THDM: $m_{H^\pm} \sim 100$ GeV is excluded for $\tan\beta > 60$ in both models.

The Tevatron and LHC experiments are both looking for a relatively light charged Higgs, namely with a mass lower than the top mass; the top could thus also decay into a charged Higgs plus a b-quark and not only into W boson plus b-quark as expected in the SM.

The charged Higgs has been searched for at the Tevatron both by CDF and D0 in the top pair production by looking for the branching ratio of a possible top decay into Hb where the charged Higgs decays into $c\bar{s}$ or $\tau\nu$ [37,38]. The results of these searches are shown in Fig. 47 in function of $\tan\beta$ and over a charged Higgs mass range between 90 to 160 GeV/c^2. In the case of the charged Higgs decay into a τ lepton, the search is achieved by measuring the branching ratio of the top into a τ lepton and by looking for a τ excess with respect to lepton universality. This measurement is achievable for $\tan\beta > 1$. The search for the decay into $c\bar{s}$ is achieved by looking for a second bump in the two jets mass distribution of the events. This is possible for $\tan\beta < 1$.

The LHC experiments are pursuing this search and look for three possible final signatures of a top pair production if a charged Higgs, namely: lepton + jets (the lepton coming from the τ decay) and jets from the W boson, or a τ + lepton, if both the charged Higgs and the W decay leptonically and a τ + jets if the charged Higgs decays into a τ lepton and the W boson into hadrons. The results obtained

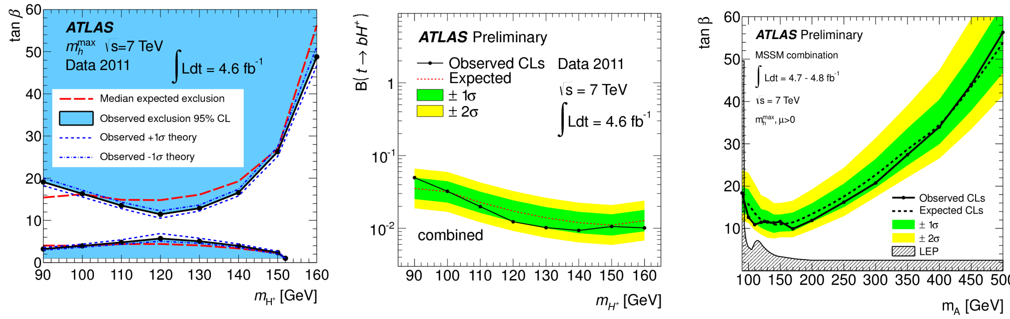

Figure 48: Present charged Higgs searches results by ATLAS at LHC, based on only $4.6 fb^{-1}$ of data collected in 2011.

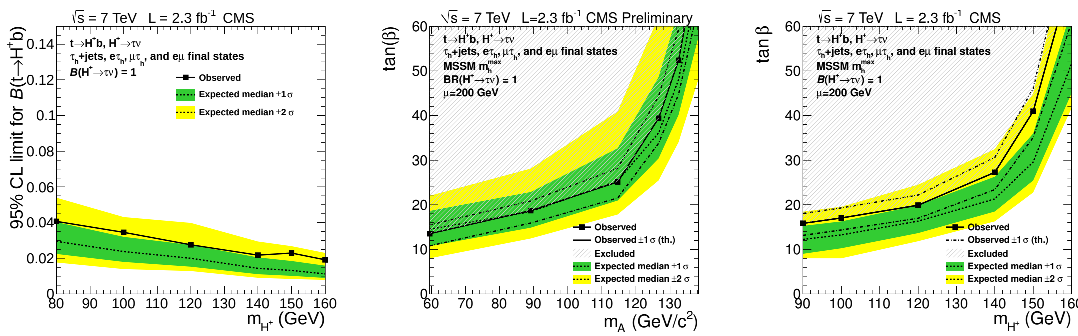

Figure 49: Present charged Higgs searches results by CMS at LHC, based on only $2.3 fb^{-1}$ of data collected in 2011.

by ATLAS based still only on the 2011 collected data [39], are shown in Fig. 48. No significant excess is observed, thus leaving very little room for a light charged Higgs with a mass below the top mass.

Similarly CMS, even with 2011 data corresponding to only to 2.3 fb^{-1} (less than 50%) of the recorded luminosity last year [40], obtains an upper limit on BR($t \to H^+ b$) that excludes a wide region of large $\tan\beta$ in the MSSM parameter space for $M_{H^+}/M_A > M_{\rm top}$ (see Fig. 49).

At the ILC, they are produced in pair in $e^+e^- \to H^+H^-$ [41]. The cross section is a function of only $m_{H^\pm}$ and is independent of the type of Yukawa interaction in the THDM. Therefore, as in the case of the HA production, the study of the final state channels can be used to determine what is the type of Yukawa interaction. When $m_{H^\pm} > m_t + m_b$, the main decay mode is tb in Type I, II and Y, while in Type X the main decay mode is $\tau\nu$ for $\tan\beta > 2$. When $H^\pm$ cannot decay into hb, the main decay mode is $\tau\nu$ except in Type Y for large $\tan\beta$ values. For $m_{H^\pm} < m_t - m_b$, the charged Higgs boson can also be studied via the decay of top quarks $t \to bH^\pm$ in THDMs except in Type X THDM case with $\tan\beta > 2$.

In the MSSM, the detailed simulation study has been performed in $e^+e^- \to H^+H^- \to t\bar{b}\bar{t}b$ for $m_{H^\pm} = 300$ GeV at $\sqrt{s} = 800$ GeV in Ref. [42]. The final states is $4b$-jets with 4 non-b-tagged jets. Assuming the integrated luminosity to be 1 ab^{-1}, a mass resolution of approximately 1.5 % can be achieved (Figure 50 (left)). The decay mode $tbtb$ can also be used to determine $\tan\beta$ especially for relatively small values of $\tan\beta$ (< 5), where the production rate of the signal strongly depends on this parameter.

The pair production is kinematically limited to relatively light charged Higgs bosons with $m_{H^\pm} < \sqrt{s}/2$. When $m_{H^\pm} > \sqrt{s}/2$, single production processes of $H^\pm$ would be used to test $H^\pm$, such as $e^+e^- \to t\bar{b}H^+$, $e^+e^- \to \tau\bar{\nu}H^+$, $e^+e^- \to W^-H^+$, $e^+e^- \to H^+e^-\nu$ and their charge conjugated ones. Cross sections of the first two are directly proportional to Yukawa coupling constants and the rest two are one-loop induced. Apart from the pair production rate, these single production processes strongly depend on the type of Yukawa interaction in the THDM structure. In general, their rates are small and quickly suppressed for larger values of $m_{H^\pm}$. They can be used only for limited parameter regions where $m_H^\pm$ is just above the threshold of the pair production $\sqrt{s}/2$ with very large or low $\tan\beta$ values. In Ref. [43], the simulation study for the process $e^+e^- \to t\bar{b}H^- + b\bar{t}H^+ \to 4b + jj + \ell + p_T^{\rm miss}$ ($\ell = e$, μ) has been done for $m_{H^\pm}$ just above the pair production threshold $m_{H^\pm} \simeq \sqrt{s}/2$. It has been shown that this process provides significant signal of $H^\pm$ only for a relatively small region just above $\sqrt{s}/2$ for very large or very small values of $\tan\beta$ assuming a high b-tagging efficiency: see Figure 50 (right).

6.3.4 *Measurement of* $\tan\beta$

The ILC would be able to precisely determine $\tan\beta$, the most important parameter in the extended Higgs sector with two Higgs doublet fields. In Ref. [44], the sensitivity to $\tan\beta$ has been studied by combining the measurements of production processes, branching ratios and decay widths of heavy Higgs bosons H, A and $H^\pm$ in the context of the MSSM. In the case of $m_A = 200$ GeV with $\sqrt{s} = 500$ GeV and 2 ab^{-1}, the sensitivity is evaluated by using a large variety of complementary methods such as the production rates of $e^+e^- \to HA \to b\bar{b}b\bar{b}$ and $e^+e^- \to H^+H^- \to t\bar{b}\bar{t}b$ which provide a good sensitivity to $\tan\beta$ for relatively low $\tan\beta$ and the rate of $e^+e^- \to b\bar{b}A$, $b\bar{b}H \to b\bar{b}b\bar{b}$ and the measurement of the total widths of H, A and $H^\pm$ which become important for large $\tan\beta$ values. For intermediate $\tan\beta$ values, the sensitivity is rather worse for the scenario (I) where heavy Higgs bosons only decay into the SM particles but it is much better for the scenario (II) where they can decay into super

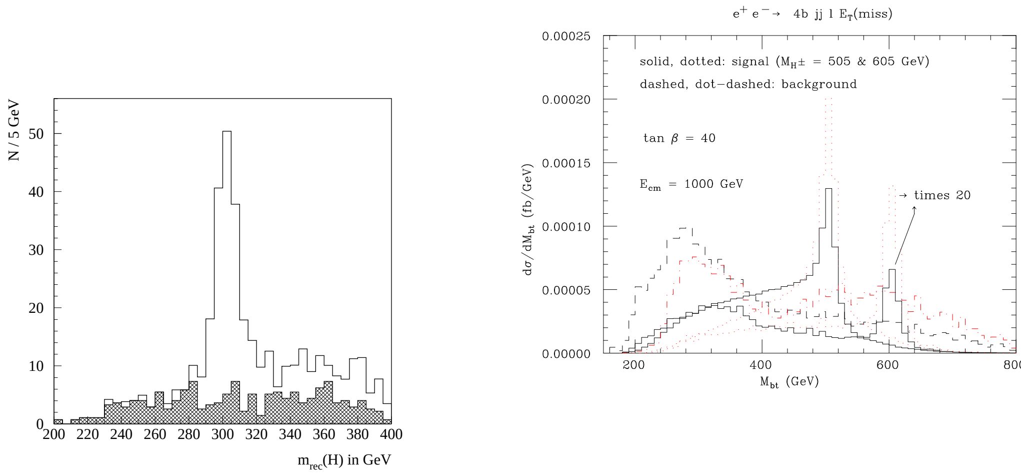

Figure 50: (Left) Fitted charged Higgs boson mass for $H^+H^- \to (t\bar{b})(\bar{t}b)$ with $m_{H^\pm} = 300$ GeV for $\sqrt{s} = 800$ GeV and 1 ab^{-1} in the MSSM. The background is shown by dark histogram [42]. (Right) Differential distribution in the reconstructed Higgs mass from both b-jets not generated in top decays and the two top systems for the signal $e^+e^- \to b\bar{t}H^+ + t\bar{b}H^- \to t\bar{t}b\bar{b}$ and the background $e^+e^- \to t\bar{t}g^* \to t\bar{t}b\bar{b}$ in the MSSM (Type II THDM) [43].

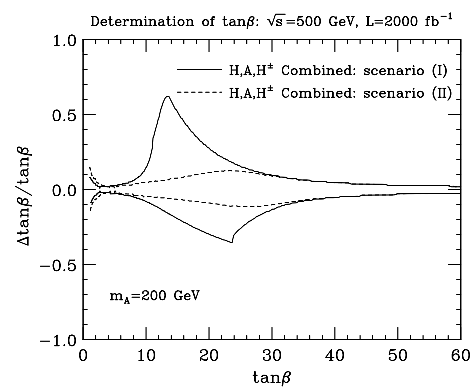

Figure 51: For the MSSM with $m_{H^\pm} \sim m_A = 200$ GeV, and assuming $\mathcal{L} = 2000$ fb^{-1} at $\sqrt{s} = 500$ GeV, the 1σ statistical upper and lower bounds, $\Delta\tan\beta/\tan\beta$, are plotted as a function of $\tan\beta$ [44].

partner particles via $H^\pm \to \tilde{\chi}^\pm\tilde{\chi}^0$ etc. For $3 < \tan\beta < 5$, where the LHC does not have a good sensitivity to $\tan\beta$, the ILC can measure $\tan\beta$ quite accurately. The

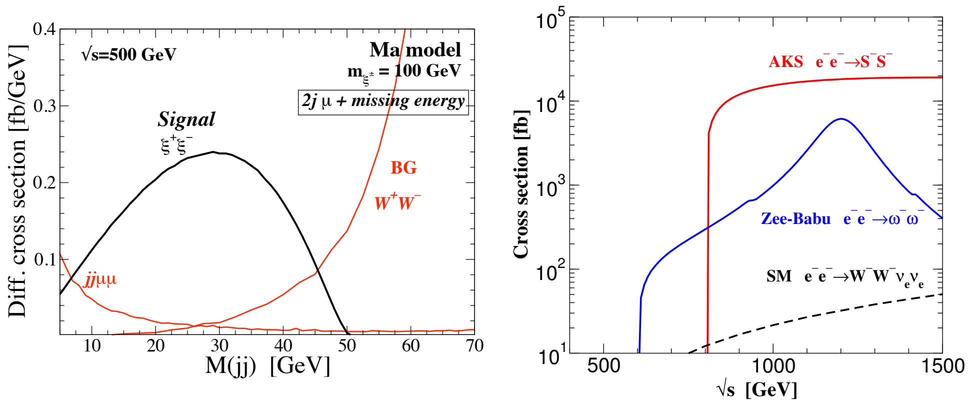

Figure 52: (Left) The jets invariant mass distributions of the production rates of the signal in the Ma model at $\sqrt{s}$ = 500 GeV. The di-jet invariant mass $M(jj)$ distribution of the signal $e^+e^- \to \xi^+\xi^- \to jj\mu\nu\xi_r^0\xi_r^0$ for $m_{\xi^\pm}$ = 100 GeV. (Right) The cross sections of like-sign charged Higgs pair productions in the Zee-Babu model ($\omega^-\omega^-$) and in the AKS model (S^-S^-) are shown as a function of the collision energy $\sqrt{s}$ [45].

combined expected errors on $\tan\beta$ is shown in Figure 51, where some more processes are included. For low $\tan\beta$ regime, a good sensitivity (a few %) to $\Delta\tan\beta/\tan\beta$ can be achieved, while for $10 < \tan\beta < 30$ it would be 10-30 %.

6.4 More possibilities

Various exotic possibilities for the extended Higgs sector are motivated by other challenging problems of particle physics. We have little direct insight from experiment into the mechanisms that lead to neutrino masses, baryogenesis, and dark matter. The answers to each of these questions might arise in an extended Higgs boson sector. Models that address these questions have striking implications for extended Higgs processes that might be observed at the ILC.

We have already pointed out that neutrino masses might be associated with the addition to the Standard Model of a triplet Higgs boson multiplet. These models, described in Section 6.2.3, lead to novel reactions at the ILC, including H^{++} pair

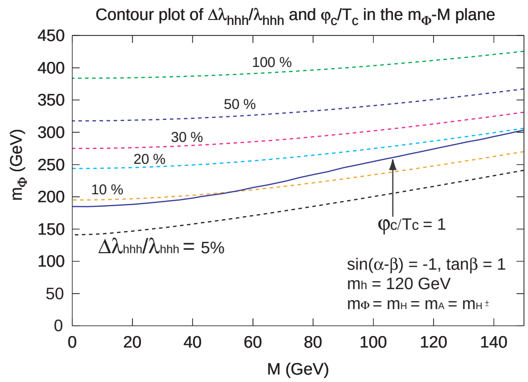

Figure 53: The region of strong first order phase transition ($\varphi_c/T_c > 1$) required for successful electroweak baryogenesis and the countour plot of the deviation in the triple Higgs boson coupling from the SM prediction [49], where m_Φ represents degenerated mass of H, A and $H^\pm$ and M is defined in Eq. (89).

production to modes that are very difficult to discover at the LHC. For example, for $m_{H^{++}} > m_{H^+} > m_{A,H}$ with the mass difference of $O(10)$ GeV and $v_\Delta \sim 10^{-5}$-10^{-3} GeV, the main decay modes are $H^{\pm\pm} \to H^\pm W^\pm$, $H^\pm \to W^+ H$ and $W^\pm A$, and $H, A \to \nu\,\overline{\nu}$ [19]. In this case, it is challenging to measure the signal at the LHC [20], but the ILC may be able to study it via $e^+e^- \to H^{++}H^{--} \to \ell^+\ell^+ jjjj\nu\nu\nu\nu$ if the background is reduced sufficiently. The cross section of $H^{++}H^{--}$ is about 100 fb for $m_{H^{\pm\pm}} = 200$ GeV, which implies that of the final state with a same sign dilepton signature with jets and missing energies can be around 10 fb including the charge conjugation final state.

Alternative scenario for neutrino masses, which are directly relevant to the TeV scale physics, is based on radiative generation of neutrino masses by the extension of the Higgs sector [46,47,48]. The source of lepton number violation in these models is a coupling in the extended Higgs sector or Majorana masses of Z_2-odd right-handed neutrinos. The ILC can test these models by measuring characteristic extra scalars. For example, in the Ma model [47] where neutrino masses are generated at the one-loop level by the Z_2 odd scalars and right handed neutrinos, the Z_2 odd scalar doublets $(\xi^+, \xi^0)^T$ would be tested at the ILC via the distribution of jets such as $e^+e^- \to \xi^+\xi^- \to jj\mu\nu\xi^0_r\xi^0_r$: see Figure 52(left). A striking test of these models would be the observation of double like-sign Higgs production in e^-e^- collisions. The cross sections for this process in the Zee-Babu model [46] and the Aoki-Kanemura-Seto model [48] are shown in Fig. 52(right).

Among the various scenarios for baryogenesis, the electroweak baryogenesis [50] is attractive because of its testability at the collider experiment. In the SM this

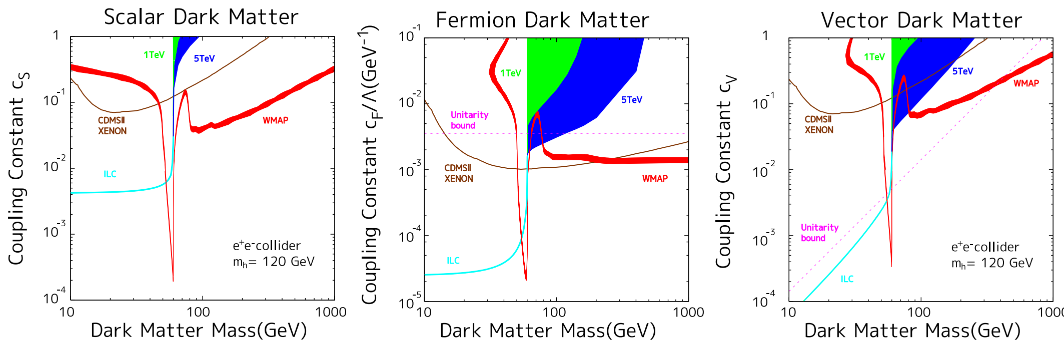

Figure 54: Sensitivities to detect the dark matter signal at the ILC and CLIC. The areas of $N_S/\sqrt{N_S + N_B} > 5$ at the e^+e^- collider for $\sqrt{s} = 1$ TeV (green) and 5 TeV (blue) with 1 ab^{-1} data are shown with assuming $m_h = 120$ GeV. Constraints on direct detection experiments and the tree level unitarity for dark matter are also shown.

scenario is already excluded by the data. The simplest viable model would be the THDM [51], which provides additional CP violating phases and sufficiently strong 1st order electroweak phase transition compatible with the 126 GeV SM-like Higgs boson by the loop effect of extra Higgs bosons. One of the interesting phenomenological predictions for such a scenario is a large quantum effect on the triple Higgs boson coupling [52,49]. The requirement of sufficiently strong 1st order phase transition results in a large deviation in the triple Higgs boson coupling as seen in Figure 53. The measurement of the triple Higgs coupling hhh is challenging at the LHC especially for $m_h \simeq 125$ GeV, and its measurement would be possible at the ILC with a substantial accuracy. The scenario of electroweak baryogenesis would be testable by measuring the triple Higgs boson coupling at the ILC.

Dark matter requires a new stable particle with mass at the weak interaction scale. Though models involving supersymmetry and extra dimensions are more fashionable, there is no reason why this particle cannot come from an extended Higgs sector. The dark matter particle can be made stable by a Z_2 or higher discrete symmetry of this sector. Models realizing this scenario are given in [53,54,55]. An important phenomenological prediction of these scenarios is the invisible decay $h \to DD$ of the SM like Higgs boson in to a dark matter pair, if this decay is kinematically allowed. At the linear collider, these invisible decays can be well measured via $e^+e^- \to Zh \to \mu^+\mu^- DD$ by measuring the recoiled muon pair. The case $m_h < 2m_D$, where the above decay mode is not open, can be studied in the ZZ fusion process. Nabeshima has analyzed the LHC and linear collider prospects for the study of this reaction as shown in Fig. 54. The dark matter consistent with the WMAP data would be tested at the ILC [56].

6.5 Summary

The Higgs sector is the window for new physics beyond the Standard Model. There is no reason to restrict this sector to the SM Higgs. There are several important theoretical frameworks that predict an enriched Higgs sector. These extended Higgs sectors possibilities are very important to explore not only for clarifying the nature of the electroweak symmetry breaking but also for investigating the beyond Standard Model Physics. The ILC will have in this respect also an important role to play for the following reasons:

1. Discovery potential: The LHC experiments have a strong potential for discovery if an extended Higgs sector; they will be able to cover a wide region in the parameter space including the possibility to reach relatively very high mass range. But the ILC will be able to scan specific important cases in a rather unique way, as long as kinematically accessible, such for instance the charged Higgs sector that are directly pair produced at this machine, or angular parameter space that are much more difficult to reach at LHC, as for instance if MSSM, and intermediate $\tan\beta$ region around 5 to 10.

2. Precision measurements: Even if LHC discovers new Higgs bosons, the ILC can play an important and complementary role. Indeed some fundamental parameters such as couplings could be measured with an increased precision at ILC such as for instance the triple gauge coupling related to a relatively low mass (125GeV) Higgs. Also some decays will be better measured at the ILC as compared to LHC, even if one may take into account that by the time the ILC will be running the precision reached by the upgraded LHC experiments will be quite impressive. Mixing angles such as $\tan\beta$ could be also very well measured at ILC. These high precision measurements will complement those performed by the LHC and will be instrumental to fully reconstruct and thus understand the Higgs sector.

3. Discriminating between several proposed Theoretical frameworks: Having two different machines, i.e. an hadron and a lepton collider allow addressing in different and complementary ways, tricky Physics scenarios as those proposed by the BSM Higgs sector. This will be essential for progressing and thus disentangling between different Physics hypotheses that give for instance similar event signatures.

The Higgs extended sector is a key-topic for exploring BSM. In order to advance in this unknown field and try to disentangle among the many present theoretical proposed frameworks, it is essential to have two complementary machines for comparing and combining their results. ILC is essential to LHC and vice and versa.

References

[1] A. Djouadi, Phys. Rept. **457**, 1 (2008) [hep-ph/0503172].

[2] A. Djouadi, Phys. Rept. **459**, 1 (2008) [hep-ph/0503173].

[3] G. C. Branco, P. M. Ferreira, L. Lavoura, M. N. Rebelo, M. Sher and J. P. Silva, Phys. Rept. **516**, 1 (2012) [arXiv:1106.0034 [hep-ph]].

[4] J. F. Gunion and H. E. Haber, Phys. Rev. D **67**, 075019 (2003) [hep-ph/0207010].

[5] V. D. Barger, J. L. Hewett and R. J. N. Phillips, Phys. Rev. D **41**, 3421 (1990).

[6] M. Aoki, S. Kanemura, K. Tsumura and K. Yagyu, Phys. Rev. D **80**, 015017 (2009) [arXiv:0902.4665 [hep-ph]].

[7] S. Su and B. Thomas, Phys. Rev. D **79**, 095014 (2009) [arXiv:0903.0667 [hep-ph]]; H. E. Logan and D. MacLennan, Phys. Rev. D **79**, 115022 (2009) [arXiv:0903.2246 [hep-ph]].

[8] R. Schabinger and J. D. Wells, Phys. Rev. D **72**, 093007 (2005) [hep-ph/0509209].

[9] S. Khalil, J. Phys. G G **35**, 055001 (2008) [hep-ph/0611205].

[10] U. Ellwanger, C. Hugonie and A. M. Teixeira, Phys. Rept. **496**, 1 (2010) [arXiv:0910.1785 [hep-ph]].

[11] T. Abe *et al.* [ILD Concept Group - Linear Collider Collaboration], arXiv:1006.3396 [hep-ex].

[12] R. Barate *et al.* [LEP Working Group for Higgs boson searches and ALEPH and DELPHI and L3 and OPAL Collaborations], Phys. Lett. B **565**, 61 (2003) [hep-ex/0306033].

[13] The ATLAS Collaboration, ATLAS-CONF-2012-093.

[14] The CMS Collaboration, CMS PAS HIG-12-020.

[15] L. Basso, S. Moretti and G. M. Pruna, Eur. Phys. J. C **71**, 1724 (2011) [arXiv:1012.0167 [hep-ph]].

[16] Specific exceptions are know; these are reviewed in I. Low and J. Lykken, JHEP **1010**, 053 (2010) [arXiv:1005.0872 [hep-ph]].

[17] R. N. Mohapatra and G. Senjanovic, Phys. Rev. D **23**. 165 (1981).

[18] G. Aad et. al, [ATLAS Collaboration], Phys. Rev. D **85**, 032004 (2012); CMS Collaboration, *Report Number* CMS-PAS-HIG-12-005.

[19] P. Fileviez Perez, T. Han, G. -y. Huang, T. Li and K. Wang, Phys. Rev. D **78**, 015018 (2008) [arXiv:0805.3536 [hep-ph]].

[20] M. Aoki, S. Kanemura and K. Yagyu, Phys. Rev. D **85**, 055007 (2012) [arXiv:1110.4625 [hep-ph]].

[21] The ATLAS Collaboration, CERN-PH-EP-2012-218, hep-ex/1207-7214v1, submitted to Phys. Lett. B, July 31,2012.

[22] The CMS Collaboration, CERN-PH-EP-2012-220, hep-ex/1207-7235, submitted to Phys. Lett. B, July 31,2012.

[23] M. Peskin, Invited Talk at the "Higgs Hunting" Workshop, July 18-20, 2012, Orsay (France), http://higgshunting.fr/

[24] The ATLAS Collaboration, ATLAS-CONF-2012-094, July 9, 2012.

[25] The CMS Collaboration, Phys.Lett B **713** 2012, 68-90; CERN-PH-EP-2012-034; HEP-EX 1202.4083.

[26] J. Incandela, on behalf of the CMS collaboration, Talk on: " Status of the CMS SM Higgs Search" given at CERN, July 4, 2012.

[27] The CMS Collaboration, CERN-PH-EP-2012-176; HEP-EX 1206.6326.

[28] J. F. Gunion, et al., Phys. Rev. D **38**, 3444 (1988); A. Djouadi, J. Kalinowski and P. M. Zerwas, Z. Phys. C **57**, 569 (1993).

[29] J. A. Aguilar-Saavedra *et al.* [ECFA/DESY LC Physics Working Group Collaboration], hep-ph/0106315.

[30] K. Desch, T. Klimkovich, T. Kuhl and A. Raspereza, hep-ph/0406229.

[31] S. Schael *et al.* [LEP Working Group for Higgs boson searches and ALEPH and DELPHI and L3 and OPAL Collaborations], Eur. Phys. J. C **47**, 547 (2006).

[32] J. Abdallah *et al.* [DELPHI Collaboration], Phys. Lett. B **552**, 127 (2003).

[33] K. Tsumura, Talk at KILC 12.

[34] A. Djouadi, K. Kalinowski, P. M. Zerwas, Modern Phys. Lett. A 7, 1765 (1992); A. Djouadi, K. Kalinowski, P. M. Zerwas, Z. Phys. C **54**, 255 (1992).

[35] M. Misiak, H. M. Asatrian, K. Bieri, M. Czakon, A. Czarnecki, T. Ewerth, A. Ferroglia and P. Gambino *et al.*, Phys. Rev. Lett. **98**, 022002 (2007) [hep-ph/0609232].

[36] M. Rozanska, PoS CHARGED **2010**, 005 (2010).

[37] The CDF Collaboration, Phys. Rev. Lett. **96**, 042003 (2006).

[38] The D0 Collaboration, HEP-EX 0908.1811v2 (2009).

[39] The ATLAS Collaboration, JHEP **039**, 2012, 1206; CERN-PH-EP-2012-083; HEP-EX 1204, 2761v1

[40] The CMS Collaboration, JHEP **07**, 2012, 143; CERN-PH-EP-2012-123; HEP-EX 1205.5736.

[41] S. Komamiya, Phys. Rev. D **38**, 2158 (1988).

[42] M. Battaglia, A. Ferrari, A. Kiiskinen and T. Maki, eConf C **010630**, E3017 (2001) [hep-ex/0112015].

[43] S. Moretti, Eur. Phys. J. C **34**, 157 (2004) [hep-ph/0306297].

[44] J. F. Gunion, T. Han, J. Jiang and A. Sopczak, Phys. Lett. B **565**, 42 (2003) [hep-ph/0212151].

[45] M. Aoki and S. Kanemura, arXiv:1007.0706 [hep-ph].

[46] A. Zee, Nucl. Phys. B **264**, 99 (1986); K. S. Babu, Phys. Lett. B **203**, 132 (1988).

[47] E. Ma, Phys. Rev. D **73**, 077301 (2006).

[48] M. Aoki, S. Kanemura and O. Seto, Phys. Rev. Lett. **102**, 051805 (2009) [arXiv:0807.0361 [hep-ph]].

[49] S. Kanemura, Y. Okada and E. Senaha, Phys. Lett. B **606** (2005) 361.

[50] V. A. Kuzmin, V. A. Rubakov, M. E. Shaposhnikov, Phys. Lett. **B155** (1985) 36.

[51] L. Fromme, S. J. Huber and M. Seniuch, JHEP **0611** (2006) 038; A. Kozhushko, V. Skalozub, Ukr. J. Phys. **56** (2011) 431-442.

[52] C. Grojean, G. Servant and J. D. Wells, Phys. Rev. D **71**, 036001 (2005) [hep-ph/0407019].

[53] J. McDonald, Phys. Rev. D **50**, 3637 (1994); C. P. Burgess, M. Pospelov and T. ter Veldhuis, Nucl. Phys. B **619**, 709 (2001).

[54] For a review, see the following and the references therein: G. Jungman, M. Kamionkowski and K. Griest, Phys. Rept. **267**, 195 (1996); G. Bertone, D. Hooper and J. Silk, Phys. Rept. **405**, 279 (2005).

[55] For a revew, see: M. Perelstein, Prog. Part. Nucl. Phys. **58**, 247 (2007).

[56] T. Nabeshima, Talk at LCWS2011, arXiv:1202.2673 [hep-ph].

7 SUSY

7.1 Introduction

While no direct evidence for the existence of non-Standard Model particles has emerged so far, there are many indications that the Standard Model (SM) is not valid up to the Planck scale. Among these, the most well-known is the gauge hierarchy problem, the instability of the weak scale against quantum corrections to fundamental scalar fields. Solutions to this problem require new particles to appear at or around the weak scale. Additional problems arise from cosmology. The SM does not contain any candidate particles to constitute the needed cold dark matter (CDM). It also lacks a sufficient source of CP violation needed to explain baryogenesis. The SM is not sufficient as a part of a complete theory of nature at very small distance scales because the SM gauge couplings do not unify when extrapolated to high energies, and because the SM has no clear way to incorporate quantum gravity.

One approach which has the potential to address all these problems is Supersymmetry (SUSY), a quantum spacetime symmetry which predicts a correspondence between bosonic and fermionic fields [1,2,3,4]. SUSY removes the quadratic divergences of scalar field theory and thus offers a solution to the aforementioned gauge hierarchy problem. This allows for stable extrapolation of the Standard Model couplings into the far ultraviolet ($E \gg M_{weak}$) regime [5,6], with the suggestion of gauge unification. SUSY provides an avenue for connecting the Standard Model to ideas of grand unification (GUTs) and/or string theory, and provides a route to unification with gravity via local SUSY, or supergravity theories [7,8,9]. SUSY theories offer several candidates [10] for dark matter, including the neutralino, the gravitino or a singlet sneutrino. In SUSY theories where the strong CP problem is solved via the Peccei-Quinn mechanism, there is the added possibility of mixed axion-neutralino [11,12,13], axion-axino [14,15,16] or axion-gravitino cold dark matter. In order to explain the measured baryon to photon ratio $\eta \sim 10^{-10}$, SUSY offers at least three prominent possibilities including electroweak baryogenesis (now nearly excluded in the minimal theory by limits on $m_{\tilde{t}_1}$ and a light Higgs scalar with $m_h \sim 125$ GeV [17]), thermal and non-thermal leptogenesis [18], and Affleck-Dine baryo- or leptogenesis [19,20].

There is good reason, then, to adopt SUSY as a well-motivated example of an extension of the Standard Model in order to discuss the potential of the ILC to solve the current puzzles of electroweak symmetry breaking, cosmology and grand unification. In this section, we will describe the capabilities offered by the ILC for the discovery of supersymmetric particles and the precision measurement of their properties. It should be stressed that the experimental capabilities of the ILC presented here apply to new particles with similar signatures whatever the nature of the high scale model.

7.2 Setting the Scene

The simplest supersymmetric theory which contains the SM is known as the Minimal Supersymmetric Standard Model, or MSSM. To construct the MSSM, one adopts the gauge symmetry of the SM and promotes all SM fields to superfields. There is a unique generalization of the SM if one imposes the requirements of gauge symmetry, renormalizability, and R-parity conservation. This model requires two Higgs doublet superfields, and thus includes an extended Higgs sector as described in Section 6 as well as corresponding higgsino particles. To be phenomenologically viable, supersymmetry must be broken. SUSY breaking is implemented explicitly in the MSSM by adding all allowed *soft* SUSY breaking terms. The resulting model contains 124 parameters, many of which lead to flavor violation (FV) or CP violation (CPV). The pMSSM ignores the FV and CPV terms, and then contains just 19 or 24 weak scale parameters, depending on whether one does or does not assume universality between the masses of the first and second generation scalar superpartners [21,22].

Because of the large number of parameters in the general MSSM, the phenomenology of SUSY has often been discussed in terms of a subspace of the more general theory with a reduced parameter set. For many years, the phenomenology of SUSY was described using the parameter space of a set of models called "minimal supergravity" [23], also known as mSUGRA or the cMSSM. These models assumed that the soft supersymmetry breaking parameters unified at the GUT scale, so that the model could be described by four parameters, a weak scale gravitino mass $m_{3/2}$ and universal scalar masses m_0, gaugino masses $m_{1/2}$ and trilinear terms A_0 at the GUT scale. Other similarly specific choices are given by the minimal gauge mediated SUSY breaking model [24] and the minimal anomaly-mediated SUSY breaking model [25,26]. In all of these schemes, the unification assumption ties together the mass scales of the supersymmetric partners of quarks, gluons, gauge bosons, and Higgs bosons.

In fact, it was realized a long time ago that the constraints linking these scales are not necessary and might not yield the most attractive models. In 1996, Cohen, Kaplan, and Nelson discussed the "more minimal supersymmetric Standard Model" in which only the partners of the third generation particles are light [27]. Over the years, other authors have discussed models in which some or all of the squarks are very heavy with respect to the electroweak scale without disturbing the naturalness of electroweak symmetry breaking [28,29,30].

Now the first data from the LHC have weighed in on this issue. Searches at ATLAS and CMS have excluded minimal supergravity or the cMSSM for all models in which the squark and gluino masses are below 1 TeV [31,32]. These powerful exclusions have, to our knowledge, not caused any theorists to abandon SUSY. However, they have led to a dramatic change in thinking about the parameter space of the MSSM.

Specifically, these exclusions have led theorists to rethink the expectations for the masses of supersymmetric particles that come from the idea that supersymmetry should naturally produce the scale of electroweak symmetry breaking. It is easy to arrange in a supersymmetric model that the Higgs bosons have a potential with a symmetry-breaking minimum. The condition for minimizing this potential can be written

$$\frac{1}{2}m_Z^2 = \frac{(m_{H_d}^2 + \Sigma_d) - (m_{H_u}^2 + \Sigma_u)\tan^2\beta}{(\tan^2\beta - 1)} - \mu^2 \ . \tag{99}$$

where, Σ_u and Σ_d arise from radiative corrections [33]. The largest contribution to Σ_u comes from the mass of the top squarks $\tilde{t}_i$, $i = 1, 2$,

$$\Sigma_u(\tilde{t}_i) \sim -\frac{3y_t^2}{16\pi^2} \times m_{\tilde{t}_i}^2 \left(\ln(m_{\tilde{t}_i^2}/v^2) - 1\right), \tag{100}$$

where y_t is the top quark Yukawa coupling and v is the Higgs vacuum expectation value. The negative sign of this radiative correction is typically the force that drives the Higgs mass term negative.

The MSSM is said to generate the electroweak scale "naturally" if the terms in (99) are all of roughly the same size, without large cancellations between the two terms on the right-hand side. By this criterion, the primary implication of the naturalness of the electroweak scale is that the parameter μ, the higgsino mass parameter, should be of the order of 100 GeV [34,35]. Other supersymmetric partners are required to be light only to the extent that they contribute to the parameters of (99) through radiative corrections. The particles primarily constrained by this criterion are the higgsinos themselves, the top squarks, which enter through (100), and the gluino, whose mass enters the radiative corrections to the top squark masses.

Imposing this criterion strictly leads to a very different spectrum from that of the cMSSM. In the cMSSM, μ is an output parameter and the values typically output are larger than the squark and gluino masses. Direct argumentation from (99), on the other hand, leads to a spectrum in which $|\mu| \sim 100 - 200$ GeV, so that the lightest neutralino is likely higgsino-like. The third generation squarks should have masses that are relatively small, though these masses might be as high as $\lesssim 1 - 1.5$ TeV [36]. The gluino could be heavier, up to a few TeV [37]. The superpartners of electroweak gauge bosons would be found at masses of 1-2 TeV, while the first and second generation scalar partners could be much heavier, possibly in the multi-TeV regime. This last condition is actually beneficial, giving at least a partial solution to the SUSY flavor, CP, proton decay, and gravitino problems. This region of the MSSM parameter space has been dubbed "natural SUSY" [38]. The extreme limit of this schema, in which only the higgsinos are light, has been studied in [39,40]. A more general exploration of the parameter space of natural SUSY can be found in [41].

The push from the LHC results toward natural SUSY has motivated many theorists to find model-building explanations for this choice of SUSY parameters. Some interesting proposals can be found in [42,43,44,45]. Not only have the LHC results on SUSY not damped theorists' enthusiasm, but they have pushed theorists increasingly toward models with higgsino-like charginos and neutralinos with masses below 250 GeV that are ideal targets for the ILC experiments.

7.3 Direct and Indirect Experimental Constraints

7.3.1 Particle Sectors of a Supersymmetric Model

In this section, we present the current direct and indirect experimental constraints on SUSY models. We have emphasized in the previous section that a SUSY model consistent with the experimental constraints from the LHC probably does not belong to the subspace of artificially unified models such as the cMSSM. We find it most useful to analyze an MSSM model in terms of distinct particle sectors with different properties and influence. At generic points in the MSSM parameter space, these sectors can have masses very different from one another. It is important to keep track of which experimental constraints apply to which sector.

The new particle sectors of an MSSM model are:

1. The first and second generation squarks.
2. The first and second generation sleptons.
3. The third generation squarks and sleptons.
4. The gauginos.
5. The higgsinos.

We have already described the constraints on the masses of these particles from the theoretical consideration of naturalness. We now review the constraints from experiment.

7.3.2 Indirect Constraints on SUSY Models

The magnetic moment of the muon $a_\mu \equiv \frac{(g-2)_\mu}{2}$ was measured by the Muon $g-2$ Collaboration [46] and has been found to give a 3.6σ discrepancy with SM calculations based on e^+e^- data [47]: $\Delta a_\mu = a_\mu^{meas} - a_\mu^{SM}[e^+e^-] = (28.7 \pm 8.0) \times 10^{-10}$.

When τ-decay data are used to estimate the hadronic vacuum polarization contribution rather than low energy e^+e^- annihilation data, the discrepancy reduces to 2.4σ, corresponding to $\Delta a_\mu = a_\mu^{meas} - a_\mu^{SM}[\tau] = (19.5 \pm 8.3) \times 10^{-10}$. The SUSY contribution to the muon magnetic moment is [48]

$$\Delta a_\mu^{SUSY} \sim \frac{m_\mu^2 \mu M_i \tan\beta}{m_{SUSY}^4} \ , \qquad (101)$$

where $i = 1, 2$ labels the electroweak gaugino masses and m_{SUSY} is the characteristic sparticle mass circulating in the muon-muon-photon vertex correction, one of: $m_{\tilde{\mu}_{L,R}}$, $m_{\tilde{\nu}_\mu}$, $m_{\tilde{\chi}_i^+}$ and $m_{\tilde{\chi}_j^0}$. Attempts to explain the muon $g-2$ anomaly using supersymmetry usually invoke sparticle mass spectra with relatively light smuons and/or large $\tan\beta$ (see *e.g.* Ref. [49]). Some SUSY models where $m_{\tilde{\mu}_{L,R}}$ is correlated with squark masses (such as mSUGRA) are now highly stressed to explain the $(g-2)_\mu$ anomaly. In addition, since naturalness favors a low value of $|\mu|$, tension again arises between a large contribution to Δa_μ^{SUSY} and naturalness conditions. These tensions motivate scenarios with non-universal scalar masses [50].

The combination of several measurements of the $b \to s\gamma$ branching fraction finds that $BF(b \to s\gamma) = (3.55 \pm 0.26) \times 10^{-4}$ [51]. This is somewhat higher than the SM prediction [52] of $BF^{SM}(b \to s\gamma) = (3.15 \pm 0.23) \times 10^{-4}$. SUSY contributions to the $b \to s\gamma$ decay rate come mainly from chargino-top squark loops and loops containing charged Higgs bosons. They are large when these particles are light and when $\tan\beta$ is large [53].

The decay $B_s \to \mu^+\mu^-$ occurs in the SM at a calculated branching ratio value of $(3.2 \pm 0.2) \times 10^{-9}$. The CMS experiment [54] has provided an upper limit on this branching fraction of $BF(B_s \to \mu^+\mu^-) < 1.9 \times 10^{-8}$ at 95% CL. The CDF experiment [55] claims a signal in this channel at $BF(B_s \to \mu^+\mu^-) = (1.8 \pm 1.0) \times 10^{-8}$ at 95% CL, which is in some discord with the CMS result. Finally, the LHCb experiment has reported a strong new bound of $BF(B_s \to \mu^+\mu^-) < 4.5 \times 10^{-9}$ [56]. In supersymmetric models, this flavor-changing decay occurs through exchange of the pseudoscalar Higgs A [57,58]. The contribution to the branching fraction from SUSY is proportional to $\tan^6\beta / m_A^4$.

The branching fraction for $B_u \to \tau^+\nu_\tau$ decay is calculated [59] in the SM to be $BF(B_u \to \tau^+\nu_\tau) = (1.10 \pm 0.29) \times 10^{-4}$. This is to be compared to the value from the Heavy Flavor Averaging group [60], which finds a measured value of $BF(B_u \to \tau^+\nu_\tau) = (1.41 \pm 0.43) \times 10^{-4}$, in agreement with the SM prediction, but leaving room for additional contributions. The main contribution from SUSY comes from tree-level charged Higgs exchange, and is large at large $\tan\beta$ and low m_{H^+}.

Finally, measurements of the cold dark matter (CDM) abundance in the universe find $\Omega_{CDM} h^2 \sim 0.11$, where Ω_{CDM} is the dark matter relic density scaled in terms of the critical density. Simple explanations for the CDM abundance in terms of thermally produced neutralino LSPs are now highly stressed by LHC SUSY searches, and are even further constrained if the light SUSY Higgs h turns out to have mass ~ 125 GeV [61]. A higgsino LSP is not a good dark matter candidate, since it has too large an annihilation rate to vector boson pairs, leading to too small a thermal relic density. However, this deficit can be repaired in well-motivated extensions of the MSSM, including mixed axion-LSP dark matter and models with late decaying moduli fields. For purposes of considering ILC or LHC physics, it seems prudent not to take dark matter abundance constraints on SUSY theories too seriously at this point in time.

7.3.3 *Impact of Higgs Searches*

The ATLAS and CMS experiments have reported the discovery of a narrow resonance with mass near 125 GeV [62,63]. At the same time, they exclude a Standard Model-like Higgs boson in the mass ranges $110 - 123$ and $130 - 558$ GeV at 95% CL. The discovery is based on an excess of events mainly in the $\gamma\gamma$, $ZZ^* \to 4\ell$ and WW^* decay channels. These excesses are also corroborated by recent reports from CDF and D0 at the Fermilab Tevatron of excess events in the $Wb\bar{b}$ and other channels over the mass range 115-130 GeV [64].

Searches by ATLAS and CMS for $H,\ A \to \tau^+\tau^-$ now exclude a large portion of the m_A *vs.* $\tan\beta$ plane [65,66]. In particular, the region around $\tan\beta \sim 50$, which is favored by Yukawa-unified SUSY GUT theories, now excludes $m_A < 500$ GeV. For $\tan\beta = 10$, only the range 120 GeV $< m_A <$ 220 GeV is excluded. ATLAS excludes charged Higgs bosons produced in association with a $t\bar{t}$ pair for $m_{H^\pm} < 150$ GeV for $\tan\beta \sim 20$ [67].

A Higgs mass of $m_h = 125 \pm 3$ GeV lies within the narrow mass range $m_h \sim 115 - 135$ GeV which is allowed between LEP searches for a SM-like Higgs boson and calculations of an upper limit to m_h within the MSSM. However, such a large value of m_h requires large radiative corrections and large mixing in the top squark sector. In models such as mSUGRA, trilinear soft parameters $A_0 \sim \pm 2m_0$ are thus preferred, and values of $A_0 \sim 0$ would be ruled out [68,69,70]. In other constrained models such as the minimal versions of GMSB or AMSB, Higgs masses of 125 GeV require even the lightest of sparticles to be in the multi-TeV range [61], leading to enormous electroweak fine-tuning. In the mSUGRA/cMSSM model, requiring a Higgs mass of about 125 GeV pushes the best fit point in m_0 and $m_{1/2}$ space into the multi-TeV range [68] and makes global fits of the model to data increasingly difficult [71]. This already motivates us to consider the prospects for precision measurements of new particles at the ILC in a more general context than the cMSSM.

7.3.4 *Direct Searches for Supersymmetric Particles*

The most model-independent limits on SUSY particles, especially the uncoloured ones, have been set by the LEP experiments [72,73,74,75,76] on *sleptons, charginos and neutralinos.* The fact that these limits have not been superseded in the general case by LHC data illustrates the complementarity of e^+e^- and pp colliders as well as the fact that the interpretation of e^+e^- data requires significantly fewer model assumptions.

The ATLAS and CMS collaborations have searched for multi-jet+$E_T^{\rm miss}$ events arising from gluino and squark pair production in 4.4 fb^{-1} of 2011 data taken at $\sqrt{s} = 7$ TeV [77,79] and in up to 5.8 fb^{-1} of 2012 data taken at $\sqrt{s} = 8$ TeV [78]. In the limit of very heavy squark masses, they exclude $m_{\tilde g} \stackrel{<}{\sim} 1.1$ TeV, while for $m_{\tilde q} \simeq m_{\tilde g}$ then $m_{\tilde g} \stackrel{<}{\sim} 1.5$ TeV is excluded, assuming $m_{tz_1} = 0$ GeV in both cases. $m_{\tilde q}$ refers to a generic first generation squark mass scale, since these are the ones whose production rates depend strongly on valence quark PDFs in the proton.

A recent ATLAS search for direct bottom squark pair production followed by $\tilde b_1 \to b\tilde\chi_1^0$ decay ($pp \to \tilde b_1 \bar{\tilde b}_1 \to b\bar b + E_T^{\rm miss}$) based on 2 fb^{-1} of data at $\sqrt{s} = 7$ TeV now excludes $m_{\tilde b_1} \stackrel{<}{\sim} 350$ GeV for $m_{\tilde\chi_1^0}$ as high as 120 GeV. For larger values of $m_{\tilde\chi_1^0}$, there is no limit at present [80]. These constraints also apply to top squark pair production where $\tilde t_1 \to b\tilde\chi^+$ decay and the $\tilde\chi^+$ decays to soft, nearly invisible particles, as would be expected in natural SUSY.

In models with gaugino mass unification and heavy squarks (such as mSUGRA with large m_0), electroweak gaugino pair production $pp \to \tilde\chi_1^\pm \tilde\chi_2^0$ is the dominant SUSY particle production cross section at LHC7 for $m_{\tilde g} > 0.5$ TeV [81]. Two searches by ATLAS in the 3 lepton final state using 2.1 fb^{-1} of 7 TeV data [82] and in the 2 lepton final state using 4.7 fb^{-1} of 8 TeV data [83] give results in the pMSSM and in a simplified model. Both cases assume that chargino and neutralino decay to intermediate sleptons, which enhances the leptonic branching fractions. The theoretically more interesting case of chargino and neutralino three-body decay through W^* and Z^* leading to a clean trilepton signature [84,85] awaits further data and analysis.

The opposite-sign/same flavor dilepton final state [83] can also originate from direct production of slepton pairs. The resulting exclusion in the slepton-LSP mass plane is rather model-independent and extends the LEP2 limit to higher slepton masses of up to 200 GeV for an LSP mass of 30 GeV. For LSP masses larger than 80 GeV, no slepton masses can be excluded beyond the LEP2 limit.

In addition, a wide variety of other searches for SUSY have been made – including searches for long-lived quasi-stable particles, electroweakinos with small mass difference, RPV SUSY, minimal gauge mediated SUSY etc. After 5 fb^{-1} of data at LHC7 and a first glimpse into another 5 fb^{-1} of data at LHC8, it is safe to say that no compelling signal for SUSY has yet emerged at LHC.

7.3.5 *Impact of the constraints on the SUSY particle sectors*

We can summarize the results of this section as constraints on the various sectors of an MSSM model set out in Section 7.3.1:

1. The first and second generation squarks: The particles in this sector are highly constrained by flavour and CP violation limits and by LHC squark searches. Typically we expect $m_{\tilde{q}} \gtrsim 1.5$ TeV. This sector has little connection to the EW scale: indeed, in split SUSY models [86] the squark (and slepton) masses are sometimes pushed to the 10^{10} GeV level.

2. The first and second generation sleptons: The particles in this sector are favored by $(g-2)_\mu$ to have masses below 1 TeV. However, the absence of leptonic flavour violating processes (*e.g* $\mu \to e\gamma$ decay) push this sector to be much heavier.

3. The third generation squarks and sleptons: The particles in this sector are influenced by large Yukawa couplings. Naturalness favors their masses to be below 1 TeV, although B-meson decay data prefer top squarks with mass at or above the TeV scale.

4. The gauginos: The particles in this sector are in principle independent of the squark mass scale and might also be independent of one another. Simple SUSY GUT models favor gaugino mass unification $M_1 = M_2 = M_3 \equiv m_{1/2}$ at M_{GUT}, giving a $1:2:7$ ratio of masses at the weak scale. More general models allow for essentially independent gauginos masses. Electroweak fine-tuning prefers gaugino masses not too far above the TeV scale. As of today, M_1 and M_2 are not substantially constrained beyond the LEP limits, but M_3, the gluino mass, probably must be above 1 TeV.

5. The higgsinos: The masses of the particles in this sector are determined by the superpotential μ term, which is not a soft SUSY breaking term. In the context of the MSSM alone, it could be expected to occur at the M_{GUT} or M_{string} scale. This however would require immense fine-tuning in the corrections to the Z mass: *c.f.* Eq'n 99. Naturalness arguments prefer a value of $|\mu|$ not far above ~ 100 GeV, close to but somewhat beyond the limits from LEP2 chargino searches.

Ironically, the LHC has its greatest capability—in terms of mass reach—to detect the first generation squarks and the gluinos. These are particles with indirect or no connection to the Z mass scale. On the other hand, the ILC has an excellent capability to detect electroweakinos. In the case where the light electroweakinos are higgsinos, the ILC would be directly probing that sector which is most directly connected to the Z-mass scale via electroweak fine-tuning. The ILC also has excellent capabilities to study the sleptons, probing a sector that is very difficult to study at the LHC. It is possible that the third generation squarks and sleptons lie within the mass range of the ILC. In that case, the ILC would greatly enhance the knowledge of these sparticles gained from the LHC, since the ILC has the capability to precisely measure not only the masses but also the quantum numbers and mixing angles of these particles. We will present examples of these ILC capabilities in the next several sections.

7.4 Two benchmark points for the ILC

In Ref. [87], a variety of post LHC7 benchmark points for ILC physics were proposed. Here, we include two of these for reference in the discussion of supersymmetric particle discovery and measurement capabilities at the ILC. These models are completely viable in the face of the LHC supersymmetry searches and they address important questions in physics beyond the Standard Model. Many of the more specific scenarios discussed in Section 7.5 can be identified within their particle spectra.

7.4.1 Natural SUSY and light higgsinos

For natural SUSY (NS), we adopt a benchmark point using input parameters $m_0(1,2) =$ 13500 GeV, $m_0(3) = 760$ GeV, $m_{1/2} = 1380$ GeV, $A_0 = -167$ GeV, $\tan\beta = 23$ GeV, $\mu = 150$ GeV and $m_A = 1550$ TeV. The resulting mass spectrum is listed in Table 1 of Ref. [87] and shown in Figure 55.

The point contains higgsino-like $\tilde{\chi}_1^0$, $\tilde{\chi}_2^0$ and $\tilde{\chi}_1^\pm$ with masses $\sim \mu = 150$ GeV, where $m_{\tilde{\chi}_1} - m_{\tilde{\chi}_1^0} = 7.4$ GeV and $m_{\tilde{\chi}_2^0} - m_{\tilde{\chi}_1^0} = 7.8$ GeV. Due to the small energy release in their three body decays, the $\tilde{\chi}_1^\pm$ and $\tilde{\chi}_2^0$ will be difficult to detect at LHC [40]. Third generation squark masses are at $m_{\tilde{t}_1} = 286.1$ GeV, $m_{\tilde{t}_2} = 914.9$ GeV and $m_{\tilde{b}_1} = 795.1$ GeV. Since the mass difference $m_{\tilde{t}_1} - m_{\tilde{\chi}_1^0}$ is less than the top mass, the decay $\tilde{t}_1 \to b\tilde{\chi}_1^\pm$ dominates, thus yielding a signature for $\tilde{t}_1$ pair production of two acollinear b-jets plus missing transverse energy. It is likely that the LHC experiments will eventually find the $\tilde{t}_1$, though at the moment the searches are not sensitive. Resolving the $\tilde{\chi}_1^\pm$, $\tilde{\chi}_1^0$ (and $\tilde{\chi}_2^0$) as distinct states will be extremely difficult at the LHC. Most other sparticles lie well beyond LHC reach.

For ILC, the spectrum of higgsino-like $\tilde{\chi}_1^\pm$, $\tilde{\chi}_1^0$ and $\tilde{\chi}_2^0$ would be accessible for $\sqrt{s} \gtrsim 320$ GeV via $\tilde{\chi}^+\tilde{\chi}^-$ and $\tilde{\chi}_2^0\tilde{\chi}_2^0$ pair production and $\tilde{\chi}_1^0\tilde{\chi}_2^0$ mixed production. although the energy release from decays will be small at beam energies near the threshold. Top squark pair production would become accessible when $\sqrt{s}$ exceeds about 575 GeV.

7.4.2 An MSSM model with light sleptons

Using the freedom in the MSSM to decouple the masses of squarks and sleptons, we generated a model in the 13-parameter pMSSM that gives a spectrum of color singlet particles close to that of the well-studied SPS1a′ point [130]. The SPA1a′ point is phenomenologically well-motivated in that it naturally reconciles the measured $(g-2)_\mu$ anomaly (which favors light smuons) with the measured $b \to s\gamma$ branching fraction (which favors rather heavy third generation squarks). It furthermore predicts a neutralino relic density compatible with cosmological observations, making use of stau coannihilation. The SPA1a′ point belongs to the cMSSM and so is now excluded by LHC searches for squarks and sleptons. But it is easy to find a more general MSSM point that shares its virtues and is not yet tested by LHC searches. We call this the $\delta M\tilde{\tau}$ model. The particle masses of this model are listed in Table 2 of Ref. [87] and displayed in Figure 55.

With gluino and first/second generation squark masses around 2 TeV, the model lies beyond current LHC limits, especially since the gluino decays dominantly via $\tilde{t}_1 t$ or $\tilde{b}_1 b$. The tau sleptons $\tilde{\tau}_1$ have masses of 104 GeV, so stau pair production would be accessible even at the first stage of ILC running. Right-selectrons and smuons with mass 135 GeV would also be produced at the ILC during the early runs, while left-sleptons and sneutrinos, with mass about 200 GeV, would be accessible when $\sqrt{s}$ exceeds 400 GeV. The $\tilde{\chi}_1^0\tilde{\chi}_2^0$ reaction opens up at $\sqrt{s} > 250$ GeV, and $\tilde{\chi}_1^+\tilde{\chi}_1^-$ pair production is accessible for $\sqrt{s} \gtrsim 310$ GeV. In addition, with $m_{A,H} \sim 400$ GeV, hA production opens at 525 GeV, stop pair production at 600 GeV, sbottom pair production at 680 GeV and finally charged Higgses and HA appear at 800 GeV.

7.5 Experimental Capabilities and Parameter Determination

In this section, we will review the ILC's experimental capabilities for precision measurements of SUSY particle properties. These measurements allow to determine the parameters of the underlying theory and to test its consistency at the quantum loop level.

As discussed above, the highly constrained cMSSM/mSUGRA models of super-

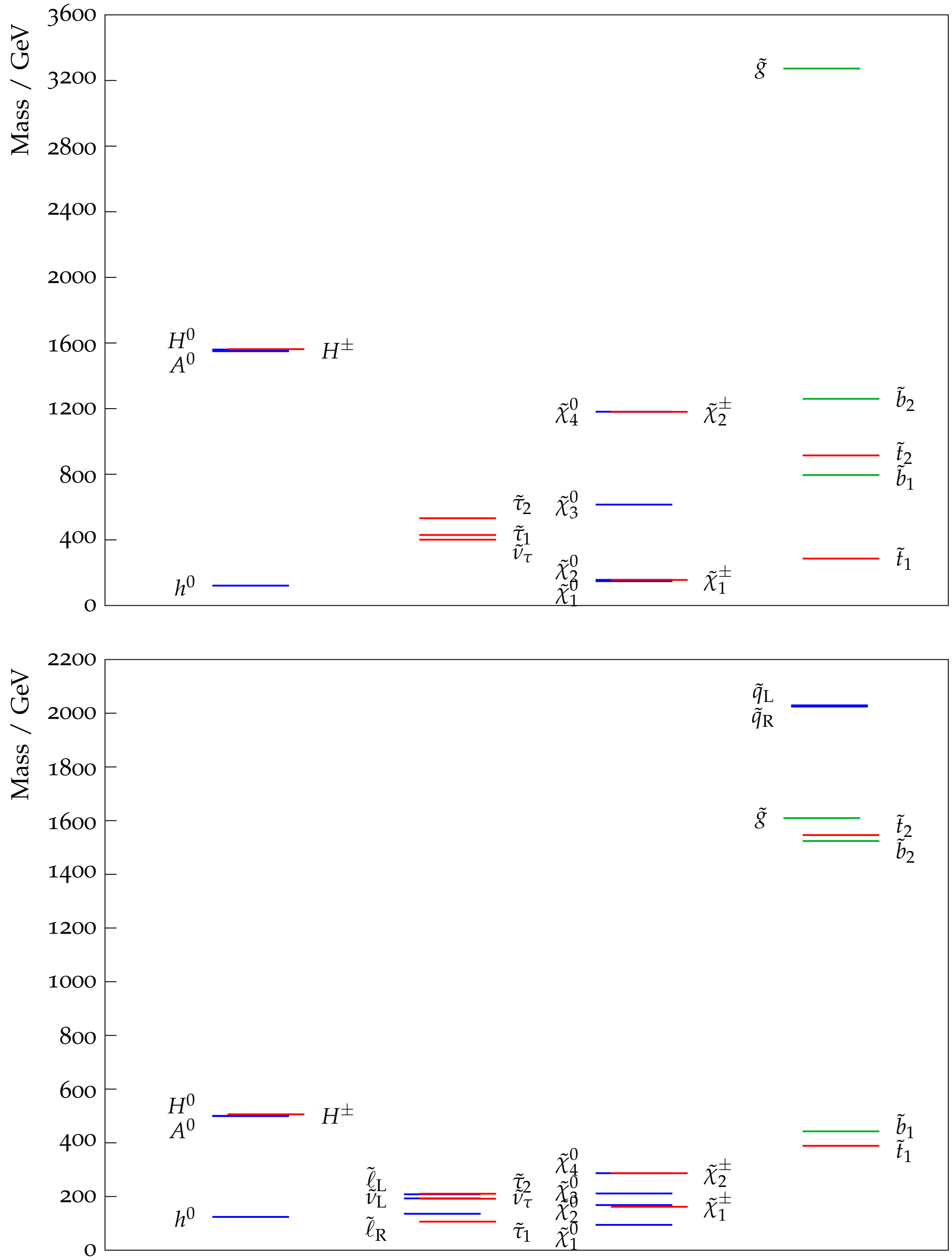

Figure 55: SUSY particle spectrum of the two benchmark scenarios discussed in Section 7.4: Top: Natural SUSY model; Bottom: $\delta M\tilde{\tau}$ model.

symmetry are under tension from several different types of LHC observations. Therefore, we will discuss SUSY measurements in the more general context of the CP and R-parity conserving MSSM. At the ILC, we will study the lightest particles of the SUSY spectrum, so the measurements that we will discuss involve simple reactions without complex cascade decay chains [92]. Thus, these measurements involve only a few of the MSSM parameters and, typically, those parameters can be determined with high precision.

We start with the minimal case in which only the lighter neutralinos and charginos are kinematically accessible. We then proceed to discuss sleptons and squarks, especially those of the third generation. Finally, we discuss possible extensions of the theory, encompassing R-parity violation, CP violation, the NMSSM and the MSSM with an additional gauge group. We close with comments on model discrimination and parameter determination.

7.5.1 Neutralino and Chargino Sector

At the ILC, the electroweak gaugino sector can be probed in a model independent way up to masses of $\sqrt{s}/2$. Associated pair production can access masses above this value. The masses of the electroweak gauginos can be measured with extremely high precision, in particular at threshold scans with a precision below the per mille level [88,89].

Most of the SUSY models consistent with all experimental data feature light electroweakinos. These can either have dominant Bino/Wino components, or—as motivated by naturalness—dominant higgsino components. Examples of the latter case include the Natural SUSY benchmark introduced in section 7.4.1, as well as models with mixed gauge-gravity mediation [90], and the remaining points in the cMSSM parameter space. A more detailed overview of the light higgsino case is given in [87]. A characteristic pattern in all cases is a very small mass splitting between the χ_1^0 and $\chi_1^\pm$ / χ_2^0 of typically a few GeV or smaller. This small splitting is very difficult to resolve at the LHC. However, these states can be discovered and disentangled at the ILC by using ISR recoil techniques to overcome the background from 2-photon processes, and taking advantage of the capability of the detectors to observe the very soft visible decay products of the $\chi_1^\pm$ / χ_2^0. These models can also lead to short displaced vertices that can be resolved thanks to the excellent vertex resolution at the ILC.

In the past, the case of small mass splitting between $\chi_1^\pm$ and χ_1^0 has been studied in the context of AMSB models [91], where it has been shown that mass differences down to 50 MeV can be resolved. For a 400 MeV mass difference, it has been shown that the $\chi_1^\pm$ mass can be determined to 1.8 GeV from the recoil against an ISR photon. Observing the energy of the single soft pion from the $\chi_1^\pm$ decay, the $\chi_1^\pm$–χ_1^0 mass difference can be determined to 7 MeV [93]. Although the minimal version of the AMSB is currently disfavoured due to its incompatibility with a Higgs mass of 125 GeV, the fact that such small mass differences can be precisely measured at the ILC remains unchanged. In the Natural SUSY example discussed above, it is also true that the χ_2^0 is nearly mass degenerate with the $\chi_1^\pm$. This creates an additional experimental complication, but on the other hand offers an additional handle for parameter determination. While a detailed experimental study is underway, the χ_2^0 / $\chi_1^\pm$ separation should be possible when the various exclusive decay modes are exploited, which is feasible due to the clean environment and excellent detector resolutions available at the ILC. The measurement of the polarization and beam energy dependence of the cross-sections of these processes then allows us to establish the higgsino character of the particles and to precisely determine μ.

If the mass difference between $\chi_1^\pm$ or χ_2^0 and χ_1^0 is larger than about 80 GeV without sleptons in between, the decays of these particles will proceed via real $W^\pm$ or Z bosons. In the challenging case where $\chi_1^\pm$ and χ_2^0 are nearly mass degenerate, their decays can be disentangled even in the fully hadronic decay mode. This case has been studied both by SiD and ILD in full detector simulation. Figure 56 shows the energy spectra of the reconstructed gauge boson candidates from signal, SUSY and SM background for the chargino and neutralino event selection. Assuming an integrated luminosity of 500 fb^{-1} at $\sqrt{s}$ = 500 GeV and a beam polarization of $P(e^+, e^-) = (30\%, -80\%)$, the edge positions can be determined to a few hundred MeV. Due to sizable correlations, this translates into uncertainties of 2.9, 1.7 and 1.0 GeV for the χ_2^0, $\chi_1^\pm$ and the χ_1^0 masses, respectively. The cross-sections can be measured to 0.8% (2.8%) in the $\chi_1^\pm$ (χ_2^0) case from the hadronic channel alone.

Independently of the mass splitting, the polarized cross-section measurements at different center-of-mass energies can be employed to determine the mixing angles in the chargino sector, as illustrated in Figure 57. This example is based on simulations performed in the SPS1a scenario; the results also apply to the $\delta M\tilde{\tau}$ scenario introduced above. The bands include both statistical and systematical uncertainties, where the limiting contribution is the precision of the chargino mass.

More recently, it has been shown that the achievable experimental precision allows us also to determine the top squark masses and mixing angle via loop contributions to the polarized chargino cross-sections and the forward-backward asymmetries [96]. This allows us to predict and to constrain the heavier states of the SUSY model and to test its structure directly independently of the SUSY breaking scheme.

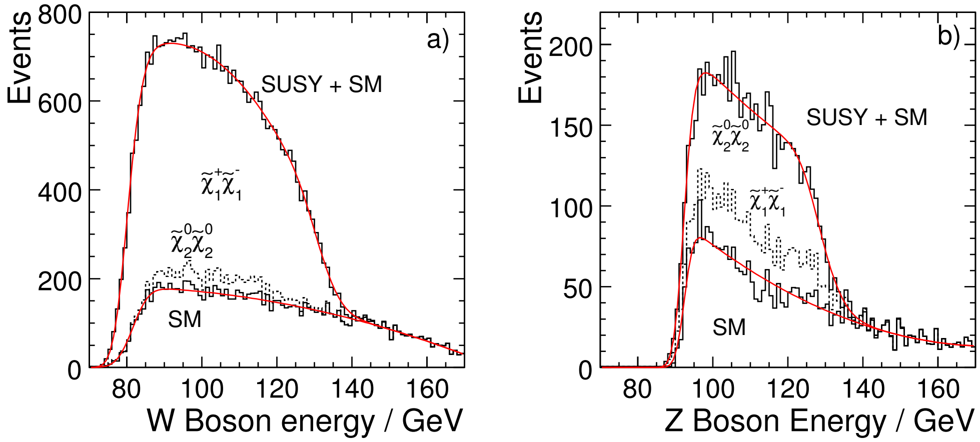

Figure 56: a) Energy spectrum of the $W^{\pm}$ candidates reconstructed from events selected as $\tilde{\chi}_1^{\pm}$ pairs and b) Energy spectrum of the Z^0 candidates reconstructed from events selected as $\tilde{\chi}_2^0$ pairs. From [94].

7.5.2 Gravitinos

If the gravitino is lighter than the lightest neutralino, the neutralino could decay into a photon plus a gravitino. In such a case, the lifetime of the neutralino is related to the mass of the gravitino: $\tau_\chi \sim m_{3/2}^2 M_{Pl}^2/m_\chi^5$. Therefore the measurement of the neutralino lifetime gives access to $m_{3/2}$ and the SUSY breaking scale. A similar statement applies to models in which a different particle is the lightest Standard Model superpartner, decaying to the gravitino. A well-studied example is that of the $\tilde{\tau}$ NLSP. The experimental capabilities of a Linear Collider in scenarios with a gravitino LSP have been evaluated comprehensively many years ago [97], where it has been demonstrated that with the permille level mass determinations from threshold scans, the clean environment and the excellent detector capabilities, especially in tracking and highly granular calorimetry, fundamental SUSY parameters can be determined to 10% or better.

Although this study was based on minimal GMSB models (which are currently disfavoured by the CERN 125 GeV resonance measurement), the signatures and experimental techniques remain perfectly valid. They could apply to other non-minimal scenarios including general gauge mediation. Aspects of the detector performance which were still speculative when the studies in [97] were performed have been established in the intervening time with testbeam data from prototype detectors. For instance, the performance of neutralino lifetime determination from non-pointing clusters in the electromagnetic calorimeter has recently been reevaluated based on full

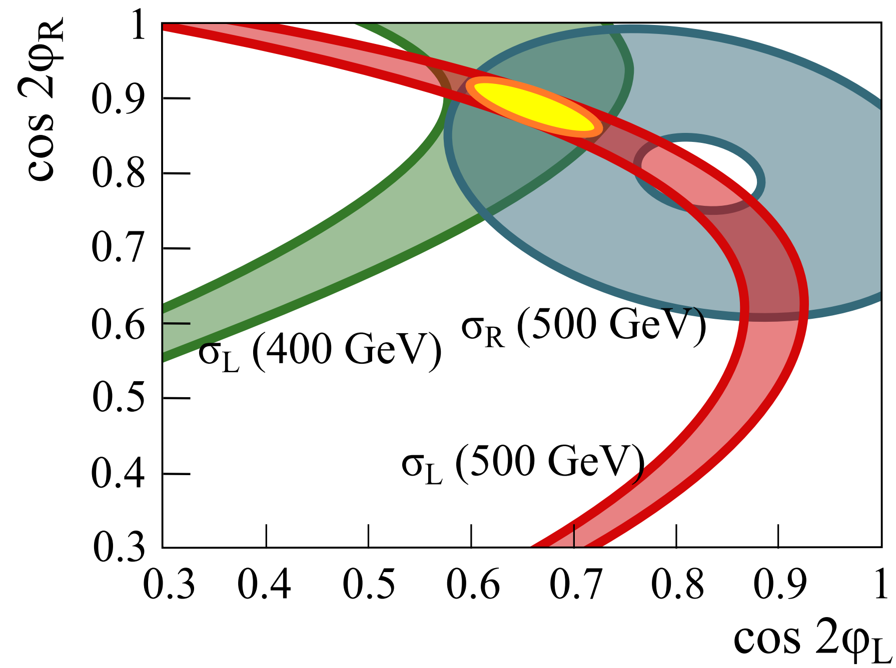

Figure 57: Measurement of the chargino mixing angles from polarised cross-sections. From [95].

detector simulation gauged against Calice testbeam data. These confirm the estimates from [97] that lifetimes between 0.1 and 10 ns can be reconstructed with a few percent accuracy, although a calibration of the lifetime reconstruction is needed [98]. Similarly it has been shown in [99], that, in the case of a $\tilde{\tau}$ NLSP, the lifetime can be measured down to 10^{-5} ns, corresponding to gravitino masses of a few eV. Figure 58 shows the 1σ and 2σ uncertainty bands as a function of the lifetime of a $\tilde{\tau}$ with a mass of 120 GeV.

Scenarios with very long-lived $\tilde{\tau}$ NLSPs which get trapped in the calorimeter and decay much later have been studied in [100]. It has been shown there that, with a suitable read-out of the ILC detectors, the gravitino mass and the SUSY breaking scale can also be determined in such cases. The first signs of these heavy, detector-stable charged particles would their large ionization losses in the tracking volume. This is a nearly background-free signature even at the LHC, so it is also possible there to discover electroweak production of very long-lived $\tilde{\tau}$ NLSPs or $\tilde{\chi}_1^{\pm}$ NLSPs. If this discovery were made, it would be important and fascinating to measure the polarized electroweak cross sections of these particles with high precision at the ILC.

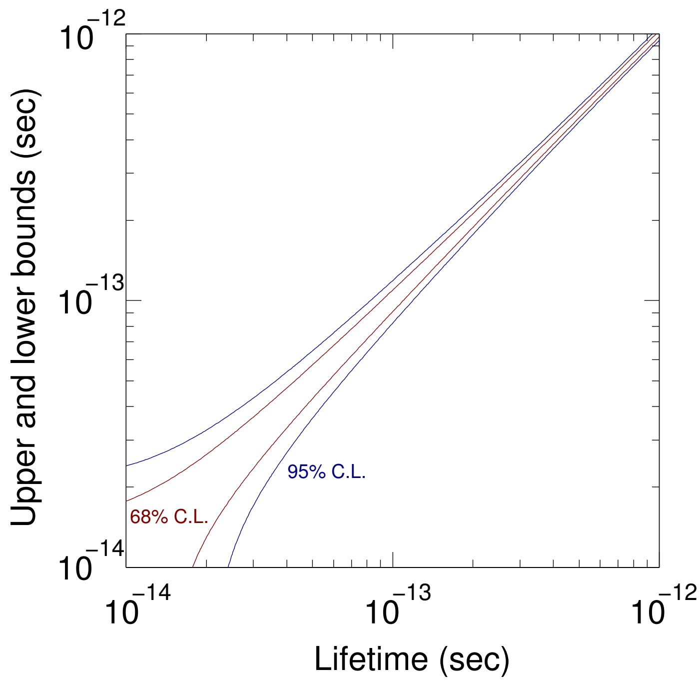

Figure 58: 1σ and 2σ uncertainty bands as a function of the lifetime of a $\tilde{\tau}$ with a mass of 120 GeV, from [99].

7.5.3 Third generation squarks

At the ILC, the stop $\tilde{t}_1$ can be probed up to $m_{\tilde{t}_1} = \sqrt{s}/2$ regardless of its decay mode and the masses of other new particles. At $\sqrt{s} = 500$ GeV, the $\tilde{t}_1$ mass can be determined to 1 GeV in the $\tilde{t}_1 \to c\tilde{\chi}_1^0$ decay mode, which dominates for small mass differences, and to 0.5 GeV in the $\tilde{t}_1 \to b\tilde{\chi}_1$ mode [101]. At the same time, the stop mixing angle can be determined to $\Delta \cos\theta_t = 0.009$ and 0.004 in the neutralino and chargino modes, respectively. A more recent study improved the mass resolution in the $\tilde{t}_1 \to c\tilde{\chi}_1^0$ decay to 0.42 GeV, including systematic uncertainties estimated based on LEP experience by assuming data from two different center-of-mass energies [102]. In a top-squark co-annihilation scenario, the predicted dark matter relic density depends strongly on the stop-neutralino mass difference. The precise ILC mass measurenents give an uncertainty on the calculated dark matter relic density of $\Delta\Omega_{\rm CDM}h^2 = 0.015$, comparable to the current WMAP precision. Figure 59 shows the correlation between the stop mass and $\Omega_{\rm CDM}h^2$ and the respective precisions. This clearly shows that sub-GeV precision on the stop mass is mandatory to establish the $\tilde{\chi}_1^0$ as a cosmic relic. Although these studies were performed with slightly lower stop masses, one can expect similar precisions in the two scenarios introduced in section 7.4

if on the way to a 1 TeV upgrade the ILC is operated at a center-of-mass energy of 600 GeV or above. And, indeed, there is still much room for the $\tilde{t}_1$ to be found at the LHC at a mass below 250 GeV.

The polarized cross sections $\sigma(e^-_L e^+_R \to \tilde{t}_1 \bar{\tilde{t}}_1)$ and $\sigma(e^-_R e^+_L \to \tilde{t}_1 \bar{\tilde{t}}_1)$ allows a direct determination of the $(\tilde{t}_L, \tilde{t}_R)$ mixing angle with an accuracy of a few degrees. This is crucial information for the theory of electroweak symmetry breaking in SUSY and for the explanation for the Higgs boson mass at 125 GeV.

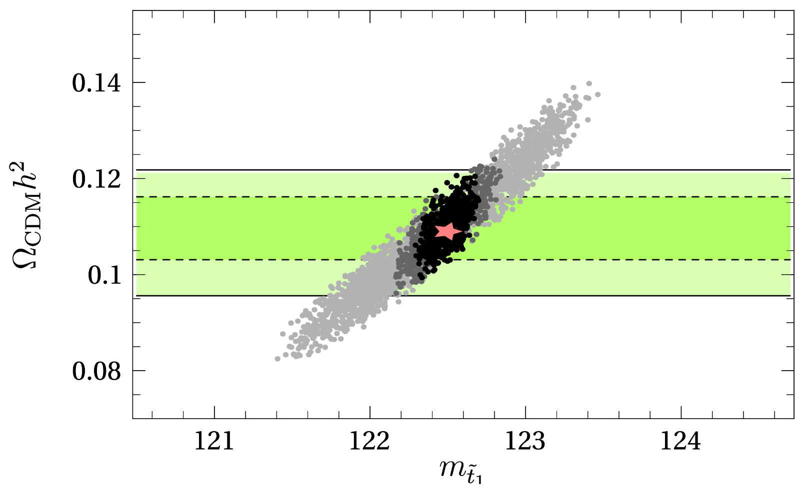

Figure 59: Predicted dark matter density Ω_{DM} vs $m_{\tilde{t}_1}$ in a stop coannihilation model. The scatter plot shows points allowed within 1σ experimental precision assuming $\delta\tilde{t}_1 = 1.2$ GeV (light gray), 0.42 GeV (dark gray) and 0.24 GeV (black). The bands show the current WMAP precision on Ω_{DM}. The input value is marked with a star. From [102].

In sbottom-co-annihilation scenarios, which typically exhibit a sbottom-LSP mass difference of about 10% of the LSP mass, the process $\tilde{b}_1 \to b\tilde{\chi}^0_1$ can be discovered for sbottom masses up to about 10 GeV below the kinematic limit and for mass differences down to only 5 GeV larger than the kinematic limit [103]. It will be extremely difficult to cover such small mass differences comprehensively at the LHC.

7.5.4 *Scalar charged leptons*

For slepton masses below $\sqrt{s}/2$, sleptons could be produced copiously at the ILC without relying on cascades from heavier sparticles. The lighter sleptons typically decay directly into the corresponding lepton and the lightest neutralino, giving a very clear signature of two isolated same flavor opposite sign leptons and missing four-momentum. The lepton energy spectrum has a box-like shape, and its lower and upper edge give direct access to the slepton and neutralino mass. In practice, the box is slightly smeared by the beam energy spectrum, ISR, detector resolution and, in case of τ leptons, by the unmeasured neutrinos from the τ decay. Nevertheless, this technique works reliably down to very small mass differences of a few GeV. For mass differences below ~ 10 GeV, the lower edge is buried in background from 2-photon processes. Then an additional observable is needed to determine the lightest neutralino mass. The adjustable center-of-mass energy of the ILC allows us to achieve even higher precision by scanning the production thresholds.

In SUSY, the superpartners of the left- and right-handed leptons are distinct scalar particles with different electroweak quantum numbers. These particles can be distinguished at the ILC in a model-independent way by the measurement of their production cross sections from left- and right-polarized beams in e^+e^- annihilation. It is not expected that the left- and right-sleptons should be mass degenerate, but, even in this case, the two particles can be studied separately, since each has enhanced production in cases with electron beams of the same handedness.

The heavier sleptons typically decay via intermediate charginos, neutralinos or sneutrinos, depending on the details of the spectrum [92]. By choosing an intermediate center-of-mass energy, the production of heavier superpartners and thus the background from their cascades can be switched off. This allows the ILC experiments to disentangle even rich spectra similar to the $\delta M\tilde{\tau}$ scenario discussed above.

The $\tilde{\tau}$ sector of a scenario very similar to $\delta M\tilde{\tau}$ has recently been studied in full simulation with the ILD detector [104], since the small $\tilde{\tau}$-$\tilde{\chi}_1^0$ mass difference provides an interesting challenge for the detector and the accelerator conditions. In this case, the beam energy spectrum was accounted for and also accelerator background from e^+e^- pairs created from beamstrahlung was overlayed in order to verify the robustness of the reconstruction even of fragile final states such as soft τ leptons against spurious tracks and clusters from beam background.

With an integrated luminosity of 500 fb^{-1} at a center-of-mass energy of $\sqrt{s} =$ 500 GeV and with $P(e^+, e^-) = (-30\%, +80\%)$, the following results were achieved for the $\tilde{\tau}$ masses using pair production cross-sections and the τ polarisation $\mathcal{P}_\tau$ from $\tilde{\tau}$ decays. Both of these quantities depend on the $\tilde{\tau}$ mixing angle, the higgsino component of the $\tilde{\chi}_1^0$ and $\tan\beta$ in a well-understood way.

$$\begin{aligned}
\delta M(\tilde{\tau}_1) &= {}^{+0.03}_{-0.05} \pm 1.1 \cdot \delta M(\tilde{\chi}_1^0) \text{ GeV (endpoint)} \\
\delta M(\tilde{\tau}_2) &= {}^{+11}_{-5} \pm 18 \cdot \delta M(\tilde{\chi}_1^0) \text{ GeV (endpoint)} \\
\frac{\delta\sigma}{\sigma}(\tilde{\tau}_1) &= 3.1\ \% \\
\frac{\delta\sigma}{\sigma}(\tilde{\tau}_2) &= 4.2\ \% \\
\mathcal{P}_\tau &= 91 \pm 6 \pm 5 \text{ (bkg)} \pm 3 \text{ (SUSY masses) \% } (\pi \text{ channel}) \\
\mathcal{P}_\tau &= 86 \pm 5 \text{ \% } (\rho \text{ channel}).
\end{aligned}$$

The measurement of the endpoint of the τ jet energy spectrum from $\tilde{\tau}_1$ decays is shown in Figure 60. The $\tilde{\tau}$ mixing angle can be determined independently of the τ polarisation from $\tilde{\tau}_1\tilde{\tau}_2$ associated production below the $\tilde{\tau}_2$ pair production threshold. With a dedicated threshold scan, the $\tilde{\tau}_2$ mass measurement can be improved to $\delta M(\tilde{\tau}_2) \approx 0.86$ GeV [105]. Even smaller mass differences have been studied in an earlier fast simulation analysis [106], which found $\delta M(\tilde{\tau}_1) \approx 0.15-0.3$ GeV depending on $\tilde{\tau}_1$ mass and the $\tilde{\tau}_1$-$\tilde{\chi}_1^0$ mass difference.

Since the measurement of isolated electrons and muons is straightforward for the ILC detectors, scalar electron and muon production have mainly been studied in fast detector simulations. In [106,107], a scenario similar to $\delta M\tilde{\tau}$ has been studied assuming an integrated luminosity of 200 fb^{-1} and beam polarisations of $P(e^+, e^-) = (-60\%, +80\%)$ at a center-of-mass energy of $\sqrt{s} = 400$ GeV. The study found precisions of $\delta M(\tilde{\mu}_R) \approx 170$ MeV and $\delta M(\tilde{e}_R) \approx 90$ MeV. Comparable values were found in [105], where in addition a precision of 20 MeV was achieved for $M(\tilde{e}_R)$ from a threshold scan. This kind of precision below 100 MeV can typically be obtained when no irreducible SUSY background from other cascades is present.

The $\delta M\tilde{\tau}$ scenario is actually challenging in this respect, since substantial background from neutralino decays into muons is present at the $\tilde{\mu}_R$ pair production threshold. This case has recently been studied using the fast simulator SGV [108] tuned to the detector performance found in full simulation of the ILD detector concept. All relevant SM backgrounds, especially $W^+W^- \to l^+\nu l^-\overline{\nu}$, $ZZ \to 4$ leptons, and μ and τ pairs, as well as all open SUSY channels were generated with Pythia 6.422 at 9 center of mass energies near the $\tilde{\mu}_R$ threshold. The simulations included beamstrahlung based on Circe 1 and the incoming beam energy spectrum according to the TDR design of the ILC. The measured cross-section as a function of the center of mass energy is shown in Figure 60 assuming 10 fb^{-1} per point with $P(e^+, e^-) = (-30\%, +80\%)$. A fit to the threshold yields a statistically limited uncertainty of about 200 MeV on the $\tilde{\mu}_R$ mass [109].

In case of the heavier smuon $\tilde{\mu}_L$, a mass resolution of 100 MeV has been achieved in full simulation for the ILD Letter of Intent assuming 500 fb^{-1} with $P(e^+, e^-) = (+30\%, -80\%)$ at $\sqrt{s} = 500$ GeV [110]. This is consistent with earlier fast simulation studies [89,105].

All resolutions here are by far statistically limited. Masses or cross-sections critical for SUSY parameter determination in a certain scenario could therefore be measured with even better precision when more integrated luminosity is accumulated in the corresponding running configuration of the machine.

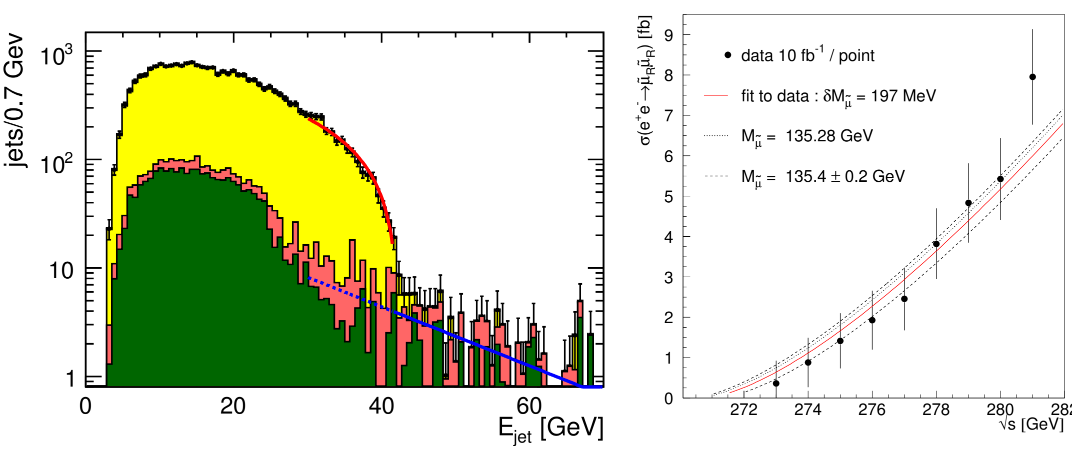

Figure 60: Left: Measurement of the $\tilde{\tau}_1$ mass from the endpoint of the τ jet energy spectrum in a scenario with small $\tilde{\tau}_1$-χ_1^0 mass difference very similar to the $\delta M\tilde{\tau}$ scenario introduced in Section 7.4.2. The stacked histogram contains (from the bottom), SUSY background, SM background, signal. The background is fitted in the signal-free region to the right (solid portion of the line), and extrapolated into the signal region (dashed). From [104]. Right: Measurement of the $\tilde{\mu}_R$ mass from a threshold scan with a total integrated luminosity of 100 fb^{-1}. The precision of about 200 MeV obtained in this study is limited by the assumed integrated luminosity [109].

7.5.5 Sneutrinos

Depending on the properties of the sparticle spectrum, sneutrinos may decay visibly into modes such as $\tilde{\nu}_\ell \to \ell\tilde{\chi}_1^+$ [111], or they may decay invisibly via $\tilde{\nu}_\ell \to \nu_\ell\tilde{\chi}_1^0$. Even in this latter case, the sneutrino mass can be measured from cascade decays of other sparticles. For instance, in the $\delta M\tilde{\tau}$ scenario, the chargino has a 13% branching fraction into a sneutrino and the corresponding charged lepton. From these decays, the sneutrino mass can be reconstructed to $\delta M(\tilde{\nu}) \approx 0.5$ GeV [112,113].

Sneutrinos which are too heavy to be produced directly still influence the cross section for chargino production and the forward-backward asymmetry of three-body chargino decays. The latter yields $\delta M(\tilde{\nu}) \approx 10$ GeV for sneutrino masses up to 1 TeV at $\sqrt{s} = 500$ GeV [89]. The chargino pair production cross-section is sensitive to sneutrino masses of up to 12 TeV at center-of-mass energies $\sqrt{s} \sim 1$ TeV [114].

7.5.6 *Beyond the CP and RP conserving MSSM*

R-Parity Violation:

R-parity violation (RPV) has two important experimental consequences at colliders: it allows for single production of SUSY particles, and it allows the LSP to decay to purely SM particles. The latter aspect makes RPV SUSY much harder to detect at the LHC due to the absence of missing transverse energy, so that the currently explored region is significantly smaller than in the R-parity conserving case, even when assuming mass unification at the GUT scale as in the cMSSM [115].

Bilinear R-parity violation (bRPV) has phenomenological motivations in neutrino mixing [116] as well as in leptogenesis [117,118]. In this case, the characteristic decay $\tilde{\chi}_1^0 \to W^{\pm} l^{\mp}$ will lead to background-free signatures at the ILC, possibly with a detectable lifetime of the $\tilde{\chi}_1^0$ depending on the strength of the RPV couplings. In the hadronic decay mode of the $W^{\pm}$, these events can be fully reconstructed and the $\tilde{\chi}_1^0$ mass can be measured to $\mathcal{O}(100)$ MeV depending on the assumed cross-section [119]. By measuring the ratio of the branching ratios for $\tilde{\chi}_1^0 \to W^{\pm}\mu^{\mp}$ and $\tilde{\chi}_1^0 \to W^{\pm}\tau^{\mp}$, the neutrino mixing angle $\sin^2\theta_{23}$ can be determined to percent-level precision, as illustrated in Figure 61. Agreement with measurements from neutrino oscillation experiments would then prove that bRPV SUSY is the origin of the structure of mixing in the neutrino sector.

In the case of trilinear R-parity violation, s-channel sneutrino-exchange can interfere with SM Bhabha scattering. For $m_{\tilde{\nu}} < \sqrt{s}$, sharp resonances are expected. In addition, heavier sneutrinos could be detected via contact interactions, for example up to $m_{\tilde{\nu}} = 1.8$ TeV for $\lambda_{1j1} = 0.1$ at $\sqrt{s} = 800$ GeV [91].

CP violation:

An attractive feature of supersymmetry is that it allows for new sources of CP violation which are needed in order to explain the baryon-antibaryon asymmetry observed in the universe. The neutralino and chargino sector can accommodate two independent CP phases, for instance on M_1 and μ when rotating away the phase of M_2 by a suitable redefinition of the fields. While the phase of μ is strongly constrained by EDM bounds, the phase of M_1 could lead to CP sensitive triple product asymmetries

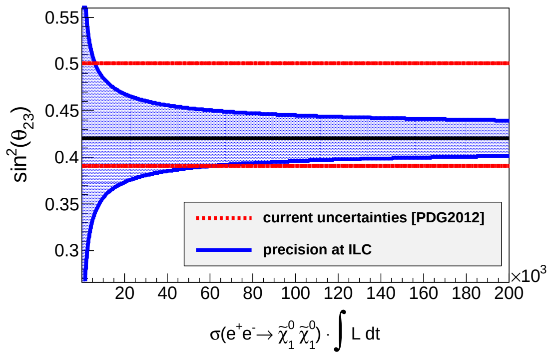

Figure 61: Achievable precision on $\sin^2\theta_{23}$ from RPV decays of the χ_1^0 as a function of the produced number of neutralino pairs compaired to the current precision from neutrino oscillation measurements. Over a large part of the m_0 vs. $m_{1/2}$ plane, the neutralino pair production cross-section is of order 100 fb.

up to 10%. These can be measured from neutralino two-body decays into slepton and lepton to ±1%. From a fit to the measured neutralino cross-sections, masses and CP-asymmetries, $|M_1|$ and $|\mu|$ can be determined to a few permille, M_2 to a few percent, Φ_1 to 10% as well as $\tan\beta$ and Φ_μ to 16% and 20%, respectively [120]. Other models of baryogenesis accessible to study at the ILC are discussed in Section 8.1.

NMSSM:

If indeed the higgsino is the LSP, as motivated by naturalness, then all by itself it is not a good dark matter candidate, since higgsino pairs annihilate rapidly into WW and ZZ. However, if we invoke an extended Higgs sector (the NMSSM) to explain the value of the Higgs boson mass, this extension adds a new SUSY partner, the singlino, which might have mass below that of the higgsino. The decay width of the higgsino to the singlino is of order 100 MeV. The pattern of decay final states is rich, and the measurement of branching ratios will illuminate the Higgs sector [121]. These decay products are quite soft, however, and are invisible under the standard LHC trigger constraints. Whether or not these particles can be seen at the LHC, the ILC would again be needed for a complete study. The annihilation cross section of singlinos, which determines the singlino thermal dark matter density, depends on the singlino-higgsino mixing angle. This could be measured at the ILC by measurement of the higgsino width using a threshold scan or by precision measurments of the NMSSM mass eigenvalues.

The capabilities of the ILC to distinguish between the NMSSM and the MSSM when the observable particle spectrum and the corresponding decay chains are very similar has been studied for instance in [122] based on analytical calculations. The study showed that with data taken at three different center-of-mass energies the distinction is possible. When exploiting the available information even more efficiently by applying a global fit, even two center-of-mass energies can be sufficient [123]. If the full neutralino/chargino spectrum is accessible, sum rules for the production cross sections can be exploited that show a different energy behaviour in the two models.

In scenarios where the lightest SUSY particle is nearly a pure singlino, the higgino lifetimes are long, leading to a displaced vertex signature. The lifetimes can be precisely resolved thanks to the excellent vertex resolution of the ILC detectors.

7.5.7 Parameter Determination and Model Discrimination

Beyond simply measuring the properties of new particles, a further goal of ILC is to fully uncover the underlying theory. This involves, among other issues, the measurement of the statistics of the new particles and the verification of symmetry predictions of the model. In this, we review some examples of such studies.

For example, if only the minimal particle content of a weakly interacting new particle χ^0 and an electrically charged partner $\chi^\pm$ is observed, the behaviour of the production cross-section at threshold and the production angle distribution of $\chi^+\chi^-$ pair production can be employed to distinguish between SUSY, where the χ's are fermions, Littlest Higgs models, where they are vector bosons, and Inert Higgs models, where they are scalar bosons [125].

If the model is indeed SUSY, we would like to establish the basic symmetry relation of supersymmety experimentally. This can be done by examining whether the gauge couplings $g(Vff)$ and $\overline{g}(V\tilde{f}\tilde{f})$ of a vector boson V and the Yukawa coupling $\tilde{g}(\tilde{V}f\tilde{f})$ for corresponding gauginos are equal. From the various cross-section measurements in the slepton and gaugino sector, these couplings can be extracted and their equality checked with sub-percent precision [89].

In addition to the couplings, the mass measurements at ILC, at the per mille level, allow one to extract the weak scale MSSM parameters. Here the polarized beams play a crucial role since they allow us to determine the mixing character both in the gaugino and in the slepton sector, especially if left- and right-handed superpartners are close in mass and thus difficult to separate kinematically. These parameters can then be extrapolated to higher energy using the renormalization group equations [126]. This might reveal that groups of these parameters unify, for example, at the GUT scale. The impact of ILC precision on this procedure has been studied in detail in [127], based on a scenario in which the color singlet sector is nearly identical to that of the $\delta M\tilde{\tau}$ scenario. They found that the weak scale parameters can be determined to percent level precision, some even to the per mille level. They further showed that ILC precision, beyond that achievable at the LHC, is needed to establish whether the weak scale parameters are consistent with a certain SUSY breaking scheme (in this case mSUGRA) or not. MSSM parameter determinations, both analytically and employing global fits, have been studied also in various other scenarios in [128,129,130,131].

Another crucial question to be answered is that of whether the lightest SUSY particle can account for some or all of the cosmological dark matter. Assuming that lightest SUSY particle was produced thermally in the early universe, its relic density can be computed from the Lagrangian parameters obtained from collider data and the result can be compared to the observed value of the dark matter density [132]. The Fittino collaboration has studied the prediction of the dark matter density from ILC data at the reference point $SPS1a'$, which, for this analysis, is very similar to the $\delta M\tilde{\tau}$ scenario [133]. Figure 62 shows the result of this comparison without assuming a specific SUSY breaking scenario, *i.e.* based on weak scale parameters. In this scenario, the ILC precision is needed to match the precision of the prediction to that expected from cosmological observations.

The $SPS1a'/\delta M\tilde{\tau}$ point is a rather special case in which $\Omega_{\mathrm{CDM}}h^2$ can be predicted with part per mille accuracy. More typically, the mechanisms that establish the dark matter relic density are more complex, and the accuracy of the prediction from collider data is less. We have seen an example already in Section 4.5.3 in our discussion of the stop coannihilation scenario. However, the more complex the physics of the dark matter density, the more important it is to make high precision measurements of the SUSY parameters. This important question will be discussed further in Section 8.2.

7.6 Conclusions

In this section, we have discussed the ILC capabilities for supersymmetry measurements in the light of the new information that we have gained from the LHC experiments. The discovery of a new boson at 125 GeV points to a mechanism of electroweak symmetry breaking that involves weakly coupled scalar fields. Supersymmetry is one of, if not the leading candidate, for such a model.

So far, the ATLAS and CMS experiments have found no evidence for supersymmetric particles. They have presented impressive limits on the masses of squarks and gluinos. However, these limits do not exclude the possibility of SUSY at the TeV scale. Rather, they push us to explore SUSY models in different parameter regions of the MSSM than those that have been given most attention in the past.

In particular, the LHC exclusions have focused much attention on models in which the first- and second-generation squarks are heavy while the naturalness of the elec-

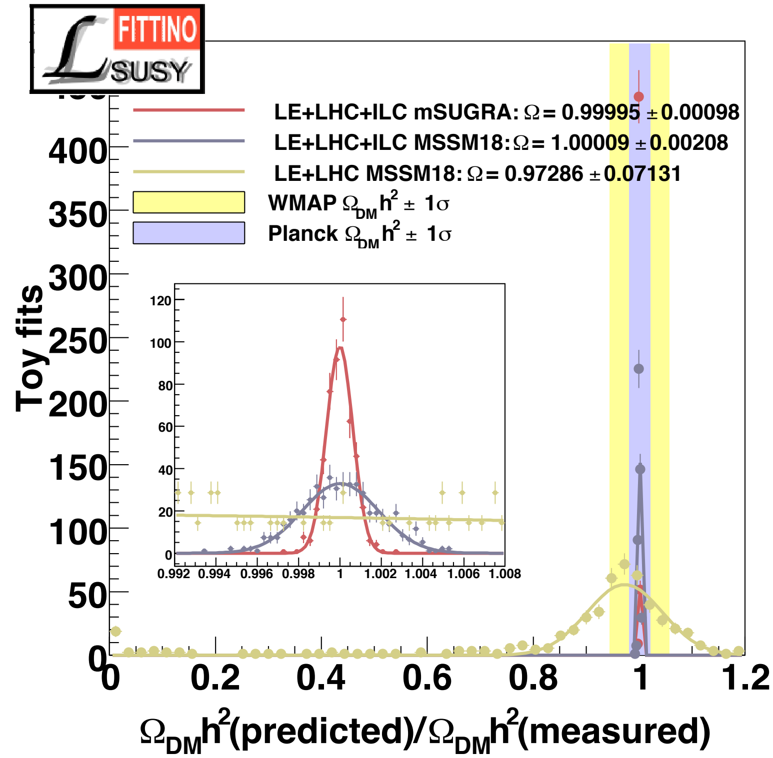

Figure 62: Ratio of the predicted value of $\Omega_{\text{pred}}h^2$ to the nominal value of $\Omega_{\text{SPS1a}}h^2$ in the SPS1a scenario for a variety of Fittino Toy Fits without using $\Omega_{\text{CDM}}h^2$ as an observable, from [133]. The anticipate predictions for LHC and ILC measurements are compared to current and projected cosmological observations.

troweak symmetry breaking scale keeps color singlet particles light. Naturalness arguments, in particular, favor a low value of $\mu \sim M_Z$, with μ ranging perhaps as high as $\sim$ 200 GeV. This then leads to a spectrum including several light higgsino-like charginos and neutralinos. The lightest neutralino, which is a possible WIMP candidate, would be predominantly higgsino-like. The light higgsinos are automatically mass-degenerate with typical mass gaps of 10-20 GeV. The small energy release from higgsino decay would be very difficult to detect at LHC. In contrast, an ILC with $\sqrt{s} = 0.25 - 1$ TeV would be a *higgsino factory*, in addition to being a Higgs factory! These arguments, and also possibly the muon $g-2$ anomaly, predict a rich array of new matter states likely accessible to the ILC.

In our review of the experiments at the ILC that would discover and measure the properties of these particles, we have emphasize the many tools that the ILC detectors will provide for exploring the nature of these new states of matter. These include the tunable beam energy, the use of beam polarization, precision tracking, vertex finding and calorimetry, which provide the ability to detect very low energetic particles as well as to observe and separate W and Z in hadronic modes. We have shown with many examples that all of these capabilities find new uses in the exploration of a new sector of particles.

The precision measurements available at the ILC will provide a window to physics at much higher energy scales, possibly those associated with grand unification and string theory. The ILC will also provide a key connection between particle physics and cosmology, especially in identifying the nature of dark matter and shedding light on possible mechanisms for baryogenesis.

Thus, the view from SUSY phenomenology is that construction of an ILC is more highly motivated now than ever before.

References

[1] J. Wess and B. Zumino, Phys. Lett. B **49**, 52 (1974).

[2] A. Salam and J. A. Strathdee, Phys. Rev. D **11**, 1521 (1975).

[3] A. Salam and J. A. Strathdee, Phys. Lett. B **51**, 353 (1974).

[4] For a review, see *e.g. Weak scale supersymmetry: From superfields to scattering events*, by H. Baer and X. Tata, Cambridge, UK: Univ. Pr. (2006), 537 p.

[5] E. Witten, Nucl. Phys. B **188**, 513 (1981).

[6] R. K. Kaul, Phys. Lett. B **109**, 19 (1982).

[7] S. Ferrara *et al.*, Phys. Rev. D **15**, 1013 (1977).

[8] E. Cremmer, S. Ferrara, L. Girardello and A. Van Proeyen, Nucl. Phys. B **212**, 413 (1983).

[9] For a review, see *e.g.* H. P. Nilles, Phys. Rept. **110**, 1 (1984).

[10] F. D. Steffen, Eur. Phys. J. C **59**, 557 (2009) [arXiv:0811.3347 [hep-ph]].

[11] K. -Y. Choi, J. E. Kim, H. M. Lee and O. Seto, Phys. Rev. D **77**, 123501 (2008) [arXiv:0801.0491 [hep-ph]].

[12] H. Baer, A. Lessa, S. Rajagopalan and W. Sreethawong, JCAP **1106**, 031 (2011) [arXiv:1103.5413 [hep-ph]].

[13] H. Baer, A. Lessa and W. Sreethawong, JCAP **1201**, 036 (2012) [arXiv:1110.2491 [hep-ph]].

[14] K. Rajagopal, M. S. Turner and F. Wilczek, Nucl. Phys. B **358**, 447 (1991).

[15] L. Covi, H. -B. Kim, J. E. Kim and L. Roszkowski, JHEP **0105**, 033 (2001) [hep-ph/0101009].

[16] H. Baer, A. D. Box and H. Summy, JHEP **0908**, 080 (2009) [arXiv:0906.2595 [hep-ph]].

[17] D. Curtin, P. Jaiswal and P. Meade, "Excluding Electroweak Baryogenesis in the MSSM," arXiv:1203.2932 [hep-ph].

[18] W. Buchmüller, R. D. Peccei and T. Yanagida, Ann. Rev. Nucl. Part. Sci. **55**, 311 (2005) [hep-ph/0502169].

[19] I. Affleck and M. Dine, Nucl. Phys. B **249**, 361 (1985).

[20] M. Dine, L. Randall and S. D. Thomas, Nucl. Phys. B **458**, 291 (1996) [hep-ph/9507453].

[21] H. Baer, F. E. Paige, S. D. Protopopescu and X. Tata, "Simulating Supersymmetry with ISAJET 7.0 / ISASUSY 1.0," hep-ph/9305342.

[22] A. Djouadi, J. -L. Kneur and G. Moultaka, Comput. Phys. Commun. **176**, 426 (2007) [hep-ph/0211331].

[23] R. Arnowitt and P. Nath, In Kane, G.L. (ed.): "Perspectives on supersymmetry II," pp. 222-243 [arXiv:0912.2273 [hep-ph]].

[24] G. F. Giudice and R. Rattazzi, Phys. Rept. **322**, 419 (1999) [hep-ph/9801271].

[25] L. Randall and R. Sundrum, Nucl. Phys. B **557**, 79 (1999) [hep-th/9810155].

[26] G. F. Giudice, M. A. Luty, H. Murayama and R. Rattazzi, JHEP **9812**, 027 (1998) [hep-ph/9810442].

[27] A. G. Cohen, D. B. Kaplan and A. E. Nelson, Phys. Lett. B **388**, 588 (1996) [hep-ph/9607394].

[28] J. L. Feng, K. T. Matchev and T. Moroi, Phys. Rev. Lett. **84**, 2322 (2000) [hep-ph/9908309].

[29] S. Dimopoulos and G. F. Giudice, Phys. Lett. B **357**, 573 (1995) [hep-ph/9507282].

[30] M. Perelstein and C. Spethmann, JHEP **0704**, 070 (2007) [hep-ph/0702038].

[31] G. Aad *et al.* [ATLAS Collaboration], Phys. Lett. B **710**, 67 (2012) [arXiv:1109.6572 [hep-ex]].

[32] S. Chatrchyan *et al.* [CMS Collaboration], Phys. Rev. Lett. **107**, 221804 (2011) [arXiv:1109.2352 [hep-ex]].

[33] R. L. Arnowitt and P. Nath, Phys. Rev. D **46**, 3981 (1992).

[34] K. L. Chan, U. Chattopadhyay and P. Nath, Phys. Rev. D **58**, 096004 (1998) [hep-ph/9710473].

[35] R. Kitano and Y. Nomura, Phys. Lett. B **631**, 58 (2005) [hep-ph/0509039]; Phys. Rev. D **73**, 095004 (2006) [hep-ph/0602096].

[36] H. Baer, V. Barger, P. Huang, A. Mustafayev and X. Tata, arXiv:1207.3343 [hep-ph].

[37] C. Brust, A. Katz, S. Lawrence and R. Sundrum, JHEP **1203**, 103 (2012) [arXiv:1110.6670 [hep-ph]].

[38] M. Papucci, J. T. Ruderman and A. Weiler, arXiv:1110.6926 [hep-ph].

[39] K. Cheung, C. -W. Chiang and J. Song, JHEP **0604**, 047 (2006) [hep-ph/0512192].

[40] H. Baer, V. Barger and P. Huang, JHEP **1111**, 031 (2011) [arXiv:1107.5581 [hep-ph]].

[41] H. Baer, V. Barger, P. Huang and X. Tata, JHEP **1205**, 109 (2012) [arXiv:1203.5539 [hep-ph]].

[42] C. Csaki, L. Randall and J. Terning, arXiv:1201.1293 [hep-ph].

[43] T. Cohen, A. Hook and G. Torroba, arXiv:1204.1337 [hep-ph].

[44] N. Craig, M. McCullough and J. Thaler, JHEP **1206**, 046 (2012) [arXiv:1203.1622 [hep-ph]].

[45] L. Randall and M. Reece, arXiv:1206.6540 [hep-ph].

[46] G. W. Bennett *et al.* [Muon G-2 Collaboration], Phys. Rev. D **73**, 072003 (2006) [arXiv:hep-ex/0602035].

[47] M. Davier, A. Hoecker, B. Malaescu and Z. Zhang, Eur. Phys. J. C **71**, 1515 (2011) [Erratum-ibid. C **72**, 1874 (2012)] [arXiv:1010.4180 [hep-ph]].

[48] T. Moroi, Phys. Rev. D **53**, 6565 (1996) [Erratum-ibid. D **56**, 4424 (1997)] [hep-ph/9512396].

[49] J. L. Feng and K. T. Matchev, Phys. Rev. Lett. **86**, 3480 (2001) [hep-ph/0102146].

[50] H. Baer, A. Belyaev, T. Krupovnickas and A. Mustafayev, JHEP **0406**, 044 (2004) [hep-ph/0403214].

[51] D. Asner *et al.* [Heavy Flavor Averaging Group], "Averages of b-hadron, c-hadron, and τ-lepton Properties," arXiv:1010.1589 [hep-ex].

[52] M. Misiak *et al.*, Phys. Rev. Lett. **98**, 022002 (2007) [hep-ph/0609232].

[53] H. Baer and M. Brhlik, Phys. Rev. D **55**, 3201 (1997) [hep-ph/9610224].

[54] S. Chatrchyan *et al.* [CMS Collaboration], Phys. Rev. Lett. **107** (2011) 191802 [arXiv:1107.5834 [hep-ex]].

[55] T. Aaltonen *et al.* [CDF Collaboration], Phys. Rev. Lett. **107** (2011) 191801 [Erratum-ibid. **107** (2011) 239903] [arXiv:1107.2304 [hep-ex]].

[56] R. Aaij *et al.* [LHCb Collaboration], "Strong constraints on the rare decays $B_s \to \mu^+\mu^-$ and $B^0 \to \mu^+\mu^-$," arXiv:1203.4493 [hep-ex].

[57] K. S. Babu and C. F. Kolda, Phys. Rev. Lett. **84**, 228 (2000) [hep-ph/9909476].

[58] J. K. Mizukoshi, X. Tata and Y. Wang, Phys. Rev. D **66**, 115003 (2002) [hep-ph/0208078].

[59] D. Eriksson, F. Mahmoudi and O. Stal, JHEP **0811**, 035 (2008) [arXiv:0808.3551 [hep-ph]].

[60] E. Barberio *et al.* [Heavy Flavor Averaging Group], "Averages of $b-$hadron and $c-$hadron Properties at the End of 2007," arXiv:0808.1297 [hep-ex].

[61] H. Baer, V. Barger and A. Mustafayev, JHEP **1205**, 091 (2012) [arXiv:1202.4038 [hep-ph]].

[62] S. Chatrchyan *et al.* [CMS Collaboration], "Observation of a new boson at a mass of 125 GeV with the CMS experiment at the LHC," Submitted to: Phys.Lett.B [arXiv:1207.7235 [hep-ex]].

[63] G. Aad *et al.* [ATLAS Collaboration], "Observation of a new particle in the search for the Standard Model Higgs boson with the ATLAS detector at the LHC," arXiv:1207.7214 [hep-ex].

[64] T. Aaltonen *et al.* [CDF and D0 Collaborations], "Evidence for a particle produced in association with weak bosons and decaying to a bottom-antibottom quark pair in Higgs boson searches at the Tevatron," arXiv:1207.6436 [hep-ex].

[65] S. Chatrchyan *et al.* [CMS Collaboration], Phys. Lett. B **713**, 68 (2012) [arXiv:1202.4083 [hep-ex]].

[66] ATLAS collaboration, "Search for neutral MSSM Higgs bosons in $\sqrt{s} = 7$ TeV pp collisions with the ATLAS detector," ATLAS-CONF-2012-094.

[67] G. Aad *et al.* [ATLAS Collaboration], JHEP **1206**, 039 (2012) [arXiv:1204.2760 [hep-ex]].

[68] H. Baer, V. Barger and A. Mustafayev, Phys. Rev. D **85**, 075010 (2012) [arXiv:1112.3017 [hep-ph]].

[69] A. Arbey, M. Battaglia, A. Djouadi, F. Mahmoudi and J. Quevillon, Phys. Lett. B **708**, 162 (2012) [arXiv:1112.3028 [hep-ph]].

[70] S. Heinemeyer, O. Stal and G. Weiglein, Phys. Lett. B **710**, 201 (2012) [arXiv:1112.3026 [hep-ph]].

[71] O. Buchmüller *et al.*, "Higgs and Supersymmetry," arXiv:1112.3564 [hep-ph].

[72] A. Heister *et al.* [ALEPH Collaboration], Phys. Lett. B **526**, 206 (2002) [hep-ex/0112011].

[73] A. Heister *et al.* [ALEPH Collaboration], Phys. Lett. B **583**, 247 (2004).

[74] J. Abdallah *et al.* [DELPHI Collaboration], Eur. Phys. J. C **31**, 421 (2003) [hep-ex/0311019].

[75] P. Achard *et al.* [L3 Collaboration], Phys. Lett. B **580**, 37 (2004) [hep-ex/0310007].

[76] G. Abbiendi *et al.* [OPAL Collaboration], Eur. Phys. J. C **32**, 453 (2004) [hep-ex/0309014].

[77] G. Aad *et al.* [ATLAS Collaboration], "Search for squarks and gluinos with the ATLAS detector in final states with jets and missing transverse momentum using 4.7 fb^{-1} of $\sqrt{s} = 7$ TeV proton-proton collision data," arXiv:1208.0949 [hep-ex].

[78] ATLAS collaboration, "Search for squarks and gluinos with the ATLAS detector using final states with jets and missing transverse momentum and $\mathcal{L} = 5.8\ \text{fb}^{-1}$ of $\sqrt{s} = 8$ TeV proton-proton collision data," ATLAS-CONF-2012-109

[79] CMS collaboration, "Search for supersymmetry with the razor variables at CMS," CMS-PAS-SUS-12-005.

[80] G. Aad *et al.* [ATLAS Collaboration], Phys. Rev. Lett. **108**, 181802 (2012) [arXiv:1112.3832 [hep-ex]].

[81] H. Baer, V. Barger, S. Kraml, A. Lessa, W. Sreethawong and X. Tata, JHEP **1203**, 092 (2012) [arXiv:1201.5382 [hep-ph]].

[82] G. Aad *et al.* [ATLAS Collaboration], Phys. Rev. Lett. **108**, 261804 (2012) [arXiv:1204.5638 [hep-ex]].

[83] G. Aad *et al.* [ATLAS Collaboration], "Search for direct slepton and gaugino production in final states with two leptons and missing transverse momentum with the ATLAS detector in pp collisions at sqrt(s) = 7 TeV," arXiv:1208.2884 [hep-ex].

[84] H. Baer and X. Tata, Phys. Lett. B **155**, 278 (1985).

[85] H. Baer, C. -h. Chen, F. Paige and X. Tata, Phys. Rev. D **50**, 4508 (1994) [hep-ph/9404212].

[86] N. Arkani-Hamed, S. Dimopoulos, G. F. Giudice and A. Romanino, Nucl. Phys. B **709**, 3 (2005) [hep-ph/0409232].

[87] H. Baer and J. List, "Post LHC7 SUSY benchmark points for ILC physics," arXiv:1205.6929 [hep-ph].

[88] J. L. Feng and M. E. Peskin, Phys. Rev. D **64**, 115002 (2001) [hep-ph/0105100].

[89] H.-U. Martyn, hep-ph/0302024.

[90] F. Brummer and W. Buchmuller, JHEP **1107**, 010 (2011) [arXiv:1105.0802 [hep-ph]].

[91] J. A. Aguilar-Saavedra *et al.* [ECFA/DESY LC Physics Working Group Collaboration], hep-ph/0106315.

[92] H. Baer, A. Bartl, D. Karatas, W. Majerotto and X. Tata, Int. J. Mod. Phys. A **4**, 4111 (1989).

[93] C. Hensel, "Search for Nearly Mass Degenerate Charginos and Neutralinos in e^+e^- Collisions," PhD Thesis, University of Hamburg, 2002, `http://www-flc.desy.de/thesis/doctor.2002.hensel.ps.gz`

[94] T. Suehara and J. List, "Chargino and Neutralino Separation with the ILD Experiment," arXiv:0906.5508 [hep-ex].

[95] K. Desch, J. Kalinowski,G. Moortget-Pick, M. M. Nojiri and G. Polesello, "SUSY Parameter Deermination in Combined Analyses at LHC/LC," arXiv:hep-ph/0312069.

[96] A. Bharucha, "Chargino Production at a future LC in the MSSM with complex Parameters: NLO Corrections," arXiv:1202.6284 [hep-ph]. And update incl. parameter determination: talk at ICHEP 2012 `https://indico.cern.ch/contributionDisplay.py?contribId=381&confId=181298`

[97] S. Ambrosanio and G. A. Blair, Eur. Phys. J. C **12**, 287 (2000) [hep-ph/9905403].

[98] N. Wattimena, "Calorimetry at the International Linear Collider: From Simulation to Reality", PhD Thesis, University of Hamburg, 2009. `http://www-library.desy.de/cgi-bin/showprep.pl?desy-thesis-10-006`

[99] S. Matsumoto and T. Moroi, Phys. Lett. B **701**, 422 (2011) [arXiv:1104.3624 [hep-ph]].

[100] H.-U. Martyn, Eur. Phys. J. C **48**, 15 (2006) [hep-ph/0605257].

[101] R. Keranen, A. Sopczak, H. Kluge and M. Berggren, Eur. Phys. J. direct C **2**, 7 (2000).

[102] A. Freitas, C. Milstene, M. Schmitt and A. Sopczak, JHEP **09**, 076 (2008)

[103] A. Belyaev, T. Lastovicka, A. Nomerotski and G. Lastovicka-Medin, Phys. Rev. D **81**, 035011 (2010) [arXiv:0912.2411 [hep-ph]].

[104] P. Bechtle, M. Berggren, J. List, P. Schade and O. Stempel, Phys. Rev. D **82**, 055016 (2010) [arXiv:0908.0876 [hep-ex]].

[105] P. D. Grannis, "A Run scenario for the linear collider," hep-ex/0211002.

[106] H.-U. Martyn, hep-ph/0408226.

[107] A. Freitas, H. -U. Martyn, U. Nauenberg and P. M. Zerwas, hep-ph/0409129.

[108] M. Berggren, "SGV 3.0 - a fast detector simulation," arXiv:1203.0217 [physics.ins-det].

[109] M. Berggren, private communication.

[110] M. Berggren, N. d'Ascenzo, P. Schade and O. Stempel, "Summary of ILD performance at SPS1a'," arXiv:0902.2434 [hep-ex].

[111] H. Baer, R. B. Munroe and X. Tata, Phys. Rev. D **54**, 6735 (1996) [Erratum-ibid. D **56**, 4424 (1997)] [hep-ph/9606325].

[112] J. Kalinowski, W. Kilian, J. Reuter, T. Robens and K. Rolbiecki, JHEP **0810**, 090 (2008) [arXiv:0809.3997 [hep-ph]].

[113] A. Freitas, W. Porod and P. M. Zerwas, Phys. Rev. D **72**, 115002 (2005) [hep-ph/0509056].

[114] M. Berggren, F. Richard and Z. Zhang, "Dark matter with (very) heavy SUSY scalars at ILC," hep-ph/0510088.

[115] H. Baer, C. -h. Chen and X. Tata, Phys. Rev. D **55**, 1466 (1997) [hep-ph/9608221].

[116] W. Porod, M. Hirsch, J. Romao and J. W. F. Valle, Phys. Rev. D **63**, 115004 (2001) [hep-ph/0011248].

[117] S. Bobrovskyi, W. Buchmuller, J. Hajer and J. Schmidt, JHEP **1010**, 061 (2010) [arXiv:1007.5007 [hep-ph]].

[118] S. Bobrovskyi, W. Buchmuller, J. Hajer and J. Schmidt, JHEP **1109**, 119 (2011) [arXiv:1107.0926 [hep-ph]].

[119] B. Vormwald, "RPV SUSY - LHC & ILC,", presentation at KILC 2012, Daegu, `http://ilcagenda.linearcollider.org/getFile.py/access?contribId=132&sessionId=`

[120] O. Kittel, G. Moortgat-Pick, K. Rolbiecki, P. Schade and M. Terwort, Eur. Phys. J. C **72**, 1854 (2012) [arXiv:1108.3220 [hep-ph]].

[121] D. Das, U. Ellwanger and A. M. Teixeira, JHEP **1204**, 067 (2012) [arXiv:1202.5244 [hep-ph]].

[122] G. A. Moortgat-Pick, S. Hesselbach, F. Franke and H. Fraas, JHEP **0506**, 048 (2005) [hep-ph/0502036].

[123] A. Hartin, "Distinguishing the NMSSM and the MSSM at the ILC using Fittino," `https://ilcagenda.linearcollider.org/materialDisplay.py?contribId=216 &sessionId=17&materialId=slides&confId=4175`

[124] F. Deppisch *et al.*, "Slepton flavor violation," hep-ph/0408140.

[125] M. Asano, T. Saito, T. Suehara, K. Fujii, R. S. Hundi, H. Itoh, S. Matsumoto and N. Okada *et al.*, Phys. Rev. D **84**, 115003 (2011) [arXiv:1106.1932 [hep-ph]].

[126] G. A. Blair, W. Porod and P. M. Zerwas, Phys. Rev. D **63**, 017703 (2001) [hep-ph/0007107].

[127] P. Bechtle, K. Desch, W. Porod and P. Wienemann, Eur. Phys. J. C **46**, 533 (2006) [hep-ph/0511006].

[128] E. Boos, H. U. Martyn, G. A. Moortgat-Pick, M. Sachwitz, A. Sherstnev and P. M. Zerwas, Eur. Phys. J. C **30**, 395 (2003) [hep-ph/0303110].

[129] G. A. Blair, A. Freitas, H. -U. Martyn, G. Polesello, W. Porod and P. M. Zerwas, Acta Phys. Polon. B **36**, 3445 (2005) [hep-ph/0512084].

[130] J. A. Aguilar-Saavedra *et al.*, Eur. Phys. J. C **46**, 43 (2006) [hep-ph/0511344].

[131] D. Zerwas, AIP Conf. Proc. **1078**, 90 (2009) [arXiv:0808.3506 [hep-ph]].

[132] E. A. Baltz, M. Battaglia, M. E. Peskin and T. Wizansky, Phys. Rev. D **74**, 103521 (2006) [hep-ph/0602187].

[133] P. Bechtle, K. Desch, M. Uhlenbrock and P. Wienemann, Eur. Phys. J. C **66**, 215 (2010) [arXiv:0907.2589 [hep-ph]].

8 Cosmological Connections

Two of the major cosmological puzzles, namely the matter antimatter asymmetry and the dark matter of the universe can be naturally explained with new weak scale physics, respectively via electroweak baryogenesis and stable weakly-interacting massive particles (WIMPs). We discuss in turn the status of these two paradigms in the context of the two main avenues for explaining the lightness of the Higgs scalar, supersymmetry and Higgs compositeness, as well as within a model independent low energy effective field theory approach.

8.1 Baryogenesis at the Electroweak Scale

The matter-antimatter asymmetry of the universe may have been produced at the electroweak epoch [1]. In this case, the sole source of baryon number violation is from the Standard Model sphalerons and an asymmetry can be generated during the EW phase transition, provided that it is first-order. The process is non-local as it relies on charge transport in the vicinity of the CP-violating bubble walls [2]. Because it involves EW scale physics only, this mechanism is particularly appealing and has started to be tested at the LHC. EW baryogenesis has been investigated in detail in the Standard Model [3] and its supersymmetric extension [6,7,8,10,11]. Within the SM parametrization of the Higgs potential, the one loop effective potential at high temperature roughly reads

$$V(\phi,T) \approx \frac{1}{2}(\mu^2+cT^2)\phi^2+\frac{\lambda}{4}\phi^4-ET\phi^3 \quad \text{where} \quad -ET\phi^3 \subset -\frac{T}{12\pi}\sum_{i=W,Z,h} m_i^3(\phi) \quad (102)$$

The last term is responsible for a barrier separating the symmetric and broken EW vacua thus for the possibility of a first-order EW phase transition. The coefficient E is due to *bosonic* degrees of freedom coupling to the Higgs. In the SM, E is too small and the phase transition can be first-order only for a very light Higgs, excluded experimentally [4]. On the other hand, in the MSSM, new bosonic degrees of freedom with large couplings to the Higgs, mostly the stop $\tilde{t}$, can enhance the value of E and guarantee that ϕ/T be large enough ($\sim$1) at the time of the transition to suppress sphaleron washout. This has led to the so-called light stop scenario for EW baryogenesis.

8.1.1 MSSM EW baryogenesis: The light stop scenario under pressure

There is a fine-tuned window of parameter space in the MSSM where EW baryogenesis is viable [9,23]. It corresponds to a stop-split supersymmetric spectrum illustrated

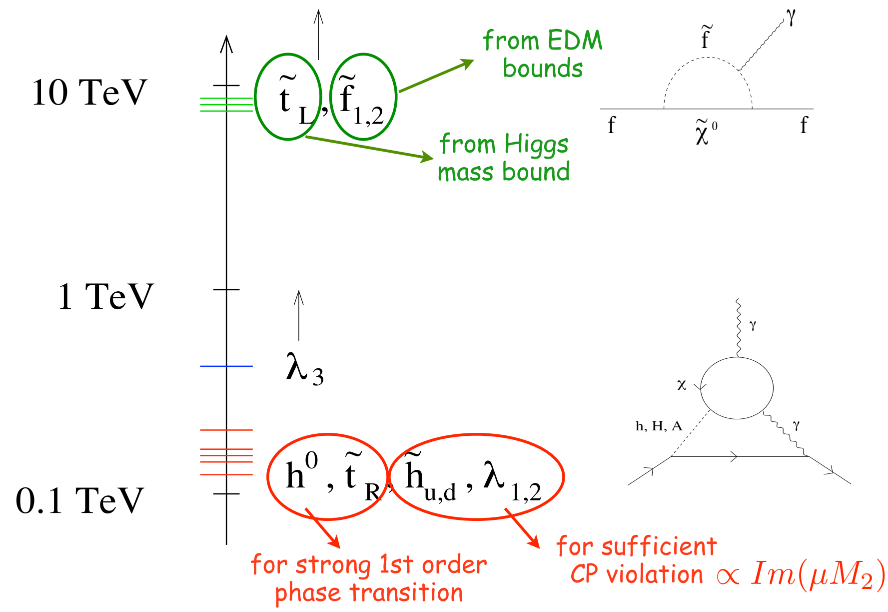

Figure 63: The stop-split supersymmetric spectrum of MSSM EW baryogenesis.

in Fig. 63. A light Higgs and a light $\tilde{t}_R$ (≤ 115 GeV) are needed for the EW phase transition to be sufficiently first-order while $\tilde{t}_L$ should be heavy to get a sufficiently heavy Higgs. Other sfermions should be heavy as well as to evade bounds from electric dipole moments. A generic difficulty of EW baryogenesis is that it requires large new sources of CP violation [5] which are typically at odds with experimental constraints from electric dipole moments. A light Higgsino and a light chargino are needed to supply CP-violating scattering processes new the expanding bubble walls during the phase transition.

Recent Higgs limits have further narrowed the region of parameter space. Moreover, additional constraints can be derived once the Higgs branching ratios are measured as new fields that couple to the Higgs can lead to significant modifications of the rates for Higgs boson production and decay. The correlation between the strength of the EW phase transition and the collider signatures of the Higgs boson were recently studied in [21] in the case of a simplified model including a new scalar field X that couples to H according to:

$$-\mathcal{L} = M_X^2|X|^2 + \frac{K}{6}|X|^4 + Q|X|^2|H|^2 = M_X^2|X|^2 + \frac{K}{6}|X|^4 + \frac{1}{2}Q(v^2 + 2vh + h^2)|X|^2 \tag{103}$$

These basic interactions describe a broad range of theories and in particular apply to the MSSM where X corresponds to a light mostly right-handed scalar top quark

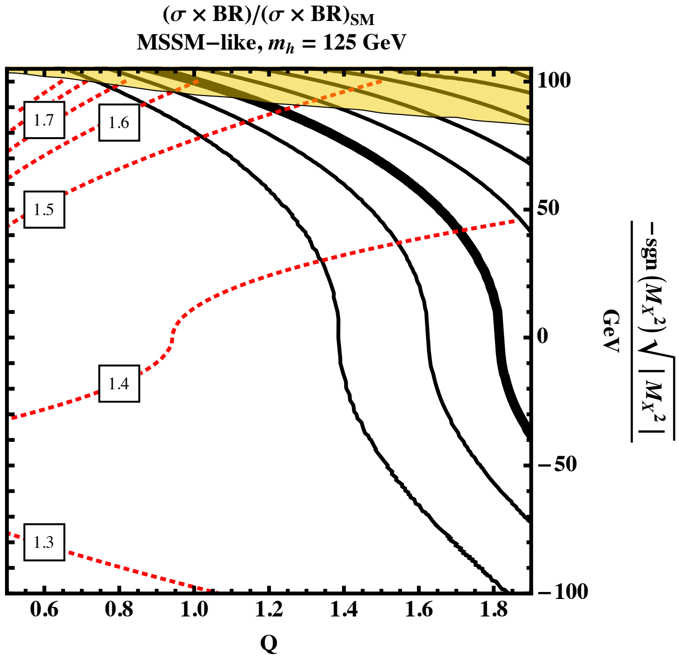

Figure 64: Contours of ϕ_c/T_c (black solid lines) for the MSSM-like model. The bolded line is for $\phi_c/T_c = 0.9$ and the adjacent solid lines delineate steps of $\Delta(\phi_c/T_c) = 0.2$. The yellow shaded region is excluded by the existence of a charge-color minimum. The red dotted lines show contours of the gluon fusion cross section times the BR to di-photons to the SM value. From [21].

responsible for one-loop thermally generated cubic Higgs interactions. However, it doe not apply to models where the strength of the EW phase transition is affected by other scalars. The Higgs production rate by gluon fusion is given at leading order by

$$\Gamma_{gg} = \frac{\alpha_s^2}{128\pi^3}\frac{m_h^3}{m_W^2}\left|\sum_i g_i T_2^i F_{s_i}(4m_i^2/m_h^2)\right|^2 \tag{104}$$

where F_{s_i} are loop functions and T_2^i is defined by $\mathrm{tr}(t_r^a t_r^b) = T_2^r \delta^{ab}$. The sum i runs over all particles that couple to the Higgs, $g_i = g$ for SM states and for an exotic scalar X coupling to the Higgs, $g_X = \frac{2}{9}\left(\frac{m_W}{m_X}\right)^2 Q$. The width to di-photons at LO is (d_i is the dimension of the $SU(3)_c$ representation):

$$\Gamma_{\gamma\gamma} = \frac{\alpha^2}{1024\pi^3}\frac{m_h^3}{m_W^2}\left|\sum_i g_i q_i^2 d_i F_{s_i}(4m_i^2/m_h^2)\right|^2 \tag{105}$$

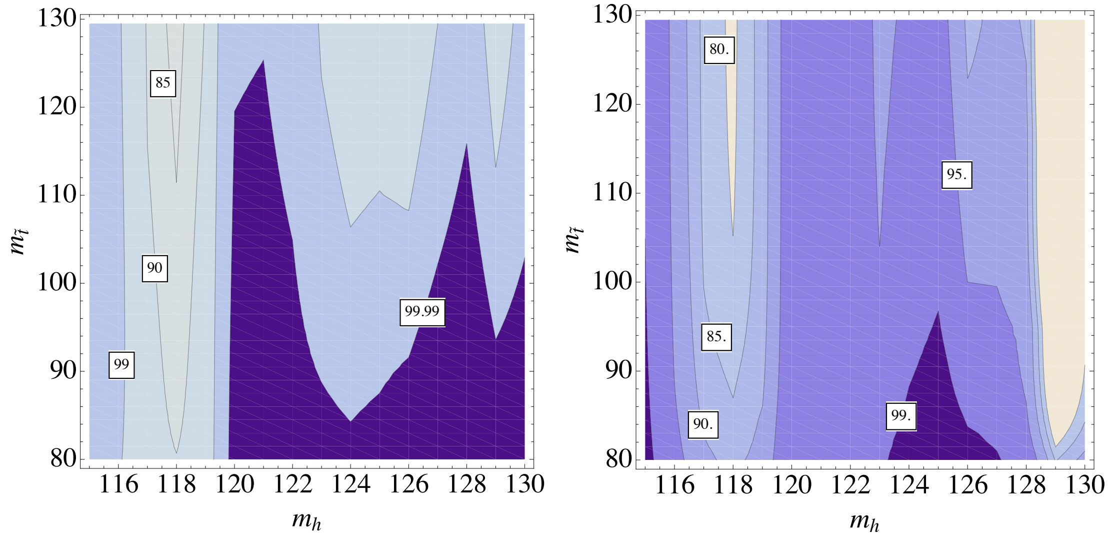

Figure 65: Confidence levels of exclusion of a general Light Stop scenario in the $(m_h, m_{\tilde{t}_R})$ plane. $\tilde{t}_L$ is taken very heavy while m_A and $\tan\beta$ are varied in the range (1500, 2000) GeV and (5,15). From [22].

The light stop interferes constructively with the top loop leading to a significant increase in the Higgs production cross section by gluon fusion. On the other hand, it decreases the decay width into di-photons. The alterations on gluon fusion and di-photon decay are the main manifestations of a new scalar strengthening the EW phase transition. The correlations are shown in Fig. 64 in the case of $m_H = 125$ GeV and for a scalar X having the same properties are $\tilde{t}_R$, therefore describing the MSSM-like case. From this plot, it is clear that in the region where the phase transition is sufficiently strongly first-order ($\phi_c/T_c > 0.9$), large deviations are expected with respect to the SM Higgs properties. Actually, it was concluded in [22] that EW baryogenesis in the MSSM can be excluded using 2011 LHC data, see Fig. 65.

Therefore, it appears that the MSSM EW baryogenesis window can be ruled out indirectly by Higgs searches at the LHC without having to rely on the much more challenging detection of the direct production of light stops [34].

One main difficulty with the MSSM baryogenesis is that the first-order phase transition is a one-loop effect. It is much easier to obtain a strong first-order phase transition by modifying the Higgs potential at tree level. One straightforward example is to add a scalar singlet. There is an extensive literature on this possibility. A recent and complete study of this scenario was provided in Ref. [26]. Interestingly, such a scenario can be theoretically well-motivated in composite models where the Higgs

G	H	N_G	NGBs rep.$[H]$ = rep.[SU(2) × SU(2)]
SO(5)	SO(4)	4	$\mathbf{4} = (\mathbf{2}, \mathbf{2})$
SO(6)	SO(5)	5	$\mathbf{5} = (\mathbf{1}, \mathbf{1}) + (\mathbf{2}, \mathbf{2})$
SO(6)	SO(4) × SO(2)	8	$\mathbf{4_{+2}} + \bar{\mathbf{4}}_{\mathbf{-2}} = 2 \times (\mathbf{2}, \mathbf{2})$
SO(7)	SO(6)	6	$\mathbf{6} = 2 \times (\mathbf{1}, \mathbf{1}) + (\mathbf{2}, \mathbf{2})$
SO(7)	G_2	7	$\mathbf{7} = (\mathbf{1}, \mathbf{3}) + (\mathbf{2}, \mathbf{2})$
SO(7)	SO(5) × SO(2)	10	$\mathbf{10_0} = (\mathbf{3}, \mathbf{1}) + (\mathbf{1}, \mathbf{3}) + (\mathbf{2}, \mathbf{2})$
SO(7)	$[\mathrm{SO}(3)]^3$	12	$(\mathbf{2}, \mathbf{2}, \mathbf{3}) = 3 \times (\mathbf{2}, \mathbf{2})$
Sp(6)	Sp(4) × SU(2)	8	$(\mathbf{4}, \mathbf{2}) = 2 \times (\mathbf{2}, \mathbf{2}), (\mathbf{2}, \mathbf{2}) + 2 \times (\mathbf{2}, \mathbf{1})$
SU(5)	SU(4) × U(1)	8	$\mathbf{4}_{-5} + \bar{\mathbf{4}}_{\mathbf{+5}} = 2 \times (\mathbf{2}, \mathbf{2})$
SU(5)	SO(5)	14	$\mathbf{14} = (\mathbf{3}, \mathbf{3}) + (\mathbf{2}, \mathbf{2}) + (\mathbf{1}, \mathbf{1})$

Figure 66: Cosets G/H from simple Lie groups and associated Goldstone spectra. From [36].

arises as a pseudo-Nambu Goldstone boson of a new strongly interacting sector, as we discuss next.

8.1.2 EW baryogenesis in Composite Higgs models

There are two main avenues for explaining the lightness of the Higgs scalar: supersymmetry and Higgs compositeness. The idea of Higgs compositeness has received a revival of interest in the last few years [18,19], boosted by the dual description in terms of warped extra dimensional models. In composite Higgs models, the hierarchy between the Planck and TeV scale is due to the slow logarithmic running of an symptomatically free interaction that becomes strong and confines close to the EW scale. In analogy with QCD, as the strong interaction confines, the global symmetry acting on the techniquarks is broken down to a subgroup, delivering Goldstone bosons which are the analogs of the pions in QCD and may be identified as the degrees of freedom belonging to the Higgs doublet. To preserve the custodial $SO(4)$ symmetry of the SM, the Higgs should transform as a $(2, 2)$ of $SU(2)_L \times SU(2)_R \sim SO(4)$. In the minimal composite Higgs model SO(5) breaks to SO(4), delivering 4 goldstone bosons which are identified as the Higgs degrees of freedom. The $SO(5)$ symmetry is broken explicitly both by the fermions which do not come in complete representations of SO(5) and by the gauging of $SU(2)_L \in SO(5)$. Loops of SM fermions or gauge bosons communicate the explicit breaking to the (pseudo) NGBs and generate a potential for the Higgs. In these models, the top quark is also composite as the Yukawa hierarchy is explained by partial fermion compositeness. Models where the

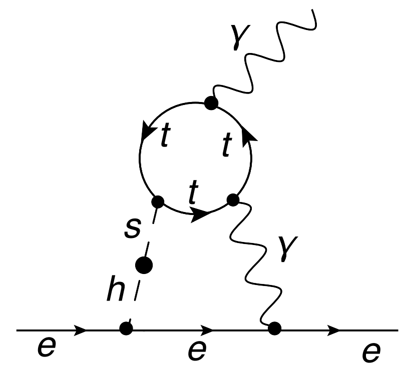

Figure 67: Diagram illustrating the largest contribution to the electron EDM due to the Higgs-singlet mixing where the new singlet s couples only to the top quark, as needed for EW baryogenesis and as motivated by the scenario of partial compositeness. From [27].

Higgs arises as a pseudo-Nambu Goldstone boson from a strongly interacting sector have become a plausible option and serious alternative to supersymmetry. They also offer new possibilities for EW baryogenesis. Naturalness in these scenario implies modifications in the Higgs and top sectors which are precisely the ones believed to be responsible for EW baryogenesis. Depending on the coset space, these models can give rise to additional goldstones in the light scalar spectrum that generically make the EW phase transition first order. For instance, if the coset is $SO(6)/SO(5)$, we expect an additional singlet [35]. For $SO(6)/SO(4) \times SO(2)$, there are instead two Higgs doublets. Various possibilities are summarized in Fig. 66 taken from Ref. [36].

The case where the coset is $SO(6)/SO(5)$ leads to an extra singlet which has a dimension-five pseudo scalar couplings to the top quarks that can break CP. EW baryogenesis in this context has been studied in Ref. [27]. The extra singlet is responsible for making the EW phase transition first order. Secondly, if that scalar couples to the top quark it can lead to a non-trivial CP-violating phase along the bubbles of the EW phase transition creating the seed for the sphaleron to generate a non-zero baryon asymmetry. It was shown that the correct amount of asymmetry can be produced in a large region of parameter space. The new complex phases and the mixing between the Higgs and the singlet lead to new contributions to the EDMs of neutron and electron not far from the reach of current and future experiments (see Fig. 67).

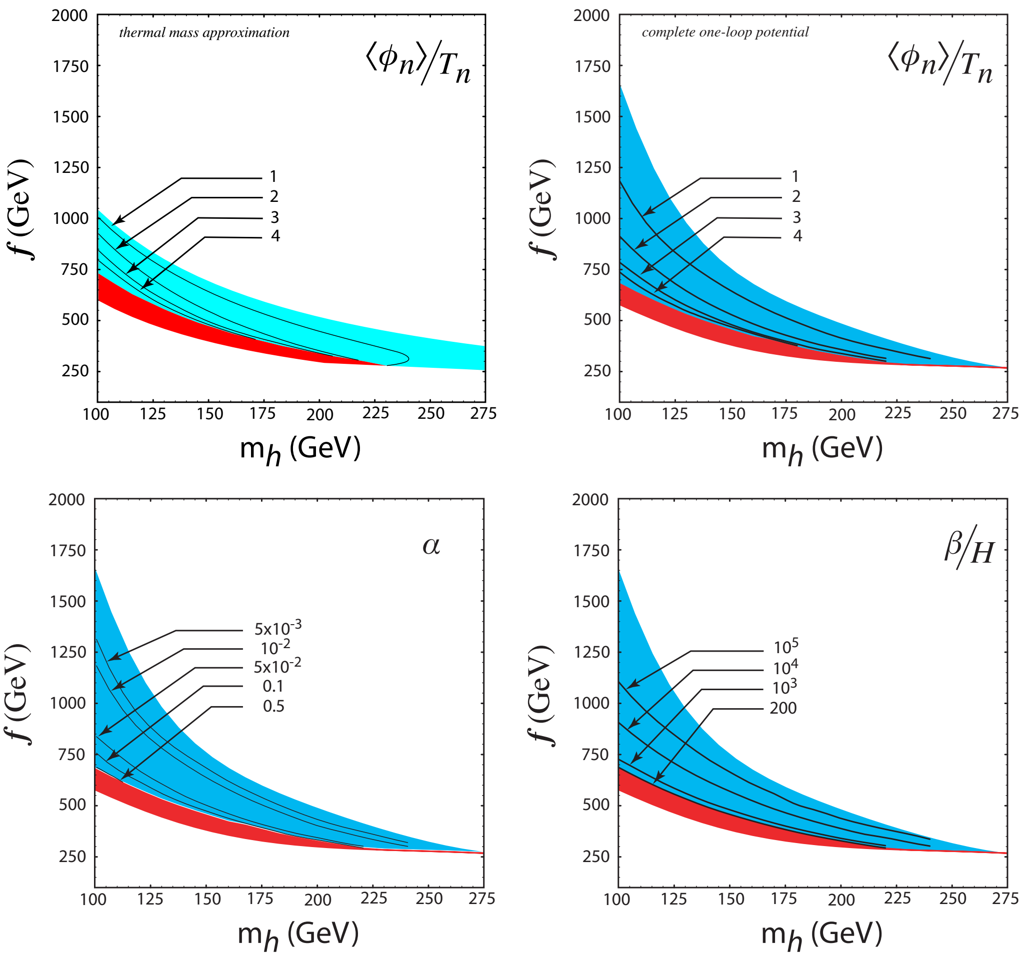

Figure 68: Upper panel: Contours of the ratio $\langle\phi\rangle/T$ evaluated at the nucleation temperature in the blue region that allows for a first-order EW phase transition. The left plot uses the thermal mass approximation [24] while the right plot uses the full one-loop potential [25]. Below the red lower bound, the EW symmetry remains intact in the vacuum while above the blue upper one, the phase transition is second order or not even occurs. Within the red band, the universe is trapped in a metastable vacuum and the transition never proceeds. The lower panel shows contours of $\alpha \approx \frac{\text{latent heat}}{\text{thermal energy density}}$ and $\beta/H = T_n d(S_3/T)/dT \approx$ number of bubbles per horizon volume that both measure the amount of overcooling. From [25].

8.1.3 *Effective field theory approach to the EW phase transition*

Tree level modifications of the Higgs potential can easily make the EW phase transition strongly first-order even for large Higgs masses. This can be further illustrated in a model-independent manner using an effective field theory approach, for instance by adding dimension-6 operators in the Higgs potential allowing for a negative quartic coupling [24,25]:

$$V(\phi) = \mu^2|\phi|^2 - \lambda|\phi|^4 + \frac{|\phi|^6}{f^2} \tag{106}$$

Fig. 68 shows contours of quantities characterizing the strength of the phase transition and amount of supercooling in the (m_h, f) plane. From these plots, it is clear that a phase transition that is strong enough for EW baryogenesis arises in a sizable region of parameter space. On the other hand, for such a typical polynomial potential, not much supercooling is expected except in a small fine-tuned region at the vicinity of the red band. Therefore, the cosmic background of gravity waves resulting from bubble collisions at the EW epoch will be too small to be observable by LISA [30,33]. Anyhow, in the parameter region of interest, a potential like (106) leads to deviations of order 1 in the Higgs self couplings $\mathcal{L} = m_H^2 H^2/2 + \mu H^3/3! + \eta H^4/4! + \cdots$ as

$$\mu = 3\frac{m_H^2}{v} + 6\frac{v^3}{f^2} \qquad \eta = 3\frac{m_H^2}{v^2} + 36\frac{v^2}{f^2}. \tag{107}$$

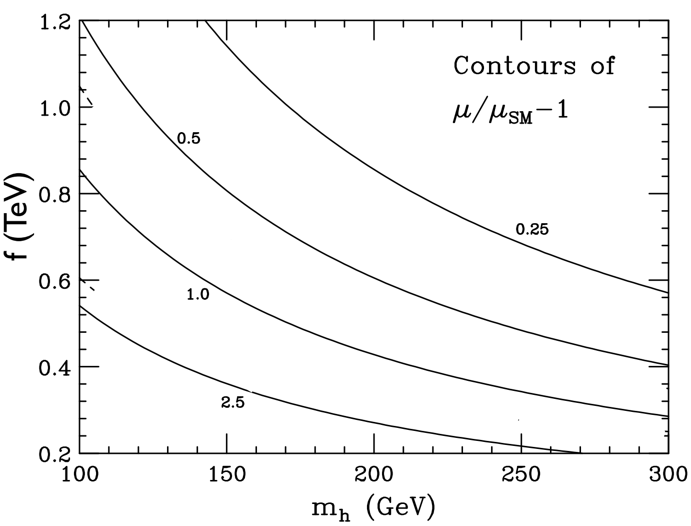

Figure 69: Contours of $\mu/\mu_{SM} - 1$ in the (m_h, f) plane.

The SM couplings are recovered as $f \to \infty$ [24]. Figure 69 shows contours of $\mu/\mu_{\rm SM}-1$ in the f vs. m_H plane. Therefore, non-trivial probes of the Higgs potential may be obtained from precise measurements of the trilinear Higgs coupling, see Ref. [29] for other examples.

Higgs self-coupling measurements are extremely challenging. At the LHC, they are typically afflicted with large backgrounds [103]. For a SM 125 GeV Higgs, it was recently shown that a target luminosity of 1000 fb^{-1} would be needed to be able to set constraints on the Higgs self-coupling [102]. Prospects for the trilinear self coupling measurement at the ILC have been studied through the process $e^+e^- \to ZHH$. For $M_H = 120$ GeV and $\sqrt{s} = 500$ GeV, it was estimated that the Higgs trilinear self coupling could be measured with a $\sim 25\%$ accuracy, see for instance [104,105,106,107].

While the nature of the EW phase transition has been studied in various non-supersymmetric extensions of the SM, e.g. in models of technicolor [12], models with flat extra dimensions [37], Randall-Sundrum models [13,14,15,16,31], no full calculation of the baryon asymmetry has been carried out in these contexts. In some of these constructions, the EW phase transition can be too strongly first-order, leading to supersonic bubble growth which suppresses diffusion of CP violating densities in front of the bubble walls, thus preventing the mechanism of EW baryogenesis [17].

The bubble wall velocity is a key quantity entering the calculation of the baryon asymmetry. A model-independent and unified description of the different regimes (detonation, deflagration, hybrid, runaway) characterizing bubble growth was presented in Ref. [17]. Results are summarized in Fig. 70 showing contours for the bubble wall velocity in the plane (η, α_N) where η and α_N are dimensionless parameters characterizing the strength of the phase transition (roughly the ratio of latent heat to thermal energy density) and the amount of friction. In the SM $\eta \sim 1/1000$ while in the SM $\eta \sim 1/30$. For any given model, one would have to calculate these quantities for a reliable computation of the baryon asymmetry.

We conclude this part by a few remarks on the cosmological signatures of a strong first-order EW phase transition. As mentioned earlier, bubbles collisions during the EW phase transition will produce a stochastic background on GW waves. Interestingly, the associated frequency is in the LISA frequency range [30,33]. Unfortunately, the expected signal is typically below LISA's sensitivity except in some specific cases. In particular, it was stressed in [31,14] that the observation of GW background peaked in the millihertz would be a signature of near conformal dynamics at the TeV scale as only a scalar potential of the type

$$V(\mu) = \mu^4 \times f(\log(\mu)) \tag{108}$$

can naturally lead to large supercooling that can result in an observable background of gravity waves. The shape of the potential and the dependence of the critical bubble

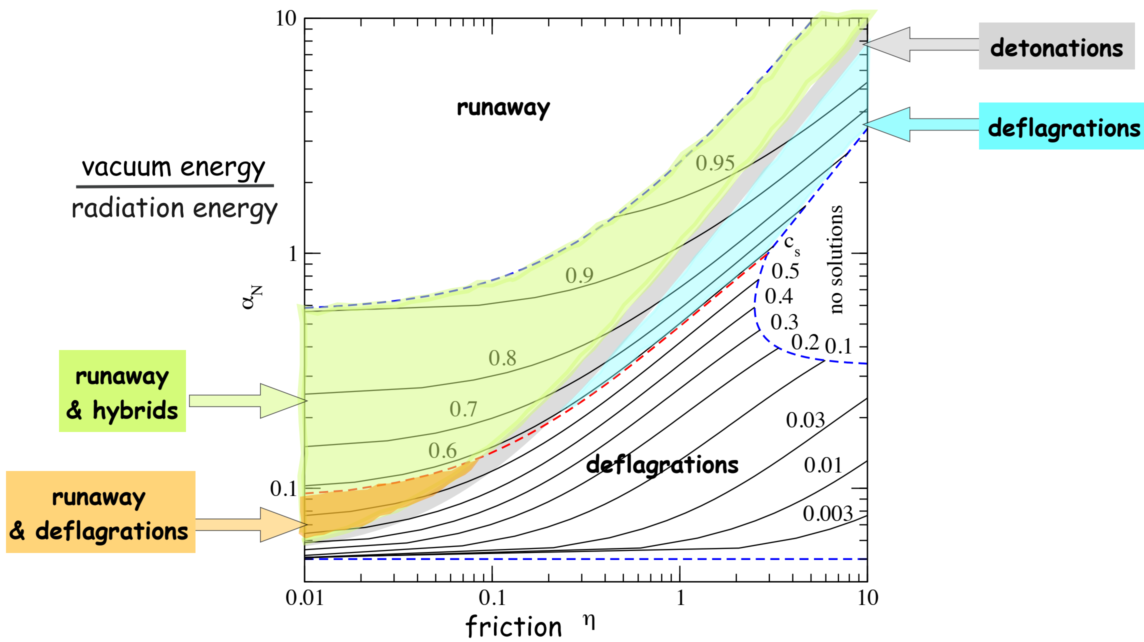

Figure 70: Contours of the bubble wall velocity in the (η, α_N), from [17].

action on temperature are shown in Fig. 71 in comparison with the ones from a standard polynomial potential. Such dynamics could apply to a dilaton (see [38] for a related discussion) and may be relevant for a very different mechanism of baryogenesis known as *cold baryogenesis* [32]. One advantage of cold baryogenesis is that it does not depend on the details of the new sources of CP violation, which can be described by dimension-six effective operators $\phi^\dagger\phi\tilde{F}F/\Lambda^2$, which are relatively unconstrained by EDMs [39].

8.2 Dark Matter and the ILC

8.2.1 Status of dark matter

The dark matter paradigm is now one of the pillars of the standard model of cosmology. There are many pieces of evidence, from galactic length scales, cluster lengths scales, and the largest observable scales in the universe, that roughly 20% of the energy and 80% of the mass in the Universe is in the form of massive, non-baryonic particles with relatively weak interactions with ordinary matter [40]. There are many proposals for the nature of this dark matter. The proposed particles span an enormous range in mass, from 10^{-5} eV to macroscopic and even planetary-scale masses. How-

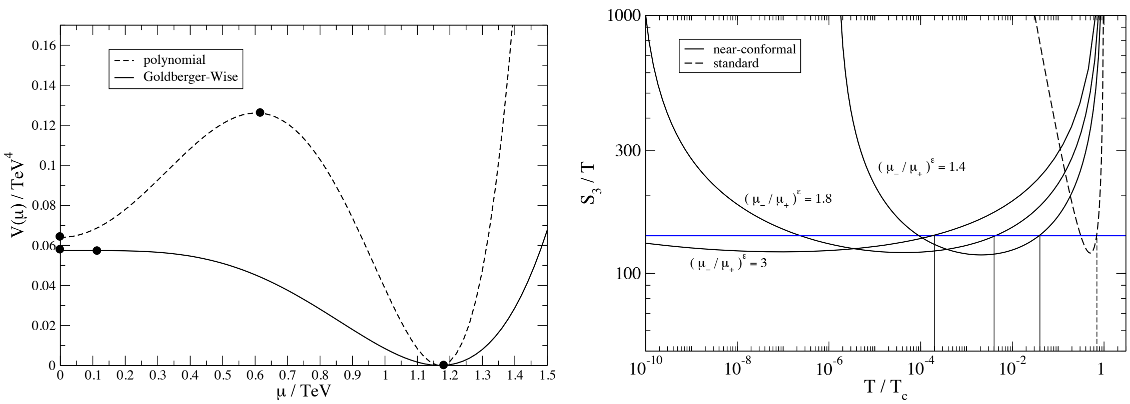

Figure 71: Left: Comparison of a typical polynomial potential given here $\lambda(\mu^2 - \mu_0^2)^2 + \Lambda^{-2}(\mu^2 - \mu_0^2)^3$ with a nearly conformal potential of the type of Eq. (108). The $\bullet$ indicates the position of the maxima. Right: The tunneling action S_3/T as a function of T/T_c for a typical nearly conformal potential (solid line) (we used the Goldberger-Wise potential for illustration) and for a usual polynomial Higgs potential (dashed line). The horizontal blue line indicates the tunneling value $S_3/T \sim 4\log(M_{Pl}/T_{EW}) \sim 140$. For a standard potential, the nucleation temperature T_n is always close to the critical one, T_c, unless some fine-tuning is invoked. For a nearly conformal potential, supercooling is a general feature and T_n can easily be several orders of magnitude below T_c.

ever, the most attractive proposal, and the one that we will concentrate on here, is that the particle that makes up dark matter is a 'weakly-interacting massive particle' (WIMP).

A WIMP is defined as a weakly interacting neutral particle that is stable over the lifetime of the universe. WIMPs can be created or destroyed only in pairs. The WIMP model further assumes that the WIMPs were in thermal equilibrium with the hot plasma of Standard Model particles early in the history of the universe. This initial condition allows us to predict the current density of WIMPs. In the model, when the temperature of the universe decreased below the WIMP mass, WIMPs began to annihilate, but, because the anninhilation requires a pair of WIMPs, the annihilation cut off when the density of WIMPs reached a well-defined small value. The density of WIMPs decreased further due to the expansion of the universe. However, as the Universe cooled, this small density of massive WIMPs eventually came to dominate the energy in radiation. By this logic, it is possible to derive the expression for the current energy density of Universe in WIMPs,

$$\Omega \sim \frac{x_F T_0^3}{\rho_c M_{Pl}} \frac{1}{\langle \sigma_{ann} v \rangle} \ . \tag{109}$$

In this expression, $x_F = m/T_F$ where m is the WIMP mass and T_F is the freeze-out temperature at which annihilation turns off, T_0 is the temperature of photons today, ρ_c is the critical energy density, M_{Pl} is the Planck scale, and $\langle\sigma_{ann}v\rangle$ is the inclusive cross section for WIMP pair annihilation into SM particles, averaged over the WIMP thermal velocity distribution at freeze-out. Typically $x_F \approx 25$, with weak dependence on the WIMP mass, and the other parameters in the equation, including Ω, are well measured. The expression (109) then determines the value of the annihilation cross section needed for the entire dark matter relic density to be composed of a single WIMP species. The result is shown in Fig. 72citeSteigman:2012nb. The required value is roughly

$$\langle\sigma_{ann}v\rangle \approx (1 \ \ \text{pb}) \cdot c \ , \tag{110}$$

indicating that a WIMP with mass and interactions at the electroweak scale naturally leads to the required density of dark matter.

This observation motivates searches for WIMPs with masses of the order of 100 GeV, making use of techniques from particle physics. The three pillars of WIMP searches are: indirect detection of residual annihilation of WIMPs in the galactic neighborhood, direct detection of ambient WIMPs scattering off of sensitive detectors on Earth, and artificial production of of WIMPs at high energy accelerators.

If a candidate particle for WIMP dark matter can be produced at the ILC, the precision study of its mass and properties available through the ILC measurements might make it possible to predict its pair annihilation cross section and thus its thermal relic density. This prediction can then be compared to the density of dark matter measured by astrophysical observations. This possibility of a direct connection between physics at the smallest and largest length scales is extremely enticing. Later in this section, we will discuss a number of scenarios in which the ILC makes such a comparison possible.

8.2.2 Theories of WIMPs

By far the most popular vision of WIMP dark matter is the neutralino found in supersymmetric theories. Supersymmetric theories are particularly amenable to searches at the LHC, because they contain a wealth of new colored states (squarks and gluons) with large hadroproduction cross sections. Such particles can decay into the dark matter plus jets of hadrons, leading to events characterized by hadronic activity together with a large imbalance of transverse momentum. As of this writing, the absence of a signal places limits on the masses of squarks and gluons to be substantially in excess of 1 TeV, depending on the fine details of the mass spectrum [56,57]. The null results of these searches, combined with the early indications that the Higgs mass may lie around 125 GeV [58,59] have lead to some speculation that if supersymmetry

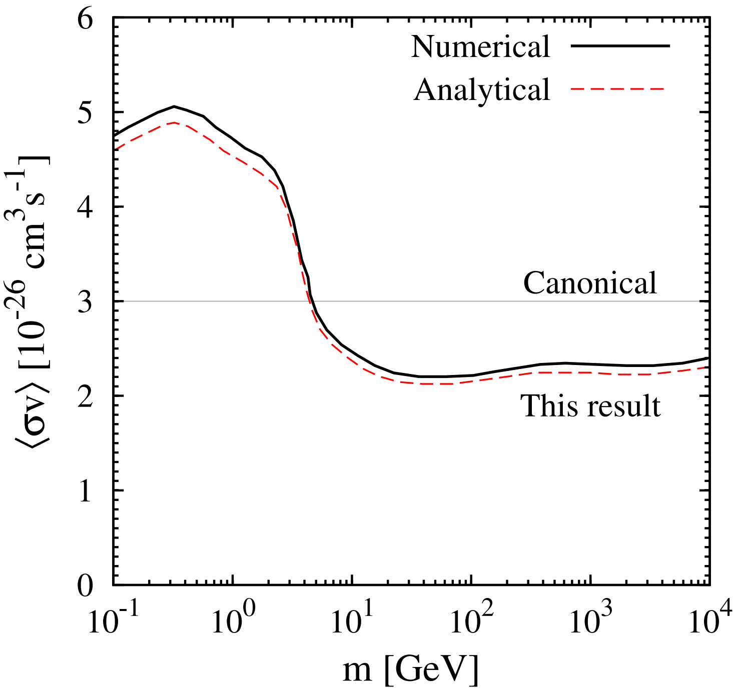

Figure 72: Desired annihilation cross section $\langle \sigma v \rangle$ to obtain the measured thermal relic density, as a function of the WIMP mass m (from Ref. [42]). The line marked "canonical" shows the oft-quoted value 3×10^{26} cm^3/s.

is realized in nature, it may not be minimal. Nonetheless, viable points with modest fine-tuning still exist [60], and for the purposes of this discussion we will stay within the minimal supersymmetric extension of the SM.

Searches for supersymmetry based on the 2011 LHC data have focused on searches for the colored superpartners [61]. Such searches are important in terms of characterizing the over-all scale of super-partner masses, but offer only a limited vista on the properties of supersymmetric dark matter. As the LHC collects more data and at higher energies, it becomes more sensitive to the electroweak super partners, and thus has more directly to say about the properties of dark matter.

Beyond supersymmetric theories, the most studied candidates for WIMP dark matter include the lightest Kaluza-Klein particle in 5-dimensional [44,45] or 6-dimensional [46,47] theories with Universal Extra Dimensions [48], and a light neutral vector boson in little Higgs theories [49,50] incorporating T-parity [51]. All of these theories are primarily distinguished from supersymmetric theories in that the WIMP is a boson rather than a Majorana fermion. One other nonsupersymmetric theory which affords some contrast is based on a warped extra dimension [52] and has a dark matter particle which is a Dirac fermion [53,54,55,108].

Recently, there has also been activity aimed at capturing features of WIMP dark matter in cases where the particles mediating the interactions are heavy compared to the energy transfer of the processes of interest, by making use of effective field theory (EFT) descriptions of WIMPs [62]-[78]. Such effective field theories allow for one to capture the low energy properties of any theory which is amenable to an EFT description, and facilitates comparisons between the different types of searches for dark matter. The picture which emerges from such studies is that there is a large degree of complementarity between direct, indirect, and collider searches. Direct and indirect detection constraints are typically stronger than collider bounds, but also subject to relatively large astrophysical uncertainties, and only apply to interactions which do not vanish in the limit in which WIMPs are non-relativistic. Instead, collider bounds apply roughly uniformly to any type of interaction involving the particles available in the initial state, but are limited for heavy WIMP masses by the finite energy available in the collision.

Another feature which is easily discerned from effective theory descriptions is that bounds from the Tevatron and LHC typically apply to WIMP couplings to quarks and gluons, whereas the couplings most relevant at a high energy e^+e^- collider are the couplings to electrons and photons. While the most popular models of dark matter predict that couplings to quarks and leptons are comparable, it is possible to construct leptophilic models [79,80,81], motivated in part by the observation of an anomalous positron flux by the PAMELA and Fermi LAT collaborations [82,83].

Beyond the straightforward freeze-out paradigm, there are other models of dark matter for which dark matter particles at the electroweak scale are relevant. The universe energy density stored in WIMPs may exhibit an explicit dependence on extra parameters, in particular the dark matter mass, for instance in models of asymmetric dark matter e.g. [109]. Dark matter may also be produced by 'freeze-in' scenarios such as that in [110] or in scenarios where DM is is produced through decays [111].

8.2.3 *Prospects for ILC determination of dark matter parameters*

Once dark matter is detected through a non-gravitational interaction, and is thus confirmed to be some kind of weakly interacting particle, the primary question will be whether or not its annihilation cross section is of the correct size for it to explain the cosmic dark matter as a thermal relic. If the annihilation cross section reconstructed from measurements on the particle is consistent with the determinations of the dark matter density, it will provide evidence that the thermal history of the Universe was (at least approximately) standard back to the time that the dark matter froze out—about 1 nsec after the Big Bang. This would parallel the argument the successful predictions of big bang nucleosynthesis based on measurements in nuclear physics lead to a compelling picture of the history of the Universe back to temperatures of order MeV [84] and times of order 1 second.

In principle, the most direct determination of the dark matter annihilation cross section would come from an observation by indirect detection experiments which look for annihilation of WIMPs in the galaxy. In practice, this is a daunting task, because of large uncertainties in astrophysical backgrounds, which can mask or pollute the signal, and in the distribution of dark matter itself, which enters into the observed photon flux as the density squared integrated along the line of sight of the observation. In addition, a relatively few final states are expected to be observable on the Earth, necessarily leading to an incomplete picture. It is also worth mentioning that if the annihilation cross section is strongly velocity-dependent, annihilation channels which were important at the time of freeze-out ($v \sim 0.1$) may be subdominant in the galaxy today ($v \sim 10^{-3}$). Similarly, direct detection experiments are really sensitive only to couplings to colored SM particles, which could turn out to represent a relatively unimportant fraction of the totality of WIMP annihilation. Direct detection also loses track of some types of interactions which may be important for WIMP annihilation, but are suppressed in the non-relativistic limit of elastic scattering.

Consequently, colliders play an essential role in providing a complete picture of the dark matter interactions with the SM, and it is further necessary to access all sectors of the SM itself. Hadron colliders such as the LHC have large rates of production for exotic colored particles (and also typically higher energies, allowing searches for more massive particles), but also larger backgrounds and less precision than e^+e^- counterparts which may render some states difficult to identify. In a typical theory of WIMPs such as the MSSM or UED models, the relic density is controlled by a a complicated interplay between annihilations into colored and uncolored states, and thus an accurate picture may require input from more than one collider.

The impact of an ILC on the measurement of dark matter properties depends on where the LHC will leave off. The following discussion is based on a few of the most detailed studies of the MSSM [85,86]. These studies assume and end stage LHC running at $\sqrt{s} = 14$ TeV and hundreds of fb^{-1}. Under such conditions, many of the measurements will be systematics limited and thus the precise assumptions for collected data sample are less important than the assumed collision energy. For a partial list of other investigations into the measurement of dark matter properties at a linear collider, see Refs. [88]-[98].

In Ref. [86,87], two mSUGRA-inspired models are investigated in terms of the ability of the LHC and 500 GeV ILC to reconstruct the spectrum and couplings of

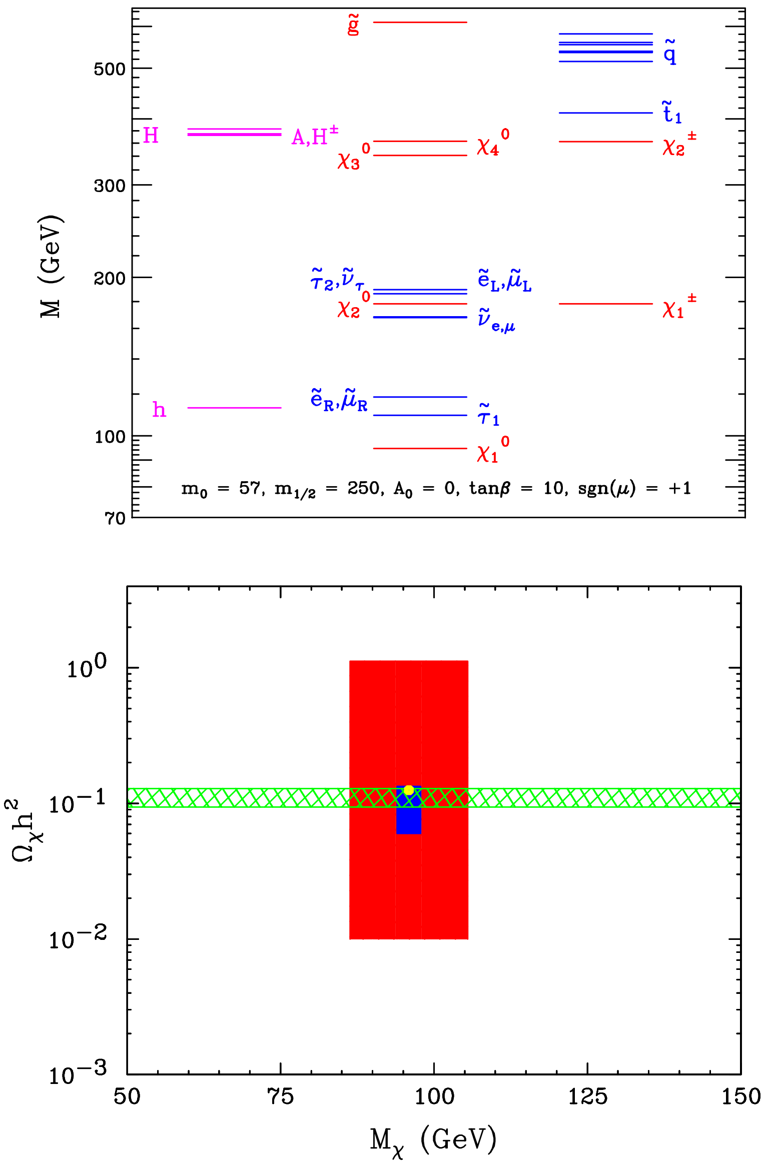

Figure 73: Spectrum (left) and projections for determination of the WIMP mass and inferred relic density (right) based on measurements at the (end stage) LHC (red rectangle) and ILC (blue rectangle), for supersymmetric model B' (from Refs. [86,87]). The measurement of the relic density from cosmology is indicated by the green hatched region, and the actual model prediction is shown as the yellow dot.

the neutralino. Model B' is characterized by low sparticle masses (in fact, masses

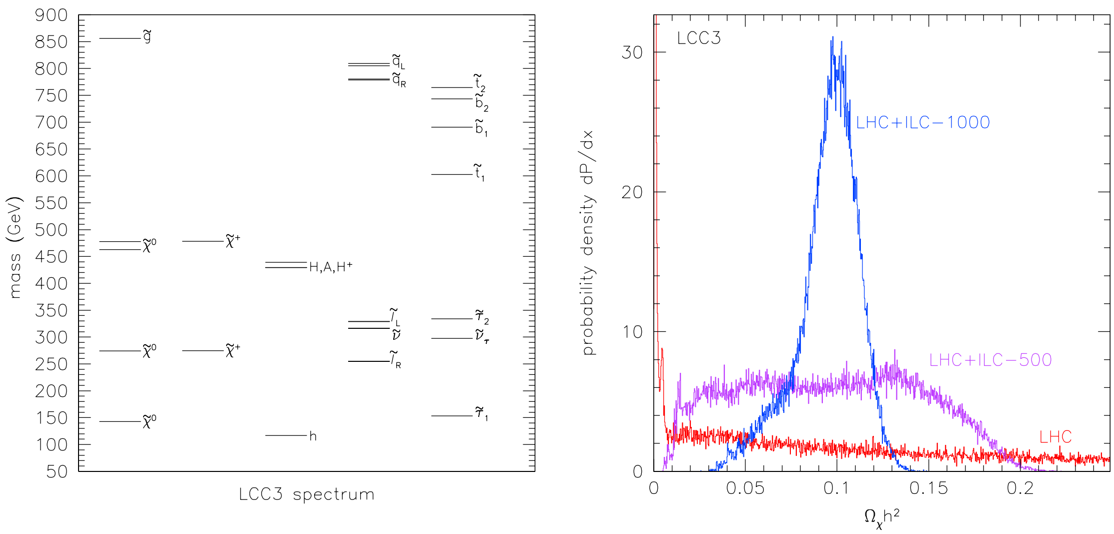

Figure 74: Mass spectrum of superparticles (left) and reconstructed relic density probability distribution (right) based on measurements at the LHC alone (red histogram), LHC + a 500 GeV ILC (magenta histogram) and LHC + a 1000 GeV ILC (blue histogram) for the MSSM point LCC3. From Ref. [85].

already ruled out by current LHC searches for colored super partners and large mass splittings, resulting in a model that is particularly amenable to reconstruction using LHC measurements alone. In Figure 73, we show the sparticle spectrum and the range of reconstructed relic densities for model B'. The derived relic density indicates that for this (ruled out) "easy case", the LHC finds a spread on the order of a factor of ten in the reconstructed relic density, whereas the ILC, which even for limited energy also finds this an easy case because of the light super-partner masses, can reduce this spread to This model is very similar to model LCC1 studied in Ref.[85], which shows that by including information from a wider range of observables, the ILC can in fact reconstruct the relic density to lie within a few percent of the WMAP-preferred value.

In Ref. [85], four MSSM parameter choices (LCC1-4) are investigated from the point of view of indirect and direct searches for dark matter, LHC searches, and an ILC at $\sqrt{s} = 500$ GeV and 1000 GeV, in order to see how many relevant dark matter properties can be reconstructed. In Model LCC3, the relic density is largely controlled by late coannihilation of the lightest neutralino with a stau. The small mass splitting renders the stau particularly challenging to reconstruct at the LHC. In Figure 74, we show the sparticle spectrum and the range of reconstructed relic densities for model LCC3. As shown, the LHC has essentially no ability to reconstruct the relic density,

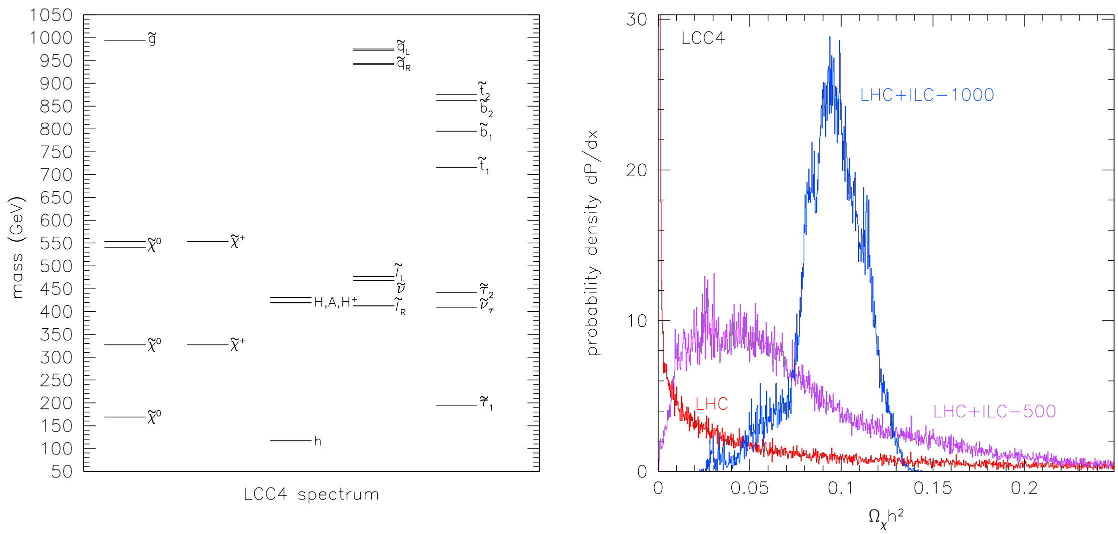

Figure 75: Mass spectrum of superparticles (left) and reconstructed relic density probability distribution (right) based on measurements at the LHC alone (red histogram), LHC + a 500 GeV ILC (magenta histogram) and LHC + a 1000 GeV ILC (blue histogram) for the MSSM point LCC4. From Ref. [85].

because it is unable to obtain precise enough measurements of the neutralino and stau masses, and the neutralino and tau compositions leave large uncertainties in the coannhilation cross section. At the 500 GeV ILC, the situation clarifies, but remains rather uncertain, because while the neutralino and stau masses become much better measured, the neutralino composition remains uncertain. A 1 TeV ILC can fill in this remaining information, and results in a reasonably precise measurement of Ωh^2 to within a factor of two.

In LCC4, the relic density is driven by neutralinos which annihilate through a heavy Higgs resonance that is approximately on-shell because the SUSY Higgses have masses $\sim 2m_{\chi_1^0}$. The colored sparticles are heavy (roughly at the current LHC exclusion limits for the gluino and first two generations of squarks and well above the current limits on third generation squarks). This point is a particular challenge for the LHC (despite the fact that it is able to observe much of the spectrum of particles) to reconstruct, because it requires very high precision measurements of the mass of the lightest neutralino and the mass and width of the pseudo-scalar Higgs boson A^0, as well as reasonably precise knowledge of the lightest neutralino composition. See Figure 75. The resulting relic density prediction is peaked at very low values, with a substantial tail that extends past the WMAP measurement. At the 500 GeV

ILC, the situation remains somewhat fuzzy, because the pseudo-scalar remains out of kinematic reach, though the composition of the neutralino becomes much-better understood. At the 1000 GeV ILC, production of $A^0 h^0$ opens up, and the picture becomes reasonably clear.

Over-all, the picture that emerges is one in which the ILC is often necessary to provide the crucial information allowing one to reconstruct the relic density of neutralinos, but whether it is effective in accomplishing this goal is largely dependent on whether or not it has enough energy to access the important states. In the case studies shown here, the LHC data will typically be able to identify the relevant mass scales for particles which may of interest, but it may remain unclear post-LHC which of those particles are in fact crucial to pin down the relic density.

As a final example, we consider a leptophilic model of dark matter. For example, if interactions between a generic Dirac WIMP χ and the SM leptons are mediated by a heavy vector particle, they may be described by the effective vertex,

$$\frac{1}{M_*^2}\,\overline{\chi}\gamma^\nu\chi\sum_{\ell=e,\mu,\tau}\overline{\ell}\gamma_\nu\ell \qquad (111)$$

and to illustrate the point, we assume that there are no couplings to quarks at tree level. M_* is a dimensionful coupling constant which maps on to the description of Z' exchange through $1/M_*^2 \leftrightarrow g_\ell g_\chi/M_{Z'}^2$. If this interaction is the only way dark matter can interact with the SM, the observed relic density will be obtained for $M_* \sim 1$ TeV for a WIMP mass around 100 GeV [79]. Such a vision of dark matter is constrained by LEP II through the L3 [99] and DELPHI [100] measurements of the process $e^+e^- \to \nu\overline{\nu}\gamma$ to $M_* \geq 480$ GeV [72]. While in principle the LHC could hope to observe processes such as $pp \to e^+e^-\chi\overline{\chi}$, the rates are very suppressed, and unlikely to provide better bounds than the LEP searches. A recent 500 GeV ILC study of the process $e^+e^- \to \chi\overline{\chi}\gamma$ reveals the ability to place much more stringent limits on the cross section, particularly if the beams may be polarized, which reduces the SM background [101]. The limits on the cross section translate into limits on M_* of about 1.7 TeV for 100 GeV mass WIMPs, leaving the ILC able to discover or rule out this class of leptophobic dark matter, and confirm its nature as a thermal relic.

References

[1] V. A. Kuzmin, V. A. Rubakov and M. E. Shaposhnikov, "On The Anomalous Electroweak Baryon Number Nonconservation In The Early Universe," Phys. Lett. B **155**, (1985) 36.

[2] A. G. Cohen, D. B. Kaplan and A. E. Nelson, Phys. Lett. B **245** (1990) 561; Nucl. Phys. B **349** (1991) 727; Nucl. Phys. B **373** (1992) 453; Phys. Lett. B **336** (1994) 41 [hep-ph/9406345]. For a review see e.g J. M. Cline, [hep-ph/0609145].

[3] M. Joyce, T. Prokopec and N. Turok, "Nonlocal electroweak baryogenesis. Part 1: Thin wall regime," Phys. Rev. D **53** (1996) 2930 [arXiv:hep-ph/9410281]. M. Joyce, T. Prokopec and N. Turok, "Nonlocal electroweak baryogenesis. Part 2: The Classical regime," Phys. Rev. D **53** (1996) 2958 [arXiv:hep-ph/9410282].

[4] F. Csikor, Z. Fodor, J. Heitger, "Endpoint of the hot electroweak phase transition," Phys. Rev. Lett. **82** (1999) 21-24. [hep-ph/9809291].

[5] M. B. Gavela, P. Hernandez, J. Orloff, O. Pene, "Standard model CP violation and baryon asymmetry," Mod. Phys. Lett. **A9**, 795-810 (1994). [hep-ph/9312215, hep-ph/9312215].

[6] P. Huet and A. E. Nelson, "Electroweak baryogenesis in supersymmetric models," Phys. Rev. D **53** (1996) 4578 [arXiv:hep-ph/9506477].

[7] J. M. Cline, M. Joyce and K. Kainulainen, "Supersymmetric electroweak baryogenesis," JHEP **0007** (2000) 018 [arXiv:hep-ph/0006119].

[8] M. S. Carena, M. Quiros, M. Seco and C. E. M. Wagner, "Improved results in supersymmetric electroweak baryogenesis," Nucl. Phys. B **650**, 24 (2003) [arXiv:hep-ph/0208043].

[9] M. Carena, G. Nardini, M. Quiros and C. E. M. Wagner, Nucl. Phys. B **812**, 243 (2009) [arXiv:0809.3760 [hep-ph]].

[10] T. Konstandin, T. Prokopec, M. G. Schmidt and M. Seco, "MSSM electroweak baryogenesis and flavour mixing in transport equations," Nucl. Phys. B **738**, 1 (2006) [arXiv:hep-ph/0505103].

[11] V. Cirigliano, S. Profumo and M. J. Ramsey-Musolf, "Baryogenesis, electric dipole moments and dark matter in the MSSM," JHEP **0607** (2006) 002 [arXiv:hep-ph/0603246].

[12] J. M. Cline, M. Jarvinen, F. Sannino, "The Electroweak Phase Transition in Nearly Conformal Technicolor," Phys. Rev. **D78**, 075027 (2008). [arXiv:0808.1512 [hep-ph]]. M. Jarvinen, T. A. Ryttov, F. Sannino, "The Electroweak Phase Transition in Ultra Minimal Technicolor," Phys. Rev. **D79**, 095008 (2009). [arXiv:0903.3115 [hep-ph]].

[13] P. Creminelli, A. Nicolis and R. Rattazzi, "Holography and the electroweak phase transition," JHEP **0203** (2002) 051 [arXiv:hep-th/0107141].

[14] L. Randall and G. Servant, "Gravitational Waves from Warped Spacetime," JHEP **0705** (2007) 054 [arXiv:hep-ph/0607158].

[15] G. Nardini, M. Quiros and A. Wulzer, "A Confining Strong First-Order Electroweak Phase Transition," JHEP **0709** (2007) 077 [arXiv:0706.3388 [hep-ph]].

[16] T. Konstandin, G. Nardini and M. Quiros, "Gravitational Backreaction Effects on the Holographic Phase Transition," arXiv:1007.1468 [hep-ph].

[17] J. R. Espinosa, T. Konstandin, J. M. No and G. Servant, "Energy Budget of Cosmological First-order Phase Transitions," JCAP **1006** (2010) 028 [arXiv:1004.4187 [hep-ph]].

[18] K. Agashe, R. Contino and A. Pomarol, Nucl. Phys. B **719**, 165 (2005) [hep-ph/0412089].

[19] R. Contino, arXiv:1005.4269 [hep-ph].

[20] J. R. Espinosa, T. Konstandin, J. M. No and G. Servant, JCAP **1006**, 028 (2010) [arXiv:1004.4187 [hep-ph]].

[21] T. Cohen, D. E. Morrissey and A. Pierce, arXiv:1203.2924 [hep-ph].

[22] D. Curtin, P. Jaiswal and P. Meade, arXiv:1203.2932 [hep-ph].

[23] A. Delgado, G. Nardini and M. Quiros, JHEP **1204**, 137 (2012) [arXiv:1201.5164 [hep-ph]].

[24] C. Grojean, G. Servant and J. D. Wells, Phys. Rev. D **71**, 036001 (2005) [hep-ph/0407019].

[25] C. Delaunay, C. Grojean and J. D. Wells, JHEP **0804**, 029 (2008) [arXiv:0711.2511 [hep-ph]].

[26] J. R. Espinosa, T. Konstandin and F. Riva, Nucl. Phys. B **854**, 592 (2012) [arXiv:1107.5441 [hep-ph]].

[27] J. R. Espinosa, B. Gripaios, T. Konstandin and F. Riva, JCAP **1201**, 012 (2012) [arXiv:1110.2876 [hep-ph]].

[28] M. Frigerio, A. Pomarol, F. Riva and A. Urbano, arXiv:1204.2808 [hep-ph].

[29] A. Noble and M. Perelstein, Phys. Rev. D **78**, 063518 (2008) [arXiv:0711.3018 [hep-ph]].

[30] C. Grojean and G. Servant, Phys. Rev. D **75**, 043507 (2007) [hep-ph/0607107].

[31] T. Konstandin and G. Servant, JCAP **1112**, 009 (2011) [arXiv:1104.4791 [hep-ph]].

[32] T. Konstandin and G. Servant, JCAP **1107**, 024 (2011) [arXiv:1104.4793 [hep-ph]].

[33] P. Binetruy, A. Bohe, C. Caprini and J. -F. Dufaux, JCAP **1206**, 027 (2012) [arXiv:1201.0983 [gr-qc]].

[34] S. Kraml and A. R. Raklev, Phys. Rev. D **73**, 075002 (2006) [hep-ph/0512284].

[35] B. Gripaios, A. Pomarol, F. Riva and J. Serra, JHEP **0904**, 070 (2009) [arXiv:0902.1483 [hep-ph]].

[36] J. Mrazek, A. Pomarol, R. Rattazzi, M. Redi, J. Serra and A. Wulzer, Nucl. Phys. B **853**, 1 (2011) [arXiv:1105.5403 [hep-ph]].

[37] G. Panico and M. Serone, JHEP **0505**, 024 (2005) [hep-ph/0502255].

[38] B. A. Campbell, J. Ellis and K. A. Olive, JHEP **1203**, 026 (2012) [arXiv:1111.4495 [hep-ph]].

[39] A. Tranberg and J. Smit, "Baryon asymmetry from electroweak tachyonic preheating," JHEP **0311**, 016 (2003) [arXiv:hep-ph/0310342].

[40] G. Bertone, D. Hooper and J. Silk, Phys. Rept. **405**, 279 (2005) [hep-ph/0404175].

[41] J. L. Feng, Ann. Rev. Astron. Astrophys. **48**, 495 (2010) [arXiv:1003.0904 [astro-ph.CO]].

[42] G. Steigman, B. Dasgupta and J. F. Beacom, arXiv:1204.3622 [hep-ph].

[43] J. L. Feng and J. Kumar, Phys. Rev. Lett. **101**, 231301 (2008) [arXiv:0803.4196 [hep-ph]].

[44] G. Servant and T. M. P. Tait, Nucl. Phys. B **650**, 391 (2003) [hep-ph/0206071].

[45] H. -C. Cheng, J. L. Feng and K. T. Matchev, Phys. Rev. Lett. **89**, 211301 (2002) [hep-ph/0207125].

[46] G. Burdman, B. A. Dobrescu and E. Ponton, JHEP **0602**, 033 (2006) [hep-ph/0506334].

[47] B. A. Dobrescu, D. Hooper, K. Kong and R. Mahbubani, JCAP **0710**, 012 (2007) [arXiv:0706.3409 [hep-ph]].

[48] T. Appelquist, H. -C. Cheng and B. A. Dobrescu, Phys. Rev. D **64**, 035002 (2001) [hep-ph/0012100].

[49] J. Hubisz and P. Meade, Phys. Rev. D **71**, 035016 (2005) [hep-ph/0411264].

[50] A. Birkedal, A. Noble, M. Perelstein and A. Spray, Phys. Rev. D **74**, 035002 (2006) [hep-ph/0603077].

[51] H. -C. Cheng and I. Low, JHEP **0309**, 051 (2003) [hep-ph/0308199].

[52] L. Randall and R. Sundrum, Phys. Rev. Lett. **83**, 3370 (1999) [hep-ph/9905221].

[53] K. Agashe and G. Servant, Phys. Rev. Lett. **93**, 231805 (2004) [hep-ph/0403143].

[54] K. Agashe and G. Servant, JCAP **0502**, 002 (2005) [hep-ph/0411254].

[55] C. B. Jackson, G. Servant, G. Shaughnessy, T. M. P. Tait and M. Taoso, JCAP **1004**, 004 (2010) [arXiv:0912.0004 [hep-ph]].

[56] ATLAS Collaboration, ATLAS-CONF-2012-033 (2012).

[57] CMS Collaboration, CMS-SUS-12-011 (2012).

[58] S. Chatrchyan *et al.* [CMS Collaboration], Phys. Lett. B **710**, 26 (2012) [arXiv:1202.1488 [hep-ex]].

[59] G. Aad *et al.* [ATLAS Collaboration], Phys. Lett. B **710**, 49 (2012) [arXiv:1202.1408 [hep-ex]].

[60] M. W. Cahill-Rowley, J. L. Hewett, A. Ismail and T. G. Rizzo, arXiv:1206.5800 [hep-ph].

[61] For a recent status report with theoretical perspective, see: S. Kraml, arXiv:1206.6618 [hep-ph].

[62] A. Birkedal, K. Matchev and M. Perelstein, Phys. Rev. D **70**, 077701 (2004) [hep-ph/0403004].

[63] Q. -H. Cao, C. -R. Chen, C. S. Li and H. Zhang, JHEP **1108**, 018 (2011) [arXiv:0912.4511 [hep-ph]].

[64] M. Beltran, D. Hooper, E. W. Kolb and Z. C. Krusberg, Phys. Rev. D **80**, 043509 (2009) [arXiv:0808.3384 [hep-ph]].

[65] W. Shepherd, T. M. P. Tait and G. Zaharijas, Phys. Rev. D **79**, 055022 (2009) [arXiv:0901.2125 [hep-ph]].

[66] M. Beltran, D. Hooper, E. W. Kolb, Z. A. C. Krusberg and T. M. P. Tait, JHEP **1009**, 037 (2010) [arXiv:1002.4137 [hep-ph]].

[67] J. Goodman, M. Ibe, A. Rajaraman, W. Shepherd, T. M. P. Tait and H. -B. Yu, Phys. Lett. B **695**, 185 (2011) [arXiv:1005.1286 [hep-ph]].

[68] Y. Bai, P. J. Fox and R. Harnik, JHEP **1012**, 048 (2010) [arXiv:1005.3797 [hep-ph]].

[69] J. Goodman, M. Ibe, A. Rajaraman, W. Shepherd, T. M. P. Tait and H. -B. Yu, Phys. Rev. D **82**, 116010 (2010) [arXiv:1008.1783 [hep-ph]].

[70] J. Goodman, M. Ibe, A. Rajaraman, W. Shepherd, T. M. P. Tait and H. -B. Yu, Nucl. Phys. B **844**, 55 (2011) [arXiv:1009.0008 [hep-ph]].

[71] K. Cheung, P. -Y. Tseng and T. -C. Yuan, JCAP **1101**, 004 (2011) [arXiv:1011.2310 [hep-ph]].

[72] P. J. Fox, R. Harnik, J. Kopp and Y. Tsai, Phys. Rev. D **84**, 014028 (2011) [arXiv:1103.0240 [hep-ph]].

[73] J. -F. Fortin and T. M. P. Tait, Phys. Rev. D **85**, 063506 (2012) [arXiv:1103.3289 [hep-ph]].

[74] K. Cheung, P. -Y. Tseng and T. -C. Yuan, JCAP **1106**, 023 (2011) [arXiv:1104.5329 [hep-ph]].

[75] A. Rajaraman, W. Shepherd, T. M. P. Tait and A. M. Wijangco, Phys. Rev. D **84**, 095013 (2011) [arXiv:1108.1196 [hep-ph]].

[76] P. J. Fox, R. Harnik, J. Kopp and Y. Tsai, Phys. Rev. D **85**, 056011 (2012) [arXiv:1109.4398 [hep-ph]].

[77] A. Rajaraman, T. M. P. Tait and D. Whiteson, arXiv:1205.4723 [hep-ph].

[78] K. Cheung, P. -Y. Tseng, Y. -L. S. Tsai and T. -C. Yuan, JCAP **1205**, 001 (2012) [arXiv:1201.3402 [hep-ph]].

[79] R. Harnik and G. D. Kribs, Phys. Rev. D **79**, 095007 (2009) [arXiv:0810.5557 [hep-ph]].

[80] P. J. Fox and E. Poppitz, Phys. Rev. D **79**, 083528 (2009) [arXiv:0811.0399 [hep-ph]].

[81] Q. -H. Cao, E. Ma and G. Shaughnessy, Phys. Lett. B **673**, 152 (2009) [arXiv:0901.1334 [hep-ph]].

[82] O. Adriani *et al.* [PAMELA Collaboration], Nature **458**, 607 (2009) [arXiv:0810.4995 [astro-ph]].

[83] M. Ackermann *et al.* [Fermi LAT Collaboration], Phys. Rev. Lett. **108**, 011103 (2012) [arXiv:1109.0521 [astro-ph.HE]].

[84] K. A. Olive, G. Steigman and T. P. Walker, Phys. Rept. **333**, 389 (2000) [astro-ph/9905320].

[85] E. A. Baltz, M. Battaglia, M. E. Peskin and T. Wizansky, Phys. Rev. D **74**, 103521 (2006) [hep-ph/0602187].

[86] A. Birkedal, K. Matchev, J. Alexander, K. Ecklund, L. Fields, R. C. Gray, D. Hertz and C. D. Jones *et al.*, eConf C **050318**, 0708 (2005) [hep-ph/0507214].

[87] A. Birkedal, AIP Conf. Proc. **805**, 55 (2006) [hep-ph/0509199].

[88] J. L. Feng, M. E. Peskin, H. Murayama and X. R. Tata, Phys. Rev. D **52**, 1418 (1995) [hep-ph/9502260].

[89] B. C. Allanach, G. Belanger, F. Boudjema and A. Pukhov, JHEP **0412**, 020 (2004) [hep-ph/0410091].

[90] M. M. Nojiri, G. Polesello and D. R. Tovey, JHEP **0603**, 063 (2006) [hep-ph/0512204].

[91] S. Matsumoto, M. Asano, K. Fujii, T. Honda, R. S. Hundi, H. Ito, S. Kanemura and T. Nabeshima *et al.*, Nuovo Cim. **034C**, 93 (2011).

[92] J. A. Conley, H. K. Dreiner and P. Wienemann, Phys. Rev. D **83** (2011) 055018 [arXiv:1012.1035 [hep-ph]].

[93] H. Baer, V. Barger, P. Huang and X. Tata, JHEP **1205**, 109 (2012) [arXiv:1203.5539 [hep-ph]].

[94] H. Baer, A. Belyaev, T. Krupovnickas and X. Tata, JHEP **0402**, 007 (2004) [hep-ph/0311351].

[95] T. Moroi, Y. Shimizu and A. Yotsuyanagi, Phys. Lett. B **625**, 79 (2005) [hep-ph/0505252].

[96] T. Moroi and Y. Shimizu, Phys. Rev. D **72**, 115012 (2005) [hep-ph/0509196].

[97] S. Kanemura, S. Matsumoto, T. Nabeshima and H. Taniguchi, Phys. Lett. B **701**, 591 (2011) [arXiv:1102.5147 [hep-ph]].

[98] E. Kato, M. Asano, K. Fujii, S. Matsumoto, Y. Takubo and H. Yamamoto, arXiv:1203.0762 [hep-ph].

[99] P. Achard *et al.* [L3 Collaboration], Phys. Lett. B **587**, 16 (2004) [hep-ex/0402002].

[100] J. Abdallah *et al.* [DELPHI Collaboration], Eur. Phys. J. C **38**, 395 (2005) [hep-ex/0406019].

[101] C. Bartels, M. Berggren and J. List, arXiv:1206.6639 [hep-ex].

[102] M. J. Dolan, C. Englert and M. Spannowsky, arXiv:1206.5001 [hep-ph].

[103] M. Moretti, S. Moretti, F. Piccinini, R. Pittau and A. D. Polosa, JHEP **0502**, 024 (2005) [hep-ph/0410334].

[104] U. Baur, Phys. Rev. D **80**, 013012 (2009) [arXiv:0906.0028 [hep-ph]].

[105] D. Boumediene and P. Gay, eConf C **0705302**, HIG06 (2007) [arXiv:0801.0866 [hep-ex]].

[106] E. Accomando *et al.* [CLIC Physics Working Group Collaboration], hep-ph/0412251.

[107] J. Tian, K. Fujii and Y. Gao, arXiv:1008.0921 [hep-ex].

[108] G. Belanger, A. Pukhov and G. Servant, JCAP **0801**, 009 (2008) [arXiv:0706.0526 [hep-ph]].

[109] M. Cirelli, P. Panci, G. Servant and G. Zaharijas, JCAP **1203**, 015 (2012) [arXiv:1110.3809 [hep-ph]].

[110] X. Chu, T. Hambye and M. H. G. Tytgat, JCAP **1205**, 034 (2012) [arXiv:1112.0493 [hep-ph]].

[111] W. Buchmuller, V. Domcke and K. Schmitz, Phys. Lett. B **713**, 63 (2012) [arXiv:1203.0285 [hep-ph]].

9 Conclusion

In this report, we have surveyed the range of physics topics that will be addressed by the ILC.

Our primary emphasis has been on the study of a Standard Model-like Higgs boson. The discovery of a new boson by the ATLAS and CMS experiments has vaulted the question of its properties of the top of the list of questions in high energy physics. We have argued that the ILC is perfectly matched to this problem. The ILC will be able to deliver a precise description of the properties of this new particle.

The ability of the ILC to operate at several different energies plays an important role it its ability to study the Higgs boson. We have described three phases of the Higgs boson program. First, at $\sqrt{s} = 250$ GeV, one may expect the precision measurement of the Higgs mass and its major branching fractions and the search for invisible and exotic modes. Second, at $\sqrt{s} = 500$ GeV, we anticipate precision measurements of the Higgs coupling to the W boson and the higher statistics study of modes with small branching fractions. Finally, at $\sqrt{s} = 1$ TeV, for the measurement of the Higgs couplings to the top quark and the muon, and the Higgs self-coupling can be made. The suite of measurements at these three energies combine to provide a complete picture of the interactions of this particle and an incisive test of its role in the generation of mass for all elementary particles.

We have also emphasized the ability of the ILC to carry out precision measurements of the properties of the W and Z bosons and the top quark, and of elementary $e^+e^- \to 2$ fermion reactions. In addition, we have shown that the ILC has excellent capabilities to study new color-singlet particles that might be present in the mass range of a few hundred GeV.

The nature of the Higgs boson and the origin of electroweak symmetry breaking remains a central and puzzling problem. The traditional approaches to this problem either involve strong coupling in the Higgs sector, building the Higgs boson as a composite state, or weak coupling in the Higgs sector, realizing the Higgs as one member of a new multiplet of particles. Both types of models have been reshaped by the discoveries and exclusions from the LHC.

If the Higgs sector is strongly coupled, the model must be one with a light composite Higgs boson and additional vectorlike particles at the TeV scale. We have shown how the precision measurement capabilities of the ILC will give important clues to the properties of these models that will not be available from the LHC.

If the Higgs sector is weakly coupled, it is very likely that there are new color-singlet particles that are extremely difficult to study at the LHC. We have argued, in particular, that the LHC results motivate models of supersymmetry that have a spectrum of this type. The colored states of the supersymmetry spectrum may well be discovered in the 14 TeV program of the LHC. The lightest particles of supersymmetry, with their possible connection to the dark matter of the universe, will require the ILC for their proper understanding. For the highly motivated case of *natural* supersymmetry, the ILC could make the definitive test of this class of models since charged higgsinos are expected to be present with mass below about 200 GeV. If these light higgsinos do indeed exist, then ILC would be a higgsino factory in addition to a Higgs factory!

For both types of models, the precision study of the Higgs boson will provide essential clues. To obtain these clues, we have shown that it will be necessary to measure the couplings of the Higgs boson at the few percent level. The ILC will give us that capability.

For all of these reasons, the physics questions that are before us now call for the ILC as the next major facility in high energy physics.